MICRO-MECHANICAL TESTING OF THE HEX-BN INTERPHASE IN SIC_f/SIC COMPOSITES FOR AERO-PROPULSION

Robin M. G. De Meyere[1] *

St Edmund Hall
University of Oxford

A thesis submitted for the degree of:
Doctor of Philosophy (DPhil)

Michaelmas 2017 - Trinity 2021

Academic Supervisors:

Prof. David E.J. Armstrong[1]
Prof. T. James Marrow[1]
[1]Department of Materials, University of Oxford

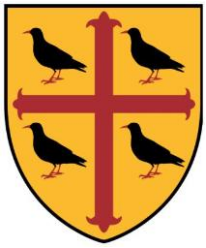
Rolls-Royce Leads:

Louise Gale, CEng
Stephen Harris
Ian Edmonds, EngD

Board of Examiners:

Prof. Elizabeth Opila[2],
Prof. Angus J. Wilkinson[1]
[2]Department of Materials, University of Virginia

This page intentionally left blank



This document may contain sensitive proprietary information – it outlines a thesis in partial fulfilment for the degree of DPhil in Materials at the University of Oxford – Submitted 30.06.2021 – Defended 18.08.2021 & Edited 06.09.2021 after minor corrections.

This document may contain Export Control 1E001-classed information. This information is controlled by the EU Dual-Use List and is being exported to a UGEA country (Australia, Canada, Japan, New Zealand, Norway, Switzerland, USA) under UGEA EU001. A further license may be required to re-export such "Controlled Technology".

I, Robin M.G. De Meyere, certify that this thesis 'Micro-Mechanical Testing of the hex-BN Interphase in SiC_f/SiC Composites for Aero-Propulsion'' was undertaken under the supervision of Prof. David E.J. Armstrong & Prof. T. James Marrow from September 2017 to June 2021, and that all written and experimental work is original - unless specifically stated otherwise, whereby appropriate referencing was employed. Where the work of others has been used, this has been acknowledged in the text. The authors have been made fully aware of the Oxford University plagiarism policies.

This thesis contains 39,701 words and thus, complies with the word limit regulation of 40,000 words.

Keywords: Aerospace, CMC, Micromechanics, Composites, Processing, SiC/SiC, SiC_f/SiC, Nano-Indentation, Interfaces, Interfacial Shear Strength, Fibre Push-out, Push-in, Push-back, In-situ Testing, Micromechanical Testing, Fracture Toughness

Acknowledgements

"Entrepreneurship is when an individual retrieves a red hot idea from the creativity furnace without the constraint of the heat of lean resources, and with each persistent blow of the innovation hammer shapes the still malleable idea against the anvil of passion, vision, insight, strategy, and principles to forge a fitting vessel of a creative concern." - Amah Lambert

I would be amiss to attribute achievements in this thesis to my efforts alone, for there are many people to thank for the past four years of my life at Oxford.

My two academic supervisors Prof. David Armstrong & Prof. James Marrow are the first I have to acknowledge, for they have provided both the perfect environment to nurture my growth, and a faultless level of support. I have always praised how lucky I was to have been paired to a project involving such talented experts and rigorous academics equipped with 'people' skills – a combination unmatched. Dave, you were sure to welcome me with open arms since day one, you personally introduced me to so many academics in the field, persistently commended me for my work ethic, and was always sure to have my back when I needed it. James, you gave me the most stringent feedback and the most meticulous eye for detail, shaping me to become the scientist I am today. Both of your management styles complemented each other very well. I am sure my DPhil would have veered for the worst if I did not have such world-class supervision and guidance.

Thank you to my Rolls-Royce leads – in particular Louise Gale, Stephen Harris and Ian Edmonds, whom have provided a structure to my thesis and my time here at Oxford. You all were incredibly friendly and constantly praising my work – both on-call and in-person. Thank you to Mike Goode and Lisa Toller-Nordström on supporting my work with Rolls-Royce and for providing company during monthly meetings and CoP's. My thanks extend to all the fellow PhD/DPhil/EngD students I met working with Rolls-Royce at the other UTC's: Oriol Gavaldà-Diaz, Riccardo Manno & my fellow Rolls-Royce Doctorate Committee members Emma, Don, Sajal, Sarah, Anthony & Yuean.

I am so grateful for all the people who have helped me create, taught at, and assisted in one way or another with my second home: The Oxford University Pole Sports club – in particular Cheryl So, Rebecca Clarke, Amelia Brasnett, Rachel Parker, Maisie Volanz, Angela Wu, Divya Maniar, Melissa Lee, Julia Humes, Rowan Davis and Emily Chen. The club is part of my legacy at Oxford, and I hope it continues to thrive and blossom over the coming years. My gratitude also extends to the Sports Federation and the colleges whom have assisted in making the club, filming the trailer (GTC, New) & funded my Olympic-level judge qualifications (St Edmund Hall). I am further grateful for having lived so symbiotically with fellow Aularians Jessica Page (my first Oxford connection), Faidra Faitaki, Ceren Zor, Ben Evans & Yusuf Ikbal; you all grounded my sanity during a global pandemic. Thank you to the purest of clouds, Kwok Cheung, I wish we had crossed paths earlier on in my DPhil years; your calming presence during ballet and your therapeutic videos helped me countlessly in my write-up stage.

I am grateful for the Oxford Micromechanics Group (OMG), a collective of academics all so welcoming and innovative, thanks to the hard work of Prof. Angus Wilkinson, Dr. Bo-Shiuan Li, Dr.

Anna Kareer, Dr. Katie Kumamoto & Dr. Phani Karamched to name a few. Thank you to Prof. Richard Todd for letting me use the ceramics & composite labs, but also for the most inspiring and comprehensive set of lectures I attended in my time here. Thank you to the DCCEM staff for training me on all the microscopes and ion beams – and for recognising my talent as an "artistic engineer".

I want to dearly thank my fellow DPhil cohort – most notably (soon to be Dr.'s) Christopher Magazzeni, Edward Roberts, Shahnaz Hoque, Bethany Jim, Thomas Zhillardt, Diana Avadanii, Dominic Spencer-Jolly, Jack Fawdon and Zhouran Zhang – whom have not only provided support in the office and labs experimentally, but have forged a comforting space for us to collectively jump over the doctorate hurdles. My academic life could not be complete without my social life; for the latter I thank my fellow LGBT+ (and allies), STEM & Teddy support systems: Jake Taylor, George Stannard, Maria Alfaro, Cameron Gardner, Samuel Weber, Léa Cantor, Cyril Deroy, George Maier, Martin Babička, & last but certainly not least, Basia Tanska.

Finally, my level of gratitude for my family is immeasurable. Thank you to my sister Olivia De Meyere with her artistic eye and moral support, for contributing to so many figures in this thesis and for designing the OMG logo, all the whilst finishing her own Maths & Comp Sci studies at Worcester College; and to mom and dad for always striking the perfect balance between pushing for our success and providing the space(s) for us to reflect.

Floreat Aula • Aula Sancti Edmundi



Abstract

This thesis provides an overview of micro-level mechanical testing of the BN interphase in SiC_f/BN/SiC composites, in the context of lifing models for aero-engine components. A wide number of variables were tackled in the development of both traditional and novel techniques to assess micro-level properties of the composites. The latter included the interfacial shear strength (varied), modulus (25.9 ± 5.4 GPa), hardness (1.3 ± 0.1 GPa), fracture toughness (6.7 ± 2.4 $MPa.m^{1/2}$), debonding toughness (13.3 $J.m^{-2}$), and frictional sliding resistance (4 ± 1 MPa) of the interphase, alongside other composite constituents where applicable.

The use of a nanoindentation apparatus was central to this work – both Berkovitch and flat-punch tip geometries were made use of. Established techniques were assessed in their viability for probing the properties of the BN interphase on its own: these included the fibre push-out, push-in and push-back. Due to the sheer volume of data, the significance of results was assessed statistically.

Upon completion of method development, material-dependent variables and their effects on the change in micro-mechanical behaviour were subsequently investigated. The parameters tackled included the variability in measurements from tow location at weave-architecture level (inter-tow), tow level (intra-tow), BN interphase thickness, nature of fibre type, cyclic testing, interphase doping levels and neighbouring fibre geometry; where it was found that a need for intra-tow variability was to be stressed over the importance of inter-tow variability in measurements of mechanical properties, although both were found to be statistically relevant.

The ceramic-matrix composites were subsequently exposed to high relative humidity and elevated temperatures; and tests repeated. The degradation from intermediate-to-high temperatures showed little to no change in mircromechanical performance (strength retention ratio of 79.1%) when compared to low-temperature high humidity exposure (strength retention ratio of less than 50% after 500 hours exposure). Despite results from these chapters, a further understanding of the dominating failure mechanism needed to be understood. This led to the development of miscellaneous micro-mechanical techniques performed in-situ (both in SEM, micro and nano-XCT), including the novel trench push-out which imaged mixed-mode failure (simultaneous inside and outside debonding) and defective interphases leading to linking of smaller cracks before push-out.

In the context of work by Rolls-Royce plc, the body of results yields both quantitative and qualitative information, for incorporation in coupon-level lifing models. The academic merit of this work lies in the investigation of variability in measurements of composite interphase properties, as well as micromechanical-technique development for a clearer understanding of the damage mechanisms at hand.

Research Output

Publications:

De Meyere R., Gale L., Harris S., Edmonds E., Reis F., Marrow TJ., Saiz E., Giulani F., Armstrong D., Gavalda-Diaz O. '*A novel trench fibre push-out method to evaluate interfacial failure in long fibre composites.'* **Journal for Materials Research** 1–10 (2021). doi:10.1557/s43578-021-00153-1

Ning Z., Spencer Jolly D., Li G., **De Meyere R.**, Pu S., Chen Y., Kasemchainan J., Ihli J., Gong C., Liu B., Bonnin A., Magdysyuk O, Adamson P., Hartley G., Monroe C., Marrow TJ, Bruce P. '*Visualising Plating-Induced Cracking in Lithium Anode Solid Electrolyte Cells*' **Nature Materials** 2020

De Meyere R., Gale L., Harris S., Edmonds E., Reis F., Marrow TJ., Armstrong D. '*Optimising The Fibre Pushout Method to Evaluate Interfacial Failure in SiC$_f$/BN/SiC Ceramic Matrix Composites for Aerospace Applications.'* **Journal of the American Ceramic Society** (2020)

Manno R., **De Meyere R**., Armstrong D., Allegri G. 2020. '*Virtual Testing of Ceramic Matrix Composites Pushouts*.' (Draft Manuscript) 2021

Pirzada T., Galano M., Singh S., **De Meyere R**., Earp P., Marrow TJ, '*Effects of processing parameters on the mechanical and thermal properties of Nextel 312 Fibre SiOC ceramic matrix composites.'* **Composites Part A** JCOMA-20-1163 2020

De Meyere R. *'London Fashion Week – Women's Collections SS20'* – **The Panoptic** 2019

Hussey, A., **De Meyere, R**., Deck C., Armstrong D., Zayachuk, Y., 2020. '*Statistically sound application of fiber push-out method for the study of locally non-uniform interfacial properties of SiC-SiC fiber composites*.' **Journal of the European Ceramic Society** 40, 1052–1056. 2019

De Meyere R. *'London Fashion Week – Men's & Women's Collections'* – **The Panoptic** 2018

De Meyere R. *'Aerospace Materials in Fashion'* – **The Panoptic** 2017

Conferences:

- *ICC8 International Conference for Ceramics 2020/21* – **Busan**
- *LGBTSTEMinar 2021* – **Oxford** (Organising Committee – Head of Abstracts)
- *The Advanced Materials Show / Ceramics UK* – **Stoneleigh** (Invited Speaker)
- *2-DRAC Research Meeting on Advanced Ceramics (IOM^3+ British Ceramic Society)* – **Virtual** (Invited Speaker)
- *Rolls-Royce Doctoral Conference 2020* – **Virtual** (Organising Committee – Head of Speakers)
- *LGBTSTEMinar 2020* – **Birmingham**
- *ECI Nanomechanical Testing in Materials Research and Development VII* – **Malaga**
- *HT-CMC10 High-Temperature Ceramic-Matrix Composites 2019* – **Bordeaux**
- *Goldmisths' Company Jewellery Materials Congress 2019* – **London**
- *XVI ECerS Conference 2019* – **Turin**
- *ECerS Summer School on Reactivity of Thermo-Structural Composites & Refractories 2019* – **Turin**
- *LGBTSTEMinar 2019* – **London**

Prizes • Qualifications:

- St Edmund Hall College | ***Simon, Arpi & Marie Simonian Prize for Excellence in Leadership***
- IUK Chapter Ceramics Talent 2020 | ***Nominee, Invited Speaker***
- International Pole Sports Federation 2020 & 2021 | ***Level 2 Judges Certification in Pole Sports***
- Royal Microscopy Society / mmC2019 International Scientific Imaging Competition | ***People's Choice Award***
- DCCEM Microscopy Competition Oxford University | ***Overall Winner (Judges' Choice) 2019***
- St Edmund Hall | ***Masterclass Award 2018***
- St Edmund Hall College | ***Graduate Travel Award 2018***

Table of Contents

ACKNOWLEDGEMENTS 2
ABSTRACT 4
RESEARCH OUTPUT 5
PUBLICATIONS
CONFERENCES
PRIZES • QUALIFICATIONS

TABLE OF CONTENTS 6
GLOSSARY & ACRONYMS 9

1 CHAPTER 1 • INTRODUCTION 10

1.1 MOTIVATION • PROJECT BACKGROUND 10
1.2 AIMS & OBJECTIVES 11

2 CHAPTER 2 • LITERATURE REVIEW 13

2.1 INTRODUCTION 13
2.1.1 CERAMIC-MATRIX COMPOSITES 13
2.1.2 CMC TOUGHENING 15
2.1.3 SiC_F/SiC IN AEROSPACE 18
2.1.4 SiC FIBRES 21
2.1.5 THE MATRIX 22
2.1.6 THE BN INTERPHASE 23
2.2 MICROMECHANICAL TESTING OF CMC'S 25
2.2.1 THE FIBRE PUSH-OUT TECHNIQUE 28
2.2.1.1 Method 28
2.2.1.2 Extractable Properties 29
2.2.1.3 The Fibre Push-Out Technique Applied to SiC_f/BN/SiC 31
2.2.1.4 Technique Limitations 31
2.2.2 THE FIBRE PUSH-IN TECHNIQUE 35
2.2.3 THE FIBRE PUSH-BACK TECHNIQUE 37
2.2.4 MISCELLANEOUS ADVANCED TECHNIQUES 37
2.2.5 MICRO-MECHANICAL TESTING SUMMARY 40
2.3 RESEARCH & DEVELOPMENT 41
2.3.1 INTERPHASE DOPING 42
2.3.2 MULTI-LAYERED INTERPHASES 42
2.3.3 FUGITIVE INTERPHASES 44
2.3.4 MATRIX GETTERS 44
2.3.5 FIBRE SUBSTITUTION 44
2.3.6 INTERPHASE SUBSTITUTION 45
2.3.7 MANUFACTURING PARAMETERS 45
2.3.8 INTERPHASE THICKNESS & BN LATTICE SPACING 46

2.3.9 CRACK HEALING 46
2.3.10 MODELLING EFFORTS 46
2.4 KNOWLEDGE GAP ANALYSIS 48
2.5 CHAPTER SUMMARY 48

3 CHAPTER 3 • EXPERIMENTAL METHODS & OPTIMISATION 49

3.1 THE MATERIAL 49
3.2 CONSTITUENT(S) HARDNESS & MODULI 50
3.2.1 BERKOVITCH INDENTATION 50
3.2.1.1 Bulk Measurements 50
3.2.1.2 Array Indentation (Melt Infiltrated Matrix) 53
3.2.1.3 Microcomposites (BN Interphase) 55
3.2.1.4 Microcomposites – Pin Cold-Set Epoxy Mounted 56
3.2.2 EXPRESS MAPPING (FAST INDENTATION) 58
3.2.3 INDENTATION SUMMARY 60
3.3 OPTIMISING FIBRE PUSH-OUT PARAMETERS 62
3.3.1 BASICS OF FIBRE PUSH-OUT 62
3.3.2 EFFECT OF SAMPLE THICKNESS 63
3.3.3 EFFECT OF TIP SIZE 66
3.3.4 EFFECT OF TIP-INDUCED PLASTIC DEFORMATION 67
3.3.5 EFFECT OF STRAIN RATE 67
3.4 INVESTIGATING LOCAL FIBRE ENVIRONMENT EFFECTS 73
3.4.1 INTER-TOW VARIATIONS 73
3.4.2 INTRA-TOW VARIATIONS 74
3.4.3 CASCADE PUSH-OUTS 74
3.5 FIBRE PUSH-INS & PUSH-BACKS 75
3.6 ADVANCED METHODS 76
3.7 CHAPTER CONCLUSIONS 76

4 CHAPTER 4 • MATERIAL VARIABLES 77

4.1 MATERIAL DATABASE 77
4.2 COMPOSITE CHARACTERISATION (GEOMETRIC VARIABLES) 78
4.3 INTERTOW VARIATIONS 80
4.4 INTRATOW VARIATIONS 81
4.4.1 EFFECT OF FIBRE TYPE 81
4.4.2 EFFECT OF TEST LOCATION WITHIN A TOW 82
4.4.3 EFFECT OF BN INTERPHASE THICKNESS 84
4.4.4 EFFECT OF NEIGHBOURING FIBRES (‘*CASCADE*’ PUSH-OUTS) 85
4.5 DISCUSSION (MATERIAL VARIABLES) 86
4.6 PUSH-INS 87
4.7 PUSH-BACKS & FRICTIONAL STUDIES 89
4.8 STATISTICAL APPROACH & SHEAR-LAG MODEL 93
4.8.1 MAXIMUM LIKELIHOOD ESTIMATES (MLE’S) 93
4.8.2 WELCH UNEQUAL VARIANCE T-TEST 94
4.8.3 WEIBULL STATISTICS 95

4.8.4 SHEAR-LAG MODEL FITTINGS 96
4.9 FATIGUE & CYCLIC TESTING OF THE INTERPHASE 98
4.10 DOPING THE INTERPHASE 101
4.11 CHAPTER SUMMARY 109

5 CHAPTER 5 • DEGRADATION 111

5.1 ABSTRACT 111
5.2 INTRODUCTION 111
5.2.1 SIC OXIDATION 111
5.2.2 FIBRE OXIDATION 112
5.2.3 BN INTERPHASE OXIDATION 112
5.3 SURFACE DEGRADATION 115
5.4 MECHANICAL PERFORMANCE 118
5.5 INTERTOW & INTRATOW VARIATIONS 121
5.6 INTRATOW VARIATIONS 123
5.7 INTERTOW VARIATIONS 125
5.8 PUSH-BACKS & FRICTION STUDIES 126
5.9 DISCUSSION 128
5.10 HIGH-TEMPERATURE FIBRE PUSH-OUTS 129
5.10.1 BACKGROUND 129
5.10.2 METHODS 129
5.10.3 RESULTS 130
5.11 CHAPTER SUMMARY 132

6 CHAPTER 6 • VISUALISING FAILURE 133

6.1 INTRODUCTION 133
6.2 IN-SITU TRENCH PUSH-OUTS 133
6.2.1 ABSTRACT 133
6.2.2 INTRODUCTION 134
6.2.3 METHODS 135
6.2.4 RESULTS 136
6.2.5 DISCUSSION 144
6.2.6 SUMMARY (TRENCH PUSH-OUT 146
6.3 DIC 146
6.4 MICRO-TOMOGRAPHY OF COMPOSITES 148
6.5 NANOTOMOGRAPHY 150
6.6 LAMELLAE, TKD & TEM 153
6.7 K_C FRACTURE TOUGHNESS MEASUREMENTS 156
6.7.1 MICRO-CANTILEVERS ON BN 156
6.7.2 INDENT CRACK MEASUREMENTS FOR THE MI MATRIX 159
6.8 CHAPTER SUMMARY 161

7 CHAPTER 7 • CONCLUSIONS 162
8 CHAPTER 8 • REFERENCES 164

Glossary & Acronyms

ANOVA	Analysis of Variance
APS	Air Plasma Spray
BN	Boron Nitride
CDF	Cumulative Distribution Function
CMC	Ceramic Matrix Composite
CTE	Coefficient of Thermal Expansion
CVD	Chemical Vapour Deposition
CVI	Chemical Vapour Infiltration
DBTT	Ductile-to-Brittle Transition Temperature
DIC	Digital Image Correlation
DOD	Domestic Object Damage
DVC	Digital Volume Correlation
EBC	Environmental Barrier Coating
EBSD	Electron Backscattered Diffraction
EDX	Electron Dispersive X-Rays / Spectroscopy
EHT	Electron High Tension (Voltage)
ESB	Energy Selective Backscattered (Detector)
FEM	Finite Element Modelling
FIB	Focused Ion Beam
FOD	Foreign Object Damage
FOV	Field Of View
FR	Fano Resonance
GE	General Electric (Aviation)
GIS	Gas Injection System
HCP	Hexagonal Closed-Packed
HN	Hi-Nicalon (Fibre)
HNS	Hi-Nicalon type S (Fibre)
ICTS	Integral Ceramic Textile Structures
IPF	Inverse Pole Figure
ISS	Interfacial Shear Stress / Strength
LO	Longitudinal Optical (Phonon)
MI	Melt Infiltration
MLE	Maximum Likelihood Estimate
nanoCT	Nano (Computer-Aided) Tomography
NASA	National Aeronautics & Space Administration (of the USA)
NDT	Non-Destructive Testing
NITE	Nano-Infiltration and Transient Eutectic-phase (Process)
OBRS	Oxide Bonded Reaction Sintering
pyC(I)	Pyrolytic Carbon (Interlayer)
ROI	Region Of Interest
RR	Rolls-Royce (plc)
SDG	Sustainable Development Goals
SEM	Scanning Electron Microscope(y)
SiC	Silicon Carbide
STEM	Scanning Transmission Electron Microscopy
TBC	Thermal Barrier Coating
TEM	Transmission Electron Microscopy
TKD	Transmission Kikuchi Diffraction
TO	Transverse Optical (Phonon)
TRL	Technology Readiness Levels
TSA3	Tyranno type SA3 (Fibre)
UN	United Nations
xCT	Micro (Computer-Aided) Tomography
XFEM	Extended Finite Element Modelling

Chapter 1 • Introduction

1.1 Motivation • Project Background

This thesis investigates the degradation of the BN interlayer in silicon carbide fibre/silicon carbide matrix composites for engine components. SiC_f/SiC composites are finding renewed interest in the aerospace community for use as high temperature parts in engines due to the potential for reducing cooling air, emissions and the potential for a significant weight savings over metallic parts (by 2/3rd when compared to Nickel superalloys) – these components include combustion liners, seal segments, aerofoils and vanes. The implementation of CMC's (Ceramic Matrix Composite) will optimise cycle efficiency and thrust-to-weight ratio by increasing operational temperature from 1100ºC (with superalloys) to 1250ºC[1], whilst reducing ICAO (International Civil Aviation Organization) noise standards in engines. Other benefits of integrating CMC's in engine components include reducing thermal expansion (due to lower CTE's), thus improving turbine blade tip clearance whilst preventing strategic material problems in supply chain management. SiC_f/SiC composites also have great creep resistance, low thermal conductivity and high neutron damage tolerance / low neutron activation – additionally qualifying them as candidate materials for control sheath rods in the nuclear industry.

Due to the low fracture toughness of monolithic silicon carbide, the most promising toughening concepts use silicon carbide fibres embedded in a silicon carbide matrix. Despite being built of brittle ceramic materials; CMC's have distinct toughening mechanisms (including fibre pull-out) which upgrade their fracture behaviour to quasi-brittle / pseudo-ductile. The toughness of the composite is achieved by the application of an interphase coating to the fibre before the matrix is applied, which allows for cracks - which initiate in the matrix - to be deflected around the reinforcing fibre; thus increasing toughness from fibre pullout and crack bridging. It is critical for the interphase coating to maintain the appropriate properties (modulus, interfacial shear strength, friction, etc.) to maintain the desired composite behaviour throughout engine-condition cycles. There are two popular options for the coating material of the composite SiC fibres due to the coherence between BN and SiC lattices, the stabilising of the friction coefficient of SiC[2] and their high-temperature melting point[3]; these are pyrolytic carbon (pyC) for nuclear applications or hexagonal-Boron Nitride (hex-BN) for aerospace applications.

The main limitation faced by SiC-based composites lies in its degradation from exposure to corrosive environments, and its current inadequacy in adopting performance lifing models[4]. Over time, the BN interphase coating can degrade due to cyclic loading and environmental exposures as a result of frictional heating and oxidation. These can change the properties of the fibre interphase resulting in regions that are embrittled or have poor load sharing. Below 600ºC, static oxidation occurs whereby the formation of boria modifies the properties of the interlayer. SiC_f/SiC composites are elsewise subject to 'pest' oxidation whereby oxidation nurtures environmentally-assisted cracking at intermediate temperatures (500ºC - 1000°C) and high stresses (Over 100 MPa)[5,6]. Potential solutions are currently being investigated to alleviate the problem. These include tampering with the interface by doping, multi-layering, manufacturing fugitive interfaces, modifying the processing conditions or even changing the location of interfacial debonding during deformation – the first of which has been attempted in this work. Processing of the composites also has a significant effect on the properties of the interlayer, because residual stresses from the mismatch in CTE (coefficient of thermal expansion)

arise during both melt infiltration process (in the matrix) and CVI processes (for the BN & CVI SiC interlayers). Current literature and this thesis both aim to solve this problem.

Extracting the interfacial properties of the composite has however proven itself to be a major engineering challenge in materials science. A few meso-scale and macro-scale techniques highlighted by Bansal & Lamon[4] such as the transverse bend test, the traverse tensile test, the Brazilian disc compression test and the bilayered flexural test have shown experimental reproducibility, but are unsupported by sufficient modelling. The most accurate methods for determining the properties are found at the micro-scale due to reinforcement dimensions. These include the push-out, push-in and push-back methods on singular fibres – which are investigated alongside other micromechanical methods throughout this project. Micro-scale techniques bridge the gap between understanding atomic and molecular scale events and relating them to macro/meso scale mechanics – they also serve to validate models or predict macroscale behaviour from micro-experiments.

1.2 Aims & Objectives

This project made use of novel micro-mechanical testing methods to measure the strength and toughness of the interfaces in both the as-fabricated virgin material and in materials which have been environmentally aged for different lengths of time. The micromechanical tests provide understanding of the interfacial properties and how these impact mechanical response of the CMC's. The tests were performed in conjunction with X-ray tomography (lab-based) in order to relate the micro-scale properties as a function of temperature and degradation to bulk behaviour.

The project itself was split into three different aims over its duration. These included firstly, finding precise techniques and developing appropriate mechanical tests to characterise the initial properties of the BN interphase coating (such as the interlayer modulus, the interfacial shear strength and the friction coefficient) – as well as performing chemical analysis.

The second aim focussed on comparing the properties of the virgin (non-degraded) BN interlayer with a damaged interlayer (exposed in oxygen, water vapour, high-temperature and other destructive environments) whilst gaining a thorough understanding of the interphase behaviour under micromechanical loading. Particular focus was given to compare the frictional strength of the virgin BN layer with that of the oxidised BN interlayer. Finally, samples of different types of fibres and with different types of interlayer thicknesses were compared all throughout.

Finally, the third aim of the project was to look at how the interfacial properties impact the crack propagation behaviour. The mechanical performance of the interlayer after monotonic loading was contrasted to that of cyclic loading conditions. In-situ (SEM, TEM) and tomographic techniques including in-lab x-ray 3D tomography, as well as analytical techniques like Digital Image Correlation (DIC) captured changes in micro-mechanical behaviour with and without environmental degradation.

The main objective of the research therefore lay in finding estimates for the cyclic life of the composites by looking at the BN interlayer resistance to degradation (more specifically the interfacial strength, the friction coefficient and the fibre pull out length). All data produced in this work alongside fit-to-models will be used to create B-basis design allowables (values for which 90% of results are included with 95% confidence) in the later stages of TRL (Technology Readiness Levels) for CMC's, illustrated in Figure 1.

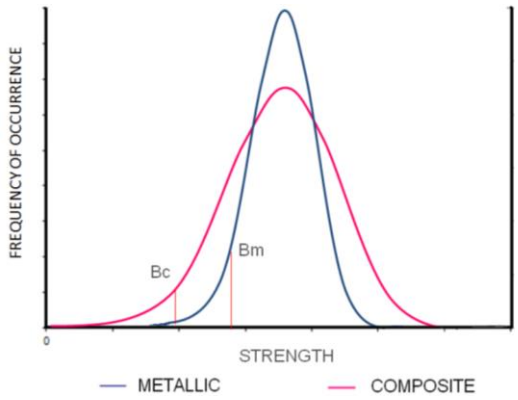


Figure 1: Illustration showing the variability of B-basis design allowables, with composites generally show larger variation in strength than their metallic counterpart - figure and caption: Spendley et al[7].

The overall project aimed to develop a more thorough understanding of the fundamental and theoretical mechanics of the interlayer at the microscale. The focus was on the internal recession of the BN interlayer (as opposed to the surface recession which will be solved by environment barrier coatings (EBC's)) and on how a degraded interface affects the tensile data at the macro scale. It is positioned to look at predictive lifing of the components – with priority use in stationary parts of the engines (such as seal segments). Parallel doctoral projects looked at the design and the manufacturing aspects of the same materials, as well as modelling of the behaviours observed – however the results of these were/are being published in peer-reviewed journals and were thus, not included in this thesis.

Chapter 2 • Literature Review

2.1 Introduction

2.1.1 Ceramic-Matrix Composites

CMC's (Ceramic Matrix Composites) consist of fibres imbedded in a matrix, bonded by an interphase[8, 9, 10] (Figure 2.a). The most common CMC's make use of carbon, alumina or silicon carbide (SiC) fibres incorporated in an alumina, carbon, SiC or mullite matrix[11]. An initial clear distinction should be made between an interphase (the 3D material layer coating the fibres) and an interface (a 2D surface connecting 2 different materials, e.g. the fibre/interphase interface or the matrix/interphase interface). The terms "interlayer" and "interphase" will be used interchangeably in this thesis, but both must be distinguished from "interface" as illustrated in Figure 2.b. CMC's have found use in multiple markets (automotive, nuclear, friction systems)[8] over the years for their high-performance mechanical and thermal properties, such as low coefficient of thermal expansion and high specific stiffness. CMC's are also notch-insensitive and have an increased damage tolerance when compared to most traditional ceramics or metals[1] – indeed their complex microstructure enables them to easily arrest or propagate cracks.

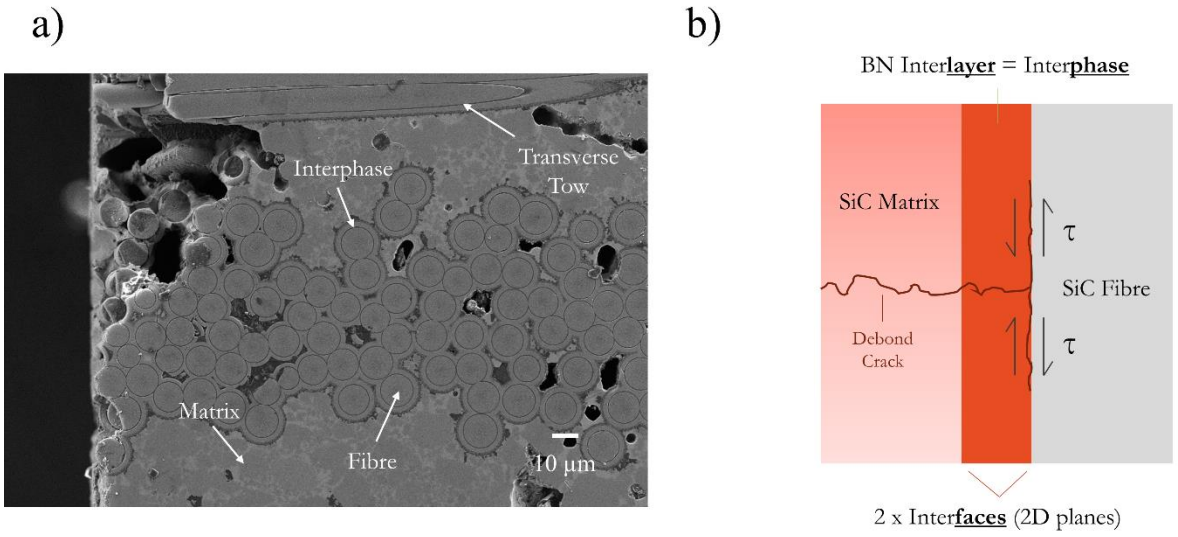


Figure 2: (a) Standard CMC microstructure and its constituents, (b) differentiating interphase and interface

In the aerospace industry, CMC's are selected for both jet and gas turbine engines (usually SiC/SiC and Ox/Ox) but also as heat shields on rocket nozzles and braking systems (usually C/C-SiC based)[12]. CMC's in engines increase cycle efficiency and thrust-to-weight ratio by increasing operational TET (Turbine Entry Temperature) from 1100 ºC (superalloy limit) to 1250 ºC[1], thereby potentially creating 6% in fuel consumption saving (equivalent to £1M in fuel savings each year per aircraft), whilst reducing ICAO (International Civil Aviation Organization) noise standards (higher bypass ratio jets, from "Chapter 4 – 2001" to "Chapter 14 - 2013" noise standards whereby people in "Day Night average sound Level (DNL) of 55 dB affected areas" are not affected anymore). Other benefits

of integrating CMC's in engine components include reducing weight (by 2/3rd when compared to nickel superalloys) – and therefore centrifugal forces generated – reducing thermal expansion (due to lower CTE's), as well as improving turbine blade tip clearance and preventing strategic material problems in supply chain management.

CMC's were first introduced on the Diamant French rocket in 1965, followed by the Ariane European rocket and the Hermes European shuttle in 1992[13]. The first demonstrator piece for CMC commercialisation was on the LEAP 1.x engine and the A3XX Neo Airbus series in 2018[14]. The first flight authorised with a CMC was on the nozzle of the TIGRE MTR-390 military helicopter in 1991 and the first EASA airworthiness certificate was attributed to the Airbus A320/CFM56 after 3 years of service and 4000 hours in flight[15]. Overall, CMC's have mostly been used in military engines in flaps, seals and after-burners in the exhaust section of the engines, but have yet to be widely commercially available[11]. The main drivers for increased CMC implementation in the military industry are the added thrust and ability for supercruise, whilst the main drivers for commercial aircrafts lie in the reductions of fuel consumption and weight. In the commercial industry, gas-turbine engines were sold at $USD 39 billion worldwide in 2015 when sales were projected to increase annually until 2028, with total valuation at $USD 1.07 trillion[16].

Whilst research on titanium alloys (which have limited temperature usability) and nickel-base super alloys (which add significant weight to the engines) has thrived, research in CMC components for engines has grown considerably in the last decades and substantial research is driven toward monitoring, lifing parts as well as repair methods – which are all well established for metallic components. For long-term solutions to component durability, three sources of attack[17] (high-velocity steam, oxidative permeation and CMAS) have been identified as the most aggressive, and therefore take priority to address. The reliability and predictability of CMC properties are also major obstacles to further engine implementation.

Indeed, the CMC fibre macrostructures demonstrate complexity, and their microstructural toughening mechanisms at the fibre/matrix interphase-scale are not fully understood. This complexity is also the source of robustness in the composites and can therefore not be simplified, both in processing or modelling. Impurities in the system, as well as sample processing and preparation, all add a layer of difficulty to our understanding of CMC behaviour. In general, different types of CMC samples can be manufactured for experimental purposes: these include microcomposites or minicomposites (single or multi-filament towed), 2D, 2.5D, 3D Orthogonal and 3D Orthogonal-Unbalanced composites – all exhibit a variety of micro mechanisms[8]. Finally, CMC's can also be split into three categories depending on their Fahrenheit maximum temperature usage: the CMC 1500 °F / 815 °C (Oxide/Oxide CMC's), 2400 °F / 1315 °C (SiC/SiC) and 2700 °F / 1482 °C (Carbide and Carbon based) families (all further discussed in Section 2.1.3) – the remainder of this thesis takes focus on the 2400 °F / 1315 °C family.

2.1.2 CMC Toughening

Despite being built of brittle ceramic materials, CMC's have good creep resistance and distinct toughening mechanisms (including fibre pull-out), which upgrade their fracture behaviour to quasi-brittle / pseudo-ductile and make them less notch-sensitive (i.e. the shaping of components is made easier as CMC's are insensitive to the roughness of outer edge). These micro-mechanisms include, but are not limited to: interface debonding, crack deflection at the interphase, crack branching inside the interphase, fibre bridging and most importantly, fibre pull-out. Fibre pull-out makes use of an interlayer between the fibre and matrix with distinct tribological properties, which enables transfer of load from one to the other[18]. Successful load transfer is characterised by high strains and premature 'yields'[19]. Fibres are able to slide along the interface, providing a source of displacement, absorbing elastic energy[20] and lowering thermal stresses at any crack tip. The end of the proportional limit on macro-testing curves usually corresponds to the saturation of matrix cracks, after which the quasi-plastic mechanisms highlighted above activate.

Provided the shear modulus is weak enough (40 GPa or less[21]), the interlayer or interphase (sometimes termed the 'ISSCL' or Interfacial Shear Strength Control Layer[22]) will fail first. This will pave the way for a matrix crack to deflect (from mode I to mode II cracking) and the fibre to pull-out – further toughening the bulk composite. The mechanism results in toughness values[3] averaging 20 $MPa.m^{1/2}$, although values in literature are varied and contested. A lack of crack deflection at the interphase results in large stress fields at the crack-tip and fibre-cut failures[23]. There is therefore an optimum debond length where toughening is provided both by crack deflection and even load sharing between composite components. Additionally, the interphase material can be thin enough (less than a micron thick – usually a few hundreds of nm), have low fracture toughness or low shear strength (less than 10 MPa) for the same fibre pull-out effect to occur. The interface between interphase and fibre directly correlates to specific composite characteristics such as the residual clamping stress and the fibre roughness – both of which increase the coefficient of friction[24]. The coefficient of friction must also adhere to a minimum value as the friction is necessary to stabilise crack propagation. Marshall mentions a subtle difference to be noted comparing the static to the dynamic friction coefficients – both of which have to be established in order to best describe crack propagation behaviour[25]. Finally, the fatigue life of specimens has been shown to negatively correlate to fibre pull-out strength[26], suggesting a balance between toughness and fatigue life needs to be struck.

In CMC's, cracking commonly occurs in the matrix first, with smaller failure strains in the matrix when compared to fibres[12]. In brittle systems akin to CMC's, Rebillat notes an increased shear stress field at the front of a crack tip causing increased microcrack density[19]. This was observed by Hilmas working on GE SiC_f/SiC composites whereby fibres breaking occurred close to macro matrix cracks and fibres first cracked around initial damage[27]. The onset of matrix cracking is termed the FCMS (the First Matrix Cracking Stress) and is used in the aerospace industry as a maximum allowable design stress for CMC's[28] (it is used in oxidising components only). In SiC_f/SiC composites, matrix cracking has been observed to initiate in weft tows away from pores[29]. Debonding with weak interlayers results in the bridging of matrix cracks (with the fibres), as well as a slowing down of the crack propagation, as the energy is transferred to de-bond the fibre from the matrix. Fibre coatings must be relatively thin (under 500 nm) in order to trigger the aforementioned fibre debonding[30] and maximise failure strains without hindering the ultimate strength properties. Matrix micro-cracking should have a high density for optimum pull-out effect[31] – matrix cracking densities can be predicted by steady-state energy balance models (e.g. Hutchinson and Evans[32]) or stress-intensity models (e.g.

Marshall[33]). Debonding was further shown to be influenced by the roughness effect[34] and the Poisson effect[35,36] on the axial stresses near indentation tips if fibre push-out tests are carried out. The Cook-Gordon mechanism states that crack tips reaching the fibre/matrix interface unfold in 4 steps[37]:

1. Matrix microcracks develop
2. Crack is deflected at the fibre interface
3. Crack propagates in mode II along fibre
4. Fibre fails and pulls out

The second step is theoretically subject to the HH (He-Hutchinson) criterion in determining whether the crack will break the fibre or be deflected[38] – this criterion is often applied in modelling composite mechanical behaviour (scenarios illustrated in Figure 3).

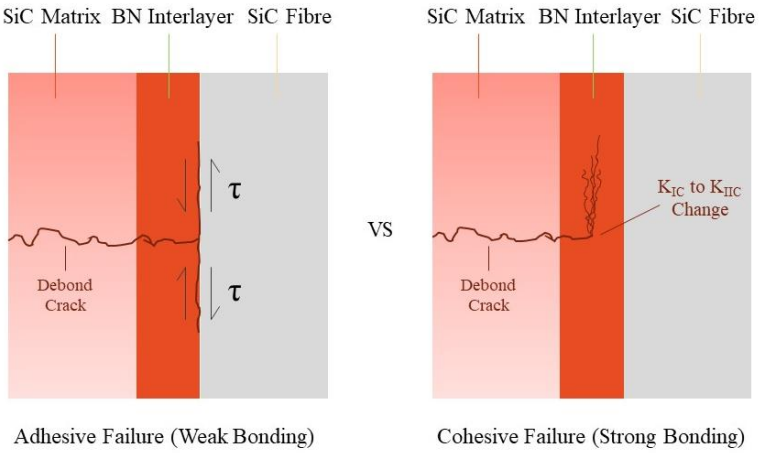


Figure 3: Adhesive (left) & cohesive (right) failures as CMC interfacial failure mechanisms

The criterion makes use of Dundur's parameter, i.e. the mismatch in elastic properties between the fibre and matrix, equations for which can be found in Sun et al.[39] – with α the mismatch in plane strain tensile moduli between fibre and matrix, and β a complex term involving elastic moduli, assumed to be 0[24] for "incompressible", i.e. highly dense or homogeneous materials like ceramics) and the fracture energy release rate Γ. Hsueh further expanded the concept and plotted a design guideline map of the ratio of fibre strength to interfacial shear stress versus the ratio of fibre and matrix moduli in Figure 4[40].

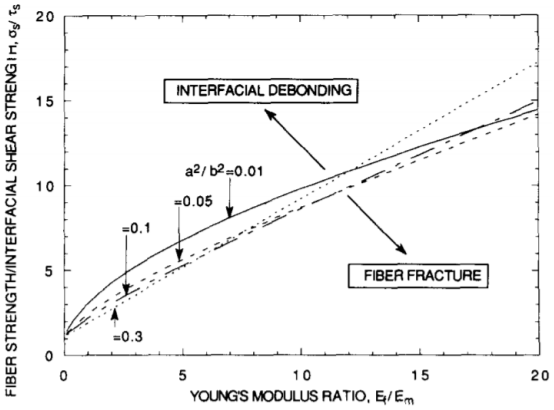


Figure 4: Failure regimes for CMC's – different lines correspond to different Poisson ratios - Figure from Hsueh[40]

In the SiC_f/SiC case, the fibre and matrix have interchangeable properties – simplifying the criterion to the following:

$$\Gamma_{interphase} \leq \frac{1}{4}\Gamma_{fibre}$$

Implying the interphase (usually hex-BN or pyC) needs a weak fracture energy release rate for optimised crack deflection (around 5 $J.m^{-2}$ if the assumption is made that most commercial fibres exhibit $\Gamma \sim 20$ $J.m^{-2}$), as well as high anisotropy (making BN a secondary choice compared to pyC with this criterion)[41]. PyC interphases have historically been associated with weak fracture energies[25, 42, 43] in the order of 10^{-2} $J.m^{-2}$, due to weaker van der Waals forces. Once deflected, cracks are further subject to remaining and travelling along the interface (echelon cracking)[44] with characteristics such as total debond length and micro-crack density affecting the overall pull-out process. At the interface during step 3, the debond shear strength and the internal friction coefficient are key parameters. Cracks along the interface must stick to a certain maximum length (of around 100 µm), for they become detrimental at greater debond lengths (when the matrix does not load-share as much). Budiansky via modelling showed that an optimum ratio of 1:5 for interface debonding energy:matrix fracture energy is to be achieved for the cracks to continually propagate in the matrix as well[32]. Experimentally, this is very difficult to validate, as data for the interface fracture energy release rate is limited, therefore the composite design phase is usually iterative, after initial values of fracture energy release rates have been obtained. Energy release rates have been previously modelled by Carrère and Lamon as follows:

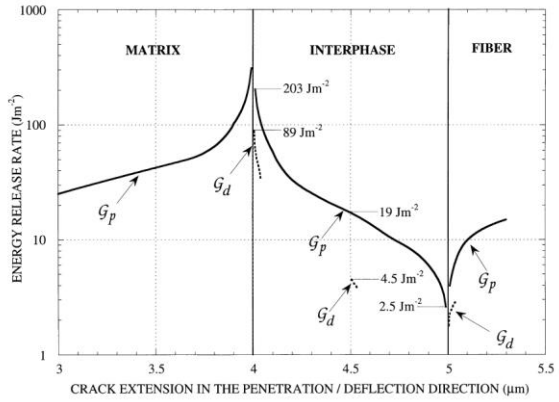


Figure 5: Energy release rate vs crack length extension in a SiC_f/pyC/SiC minicomposite – Figure from Carrère, Lamon[41]

Depending on a specific energy release rate, A toughness map can be created, which shows that a strong interfacial bond (inside the shaded region on Figure 6) will lead to a crack deflection within the interphase for carbon-based interlayers.

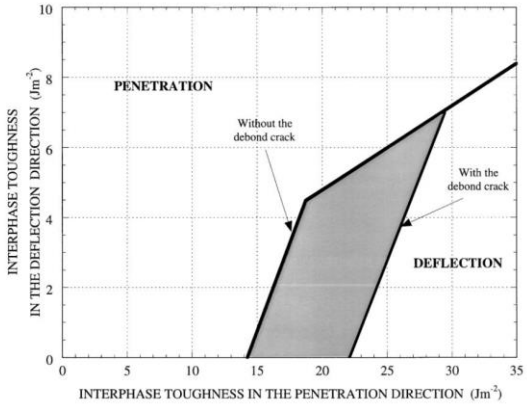


Figure 6: Influence of the presence of a debond crack at the interphase/fibre interface on the criterion of crack deflection within the interphase of a SiC$_f$/pyC/SiC microcomposite (the length of the debond crack is 2 mm). – Figure from Carrère and Lamon[41]

Cracks can also be deflected by pores in the matrix[45]. The mechanical performance of CMC's can therefore be enhanced provided the matrix is porous, but not microcracked[46] (micro-cracks occur in thermal cyclic conditions). The measured fracture toughness is therefore correlated to higher-entropy mechanisms such as fibre sliding and matrix cracking – an enhanced composite toughness relates to a low fracture energy and an average sliding stress. An adhesive failure – with weak fibre-to-matrix bonding, whereby cracks are able to propagate inside the interphase in mode II from the matrix – enables loading of fibres to their intrinsic failure strain, resulting in increased toughness of the material[47].

Once cracks have fully developed and the fibre(s) start(s) sliding, Callaway et al.[48] have identified a need to separate sliding behaviour into a yielding parameter and a Dugdale-like crack growth zone in the context of SiC$_f$/BN/SiC CMC's. Prior to rupture in the "elastic" domain, their model found only a weak correlation between shear stresses and BN interphase thickness.

In summary, CMC's fail by cohesive (strong interfaces, short cracks within the interphase, matrix load sharing, matrix cracking – no slip with an energy hysteresis during macro failure[49], failure is initiation-controlled) or the more adequate adhesive (weak interfaces, fibre de-bonding, crack bridging, fibre pull-out, slip with no to little friction and no hysteresis in macro failure, failure is propagation-controlled) modes as highlighted on Figure 3.

2.1.3 SiC$_f$/SiC in Aerospace

The introductory sections included details on the use of CMC's in the aerospace industry; the following paragraphs hone down on SiC$_f$/SiC in particular. SiC$_f$/SiC ceramic matrix composites are popular in the aerospace industry[45] for their potential as alternative material in high temperature applications such as combustor liners, ducts, seal rings, shrouds, vanes, and nozzles in hot parts of aircraft engines. NASA has previously developed and implemented SiC$_f$/SiC stator components including subelement vanes[50], and SiC$_f$/SiC composites were first validated in February 2015 by General Electric for use in rotary parts (such as the F414 turbofan low-pressure blades)[51]. Alternative

advanced materials for rotary components include titanium- or carbon- fibres-based CMC's. SiC_f/SiC are used as substitutes of carbon-fibre based composites since their compatibility with SiC matrices is superior. Carbon-fibre composites with SiC matrices (C/SiC) have historically been used in the aerospace industry due to their higher strength and higher temperature resistance, but their lifespan has narrowed their application range to hypersonic rocket engines alone, where required lifing is shorter[16]. A third note-worthy class of CMC's lie in the Oxide/Oxide (Ox/Ox) composites, which display both higher resistance to oxidation but poor creep properties, limiting them to exhaust mixers[16]. On the other hand, SiC_f/SiC have mechanical properties which withstand elevated temperatures, added to distinguished resistances to oxidation[52] and neutronic irradiation damage (low tritium permeability and thermal neutron capture area)[45], and are thus ideal for exhaust-wash structural applications. Implementing SiC_f/SiC as combustor liners raises the theoretical temperature capability of the chamber to 1350°C, improving heat-resistance by an estimated 20%[51]. With their ability to reach higher turbine temperatures, CMC engines will therefore consume (30%) less specific fuel and energy in cooling the system, whilst producing fewer nitrous oxides[53]. Comparatively, SiC_f/SiC have higher robustness, as the energy required to break a Si-Si bond is superior to that of a C-Si bond[54]. Indeed, cracks propagating in a SiC_f/SiC matrix – where high residual silicon contents are present from manufacturing – result in tougher composites.

SiC_f/SiC composites are light with densities reaching 2.5 $g.cm^{-3}$ at 11% porosity[30]. Comparable SiC_f/SiC composites from GE[55] have reached densities ranging from 2.77 to 2.85 $g.cm^{-3}$. Such levels of porosity make the composite both weak and insulating when testing through thickness[6].

Intermediate temperatures of 400 – 800 °C are of particular importance, present in thermal gradients created in engine components from the attachment points and backside cooling. Both the SiC fibres and matrix are electrical conductors, however the metallic nature of the residual Si in the matrix renders it the primary conductor of any current across the composite (conversely the BN interphase is usually a poor conductor, especially if not crystalline[56])[57] – this property is useful in evaluating transverse matrix cracking. Si is further prone to reacting with all species in the first two columns of the periodic table, resulting in lowered composite oxidation and creep performances[51]. Finally, SiC_f/SiC composites could possibly raise the safety margins in 'Beyond-design-basis Accidents' scenarios when used in nuclear cladding or combustion chamber liners[58].

When used as combustor liners, SiC_f/SiC components can endure through 52,000 hours of turbine operation in hot steam conditions[59]. The water vapour partial pressure in the after-burner sections of the engines can reach values of 0.77 bar[60]. Therefore, in order to reproduce turbine blade hot gas stream environments, thermal fatigue cycling tests are usually performed with a burner rig only exposing one half/side of the sample to combustion conditions (leaving the other half to heat exposure by convection only)[26]. Other possible simulations performed in literature are listed in Table 1.

Table 1: Relating experimental parameters to aerospace simulations - Table adapted from Kim et al.[26]

Mechanical Loading Type	Thermal Loading Type	Test Described As	Simulation Of:
Static	Constant (Elevated)	Creep or Creep-Rupture	Turbine rotor blades under constant stress in radial direction
Cyclic	Constant (Elevated)	Mechanical Fatigue Interacting with Creep	Hot-section components undergoing take-off and landing as well as manoeuvring
Static	Cyclic	Thermal Fatigue; Dwelling Effects	Operating conditions of high-end engines
Cyclic	Cyclic	In-Phase or Out-of-Phase Fatigue	Worst case scenario for hot-section components

Typical conditions approached by Rolls-Royce include temperatures of over 1726 °C, pressures of over 50 bar and stream velocities of around Mach 1. Loads applied correspond to levels below the proportional limit, but after initial matrix cracking, as referenced in section 0. Current research and limitations of SiC_f/SiC composites lie in preventing high-temperature corrosion, increasing fracture toughness, reducing creep and preventing formation of macro-flaws. CMC's and the coating EBC's (Environmental Barrier Coatings) are faced with numerous additional environmental threats such as CMAS (Calcium-Magnesium-Aluminosilicate) from volcanic ashes, sodium sulphates, humidity, pressure, gas velocity, FOD (Foreign Object Damage), DOD (Domestic Object Damage), sand, erosion and the underlying boria. Implementation of CMC's in engines is measured in TRL (Technologies Readiness Levels) where TRL 4-6 means the technology is already implemented at engine-level. Demand for SiC_f/SiC-based engine components is predicted by GE to increase tenfold in the next decade, in alignment with Paris Accords and UN Sustainability Development Goals[51].

2.1.4 SiC Fibres

The composites in this work make use of SiC-based fibres embedded in a SiC matrix with a BN interphase. SiC fibres have developed over the years to become thinner[61] and to display the following property improvements[1]: high thermal conductivity (greater than 50 $W.m^{-1}.K^{-1}$), high mechanical properties (strength, stiffness and modulus) at elevated temperatures obtained by 500 nm grain sizes at maximum, high density (of over 3 $g.cm^{-3}$), low porosity and almost perfect stoichiometry (leaving very little residual elements). In recent years, three major companies (Nippon Carbon, ATK-COI Ceramics and Ube Industries) have been producing three standout types of fibres (Hi-Nicalon type S, iBN-Sylramic & Tyranno SA3 respectively) conventionally made with different sintering aids, and therefore exhibiting slightly different properties (e.g. residual aluminium can be found from sintering additives on Tyranno fibre surfaces). Developments for new generations of fibres are driven by the needs to push heat, oxidation and creep resistances of the fibres to new limits[51]. The market demand for fibres themselves was estimated at 10 tonnes per year for the entire industry in 2002, and was successfully projected to reach 20 tonnes by 2008[13].

First generation fibres (e.g. Nicalon and Tyranno) were used extensively in the 80's before their limitations in fatigue properties and mechanical properties (from processing) were quickly highlighted. For example, authors such as Prewo[62] and Dugne[47] showed that the strength of Nicalon fibres was severely reduced when tested on their own after being extracted from a fully formed composite. Their high surface roughness (of 30 – 60 nm, even when de-sized) created microcavities when depositing BN[47] – thus increasing fibre to interphase bonding by mechanical keying in a random manner, making it difficult to measure any realistic interfacial shear stresses[63]. Second generation fibres (e.g. Hi-Nicalon or Tyranno ZMI) lowered oxygen content in fibres over time, down to 1.0 wt% or less[51]. However, both a remaining SiCO tertiary phase and high residual carbon content could still be detected on Hi-Nicalon fibres[64], resulting in poor oxidation performances when compared to their next-generation peers. Hi-Nicalon type S (Si-C-O) or Tyranno type SA1-3 fibres – with a large grain size – are termed 'third generation' Polycarbosilane-derived fibres, and are used as reinforcement for their ease in microstructure tailoring during manufacturing, combined with their meeting requirements for aerospace applications. Third generation fibres have grain sizes averaging 50 nm and root mean squared surface roughnesses of 2.33 nm[65] (with Tyranno type SA found to be significantly rougher than second generation Hi-Nicalon fibres[66]) – these fibres improve on the performance of more senior generations by containing less oxygen and more residual carbon, achieving near-stoichiometric (C/Si ≈ 1) composition. The intra-generational quality of these fibres is determined by the amount of amorphous carbon and glassy β-SiC phases[45], which in Hi-Nicalon fibres, is very low. This high crystallinity paired with lower oxygen content (when contrasted to older fibre generations) result in a higher thermal resistance (up to 1800 °C)[56]. The same fibres have a greater density, a coarser grain size and a low fracture strain when compared to previous generations[67]. In contrast to Hi-Nicalon type S, Tyranno type SA3 fibres are half the diameter (around 7-8 µm), have 100 – 200 nm wide grains, and have less residual carbon or β-SiC crystallites[51]. Tyranno type SA3 fibres – from Ube Industries – have been shown to contain higher porosity and carbon content in the centre of the fibres, rendering them very soft and sensitive to nanoindentation experiments (e.g. 26 GPa in hardness compared to 38 GPa in the matrix SiC[68]). Tyranno type SA3 fibres are additionally manufactured with an aluminium sintering aid, at times resulting in the formation of corrosion-resistant, amphoteric Al_2O_3 in the fibre vicinity. Both Hi-Nicalon type S and Tyranno type SA3 are known to have equiaxed grains, which can grow columnar perpendicularly to the a-c interphase after irradiation or amorphisation[69, 70]. When comparing the mechanical performance of both third-generation fibres, it was shown that Hi-Nicalon type S fibres were damage

tolerant whereas Tyranno SA3 fibres showed erratic (high interfacial stress, low strain-to-failure) behaviours, attributed to the aforementioned discrepancy in surface roughness[65]. Sylramic fibres – developed by COI Ceramics – contain an addition of Ti and an excess amount of C compared to the other fibres. On another hand, Sylramic fibres are sintered with additional TiB_2 and B_4C particles, to further slow fibre oxidation and promote diffusion during sintering; however i-BN Sylramic fibres (with an additional N_2 heat treatment compared to Sylramic fibres) have been shown to display poor fracture toughness properties[55].

SiC fibres are known to degrade in thermal cyclic conditions at around 1000 ºC[71], 1600 ºC under no cyclic conditions and disintegrate stoichiometrically at 2540 ºC into solid carbon and liquid Si(C)[67]. SiC fibres degrade at temperatures exceeding 1600 ºC as they are prone to volatilisation and creation of fibre pores[72] – mass loss due to scale spallation and the creation of large surface nodules at 1700 ºC is very significant[73]. Non-cyclic constant (creep) stress rupture lifetimes for different fibres were highlighted by Gauthier et al[74] (adapted from Gale) investigating the effect of oxygen on fibre failure:

Table 2: Indicative fibre type lifetimes, residual carbon content and grain sizes. Adapted from Gale, Gauthier et al[74]

Fibre Type	Tyranno SA3 (3rd Gen)	Hi Nicalon S (3rd Gen)	Hi Nicalon (2nd Gen)	Nicalon (1st Gen)
Lifetime Rank	1	2	3	4
Free Carbon	2%	3%	17%	15%
Grain Size	100-50 nm	20 nm	10 nm	5 nm

The highest rank (1) in Table 2 corresponds to the longest lifetime. The differences in lifetime were mainly attributed to the amount of residual carbon in the fibre grain boundaries and the swelling from oxidation.

2.1.5 The Matrix

The SiC matrix is composed of β-SiC grains and residual Silicon from melt-infiltration, (MI) however the matrix can also be fully deposited by CVI or CVD at the expense of both cost and time. The focus in literature on the matrix is limited – studies on the matrix look at the residual stresses from MI, the presence of microcracks, the matrix density and matrix getters. Some manufacturing methods of SiC_f/SiC composites resulting in a residual amount – sometimes up to 20%[75] of unreacted silicon in the matrix – produce local compressive stress states on the silicon upon cooling of the body to room temperature[76]. Indeed, the difference in thermal expansion coefficients between Si (3×10^{-6}/ºC) and SiC (4.5×10^{-6}/ºC) from cooling during processing[77] results in thermal residual stresses accumulating in both the fibres (tensile) and matrix (compressive as it is also boron-doped). These micro-stresses were estimated by Wing to reach 2.4 to 3.1 GPa[75] in magnitude, and more recently by Kollins et al.[78] reaching 2 GPa in the Si and -1.45 GPa in the SiC (compared to 26 MPa in SiC and 103 MPa in the Si using Kingery-Turner[79] and bulk moduli estimates). The stresses were found to be spaced at grain-size level in the matrix[75]. The residual stresses measured by Wing[75] also showed no variation with respect to proximity ~~to~~ for tows or tow position in the sample at the macroscale (where amounts of infiltrated Si differ). The DBTT for Si – noted around 500-600 ºC – and the free silicon volume expansion of 11% from liquid to solid[75] both add to system complexity when modelling and testing. Further discussion on residual stresses is included in section 2.2.1.4.B.

2.1.6 The BN interphase

Fibres coated with hex-BN interphases are also usually supplemented with CVI layers of SiC. The BN interphase material typically amounts to 30% of the CMC production cost just by its processing route – which is another reason why research is focused on finding alternative interphases or production methods (c.f. Section - 2.3, Research & Development).

BN is a wide band-gap semiconductor with 2 dominant polytypes – namely sp^2 bonded hexagonal structure (graphite-like and turbostratic) and sp^3 cubic (or wurzite) structure (analogous to diamond)[80]. The hex-BN interlayer is electrically insulating (but a direct semi-conductor, thus making it difficult to detect using SIMS) and is one of two popular options (the other option being pyrolytic carbon, pyC) for coating material of the composite SiC fibres. The choice stems from the coherence between BN and SiC lattices (both basal and perpendicular to basal directions were considered)[81], the stabilising of the friction coefficient of SiC[2] and their high-temperature melting point[3]. Hex-BN is typically produced at 1500 - 1600 °K from the reaction of boron-trihalides (BCl_3, BF_3) with ammonia[82]. Hex-BN and pyC both have inherent layered crystal planes (parallel to fibre orientation), with weak forces linking crystal planes with one another, providing ideal 'sliding' properties and lubricity[45] in an aromatic stacking configuration. Interfacial frictional stresses – which provide a good measure of the mechanical durability of the interphase – have been reported to be similar between pyC (~ 2 MPa[25]) and hex-BN[83], but the BN/SiC fibre bond is stronger than the pyC/SiC bond[23]. BN is the preferred coating for applications where oxidation can occur in high-temperature environments, including aero-engines. Pioneering work by Filipuzzi[86] on SiC_f/pyC/SiC minicomposites helped model the oxidation behaviour of said composites with PyC interphases, showing that long exposures (300 hours) at 900 °C induced deleterious damage in the forms of microcrakcs due to SiC/SiO_2 conversion. In BN interphases, the more stable boria is formed over a wide range of temperatures (600 – 1200 °C)[12], but has a low melting temperature of 450 °C. By oxidising to boria, the interphase and composite gain in mass, whereas pyC volatilises to CO_2, thus reducing component mass. Hex-BN is therefore the preferred coating for applications where oxidation can occur in high-temperature environments. The choice is due to a higher density of π-bonds, and therefore a more elevated oxidation start temperature of 850 °C (as compared to 400 °C for carbon)[87, 88, 61, 89]. However, boria has also been hypothesised to be the leading agent of oxygen ingress 800 µm-deep inside the composite material, in what is termed 'ends-on-oxidation'[90,91]. In aqueous environments, the oxidation resistance of BN has additionally substantially been questioned[92, 93]. It is also worthwhile noting that even for amorphous BN interphases, short-range order can still be present and deflect cracks at the interphase.

Hex-BN interlayers are usually no thicker than a micron. The thickness (and indirectly the porosity) of the interphase in CMC's directly correlate(s) to a reduction in clamping stress induced by thermal expansion mismatches during sample fabrication[65]. Optimum thicknesses have been found by Delpouve H. & Sylvain J. to reach 500 nm in thickness (for poorly crystalline BN), whilst no optimum thickness for highly crystalline BN has been found. The crystallinity of the BN interphase is a key processing parameter: 'amorphous' BN typically refers to a poorly crystalline thin film with regions of disordered turbostratic boron nitride in a sea of amorphous B and N[80], best detected by means of infrared spectroscopy for increased B-N polar bonds sensitivity (a high quality film will therefore exhibit little signal in IR). Raman scattering on the other hand can help identify the ratio of hexagonal to cubic BN (if any)[80] with BN coating showing high fluorescence in SiC_f/SiC composites[75]. The hex-BN film also helps protect the SiC from both mechanical abrasion and chemical attacks during manufacturing[3]. However, the same Boron can also contaminate the SiC as

impurity (with maximum solubility of Boron[94] in SiC reaching values of 0.2 wt%). It can further decrease mechanical performance: with measured interfacial shear stresses of 10 or 20 MPa[95,19] in contrast to interphase shear strengths of 105 ± 11 MPa[96] to 105.9MPa[46] for PyC interfaces. As aforementioned, the interface strongly correlates to specific composite characteristics such as the residual clamping stress and the fibre roughness – both of which increase the friction coefficient of the interphase[24].

When relating to pure micro-mechanics, SiC_f/BN/SiC composites have been shown to fail at fibres which are too strongly bonded to the interphase, and therefore do not allow for adequate load transfer. 'Strongly' bonded fibres fail consecutively, akin to Weibull chains – opening unbridged pathways for transverse cracks to traverse[4]. Crack deflections at hex-BN interphases are more likely to occur at the SiC_f/BN interface than at the SiC_m/BN interface due to the higher debond stresses[97].

2.2 Micromechanical Testing of CMC's

Due to the growing implementation of ceramic-matrix composites in multiple industries – including aerospace and nuclear – characterisation of the composite interphase is necessary to better life components. As a consequence of the interphase scale, extracting the interfacial properties of ceramic-matrix composite poses a major engineering challenge in materials science. A few meso-scale and macro-scale techniques highlighted by Bansal & Lamon[4] such as the transverse bend test, the traverse tensile test, the Brazilian disc compression test and the bilayered flexural test have shown experimental reproducibility, but are unsupported by sufficient modelling. Micro-scale techniques bridge the gap between understanding atomic and molecular scale events and relating them to macro/meso scale mechanics – they also serve to validate models or predict macroscale behaviour from micro-experiments.

There are multiple advantages to employing micro-mechanics for CMC's. Micro-mechanical tests help reveal intrinsic properties, which in the case of composites, segregate properties of each constituent rather than measuring the property of the composites as a whole. Micro-mechanical tests are usually conducted on coupon-sized specimen, which are easier to test for fundamental understanding of the CMC failure mechanisms. The use of coupons further reduces destructive testing costs, since sample sizes are smaller than those of macro-scale experiments. Most micromechanical instruments and techniques are moreover tailored for ease of use and automation of acquisition, mass producing results[98]. For example, this warrants separate testing of variables which all influence macro-scale tests simultaneously. These include (i) the strain rate, (ii) the cyclic loading with hysteresis loops (to investigate creep[99]) and (iii) the step loading sensitivity during mechanical testing. Micro-mechanical techniques are also key to elucidating the anisotropy of any mechanical response. In heterogeneous and complex materials such as composites, micromechanical features can be individually probed. For example, micro 3-pt bend tests of single fibres (or minicomposites) target fibre surfaces alone, thus minimising the effects of composite porosity. Authors such as Prewo[62] and Curtin[31] highlighted the importance of using micromechanics to measure post-processing properties in-situ (at the time using techniques such as the fracture-mirror experiment) on SiC_f/SiC CMC's, due to the differences in strengths they observed when measuring fibres on their own versus fibres inside a composite. Finally, micromechanics can investigate any down scaling and size effects. The numerical properties generated at the micro-scale can complement data in multi-scale models. This is applicable to ceramics, which are in general brittle at the macroscale, yet can exhibit room temperature plasticity[100] at the nanoscale.

Conversely, micro-mechanical techniques present some overarching limitations. Such collaterals include micro and nanoindentation bending of the specimen or the holder during testing, which impedes accurate measurements. Micro-mechanical techniques can yield useful metrics for comparison of samples, but rarely produce absolute values as they lack in robust standards and statistically relevant data (moreover so for interfacial CMC properties)[101].

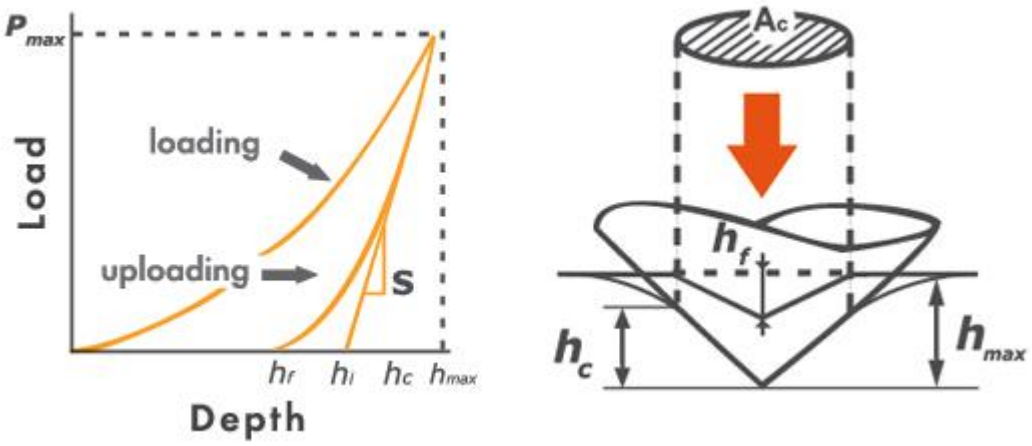


Figure 7: Standard load/displacement data and corresponding indent. Figure from Nanoscan ® [102]

Most micro-mechanical techniques make use of a nanoindentation instrument, a now widely-used technique which relies on a piezo-electric or magnetic actuator guiding a tip indenting materials. Data can be extracted from the load measured and the area of the indent imprint shown in Figure 7, amongst other parameters. The data analysis from nanoindentation usually relies on fitting an area tip function to measure hardness and modulus of a component when contrasted to a baseline (calibration) material with known properties. Post-data analysis commonly refers to the Oliver & Pharr method, but said authors have also highlighted the limitation of the analysis when looking at (mostly metallic) materials experiencing significant work hardening and pile-up[103]. The post-data acquisition analysis takes the maximum load P_{max}, displacement h_{max} and the slope of the unloading curve dP/dh to calculate a contact stiffness S and a hardness H through the following equations – which can then both be fitted to a tip area function A using [1] and [2] to obtain a material specific elastic modulus and hardness.

$$H = \frac{P_{max}}{A} \quad [1]$$

$$S = \frac{dP}{dh} \approx 1.05 \times \frac{2}{\sqrt{\pi}} E_{eff} \sqrt{A} \quad [2]$$

With E_{eff} the effective modulus taking into account both indenter tip and material elastic displacements and is tip geometry-dependent[103]. Common tip geometries (and corresponding application) include (i) Berkovich (to measure hardness and modulus), (ii) flat-punch (to perform fibre push-outs) and (iii) spherical[104] (to clearly separate elastic and plastic deformation during indentation and approximate a work-hardening exponent). For any indentation system, a system calibration is commonly performed prior to indentation[103] to account for instrument compliance $C_{load\ frame}$:

$$C_{total} = C_{load\ frame} + C_{contact} = C_{lf} + \frac{\sqrt{\pi}}{2E_{eff}} \frac{1}{\sqrt{A}} \quad [3]$$

The use of a nanoindentation tool is common to all techniques subsequently presented in this review.

Despite no standard being widely accepted in the community, common methods for determining the interfacial composite properties at the micro-scale involve the push-out, push-in & push-back methods on singular fibres[105]. The three techniques can be found under other names (the fibre push-through, push-down and reverse push-out respectively), can be performed in or ex-situ, and their differences illustrated in Figure 8.

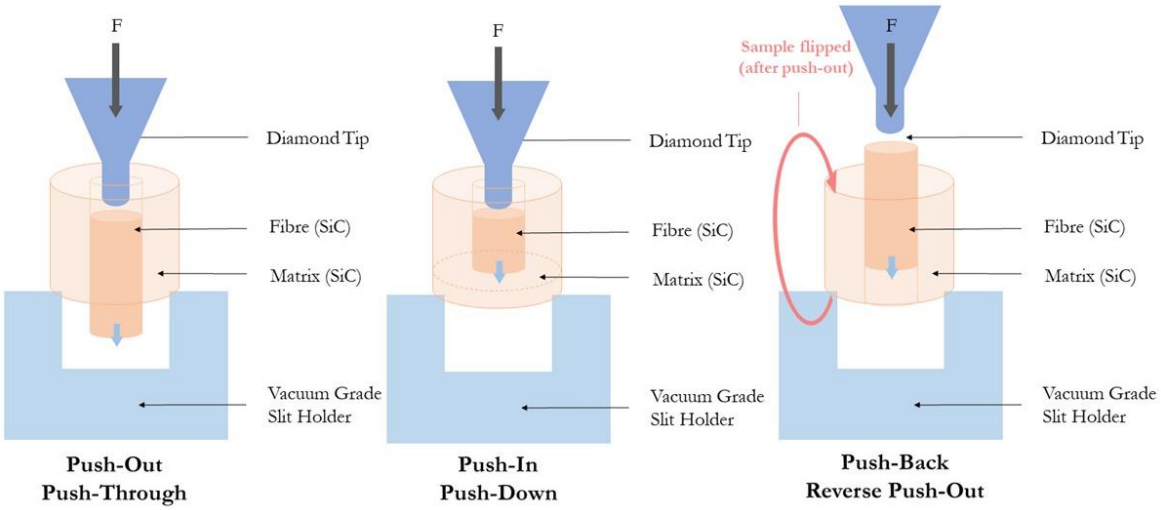


Figure 8: Illustration of the differences in performing a push-out, push-in and push-back on singular fibres in CMC's. Please note diagrams not to scale.

The push-out (or push-through) technique must not be confused with the push-in (or push-down) technique. In the latter, the fibre is pushed down – irrespective of the overall sample thickness – and has a higher probability of inducing a fracture beneath it in the underlying perpendicular tow (commonly found 200 µm deep in woven CMC structures), or breaking itself. Thirdly, the push-back technique consists of pushing a fibre back through the hole created after a fibre push-out, by flipping the sample. All three techniques are detailed in sections 0, 2.2.2, and 2.2.3 respectively. The three aforementioned techniques should also not be confused with the fibre pull-out, where a fibre is attached to the tip and pulled out of its matrix sheath. The fibre pull-out is usually performed on microcomposites (a single bundle of fibres) much like both the fibre fragmentation and single fibre compression tests[101]. Limitations of the fibre pull-out compared to the fibre push-out include high efforts to mass testing (since the tip must be attached to each fibre prior to testing) and its lack of exploring both friction and transverse loading conditions[106].

Following acquisition of desired properties, the data can then inform on how the mechanical properties of the interphase can be tweaked and optimised. Kabel et al.[24] highlighted that the microscale properties of interest are either tailored intrinsically by modifying the chemistry (such as the fracture energy release rate, the debonding shear strength and the friction coefficients, both internal and dynamic) or extrinsically by modifying processing and manufacturing (fibre roughness, residual clamping stress from thermal mismatch and interphase thickness).

2.2.1 The Fibre Push-out Technique

2.2.1.1 Method

The very first fibre push-outs were performed by Marshall & Oliver[107] in 1985. Using the plateau force P_{max} on the load/displacement response corresponding to a fibre sliding resisted by Coulomb friction, one can derive an estimate [4] of the Interfacial Shear Stress (ISS) exerted on the interphase τ [96]:

$$\tau = \frac{P_{max}}{2\pi r l} \quad [4]$$

r the fibre radius and l the fibre length. To calculate a failure criterion ISS from fitting to shear-lag models, a preceding 'n' elastic term is added to the equation[99], more detail for which is included in section 2.2.2. In practise, one can estimate the maximum sample thickness l using this equation from the instrument load limit (e.g. for a MicroMaterials G200 instrument with a maximum load cell of 600mN, assuming a maximum of 200 MPa interfacial shear stress and a fibre radius of 15 μm, the maximum thickness under which push-outs will occur can be estimated at 190 μm). Equation [4] can be derived starting from the following generic force balance [5]:

$$\sigma_0^* \pi r^2 = \tau_0 L 2\pi r \quad [5]$$

Due to the stochastic nature of fibre push-outs and the range of values the interfacial shear stress may obtain (e.g. 10 to 20 MPa for weak interphases and 100 to 300 MPa for strong interphases[19]), the data can be presented as cumulative frequencies in order to yield best and worse-case design scenarios for performance envelope libraries.

Kerans & Parthasarathy provided an overview of the theoretical analysis of the fibre pull-out and push-out techniques 4 years later[36] including over 10 papers and authors, who iteratively added assumptions to the shear-lag model first applied in 1972 by Lawrence[108] to the technique. Kerans found that the linear section of a push-out load/displacement curve can yield 4 parameters: (i) the coefficient of friction, (ii) the radial stress at the interface (acting from the composite matrix onto the fibre), (iii) the fracture toughness of the interphase and (iv) the residual axial strain along the fibre[36]. Conversely, the peak load from the push-out technique cannot yield any useful interfacial parameter as cracks develop too close to the top or bottom edges of the sample. This is similar for the push-in technique where the peak load was shown to be unrelated to interphase toughness[101]. The onset of non-linearity suggests an interfacial crack has created, as the applied load simultaneously overcomes both the debond resistance energy and the axial residual compressive stresses on the fibre[63, 109]. Overall, displacement-control is preferred to load-control for push-outs, as load-control induces an instability in the load/displacement curve which affects any result derived from the data[21]. In displacement-control, a flat curve on a load/displacement response during a nanoindentation test corresponds to a fibre splitting and breaking down[99], whereas flat plateaux represent fully debonded fibres sliding in load-control environments.

2.2.1.2 Extractable Properties

The fibre push-out can be used to extract other interfacial properties than the ISS, highlighted in this section. The interfacial fracture energy 2Γ was first determined in models developed by Marshall[33], Oliver[110] & Hsueh[111] using equation [6]:

$$2\Gamma = \frac{F^2}{4\pi^2 r^3 E_f} - \tau\delta \quad [6]$$

(δ a commensurate geometric term relating to crack displacement as a function of interphase thickness). The interphase roughness A and the residual clamping stress σ_C can be related with each other using equation [7] [36]:

$$A = \left(-\sigma_c\left[\frac{E_f(1-\nu_m)+E_m(1-\nu_f)}{qE_mE_f}\right] - \Delta\alpha\Delta T\right)r \quad [7]$$

q is a parameter which is equal to unity for an infinite matrix-case, and is less than unity in any other case. The model is assuming that the fibre displacement is more than half of the roughness wavelength[34] and is only influenced at the local interphase scale. The fibre roughness can also be inferred from external techniques such as AFM, IR or optical interferometric profilometry[22]. Furthermore, Jero, Kerans & Parthasarathy[112] have shown that the radial thermal stresses σ_r can be computed from knowing both the temperature difference between fabrication and the push-out test (ΔT) and the fibre sliding behaviour using equation [8]:

$$\sigma_r = \kappa(\alpha_m - \alpha_f)\Delta T + \kappa\left(\frac{A}{r}\right) \quad [8]$$

Where α_m and α_f are the coefficient of thermal expansion (in the radial direction) for both the matrix and fibre respectively, and where:

$$\kappa = \frac{E_mE_f}{E_m(1-\nu_f)+E_f(1+\nu_m)} \quad [9]$$

A debond stress σ_d can be found from the experimental data, however the latter can be fitted to either a strength-based or energy-based model[111]. Additionally, energy-based finite fracture mechanics approaches such as the Coupled Criterion (CC) model developed by Herbreteau[113] are also able to calculate interfacial toughness G_{1C} provided the finite element model can obtain a normalised incremental energy release rate term A_i*:

$$F^* = \sqrt{\frac{\pi^2 E_i r_f^3}{8A_i^*}G_i^C} \quad [10]$$

(Where F* is the maximum load at plateau). The fracture toughness of the interphase is an important parameter to derive as it has the highest applicability to composite lifing models[96]. When determining the fracture toughness from push-outs performed cyclically, a simple integration of the normalised load-displacement curve will yield an energy term which can be divided by a crack area (the cylindrical area of the fibre)[96] – however this ignores all fibre Poisson contraction/expansion and

residual stresses phenomena. Cyclic push-outs yield a dissimilar interfacial shear stress, obtained empirically from the hysteresis of load/displacement curve should a load/unload cycle be applied[114]:

$$\tau = \varphi \times \frac{Nr\left(1-\frac{E_f}{E_c}V_f\right)^2}{2V_f^2 E_m}\left(\frac{\sigma_i^2}{\Delta\sigma}\right)\left(\frac{\sigma}{\sigma_i}\right)\left(\frac{1-\sigma}{\sigma_i}\right) \quad [11]$$

Where

$$\varphi = \frac{(1+\nu)E_m\left[E_f+(1+2\nu)E_c\right]}{E_f\left[(1+\nu)E_f+(1-\nu)E_c\right]} \quad [12]$$

With ν the Poisson ratio, V_f the fibre volume fraction, N the number of matrix cracks in gauge (which can be experimentally measured with SEM or X-Ray tomography), E_f, E_m, E_c the Young's moduli of the fibre, matrix and composite respectively, σ_i, σ and Δσ the unloading stress, the applied stress and the hysteresis loop width. The interfacial shear stresses can therefore be inferred from the spacing distance of the matrix cracks at failure[33]. The rule of mixtures can be applied to calculate the elastic properties of the matrix should the volume and packing fractions of the fibres be high enough[111] – in this case, a self-consistent model is needed.

The shear-lag model predicts a highest interfacial shear stress at the top surface of the fibre close to loading contact point[40], but also often over predicts the debond length by a factor of 1.5 times the fibre radius[109] when using equation [9] from Bechel[109]. If the interfacial shear stresses measured show high values, the fibre surface roughness plays an increasingly important role in the failure mechanism[21]. In order to obtain numerical values of the interface strength without using Finite Element (FE) modelling, shear-lag formulae yield the following:

$$\tau_{debonding} = \frac{\beta F_{debonding}}{2\pi r^2} \quad [13]$$

Where

$$\beta^2 = \frac{2E_{matrix}}{E_{fibre}(1+\nu_{matrix})\ln\left(\frac{2\pi}{\sqrt{3}\times V_{fibre}}\right)} \quad [14]$$

With E the Young's modulus, ν the Poisson ratio and V the fibre volume fraction, r the fibre radius and F the decohesion force. Fibre decohesion was found to occur in matrix-rich zones, but is also dependent on the following fibre parameters: diameter, volume fraction and transverse strength[99]. In this case, the Shear-lag model assumes no radial stresses elsewhere (matrix, fibre or interface), which makes FE modelling yield more accurate results. This is the only value which can be extracted for thick (>100 µm) samples[99] during fibre push-outs. FEM results have been shown to converge with those from shear-lag analysis when the surface area probed was similar to fibre diameter[115] (i.e. the tip was similar in size to the fibres). The interfacial shear strength can finally be derived from the stress/strain curve following stress-dependent crack density models[77], which fits strains to a normalised AE energy (correlated to the distribution of matrix cracks).

2.2.1.3 The Fibre Push-Out Technique Applied to SiC_f/BN/SiC

The fibre push-out technique has been applied to both SiC_f/BN/SiC and SiC_f/pyC/SiC before, but not to the scale introduced by the work in this thesis.

In SiC_f/BN/SiC composites, a high packing fraction was found to induce higher rates of outside debonding (debonding between the BN interlayer and the matrix) during push-outs as observed by Morscher[77] et al, due to the potential for doubling degradation rates (oxidation of one BN interlayer affects two fibres or more). Conversely, Mueller et al. observed little effect of the local fibre volume fraction on the scatter of measured shear stresses[96]. Debonding was found to be more favourable if separating the matrix from the interlayer, than the interlayer with the fibres[77]. These mechanisms are termed 'outside' and 'inside' debonding respectively, with the latter worsening the stress-oxidation capabilities of the composite. 'Outside' debonding yields the most improvement in fibre stress when compared to treating the inter-fibre distance or the silicon doping[116] – two solutions to interphase tailoring addressed in section 2.3. Outside debonding was found to induce much longer push-out lengths and weaker interfacial shear strength (~ 10 MPa)[77] when compared to inside debonding (~ 70 MPa). The disparity between where the crack propagates has been attributed theoretically to processing, where a crack closure effect was observed. This suggested that the fibres express residual tensile stresses whereas the free Silicon in the matrix and the CVI SiC are both in residual compressive states from ~9% thermal contraction when cooled from 1400ºC during manufacturing.

Outside debonding results from an early onset of oxidation, as the SiC acts an oxygen getter on the pulled out fibre (Ellingham diagrams show that the BN is kinetically favoured but the SiC is thermodynamically favoured)[21]. Inside debonding was the dominating mechanism in the SiC_f/BN/SiC composites studied by Rebillat[19], the macro-scale push-outs performed by Desaeger[99] and the SiC_f/pyC/SiC composites tested by Yang[66] (the debond energies for C & BN usually average 1 and 3 $J.m^{-2}$ respectively[118]). The packing fraction of the fibres also influences the fibre local environment during a fibre push-out, however Zhang et al have inferred that there is no direct correlation between testing fibres next to un-tested or previously tested (pushed out) fibres[119].

2.2.1.4 Technique Limitations

The major limitation of performing the fibre push-out is that its representation of in-service conditions (especially during cracking) remains sparse, as fibres are more likely to pull-out instead. However, several more limitations arise from the fibre push-out technique, making it difficult to achieve experimentally.

A) Sample Thickness

The thickness of the samples needed for push-out has been an ongoing problem in the micromechanical community. Thicker samples will likely experience exaggerated shear stresses at the interface due to fibre/matrix elastic incompatibilities[99], enhanced effects of the load train/instrument compliance (although Mueller argued that there is little to no effect from the sample flexural stiffness on shear measurements[96]) or the increasing number of protruding fibres during sample preparation as both stresses relax and interphases degrade. The polishing was also speculated to further introduce in-plane compressive stresses[99]. At 100 µm thicknesses, the weave dimensions are reduced to single tow thicknesses, which removes the composite geometry variable in calculating absolute values. However, this can sometimes induce problems during sample preparation as others

have reported fibre tows unsheathing from their surrounding matrix during polishing[120] as a result of residual compressive stresses relaxing. Rebillat[63] further showed that fibres could not be pushed out more than 10 times their diameter size (which is roughly from 10 to 15 µm for third generation fibres) when wear starts being too significant. For first and second generation fibres[21], the testing thickness should not exceed 180 µm. Novel solutions to sample thinning include the argon ion slicing process highlighted by Herbreteau[113] et al. and the wedge-shape preparation[21] – both complex and time-consuming techniques.

B) Residual Stresses in the Matrix

A Poisson phenomenon and a differential thermal contraction (from the difference in coefficient of thermal expansion during manufacture) also cause the fibre to expand during push-out – which induces (rather than offsets) radial compressive stresses across the interface[107]. The Poisson effect converts axial stresses into radial ones and is complex to quantify as it occurs contiguously with residual axial stresses from the lattice mismatch between interphase and fibre[111]. Some authors have noted zero stresses from Poisson contraction, and therefore no plastic deformation in the surrounding matrix in C/C-CVI-SiC composites[119]. When simulating fibre push-ins, Rodríguez[101] et al. also found no axial (normal) stresses. Kallas[121] and Bechel[122] both found that the radial stresses were tensile at the bottom of the sample/fibre being pushed out in thin specimens – resulting in a crack initiation at the bottom end of the sample during fibre push-out (also highlighted by Tanoglu[123]). Crack initiation from the bottom of the sample was also theorised to occur by the same authors[121,122] when the fibre/matrix moduli ratio is greater than four, and occurs from the top when the same ratio is less than three[109]. Conversely, Rebillat found debonding to initiate at top surfaces in fibres[21] when testing SiC_f/pyC/SiC composites. The thermal residual stresses are also anisotropic since fibres are usually oriented along the axial direction. Additional interfacial compressive stresses should also be considered during the push-out should interfacial asperities from processing subsist, as these will inhibit the fibre from sliding[111]. All these constraints have been modelled elastically so that properties can be extracted from experimental measurements by Hsueh & Shetty[111, 35]. The Hsueh model has however been experimentally trialled and found to have poor cross-correlation properties and show significant scatter in results[21].

C) Tip Positioning & Tip Radius

Moreover, Kabel[24] highlighted the fact that poor calibration of the microscope to indenter positioning can result in lower throughput and data yield, as the experimental acquisition is slowed down. The importance of indenter positioning with respect to the fibre cross-section was highlighted before in Desaeger's work[99] where any indent/push-out performed at an r_i/r_f greater than 0.3 was discarded (r_i being the distance between indenter centre and the fibre centre, and r_f being the fibre radius). This was also demonstrated in a model by Rodríguez[101] showing that push-in behaviour is independent of flat punch tip radius provided a r_i/r_f ratio exceeding 0.6 is maintained. This effect is further accentuated when Berkovitch tips are used as fibre cracking is more easily induced with misalignment to fibre center[101].

D) Debonding Location (Interphase-scale)

As previously highlighted in section 2.2.1.3, the outside or inside debonding plays an important role in lifing the CMC's.

E) Fibre Local Environment (Intra-Tow Variability)

The analysis of neighbouring fibres and local fibre environment is a clear gap of knowledge in the community, as previous fibre push-outs paid no to little attention for neighbouring fibres[96]. For example, a SiC fibre in a SiC_f/BN/SiC preferentially oxidises when in contact with a neighbouring fibre (as shown by the Opila group[55]) because the SiC acts as an oxygen getter; however little knowledge is available on consequential effects on CMC mechanical performance. Recent research – including Molina-Aldareguía et al. [124], Rodríguez et al.[101] & Xu et al.[125] – has begun investigating the effect of local fibre environment. The groups purposely pushed fibres which possessed hexagonal neighbouring symmetries (termed 'highly-packed fibre clusters') showing that the fibre local environment had a significantly large effect of data scatter.

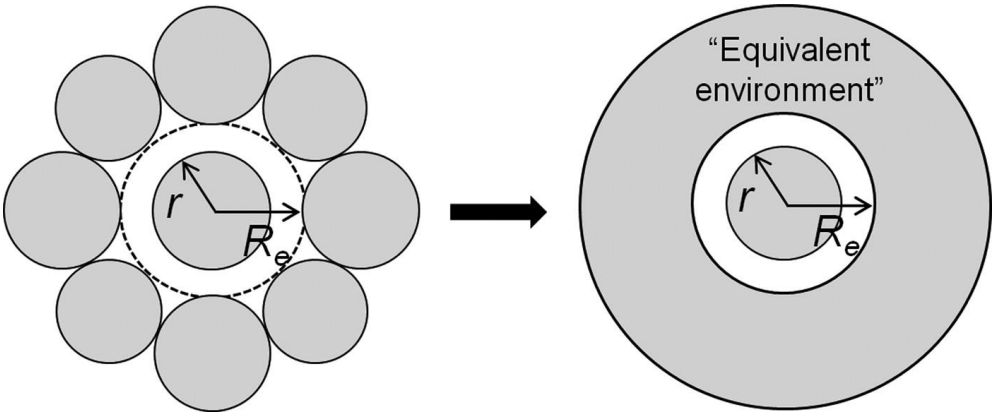


Figure 9: Modelling the effect of local neighbouring geometry, courtesy of Molina-Aldaregiua et al[124]

Rodríguez et al[101] further showed that experimentally and when modelling as shown on Figure 9, only the closest proximity of the fibre (i.e. one fibre away) should be taken into account; thus showing that a fibre with a 6-fold hexagonal neighbouring symmetry was not influenced by the matrix stresses or any plastic deformation. Furthermore, pushing out fibres in the middle or at the edge of tows influences results[96] as the number of fibres surrounding the tested fibre has an influence on radial stresses. Similarly, variations in interfacial shear stresses found in fibres of similar environments may be due to the variations in thermal residual stresses between the BN coating and the fibre from processing.

F) Tow Environment (Inter-Tow Variability)

Variations in inter-tow mechanical properties (as opposed to intra-tow variations) were investigated by Zok et al.[17] whom found no direct correlation between testing fibres close (1 mm) or from a distance (10 mm) to the fracture plane, as well as no evidence of fibres locking (from interphase debris or other fibres) during testing. However, there exists a difference in coating thickness (for both BN and SiC) deposited by CVI proportional to the distance of the tow to the outskirts of the CMC – thus potentially influencing the interfacial measurements. The latter subtlety has not been addressed in literature to the knowledge of the author at time of writing.

G) Statistical Studies

Most studies on fibre push-outs are conducted on a very small number of fibre push-outs or push-backs, thus limiting the understanding and analysis/interpolation of the results obtained, and further not taking into account the influence of parameters highlighted in points A-F. The significance of the number of tests needed for acquisition of a representative population is further discussed in the results of Chapter 4.

H) Surface Deformation of the Fibre from Tip

Nanoindentation is ideal for fibre push-out when the tip is rounded or flat-punched, preventing fibre decohesion or breakage[99]. A flatter tip will also reduce indenter penetration[96] (from higher contact area) and decrease the amount of material that is wedged over as surplus from the surface of what is being indented; this phenomenon is commonly referred to as "pile-up" in Berkovitch indentation (less common in non-metallic materials). Berkovitch indents have the added difficulty of easily splitting fibres, which is controlled by multiple parameters used in the data fitting (fibre transverse strength, fibre diameter and volume fraction[99]) – on load-controlled instruments, this is translated to a plateau region undistinguishable from a push-out[99]. However, it was shown by Mueller et al[96] that load/displacement curves are significantly different from Berkovitch push-out and that a parallel alignment of the tip and fibre surfaces is necessary for this effect to truly bypass limitations presented by sharper indenters. These include the tip plastically deforming the fibre before pushing out (imprints of around 200 nm were found by Medina[105] et al), fibre fracture from high stress intensity stress fields at tip contact level, and the tip hitting the edges of the sample at deeper push out lengths[24]. Mueller showed later on using a flat-punch tip that the determination of the total push-out depth was more complex[96]. Indeed, the total indenter displacement measured was calculated as the sum of the plastic push-in depth, the imprint depth (the tip indenting the fibre surface) and the elastic deformation of both the fibre and matrix – even though the tip imprint is usually neglected in models[101].

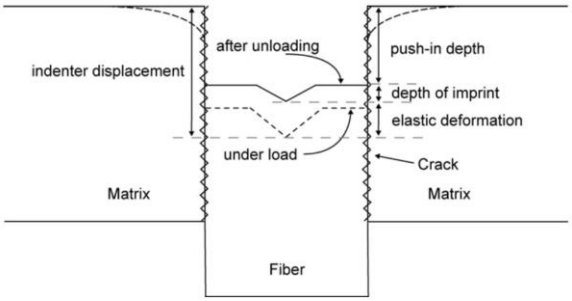


Figure 10: Measured indenter displacement after unloading during a push-out test. Figure from Mueller[96].

Mueller further stressed that these displacements also did not take into account any fibre relaxation. It is worth noting that the plastic deformation from tip imprints can be corrected for if indenting plastic fibre composites following ASTM Standard D965-15[125], but no standard has been established for metallic or ceramic fibres.

Additional fibre push-outs limitations – including sample preparation and in-situ specific challenges – were explored in the introduction section of Chapter 6 (Section 6.2).

2.2.2 The Fibre Push-In Technique

The fibre push-in is similar to a fibre push-out – with the exception that the fibre is (seldom) pushed through the entirety of the sample thickness, rather inducing fracture in the fibre, matrix or underlying material (when woven). Due to the nature of the fibre push-in and its experimental set-up, there is a need for checking the compliance of the system (e.g. if samples are mounted on an aluminium holder, the maximum interphase shear strength needs to be lower than the compressive stress of the underlying aluminium). The fibre push-in was contrasted to the historically relevant slice compression test[126], where two plates compress the material regardless of its thickness and the imprint of the fibre is measured on the plate. In 1991, Weihs et al. [127] showed that the push-in (or push-down) technique was reproducible experimentally, but that the numerical outputs strongly varied and that Poisson's effect had little effect on that specific composite (SiC/LAS). The fibre push-in can be performed in monotonic tension, cyclic, or static fatigue. The push-in technique was shown in 2012 by Rodríguez[101] et al., 2016 by Medina[105] et al., and in 2018 by Xu[125] et al. to display similar outputs to the push-out technique if using the following analysis for push-ins:

$$\tau = n \times \tau_{pushout} = \frac{nP_c}{2\pi r^2} = \frac{S_0 P_c}{2\pi^2 r^3 E_f} \quad [15]$$

Where S_0 is the slope of the unanalysed load-displacement curve and n is defined by:

$$n = \frac{S_0}{\pi r E_f} \quad [16]$$

Noting that the critical load P_c differs to that found during push-out tests, and can be found with post-data acquisition analysis where a subtraction of the elastic deformation of the fibre must be performed (the algorithm for determining P_c is detailed elsewhere[125]). Xu et al. further analysed the push-in ISS probabilistically by using the Welch unequal variance t-test[125] in order to compare samples with one another – this can be reproduced for the other techniques. The push-in technique can essentially be considered a push-out during which only elastic compression of the fibre occurs, as imaged by Zhang et al[119]. Other advantages of the push-in technique include the ability to test the same fibre under cyclic loading to higher loads or failure, the ability to extract the density of fibre bridging cracks[128], and the ability to give an estimate of fibre fracture toughness when the fibre breaks – all due to a more stable crack growth under shear loading[96]. Lewinsohn[128] later showed that the push-in technique could also be used to directly measure interphase recession from oxidation conditions, however the depths they measured had a greater scatter when compared to optical measurements, most probably due to fibre buckling during testing. The hysteresis loop from cyclic tests can be used to calculate an initial interfacial shear strength τ_i for reference sliding stress. Rebillat[19] further argued that push-in tests were the least reliable micro-mechanical technique, as several characteristics typically used in post-acquisition analysis remained unknown (e.g. total debond length along the interphase, fibre damage and bending of the fibre or sample from high loads).

The interfacial properties of CMC's can also be found by either scaling bulk monolithic properties down with Weibull type statistics, or by using extrapolating methods such as cyclic testing. This was done by Zok et al.[17] using the fibre push-in in cycles whereby a debond toughness Γ and an interfacial shear stress τ could be obtained via the following set of equations:

$$\Gamma = \left(\frac{F_c}{2\pi}\right)^2 \frac{1}{r^3 E_f} \quad [17]$$

$$\tau = \frac{{F_{cycle}}^2}{4\pi^2 r^3 E_f \Delta_*} \quad [18]$$

Where Δ_* can be found by fitting a variation in loop width Δ with normalised force during cycles (illustrated in Chapter 3). In SiC_f/SiC composites, the magnitude of debond toughness averaged 5 $J.m^{-2}$ whilst the sliding stresses reached 30 MPa[17]. Extrapolating interfacial shear strengths from hysteresis stress/strain responses usually yielded higher values than those obtained via the Hsueh model with push-outs[19]. Overall, push-ins usually yield information on fracture toughness since fibres commonly break.

2.2.3 The Fibre Push-Back Technique

Push-backs occur after push-outs, during which the indenter presses on the pushed-out fibre from the sample backside plane. In contrast to fibre push-ins, push-backs yield more information on the frictional component of the push-out behaviour, as a crack has already fully propagated and the fibre has already debonded from its interfacial sheath. As such, only tribological properties need to be considered. In ceramic materials, the friction is increased with either increased abrasion (from asperities, third-body wear debris) or with favourable bonding (between similar-sized atomic radii, with dangling bonds or in vacuum). Friction is decreased with site passivation or oxidation (in the case of turbostratic BN planes, the chemisorption of moisture reduces van der Waals bonding strength)[129].

Push-backs are only viable on samples with a sufficiently high thickness/interfacial strength ratio[4] and better investigate 'stick-slip' phenomena previously studied during the initial days of push-outs[130]. The coefficient of friction from fibre push-backs can be found according to Coulomb friction principals[111]:

$$\tau = -\mu\left(\sigma_c + \sigma_p\right) \quad [19]$$

Where τ is the interfacial shear stress, μ the coefficient of friction, σ_p the interfacial radial stress and σ_c the residual clamping stress. Push-back stresses are lower than those of initial push-outs since the interphase has previously experienced mechanical damage, which reduces the friction coefficient[111]. Fibre push-backs also experience a 're-seating' effect whereby the fibre reassumes its initial position (from before being pushed out). Experimentally, this translates into a slight load increase[63], itself directly correlated to the fibre roughness. The fibre push-back is however only detectable on displacement-control instruments, as the re-seating effect lies after the maximum load is reached. Therefore, the roughness effect of the initial push-out test can be tested by subtracting the push-out interfacial shear stress to the re-seating stress measured during push-back[34]. Push-backs have however been found to severely underestimate interfacial properties due to secondary wear effects[21].

2.2.4 Miscellaneous Advanced Techniques

Due to some of the limitations of the three techniques highlighted above, the need for more novel micromechanical techniques has spurred interest. Examples of such novel methods were included in this section. The rate-dependence of the interfacial properties can be investigated by means of other novel micromechanical techniques such as the dynamic micro-debonding technique[123] developed by Tanoglu using the DILA (dynamic interphase-loading) apparatus, which can reach rates up to 3,000 $\mu.s^{-1}$. Tanoglu found that the ISS and the coefficient of friction both increase with displacement rate in e-glass fibre/epoxy-amine interphases.

Whilst the fracture toughness of the interphase can be correlated to the axial stress close to the fibre surface at crack initiation during a fibre push-out[36,109] (assuming zero friction) using:

$$G_i = \frac{\left(1 - 2\nu_f k\right)P_d^2}{4\pi^2 r^3 E_f} \quad [20]$$

Where P_d is the debonding load and k is a combination of the elastic properties of the fibre and matrix, given by Kerans et al[36], however the fracture toughness found by shear-lag model fitting is usually overestimated[109]. Consequentially, the fracture toughness can be obtained by other micromechanical experiments including the Single Notch Cantilever Bending (Matoy[131] 2009), the Clamped Beam Bending (Jaya[132] 2012), the Double Cantilever Bending (Liu[133] 2013) and the Pillar Splitting (Sebastiani[134] 2014) methods – all of which can be fitted using corrected beam theory for property extraction, and all exhibit their own pros and cons.

Focused Ion Beam techniques have been highlighted as a promising future for the field of micromechanics[101]. Indeed, the more traditional fibre push-out, push-in and push-back techniques do not require sample preparation by ion milling. For example, micro-pillar compression was investigated by a few teams[135,136] including Zayachuk et al.[24] as a more reliable method than fibre push-outs for evaluating interfacial properties in CMC's. Friction coefficients at the interface can be found with other techniques if fibre stresses are known, however micro-pillar compression tests are more efficient and reliable for finding friction coefficients. Micro-pillars are commonly sized to 3 µm in dimensions, and can provide an estimate of fracture energy release rate, when considering both Mohr's fracture criterion and fracture path tortuosity. Despite its relatively high spatial resolution, its propensity to ex-situ testing and ease in sample fabrication, the technique has its own limitations since pillars can often be too fragile and exhibit instant debonding. Furthermore, no information on residual stresses and no kinetic properties from the stage after debonding can be obtained reliably[137]. Finally, the micro-pillar technique has been highlighted by Ast et al. to have unstable crack behaviour in the majority of CMC's when looking at a toughness/hardness Ashby map[138] (with very few CMC's reaching the threshold K_c/HV ratio of 0.008). In order to promote and obtain stable crack propagation measurements, the mode 1 damage tolerance R-curve must be acquired via alternative techniques. Another interesting FIB-based technique lies in the 'via-pillar-push-out' method introduced by Wu et al.[139] as a micromechanical alternative to the fibre push-out – producing both a maximum interfacial shear strength and a steady-state frictional shear strength, obtained by the following equations:

$$F = \frac{\pi D_f^2 E_f \Delta}{4\lambda} \tanh\left(\frac{l}{\lambda}\right) \quad [21]$$

Where D_f is the via diameter, l is the initial bonded length, Δ the maximum displacement, and k is the slope of the elastic portion of the experiment (λ being the characteristic length), itself obtained by:

$$\lambda = \sqrt{\frac{E_f D_f}{4k}} \quad [22]$$

$$\tau_{max} = \frac{F_{max}}{2\pi r l} \quad [23]$$

$$\tau_{friction} = \frac{F_{friction}}{2\pi r l} \quad [24]$$

More advanced methods developed over the last few years include the in-situ trench push-out developed in this thesis[140], as well as the novel fibre-fretting technique by Kabel[141]. The fibre-fretting

technique makes use of Bowden & Tabor's deconvolution law separating the friction force during fibre sliding into an adhesive component and a ploughing component[142]. Kabel highlighted that due to its claw-type tip geometry, the fibre-fretting test is limited to compressive loads of around 100 mN, which is sometimes not enough to push a fibre out in SiC-based CMC's[141]. The majority of these micromechanical techniques require sample preparation by FIB milling, which can induce damage[143] prior to mechanical testing; however damage from 1 – 12 nA beam conditions has been shown to be limited to less than 50 nm in depth for SiC CMC's[144], which is equivalent to 0.1% of fibre volume. All FIB damage can be visualised using low EHT (<2keV), an inLens detector or ESB for chemical bonding imaging; it can be minimised by using short miling times to prevent redeposition or gun drift, by annealing to recover damage or by using a Xe/He gun instead of a Gallium gun (as Gallium induces liquid metal embrittlement at times). Sample preparation itself can make use of alternative methods such as chemical etching, femtosecond laser ablation or micro-electrical discharge machining[138].

The majority of the models to fit fibre push-out/push-in/push-back data require an estimate of the residual stresses acting on the target fibre, as detailed in section 0. Residual stress measurements can be obtained from other characterisation techniques such as the curvature method[145], the $\sin^2\psi$ XRD method[146], the high resolution XRD method[147] or FIB in-situ methods including DIC on micro-pillars[148], slot milling[149], hole drilling[150], ring-core[151], micro cantilevers[152], h-bar milling[153] and flour-slot[154] methods.

2.2.5 Micro-Mechanical Testing Summary

Overall, the breadth of micromechanical techniques which can be applied to CMC's is unparalleled when compared to macro-scale testing. An overview of the micromechanical methods used in the context of testing CMC's is given below in Table 3.

Table 3: Summary table of micromechanical methods discussed in this review"

Method	Commonly performed	Use of FIB ?	Main Extractable Propert(ies)	Throughput Yield
Nanoindentation	Ex-situ	No	Modulus, Hardness	High
Fibre Push-Out	Ex-situ	No	Interfacial Shear Strength, Residual Clamping Stress	High
Fibre Push-In (Cyclic)	In-situ	No	Clamping Stress from Thermal Expansion	Medium
Fibre Push-In (Monotonic)	Ex-situ	No	Fracture Toughness (Fibre)	High
Fibre Push-Back	Ex-situ	No	Friction Coefficient, Roughness	Medium
Trench Push-Out	In-situ	Yes	Friction Coefficient, Sliding Stresses, Roughness	Medium
Micro-Pillar Compression	In-situ	Yes	Fracture Toughness (Fibre)	Medium
Micro-Pillar Splitting	In-situ	Yes	Debonding Shear Strength, Fracture Energy	Low
Dynamic Micro-Debonding	Ex-situ	No	Strain Rate Sensitivity, Friction Coefficient	Medium
Micro-Cantilever	In-situ	Yes	Fracture Toughness (Interphase)	Low
Fibre Fretting	In-situ	Yes	Friction Coefficient, Sliding Stresses, Roughness	High

2.3 Research & Development

Research on all CMC-based technologies has grown over recent years – high-temperature CMC-based publications (C/C-SiC, SiC/SiC) have increased from 1 to 33 in 15 years as of 2020[155], as highlighted on Figure 11. However, this figure fails to contrast results to other fields, and to the general rise in publication rates over the same period. This increase in research output nevertheless reflects on the necessity for the aerospace industry to reach its carbon output as set by the UN SDG's (Sustainable Development Goals).

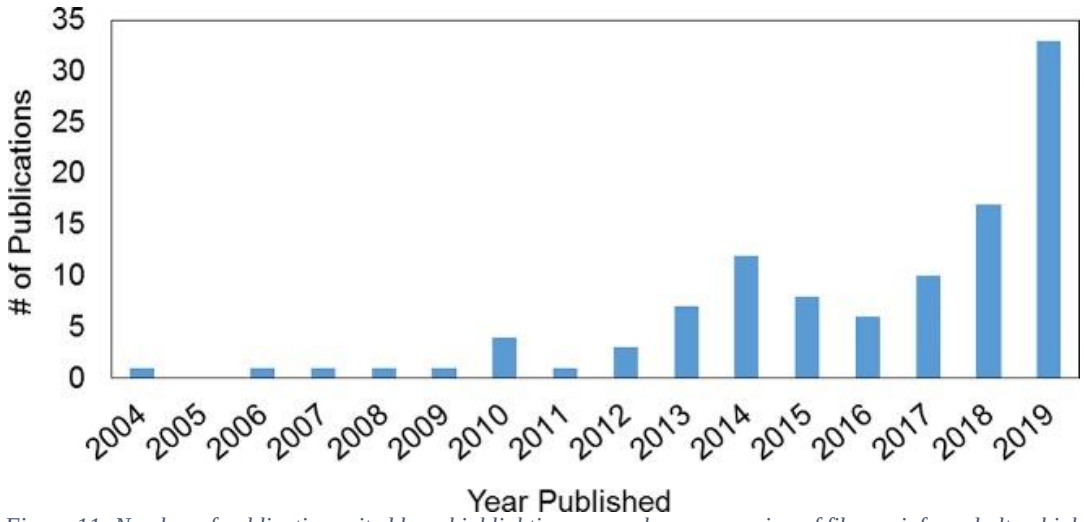


Figure 11: Number of publications cited here highlighting research on processing of fibre-reinforced ultra-high temperature ceramics materials as a function of year published. Figure from Rueschhoff [155]

Research on SiC_f/SiC has insofar focused on improving composite durability & crack-healing properties. For example, Sun[39] et al. reported numerous techniques for improving the oxidation resistance and have grouped them into either crack-healing matrices or substituting the fibre, matrix or coating type. The problem of pest oxidation and overall oxidation resistance of SiC_f/SiC components has been summarised in Chapter 5.

Improvements of the interlayer focus on the oxidation resistance of hex-BN because no oxide material (other than monazite and hibonite) with the correct tribological properties has so far been able to substitute as interlayer[45]. The use of Environmental Barrier Coatings (EBC) to protect the SiC_f/SiC components is at times unreliable[55] and is also costly, complex and time-demanding. The EBC has 8 design requirements: it needs to adhere to the underlying SiC_f/SiC, have a compatible CTE match with SiC, be thermodynamically stable in steam, stop H_2O diffusion, coat complex 3D shapes, be clean (and easily cut), maintain a 0.4 µm clearance with respect to casing and resist Foreign Object Damage (FOD). State-of-the-arts EBC's currently make use of rare-earth silicates in their compositions and are commonly termed third generation EBC's[156]. The EBC coating the Rolls-Royce CMC component is manufactured by OBRS (Oxide Bonded Reaction Sintering) and Air Plasma Spray, and is composed of a Si bond coat, a low-CTE EBC, an abradable and an overcoat (the TBC) – research is ongoing. Research on the more porous TBC's (Thermal Barrier Coatings) is currently focusing on reducing thermal conductivity and photo scattering effects at higher temperatures[16] as well as developing 'health monitoring' layers in the TBC's, which would enable fast NDT of the composites when in-service. Any oxidation studies on the CMC oxidation assumes a hermetically closed component due to EBC advancements.

Research is still ongoing for engineering techniques to tailor the interphase for a better control of its micromechanics. These include tempering the interface by doping[116, 158], multi-layering[12, 52, 63], fugitive interfaces[159, 117] or modifying the processing conditions[89, 160, 161] – further detailed below. Regardless of the solution proposed, a reliable and quantifiable method of measuring interfacial properties is still required to measure performance, especially if microstructurally informed rather than empirical methods are to be developed.

2.3.1 Interphase Doping

Si-doped BN interlayers have been shown to degrade less in humid environments, but were often weaker mechanically when compared to traditional BN interlayers[158, 116]; experiments involving Si-doped BN interlayered composites tested for 40 hours of stress-rupture did not oxidise - even in the crack[158]. Similar trends were reported by Opila[55] on the GE SiC_f/SiC material with i-BN Sylramic fibres – with the doped interphase bonding well with exposed fibres. Microstructurally, doping could disrupt the hexagonal aromatic network and thus reduce the area contributing to friction around the fibre, thereby increasing path tortuosity and the amount of work to fail the material[24]. Doping with silicon may result in the oxidation of the composite to silica (as opposed to boria)[158], thus shifting oxygen ingress from matrix diffusion-controlled to reaction-rate controlled at the SiBN interphase level[162]. Doping with aluminium (a pre-cursor for specific fibres like Tyranno type SA3) results in poor oxidation resistance at 800°C but improved oxidation resistance at higher temperatures above 1000°C due to the creation of an alumina layer ahead of the borosilicate glass layer – thus limiting oxygen ingress inside the material[163,164,165]. Rare-earth additives to the fibre coatings were found to raise the minimum oxidation temperature by adding asperities and increasing the surface roughness of the fibres[166]. Another alternative lies in using carbon-based, but boron-doped interphases[67] – however this introduces the problems of SiC and boria syntheses at the interphase, both of which seal cracks instead of propagating them. Overall, doping the matrix alone was found to have a negative effect on the composite oxidation resistance[167].

2.3.2 Multi-Layered Interphases

The interlayers – whether PyC or hex-BN – can both be superposed with n SiC-CVD deposited layers to create complex microstructures of $(BN\text{-}SiC)_n$ at the interlayer[52,12]. Layered interphases deflect cracks by multiplying the number of interfaces. As cracks propagate from one interface to the other, more energy is consumed, thus prolonging composite lifetime.

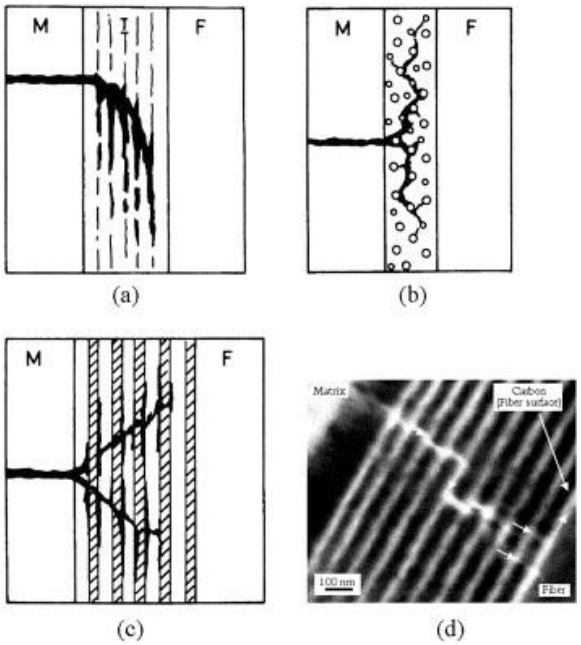


Figure 12: Different simple or engineered interphases used in SiC-matrix composites: (a) single layer pyrocarbon or hexagonal BN interphases, (b) porous SiC single layer interphase, (c) multilayered $(X-Y)_n$ interphase, with X=PyC or BN and Y=SiC (schematic), (d) crack deflection in a multilayered $(PyC–SiC)_{10}$ interphase, Figure courtesy of Naslain[52]

Layering both the pyC (relatively compliant) and hex-BN (self-healing and somewhat oxidation resistant) interphases multiplies the benefits of each, but also decuples complexity in modelling[41]. Examples of these multi-layered interphases include the SiC_f/B-doped $pyC_{(n)}/B_4C+SiC_{(n)}$/SiC composites from Naslain et al. which heal by forming boria-rich phases[12], or the added 250 nm thick CVD-SiC layer coating the fibres before the 130 nm thick pyC interphase (reportedly ensuring crack propagation in the pyC layer itself) from Hinoki et Yang[22].

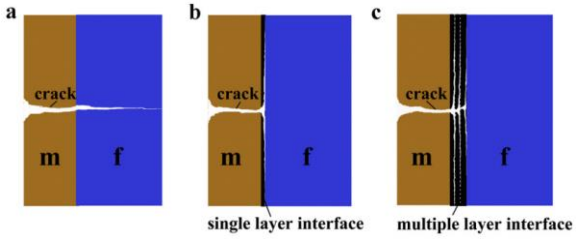


Figure 13: Crack paths differences with single-layer and multi-layered interphases. Figure from Wang et al.[88]

Layering also adds distance from the fibre to the matrix. In practise, this increases the thickness of hex-BN coatings – making them more akin to pyC coatings (shown to have increasing aromatic ordering the further away from the fibre they are[168]). Experimentally, when comparing these new interphases to more traditional ones, non-multi-layered coatings of sub-micron thicknesses showed no sign of oxidation at 1200ºC and 1285ºC[90], however lower-temperature regimes are known to be more problematic.

Layers also enable separation (and therefore more parametric control) of interphase properties. For example, the layer closest to the fibre can act as an adherent glue, whilst the second layer can be

oxidation-resistant and a third layer can solely control crack deflection[63]. Another advantage of these multi-layers is the ability to tailor exactly how much interfacial strength lies at the interface, and therefore how much fracture toughness is exhibited by the overall composite[37]. The latter has however been disputed by Yu et al, whom observed no direct correlation between the change in shear strength and the number of coated layers added[20]. Finally, the BN layer was found to have damaged the underlying pyC layer[23] when dip-coating and layering interphases during manufacturing by Yang et al, thereby increasing the chance of interphase damage.

2.3.3 Fugitive Interphases

The fibre interfacial coating can be incinerated or diffused out to create an interface-free composite (whereby fibre and matrix are separated by an air gap) – termed fugitive interfaces[159,117]. This is similar to the Nano-Infiltration and Transient Eutectic-phase (NITE) process developed by Shimoda et Hinoki[169] whereby BN particles are embedded in the matrix and there is only a residual $Al(OH)_3$ interphase from fibre manufacturing. The fugitive interphase concept stemmed from assuming that the interphase was – and is – the primary route for oxygen ingress within the material, and that its total removal was the most efficient solution. These composites perform well mechanically especially in fatigue life (with oxidation only visible at surface level even 10^6 cycles[170]) but will inherently pose problems with hermeticity – especially in both the nuclear and aerospace industries (more so on the latter).

2.3.4 Matrix Getters

Matrix getters will mitigate and diminish the effect of oxidation of the BN interphase[4]. More complex designs such as those highlighted by Monteverde[171] utilise granules inside the matrix (acting as a sub-composite within the composite) to further reduce impact from environmental degradation. Other types of matrix getters include buffer layers around the fibres such as ZrB_2, Si_3N_4, SiCN or HFSiCN to prevent fibre damage from MoSi attack. Rebillat's work[10] on a Si-B-C self-healing matrix only showed success at low (<150°C) or high (>800°C) temperatures, but lacked blanket coverage at intermediate pest temperatures.

2.3.5 Fibre Substitution

Using Sylramic fibres (which contain boron) improves the corrosion resistance[117] of SiC_f/BN/SiC composites – the fibres being more adherent to the interphase. NASA has developed a thermal programme which extracts the boron atoms from the Sylramic fibres to the edges so as to form thin BN layers – with interfacial shear strengths reaching values of 70MPa (higher than CVI or CVD boron layers)[172]. The Sylramic fibres (with PVA sizing) were also the only fibres which did not degrade in the original study by Ogbuji[61] on pest oxidation.

2.3.6 Interphase Substitution

Interphase materials have been less researched due to the numerous requirements needed (high friction coefficient, good oxidation resistance, inter-atomic shearing etc..). A $SiO_2/ZrO_2/SiO_2$ coating of the fibres is an example of a more stable interphase when exposed to more aggressive conditions, however it lacks the suitability in both mechanical and rheological properties, and has thus far only been tested on minicomposites[173]. Another example is $Re_2Si_2O_7$ and other types of rare-earth di-silicates with quasi-ductile polymorphs. These have been investigated and reported to display similar properties to their more common counterparts, but at a higher cost[118].

2.3.7 Manufacturing Parameters

High-temperature processing of the hex-BN film is also crucial to improving its oxidative pervasive resistance[160]. Indeed, Naslain[174] showed that a higher processing temperature resulted in more crystalline BN, resulting in more oxidation-resistant fibres but more prone to fibre damage (an optimisation therefore needed to be struck). The BN interphase in SiC_f/SiC samples isothermally and isobarically[47] processed by Chemical Vapour Infiltration (CVI) from BCl_3-NH_3 gas mixtures usually deposit at a rate of 1 µm / 20 hours, and deposit no solid reaction product (B_4C or Si_3N_4) if deposited at equilibrium above 1000°C[47]. CVI-deposited BN samples were found to degrade more in oxidising conditions (high temperature 1200ºC, high water content, 1.5 atm) than samples processed by Melt Infiltration (MI) [175], as highlighted in Figure 14.

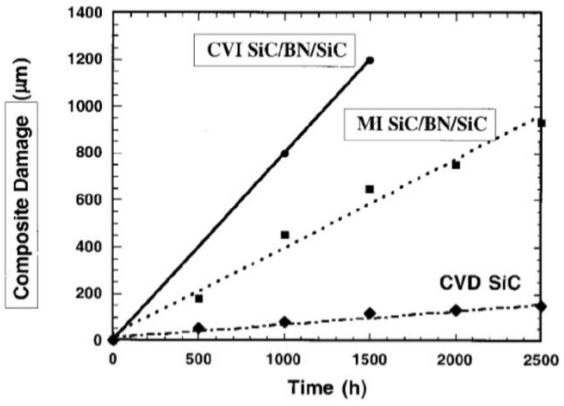


Figure 14: Comparison of damage depths between different processed SiC_f/SiC samples exposed at the same oxidation conditions as manufacturing conditions. Figure from More et al.[175]

Poor processing essentially results in the creation of a complex fibre-to-matrix transition composed of three amorphous interphases; namely a thin (~ 40 nm) SiO_2 layer, a BN layer and a thin (~ 80 nm) carbon sublayer close to the fibre surface[47]. In the event that thin sublayers are created, matrix cracks are able to deflect at those interfaces. After processing, any un-reacted species inside the BN interlayer should also be treated at 1200ºC for 5 hours in Argon to decompose[89] and improve overall interface quality. Argon treatments have been previously shown to seldom affect frictional behaviour[25]. Any carbonic layer left untouched on the fibre surface will have deleterious effects on oxidation[176]. This was also shown by Rebillat[63] whom tested composites with sized fibres and observed extensive crack branching at the interphase. Alternative solutions have been proposed,

including layering the highly crystalline BN next to the conventional BN layer in unpublished work[61] by Yun H. and DiCarlo J.

Increasing processing temperatures can also have other undesirable effects such as increasing the deposition rates – thereby completely chemically vapour infiltrating tows and preventing stacking of fibre preforms[161]. However, Rebillat[19] et al experimentally found no correlation between BN processing conditions and interfacial shear strength. Finally, another processing innovation includes substituting pure Si with alloys of Silicon or other refractories to perform the melt infiltration and leave less residual Silicon in the matrix[9].

2.3.8 Interphase Thickness & BN Lattice Spacing

The amount of space between fibres directly influences how much of the interphase oxidises to glass. The ideal interphase thickness lies at values greater than 100 nm[4] – smaller values result in undesirable bridging of fibres to themselves, or the matrix. Yang et al. reported needing thicknesses of 200 nm and above for stable debonding behaviour[66]. Plaisantin and Delpouve reported an optimum thickness of 500 nm for poorly crystalline BN, and no optimum thickness for highly crystalline BN[177]. Jacques reported that any interlayer thicker than 4 μm is of no use, since this only protects the interlayer in one direction (for crystalline anisotropic BN)[163]. This assumption was further shown by Jacobson[160] and Collier et Zok's modelling efforts[178], which showed an increase in thickness of the BN directly correlated to an accelerated recession. An increasing interphase thickness has been reported[83] to decrease both matrix cracking and interfacial frictional stresses (as well as higher pull-out success rates). The optimal {002} interplanar spacing between hex-BN layers for maximal oxidation resistance has been shown to approach 3.35Å[93]. However, in order to prepare thicker interphases, micrometer-level separation of the fibres has been achieved in numerous ways including tow 'fluffing'[116], pre-CVD-Boron treatments[172] and tape lay-ups[91].

2.3.9 Crack Healing

It has been reported that fusing silica with boria in the matrix has a positive effect on the mechanical properties of the composite[179], although excess amounts of boria can also be deleterious. Indeed, a fusible oxide formed when B_4C and Si-C-B compounds were present[67]. The healing was also directly observed in SiC_f/pyC/SiC composites by Terrani et al. after exposing the composites to steam at 1500°C for 24 hours[73], where surface cracks were deviated at the interphase and subsequently filled with oxide.

2.3.10 Modelling Efforts

Modelling of the degradation of BN interlayers in SiC_f/SiC is extremely varied and complex. Different microstructural failure mechanisms arise depending on the temperature range, the humidity range, the crack density, the coating thickness, the fibre quality etc… Modelling within Rolls-Royce is tasked to create a library of performance envelopes. It has focused on integrated and multi-scale methods (micro being fibre-level, meso being weave/yarn level and macro equating to component level) to look at both on- and off-cycle conditions, including all sources of damages from both the

environment (recession, ingress) coupled with mechanical damage (matrix cracking, fibre tow failure, load transfer, constituent creep etc..). Modelling of CMC's lies in the wider effort to develop ICTS' (Integral Ceramic Textile Structures), which will improve CMC part geometries by 3D computational iterations. Examples of applications of the aforementioned include placing fibre tows precisely to avoid superposition with cooling holes, or creating warp fibre tows to reduce fibre splitting[16]. An excellent overview of the mechanical models developed on CMC's at the microscale has been provided by Fang et al.[180,181] – the authors highlighted advances in developing a) energy-based and fracture mechanics-based models looking at crack deflection prediction and taking into account energy release rates, b) numerical models including FEM and VCCT (Virtual Crack Closure Technique) looking at interphase thickness, to finally developing c) an XFEM (Extended FEM) model to alleviate limitations found in more traditional FEM methods (e.g. allowing for crack initiation). When modelling SiC_f/BN/SiC using XFEM more specifically, Fang et al.[180] found that secondary crack initiation within the BN (before propagation of a matrix crack) was the dominating mechanism for crack deflection. Chemical and thermal modelling efforts of the phenomenon have revealed the significance of channel sealing[160], whereby boron diffusion to the surface is limited by the formation of viscous borosilicate liquid. It also revealed that outermost fibres are more prone to oxidation and therefore development of unbridged cracks inside the bulk will be favoured[6]. Modelling by Morscher et al.[116] at 815°C showed that low stresses induced single fibre failure whereas high stresses related failure to oxidation-damage depth. Morscher also highlighted that Hi-Nicalon fibres were more prone to oxidation damage when compared to Sylramic fibres. Modelling (combined with experimental data) by Jones et al.[92] has also produced a failure mechanisms map in SiC/SiC composites:

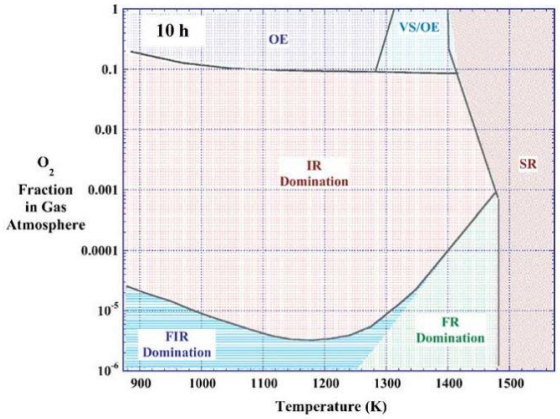


Figure 15: Failure Mechanisms Map in SiC_f/SiC by Jones et al.[92] Key: OE = Oxidation Embrittlement, VS = Viscous sliding of Oxide in Interphase, IR = Interphase Removal (due to Oxidative volatilization), FIR = Irradiation enhanced creep of fibres (and crack growth), FR = Fibre relaxation and Creep, SR = Fibre Stress-Rupture

Modelling efforts on the fibre push-out have internally coupled a cohesive law with residual frictional shear and a friction reduction. Overall, the wealth of research published on CMC modelling highlights the need for higher fidelity measurements of micro-scale tribological properties.

2.4 Knowledge Gap Analysis

The sources gathered in this review chapter have helped identify the following limitations – the majority of which will be addressed in this thesis. First and foremost, there is a clear lack of statistical data on the fibre push-out technique – even more so when applied to SiC_f/BN/SiC composites – for meaningful results to have been produced. This is also layered to added experimental limitations highlighted in Section 2.2.1.4, including tackling debonding location and inter/intra-tow variability in measurements – all undertaken in Chapter 4. The technique development itself has been detailed in Chapter 3, alongside traditional nanoindentation on our target materials. The effect of water vapour – a significant limiting factor in the direct implementation of SiC-based CMC's in aero-engines – has been tackled in Chapter 5 (which also includes an oxidation-specific introduction and review), alongside the effect of intermediate-temperature deformation. Finally, the lack of in-situ visualisation of the dominating failure mechanism at the microscale has resulted in the production of Chapter 6, which aims to observe said mechanism whilst providing more insights for better understanding of CMC behaviour.

2.5 Chapter Summary

CMC's, SiC_f/SiC composites, and their constituencies are seeing renewed interest for their applicability in both the aerospace and nuclear industries. The toughness of the composites can be achieved through various micro-mechanisms including fibre pull-out at the interface – which requires adequate tailoring of rheological properties. The different types of SiC fibres, CMC interphase material (pyC and BN), and the use of SiC_f/SiC composites in an aero-engine context were all summarised. An overview of the micro-mechanics and micro-mechanical techniques surrounding measuring composite properties was given – these included the fibre push-out, push-in and push-back amongst others.

For SiC_f/SiC with BN interlayers the most prominent problem to date remains pest oxidation - excessive degradation at intermediate temperatures (600 – 800 ºC) in humid engine exhaust environments. The current knowledge behind pest oxidation and hex-BN interlayer oxidation more specifically has been collated in Chapter 5. However, current advancements in measuring interfacial properties and an overview of potential solutions to alleviate the problem have been presented in this chapter. Some of the latter include tempering with the interface by doping, multi-layering or fugitive interfaces, modifying the processing conditions or even changing the location of interfacial debonding during deformation.

Chapter 3 • Experimental Methods & Optimisation

3.1 The Material

This quick overview serves as a guide to understanding and optimising the experimental techniques developed in Chapter 3. A more detailed description and analysis of all samples is performed in subsequent Chapters 4 – 7.

The SiC_f/BN/SiC composites in this thesis have either a thin (~ 200 nm), medium (~ 400 nm) or thick (~ 600 nm) BN CVD interphase coating the fibres. The quality of the CVD process means that the BN interphase is of average quality, with crystallinity levels reaching 50% at maximum, and whereby crystallite pockets of differently-oriented aromatic BN planes are scattered in a sea of glassy (amorphous) BN. The fibres themselves are second-generation (Hi-Nicalon™ from NGS Advanced Fibers & Co.) or third-generation fibres (either Hi-Nicalon™ type S from NGS Advanced Fibers & Co. or Tyranno SA grade 3 ® from Ube Industries Ltd.). The fibre tows are woven into a balanced 2D 5HS woven fabric and stacked to form a preform that is then coated with a BN interphase through CVI and a CVI SiC tow coating layer. These porous preforms are then densified with SiC slurry and finally a Si melt infiltration, which results in a matrix composed of β-SiC crystalline grains and α-SiC particles in a sea of residual silicon. Typical samples used in Chapter 3 have constitutive properties highlighted in Table 4.

Table 4: Fibre type, diameter and interphase thickness for selected samples used in this study

Sample	Fibre Type	Fibre Diameter	Interphase Thickness	Root-Mean Square Fibre Roughness
HN	Hi-Nicalon	12 ± 3 µm	200 ± 50 nm	5.42 nm[182]
HNS – Thin BN	Hi-Nicalon Type S	12 ± 3 µm	200 ± 50 nm	2.33 nm[65]
HNS – Medium BN	Hi-Nicalon Type S	12 ± 3 µm	400 ± 50 nm	2.33 nm[65]
HNS – Thick BN	Hi-Nicalon Type S	12 ± 3 µm	600 ± 50 nm	2.33 nm[65]
TSA3 – Thin BN	Tyranno Type SA3	8 ± 2 µm	200 ± 50 nm	8.04 nm[65]
TSA3 – Medium BN	Tyranno Type SA3	8 ± 2 µm	400 ± 50 nm	8.04 nm[65]
TSA3 – Thick BN	Tyranno Type SA3	8 ± 2 µm	600 ± 50 nm	8.04 nm[65]

Whilst some commercially available constitutive properties of the fibres are included both in Table 4 and a box schematic of sample categories in Figure 16, more detail is presented in Chapter 4.

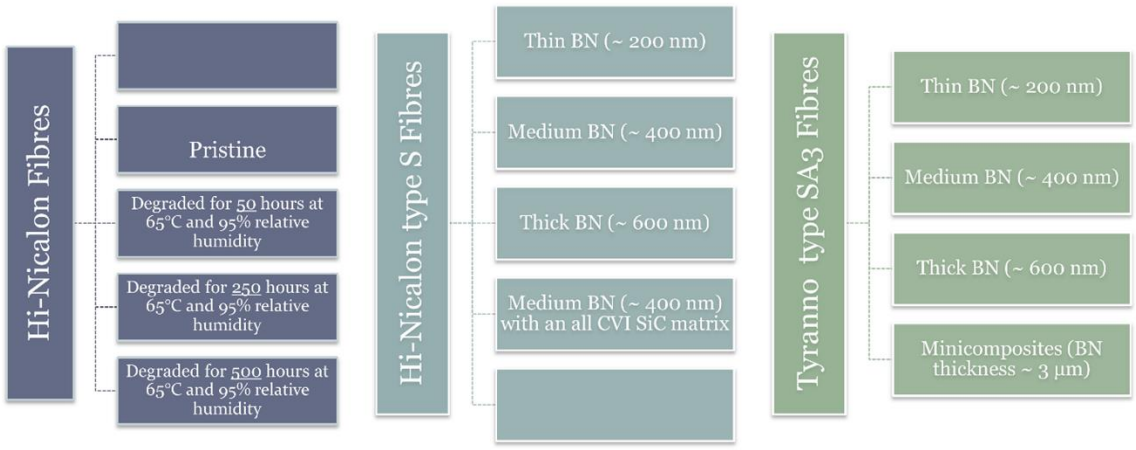


Figure 16: Box schematic of all sample types, [redacted]

3.2 Constituent(s) Hardness & Moduli

This section details indentation measurements made both on regular composites (Table 4) and microcomposites (bottom right, Figure 16) consisting of a single bundle of fibres coated in a BN interlayer of much more prominent thickness (3000 ± 600 nm) imbedded in CVI SiC. Using microcomposites resulted in more accurate measurements of elastic properties – especially as the BN interphase could more easily be probed. The reasoning behind using microcomposites instead of more representative composites is further detailed in the introduction of Chapter 6. The microcomposites[183] are composed of Tyranno type SA3 fibres coated with a significantly thicker layer of BN & CVI SiC, volume fractions of 33.9 %, 27.7 % & 38.4 % for the fibre, BN & CVI interlayer respectively, resulting in a porous surface area of 0.17 % per cross-section.

3.2.1 Berkovitch Indentation

Initial nanoindentation tests were used as calibration measurements to evaluate the hardness, modulus, indentation load and depth of the various composite components.

3.2.1.1 Bulk Measurements

Measurements of hardnesses and moduli on fibres, matrices and interlayers were performed 20 times on each sample in order to obtain a reliable method to quantify the mechanical properties of the composite. The input parameters on the Nanosuite software were set to the following: a 2000 nm surface find was used to approach the distance at a speed of 30 $nm.s^{-1}$, alongside a frequency of 42 Hz. Two calibrations were performed before batch indenting, the first was a tip-area function calibration of the Berkovitch tip on fused silica (a material with known standard modulus of 72 GPa) and the second calibration was a cross-hair calibration on the SiC composites.

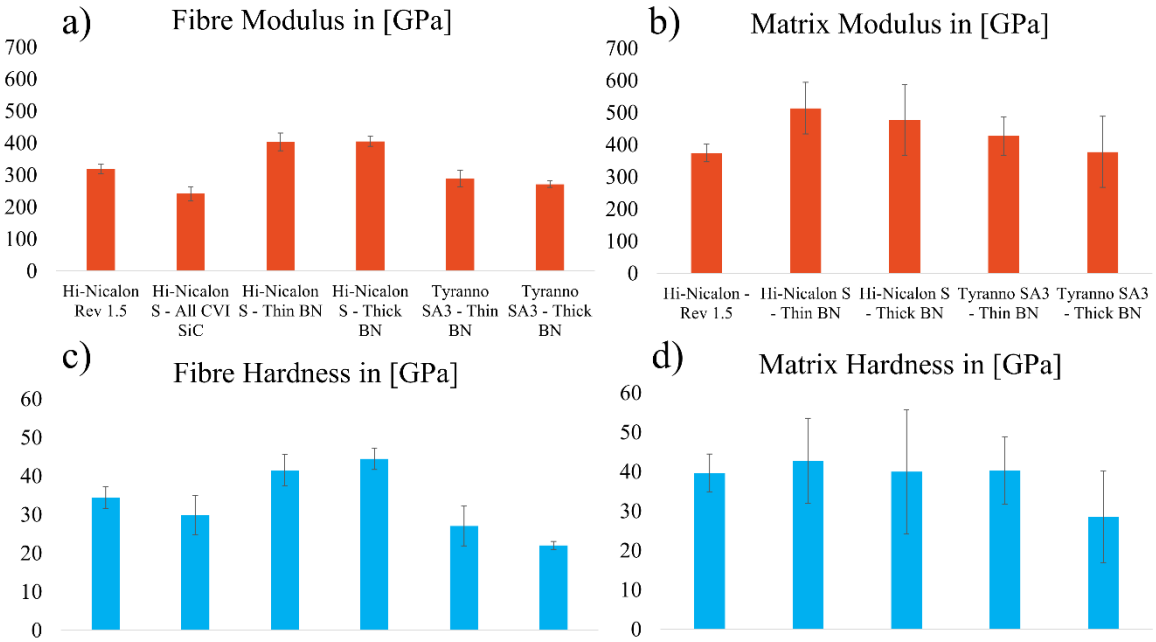


Figure 17: (a, b) Modulus and (c, d) Hardness data from indents inside single fibres (a, c) and random indents in the matrix (b, d).

Data in Figure 17 shows a clear difference in error bars when comparing indents performed in the middle of fibres with those randomly distributed in the matrix. Indeed, the matrix contains multiple elements including β-SiC grains, α-SiC particles and residual Si. Even with potential residual silicon being hit in the matrix indents, the overall hardnesses for the matrices surpassed that of the fibres. Subsurface effects like the indent reaching a SiC grain below the residual silicon on the surface have to be acknowledged in their role of increasing variability. Comparing fibre types in Figure 17, Hi-Nicalon type S displayed superior mechanical properties, this may have been due to the more pronounced porosity in the centre of Tyranno type SA3 fibres (since indents targeted the centre of fibres).

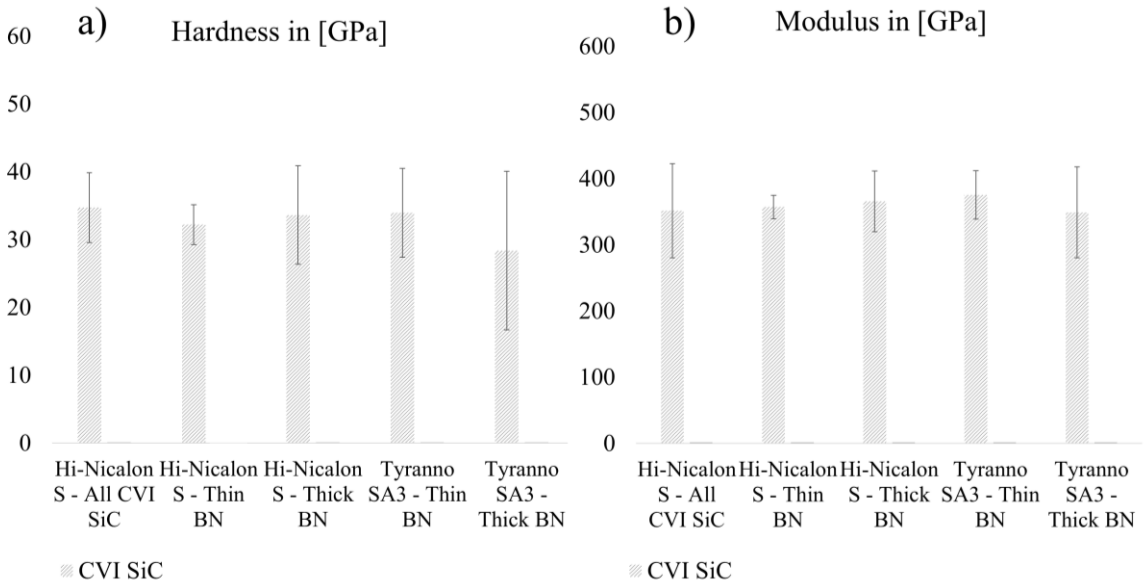


Figure 18: (a) Hardness & (b) Modulus data for all CVI SiC [redacted] in target samples.

Data in Figure 18 showed how the expected uniform mechanical properties differed between samples, even with the same calibration whereby shallower indents (of depths not exceeding 600 nm) were made to assess mechanical properties. [redacted] The modulus of the CVI SiC interlayer was homogeneous across all samples. This helped show that the manufacturing technique produced high quality material. The mechanical properties of the CVI SiC seemed unaffected by the thickness of the neighbouring BN.

3.2.1.2 Array Indentation (Melt Infiltrated Matrix)

In order to investigate the variation in mechanical properties of the matrix, bulk indentation was subsequently performed on the melt-infiltrated matrix alone. 150 indents, 1200 nm-deep and separated by 15 µm (at least 10 times the indentation depth) were performed in a rectangular array on a Hi-Nicalon type S sample with a thick BN interlayer.

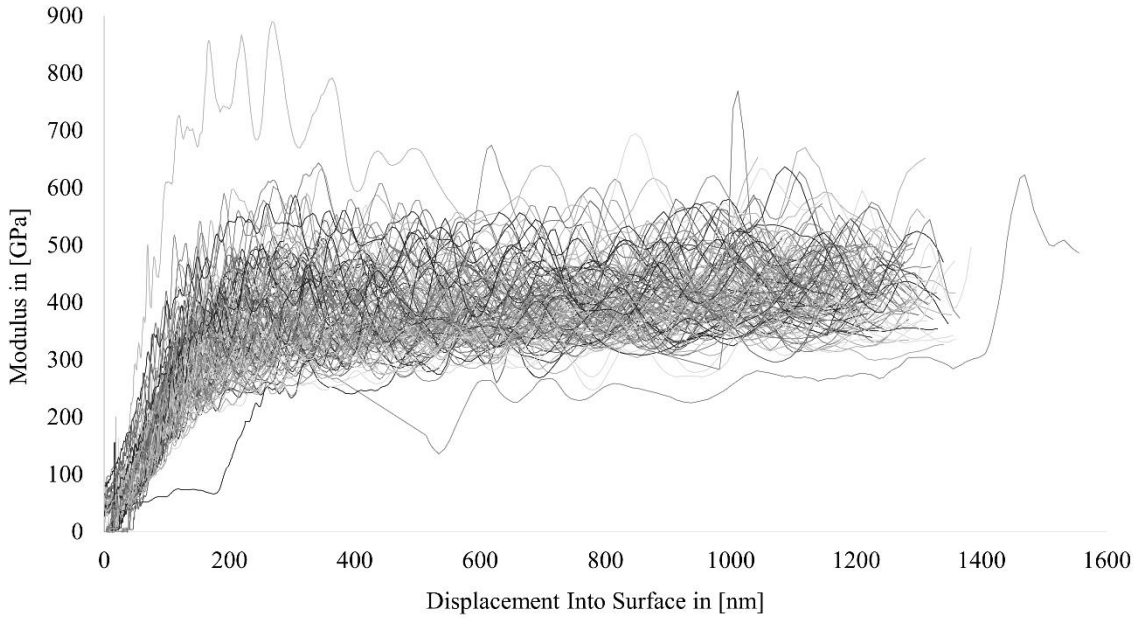


Figure 19: Load/displacement data as acquired from the 150 indents performed in the matrix of a Hi-Nicalon type S with a thick BN, showing strong variation in signal along indentation depth

Figure 19 shows the wide variation in load/displacement data when indenting the matrix, as various matrix components are probed at different indentation depths. These include SiC grains, residual Si and boride-rich inclusions – some of which result in surface spallation and significant pile-up post-indentation, as seen with the white arrow on Figure 20.b. Imprint sizes remained similar to non-spalled indents.

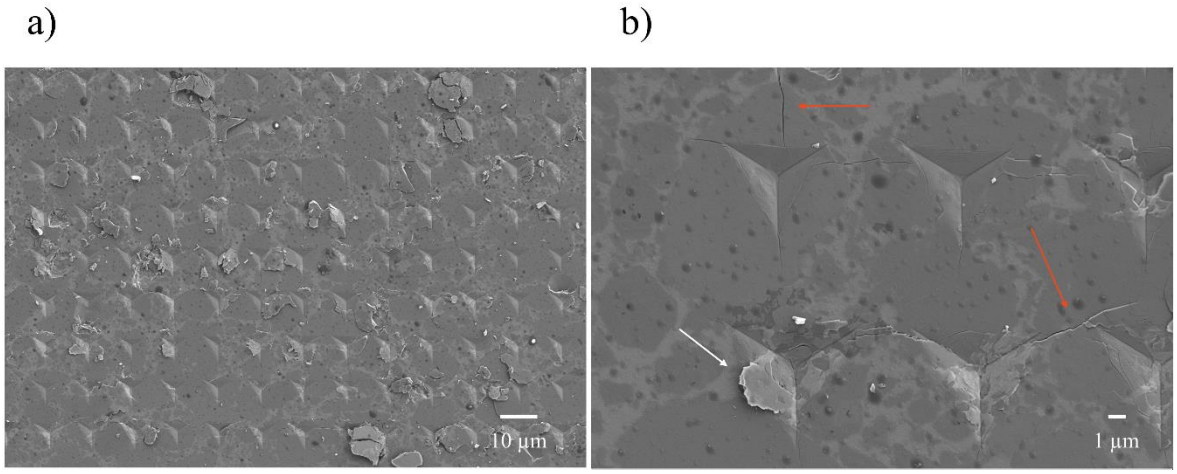


Figure 20: SEM micrographs showing (a) the regular array of indents in the melt infiltrated matrix and (b) some radial cracks propagating within and between grains (red arrows) in addition to pile-up and spallation effects (white arrow)

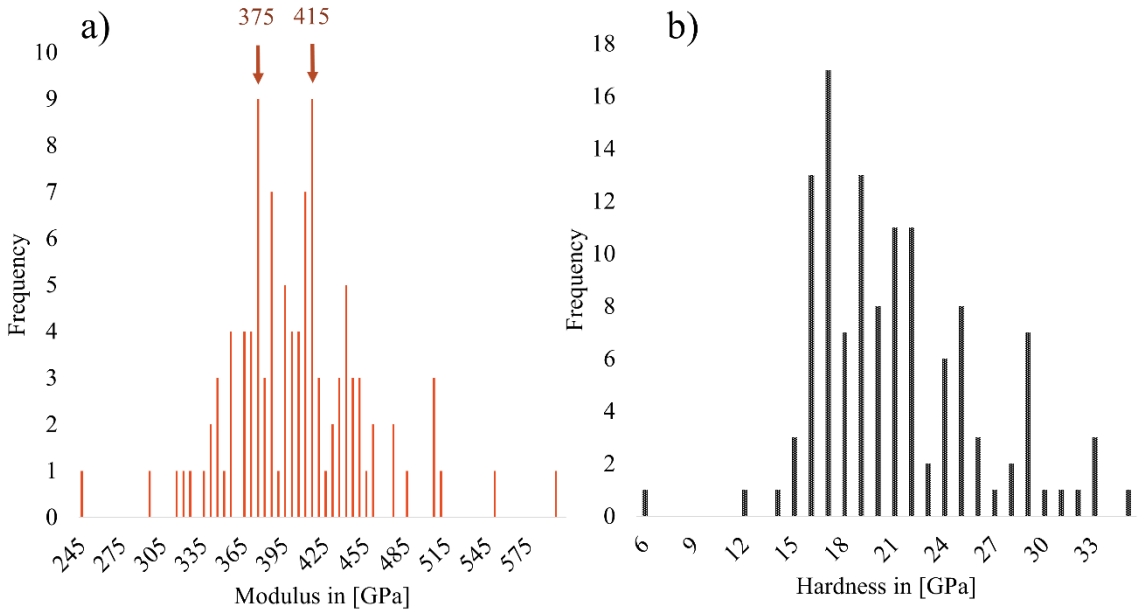


Figure 21: Binomial distributions of the (a) moduli & (b) hardnesses calculated averaged at 500 nm to 1000 nm depths

The hardnesses & moduli obtained from indentations were averaged over depths ranging from 500 nm to 1000 nm (after taking into account initial contact damage & variations from surface flattening/asperities) and binned in columns of 5 GPa and 1 GPa respectively. The two emergent peaks at 375 GPa and 415 GPa on Figure 21 potentially corresponded to the boride and β-SiC grains - however this conclusion assumed that the volume fraction of boride was enough to produce a peak of that frequency (unlikely), and also assumed that the depth of calculation of the elastic properties was smaller than the SiC grain size width. No significant peak was found to correlate to residual Silicon in the matrix.

3.2.1.3 Microcomposites (BN Interphase)

The most challenging component properties to measure were those of the BN. The microcomposites were therefore mounted with wax on a SEM stub for direct indentation of cross-section after manual polishing. Different indentation depths were probed using a Berkovitch diamond tip depending on the constituent: 500 nm for the BN, 1500 nm for the Tyranno type SA3 fibres and 2000 nm for the matrix (in this scenario, the matrix refers to the CVI SiC coating the BN, as there is no melt-infiltration of the microcomposites). The difference in indentation depth was due to the difference in geometry of the constituents – for example the BN had shallower indents because of a higher probability of touching the neighbouring CVI SiC or fibre at greater depths. Data from Figure 19 showed that indentation depths greater than 200 nm were sufficient to achieve relatively homogeneous values for the mechanical properties; the modulus and hardness were therefore insensitive to indentation depth provided the indents surpassed 200 nm.

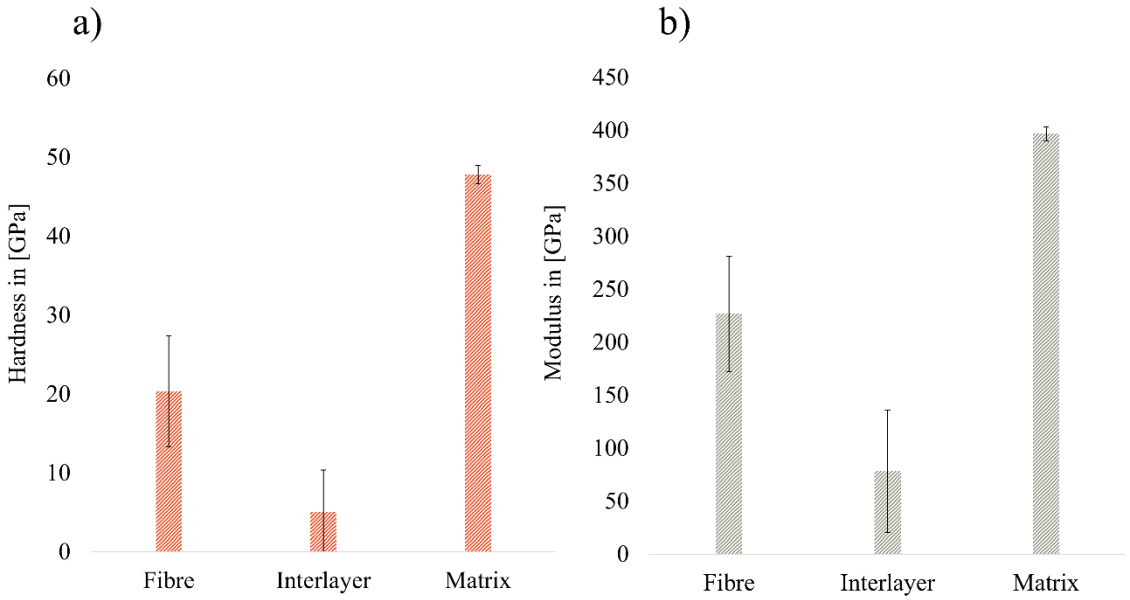


Figure 22: (a) Hardness & (b) Modulus data for the microcomposites

Values for the BN interlayer on Figure 22 were **5.31** ± 5.05 GPa for the hardness and **78.3** ± 57.6 GPa for the modulus. The error bars carried during the test were too significant for any conclusion to be drawn. The commercial value quoted by Ube Industries for their SA3 fibres averages 380 GPa (for tensile modulus), therefore the modulus measured was underestimated. This was probably due to performing the indentation in the more porous core of the Tyranno type SA3 fibres. Additionally, values quoted by manufacturers are commonly obtained from single-fibre tensile tests, or extrapolated from bundle tensile tests, as opposed to measured by nanoindentation. The larger spread on the BN interlayer might have also been due to the increased probability of probing the neighbouring SiC fibre or matrix (geometric constraints), thus requiring an upper-limit censoring of the raw data. The censor values used for indents close to BN/fibre interface were 28.17 GPa in hardness – measured by Harris et al.[184] on indents in polycrystalline cBN) and 290 GPa in elastic modulus – calculated by Petrescu et al.[185] on theoretical cBN. In contrast, the error bar for the matrix was relatively narrow (the CVI SiC had a larger surface area to probe).

3.2.1.4 Microcomposites – Pin Cold-Set Epoxy Mounted

Due to the large standard deviation of measurements – particularly on the BN from section 3.2.1.3 – microcomposites were subsequently attached to an aluminium pin by wax and mounted vertically using cold set epoxy, before being polished for testing, as shown in Figure 23.

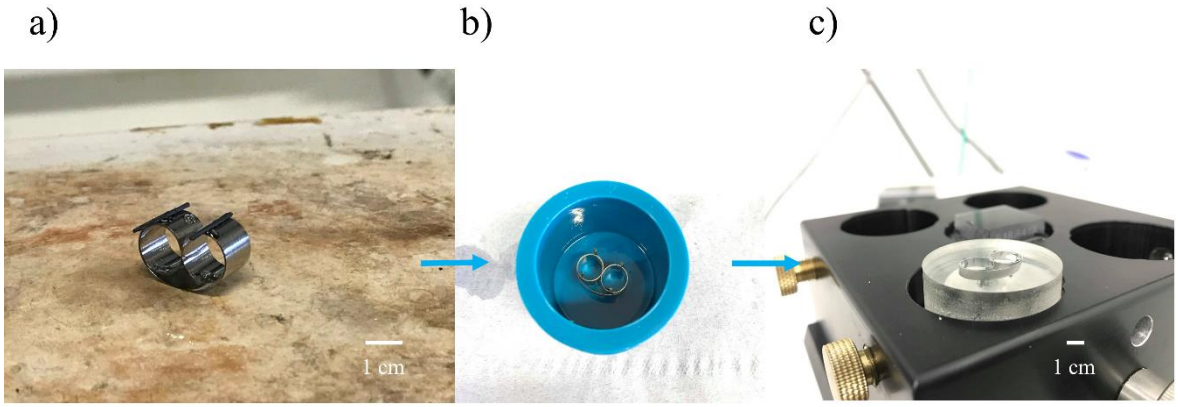


Figure 23: (a) Microcomposites attached to the aluminium pin and subsequently (b) mounted in cold set epoxy vertically for (c) indentation after polish

Over 100 indents were performed to 300 nm in depth probing the 3-µm-thick BN interphase. A similar number of indents but with increased indentation depths was performed on the Tyranno type SA3 fibres & the purely CVI SiC coating. The indents which came into contact by misalignment with the neighbouring fibre or CVI SiC were censored off the data (the hardness threshold was set to any measurements greater than 1.8 GPa at 300 nm indentation depths, or any of the modulus censoring values highlighted in the previous section 3.2.1.3) from results as shown in Figure 24.

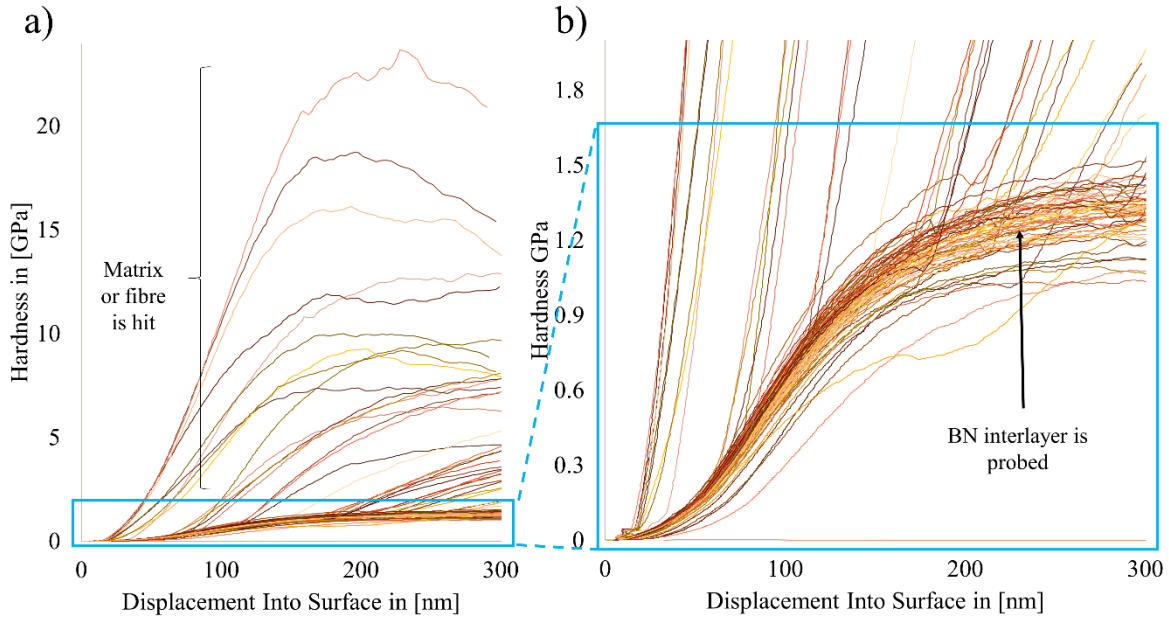


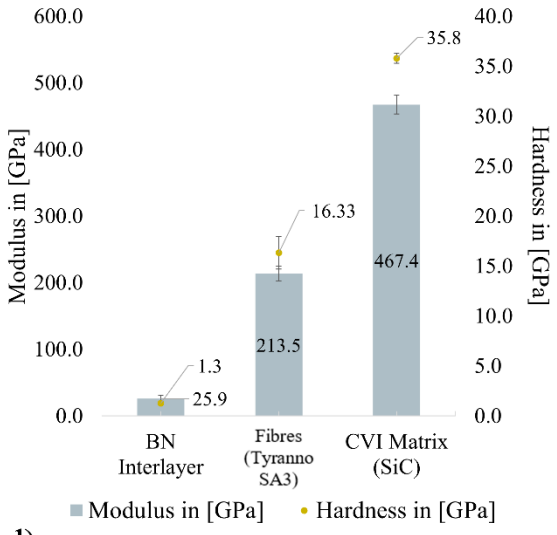
Figure 24: Load displacement data from 300 nm deep indents on the thick BN interphase showing censoring of data from indentations in contact with the neighbouring SiC fibre or coating

The resulting BN interphase modulus and hardness reached values of **25.9** ± 5.4 GPa and **1.3** ± 0.1 GPa at room temperature. By contrast, the deeper indents on the fibres and the CVI matrix showed values of **213.5** ± 11.3 GPa and **467.4** ± 14.1 GPa for moduli, which are consistent with the centrally porous Tyranno type SA3 fibres and the CVI SiC measurements made in the first iteration (Section 3.2.1.3). These values slightly decreased to 18.3 ± 2.8 GPa and 0.8 ± 0.1 GPa for the modulus and hardness of the BN respectively, after having milled the surface of the polished microcomposite using a Ga^+ FIB to investigate the effect of compressive stresses. These results were consistent, as Gallium damage and implantation are accentuated in amorphous materials.

a)

	Modulus in [GPa]	Hardness in [GPa]
BN Interlayer	**25.9**	**1.3**
±	5.4	0.1
Fibres (Tyranno SA3)	**213.5**	**16.33**
±	11.3	1.65
CVI Matrix (SiC)	**467.4**	**35.8**
±	14.1	0.5

b)



c)

	Modulus in [GPa]	Hardness in [GPa]
BN Interlayer	**18.3**	**0.8**
±	2.8	0.1
Fibres (Tyranno SA3)	**192.8**	**13.37**
±	21.7	2.06
CVI Matrix (SiC)	**453.5**	**34.58**
±	31.2	2.83

d)

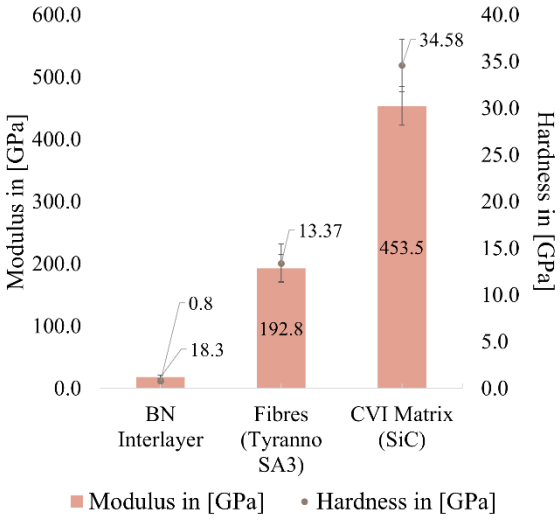
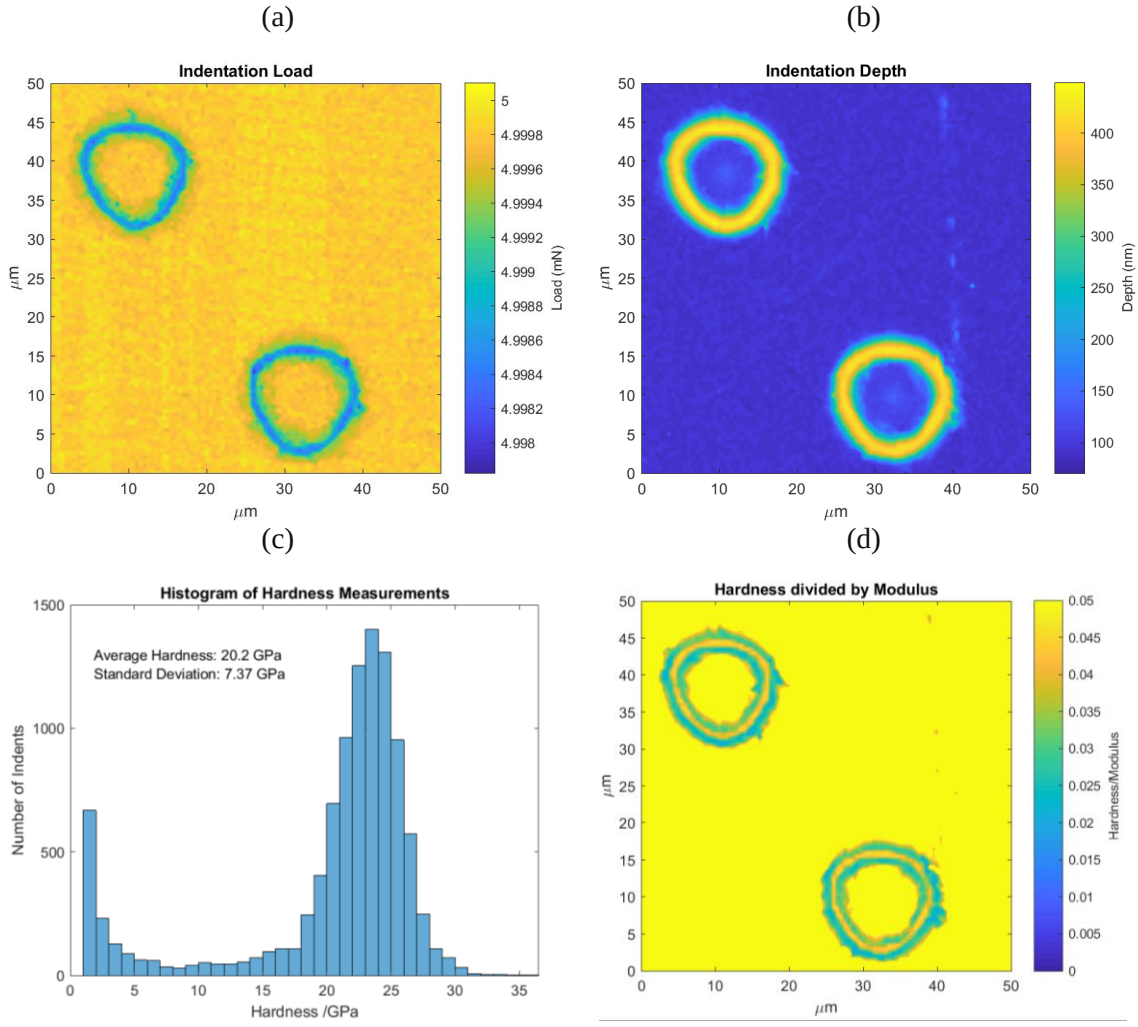


Figure 25: Microcomposite elastic properties mounted by pin cold-set epoxy (a, b) before and (c, d) after FIB milling

3.2.2 Express Mapping (Fast Indentation)

In order to obtain a higher resolution for in-plane measurements and variations, an express indentation mapping[1] was performed on the microcomposite surface prepared with the cold-set epoxy configuration. Maps spanned a region of 50 x 50 µm encasing two fibres with thick BN interphases, to a maximum of 2 mN on a load-controlled instrument (thus targeting an 80 nm depth) with indents spaced 8 µm apart. No information on strain rate could be obtained since no data from load-displacement curves were collected (only the hardness and modulus for each data point was stored). Results were summarised in Figure 26, where histograms of the hardness & modulus data (Figure 26.c) also gave overviews of elastic properties.



[1] Experimental data acquisition was made by Christopher Magazzeni & Dr. John Waite

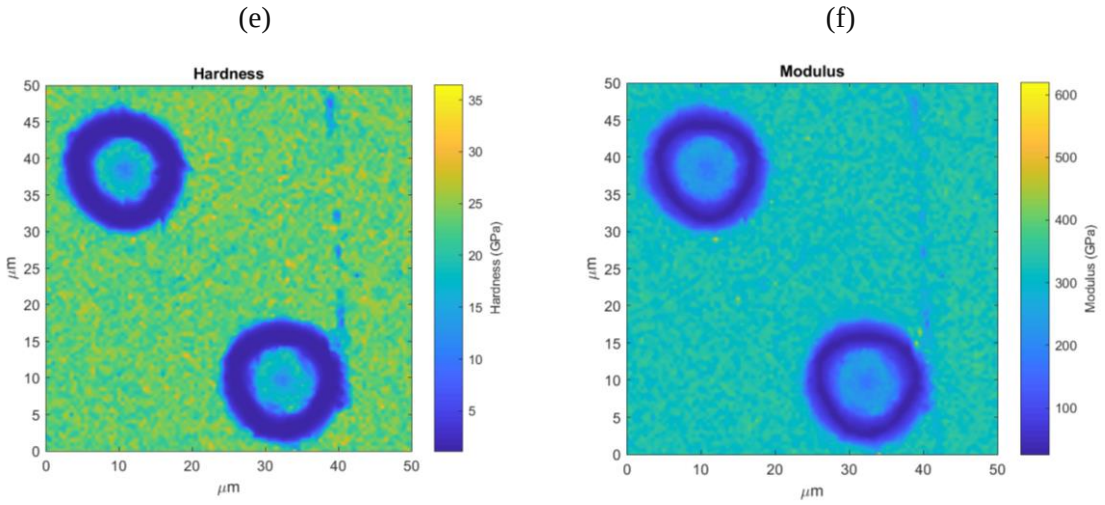


Figure 26: Results from express mapping performed on 2 fibres imbedded on the edge of the microcomposite made of a single Tyranno SA3 fibre bundle

The more porous centre of Tyranno type SA3 fibres was clearly visible (softer on the hardness and moduli plots Figure 26.e and Figure 26.f). The microcomposite was then coated with a thin layer of Pt for imaging after express mapping. Micrographs in Figure 27 showed that there was a slight drift in the array (Figure 27.a), and that microcracks formed on the surface of the sample (Figure 27.c and d) The cracking silica and boria products formed on the surface due to differences in thermal mismatch. The imprints created during the express mapping indentation could have acted as channels for Oxygen to diffuse below the surface, thus accentuating and multiplying the number of cracks.

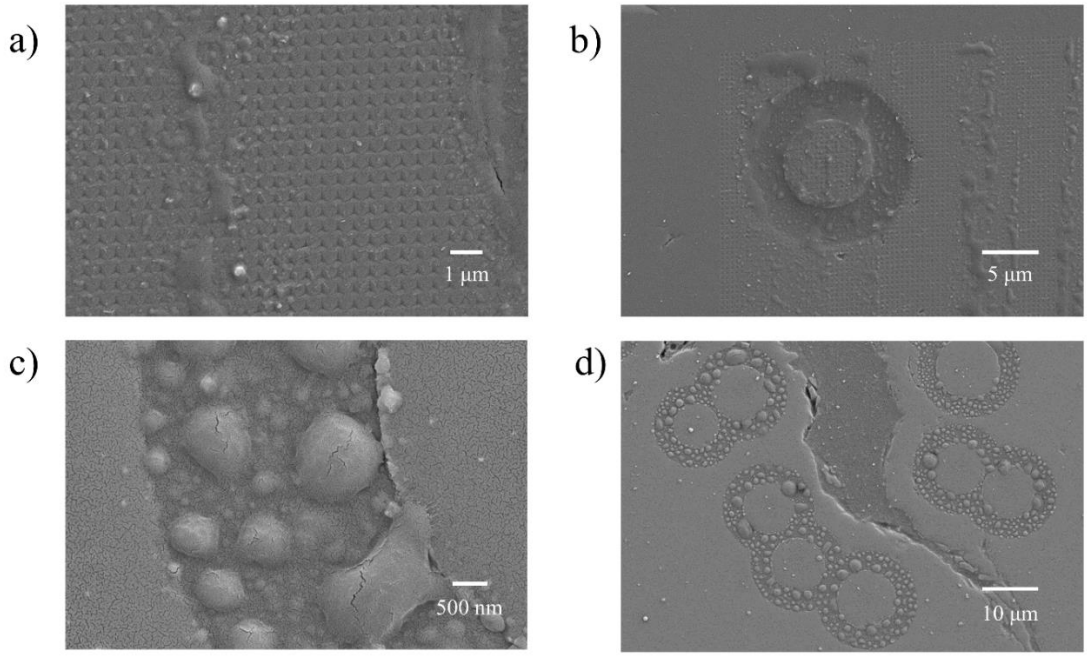


Figure 27: SEM micrographs of the microcomposite after hardness express mapping showing (a) regular array of indents with drift, (b) indents around a full fibre cross-section, (c) and (d) some microcracks on the surface of the sample after testing.

From the data collected in Figure 26, a segregation and binning of values enabled numerical estimates of the mechanical properties of the microcomposite. Regions where the modulus was less than 150 GPa were defined as belonging to the BN interphase, as shown in Figure 28.d. This resulted in the sharpest histogram difference from Figure 26.c – yielding values of **2.5** ± 1.7 GPa and **73** ± 34 GPa in hardness and modulus for the BN respectively. In contrast, the CVI and SiC fibre values for hardness and modulus stood at 22.5 ± 3.6 GPa and 316 ± 42 GPa respectively.

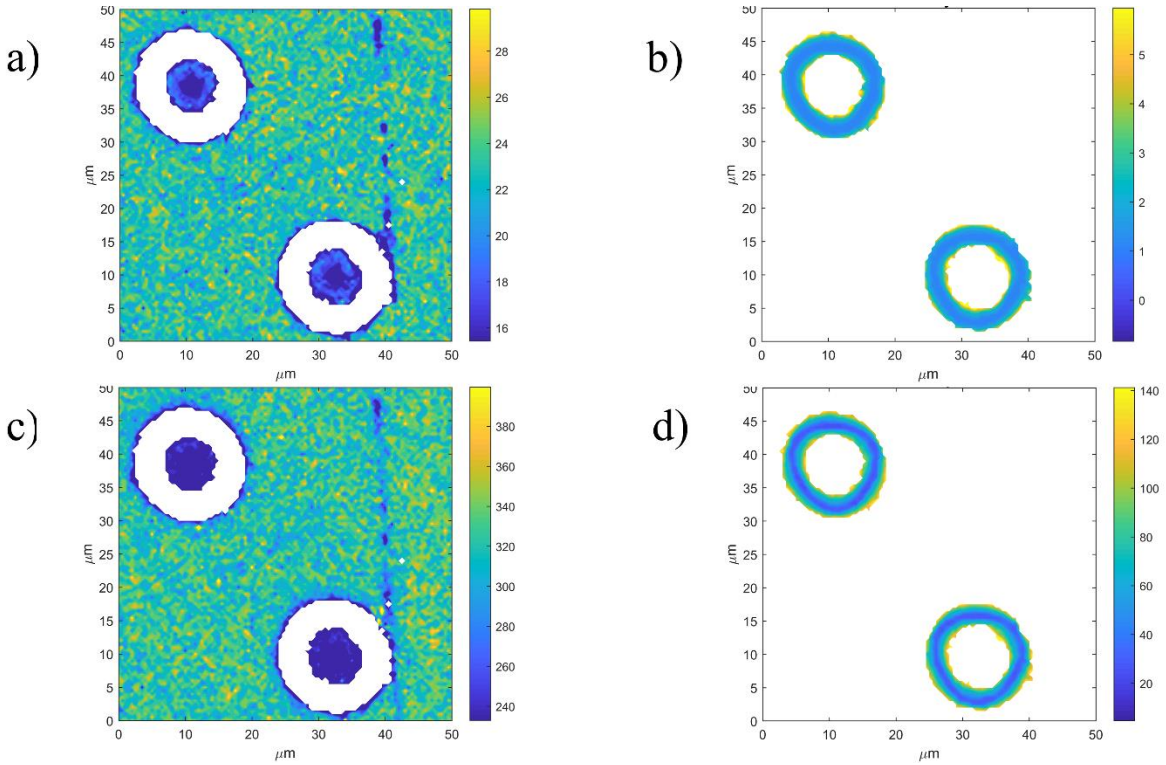


Figure 28: MatLAB 2D projections of the indentation map showing (a, b) hardnesses and (c, d) moduli of the (a, c) CVI & fibre SiC and (b, d) the BN interphase

From Figure 28.d, it is apparent that the modulus of the interphase was lower at interphase centre than at the edges of the interphase. The centre of the interphase also curved to create a downward facing triangle – akin to Berkovitch geometry, suggesting the shape of the tip had an effect on the convolution and extraction of a more realistic value of the modulus. The BN hardness and modulus can therefore be assumed to be lower than those reported in this section, considering that the "edge" values of the interphase were affected by the tip making contact with neighbouring CVI SiC or the fibre. This could be extracted by producing line plots of modulus and hardness as a function of radial distance from fibre centre, further convoluted by azimuthal integration of the signal for a better quantitative measurement of the elastic properties.

3.2.3 Indentation Summary

The following tables showing hardness (Table 5) and modulus (Table 6) serve as summary of the indentation work.

*Table 5: Summary of **hardness** results and corresponding techniques. All data in GPa*

Constituent	Targeted Indentation	Array Indentation	Microcomposites (Wax + Stub)	Microcomposites (Cold-Set Epoxy)	Express Mapping
Fibre (HNS)	40.1 ± 3.2	N/A	N/A	N/A	N/A
Fibre (TSA3)	25.1 ± 5.5	N/A	20.3 ± 7.0	16.3 ± 1.6	20.2 ± 3.2
BN	4.6 ± 2.8	N/A	5.3 ± 5.0	1.3 ± 0.1	2.5 ± 1.7
CVI SiC	28.7 ± 6.1	17 ± 4	47.8 ± 1.1	35.8 ± 0.5	22.5 ± 3.6
MI Matrix	36.4 ± 12.0	21 ± 6	N/A	N/A	N/A

*Table 6: Summary of **modulus** results and corresponding techniques. All data in GPa*

Constituent	Targeted Indentation	Array Indentation	Microcomposites (Wax + Stub)	Microcomposites (Cold-Set Epoxy)	Express Mapping
Fibre (HNS)	376 ± 19	N/A	N/A	N/A	N/A
Fibre (TSA3)	277 ± 45	N/A	227 ± 54	214 ± 11	245 ± 38
BN	78 ± 46	N/A	78 ± 58	26 ± 5	73 ± 34
CVI SiC	360 ± 56	375 ± 50	397 ± 6	467 ± 14	316 ± 42
MI Matrix	433 ± 87	415 ± 50	N/A	N/A	N/A

From data in Table 5 and Table 6, the indentation method which yielded the smallest deviations in measurements for the BN was the cold-set epoxy microcomposite set-up. When appreciating the magnitude of the deviations, array indentation was the best method for measuring indentation of the melt-infiltrated matrix, whereas the microcomposites indentation was preferred for the fibres. The different techniques could therefore be concluded to best target a different CMC constituent each (e.g. targeted indentation for the fibres, and cold-set epoxy set-up for the BN on microcomposites) due to the geometry of each test. The express mapping yielded the highest amount of data, but calibrations from the numerous indents made tip damage highly likely (as observed in other experiments with the same set-up on other materials[186]), and therefore only the ratios of values measured by express mapping were taken into account.

3.3 Optimising Fibre Push-out Parameters

3.3.1 Basics of Fibre Push-out

Sample preparation for fibre push-out is crucial, as slight variations in samples induce significant changes in measurements of the micro-scale properties. Samples were first cut and ground using oil-based diamond solutions to avoid BN environmental degradation from reactions with direct water contact forming Boria glass[55]. Samples – of around 1 x 0.5 cm in area – were then mounted on a custom-built holder for grinding to a specific 100-µm-thickness, with an allowable thickness variation of ±10 µm across the samples. Samples were polished down to 1/10th µm diamond paste size and cleaned with propan-2-ol in between steps. Polishing quality was verified via means of optical microscopy – fibres ideally presented as round (elliptical, a = b) on the *'roundness'* tool in ImageJ (v. 1.51) with no damage, damaged samples were either discarded or ground again. Sample cleaning post-polishing included 1 acetone bath (10 minutes) and 2 ethanol baths (5 minutes each) in ultrasonic environment. Samples were then flipped and polished on the reverse side for pushed-out fibres to be clearly visible. No surface damage to the BN layer was observed in this process.

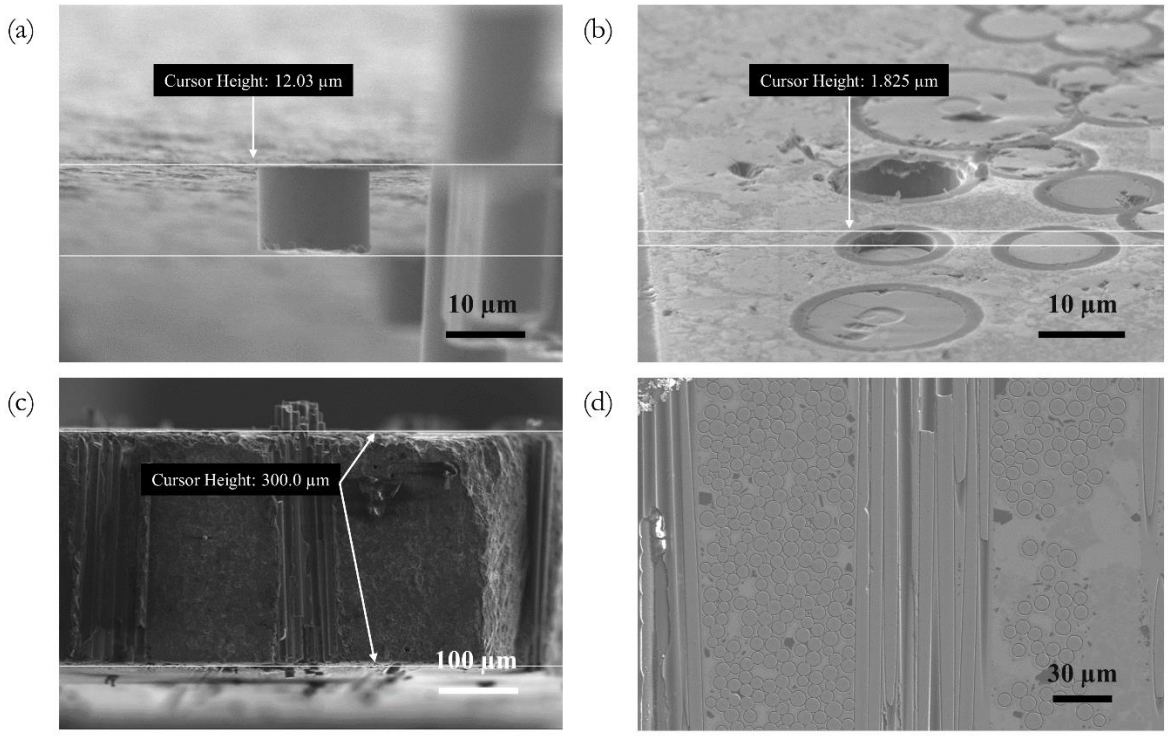


Figure 29: SEM micrographs taken at a working distance of 10.5 mm and accelerating voltage of 10 keV and a probe size of 800 pA showing measurements of (a) a fibre push-out from the undercut (12.03 µm), (b) a push-out length from the top (1.825 µm) from another fibre, (c) a sample thickness (300.00 µm) before grinding, d) typical microstructure of a Tyranno type SA3 composite with a thick BN interphase

Once polished on both sides, samples were subsequently mounted with minimal amounts of Quickstick 135°C Mounting Wax (South Bay Technology ®) on a custom-build holder with 1 mm-wide slits for fibres to be pushed into, whilst supporting the sample to prevent macroscopic bending. The holder itself was mounted in a G200 Nanoindenter (Agilent, USA) instrument for testing.

Push-outs were performed at a prescribed displacement rate of 30 nm.s^{-1} to a maximum 3-µm-displacement, to avoid the conical shaped flat-punch tip hitting the matrix at the edge of the fibre. The tips used were 3, 5 and 7 µm in diameter. Samples were not cleaned after fibre push-outs to prevent tested fibres from further damage or falling out. Samples were subsequently analysed under SEM using a vertical sample holder to measure sample cross-sectional thickness, as seen in Figure 29.c, fibre diameters and push-out lengths (accounting for sample tilt corrections) for each successful push-out. Due to the plastic deformation induced by the tip on the fibre itself (c.f. section 2.2.1.4.H)), the first 400 nm ± 61 nm displacements were omitted before calculating interfacial shear stresses – this depth was double that found by Medina et al[105] (more detail is included in section 0). Only plateaued load curves (showing load bursts attributed to full crack propagation and fibre sliding) were therefore used for data analysis. The thickness, fibre diameters and load/displacement values were used to calculate a simple force-balance derived interfacial shear stress τ from equation [5] (Section 2.2.1.1).

3.3.2 Effect of Sample Thickness

In order to explore how the thickness of the overall sample affected batch push-outs, the success rate of 100 fibre push-outs on each of 4 samples of the same fibre type (Hi-Nicalon type S) and BN thickness (600 nm) was plotted against measured sample thickness (Figure 30). The samples were ground to respective thicknesses of 83, 167, 200 & 287 µm. In this context, the success rate refers to the number of fibres showing a distinct load plateau at push-out event, over the total number of tests.

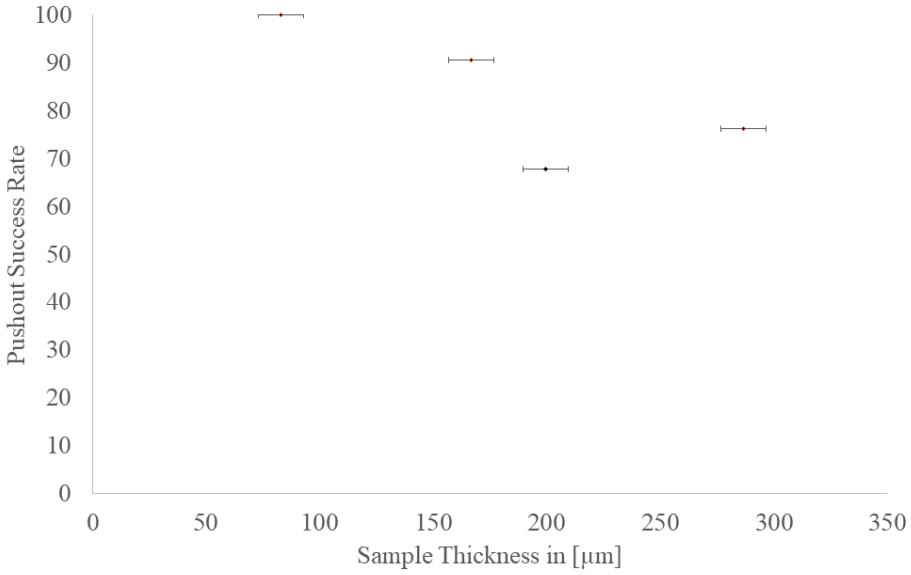


Figure 30: Push-out success rates as a function of sample thickness

A decreasing trend can be observed on Figure 30 where the push-out success rate reaches 100% when the sample thickness decreases below 100 µm. Thicker samples will indeed likely experience exaggerated shear stresses at the interface due to fibre/matrix elastic incompatibilities, as also highlighted by Desaeger et al. [99] and increased risk of fibre misalignment/termination. No fibre unsheathing or protrusion was observed after or before polishing unlike Rollin et al.[120].

However, considering the thickness with near-perfect success rate was close to 10 times the fibre diameter, our observations are consistent with Rebillat[63] and show there is a sample thickness/fibre diameter ratio to adhere to for optimised measurements of the ISS.

Looking at the fractography and the effect of sample thickness, it was found that thinner samples also resulted in smoother fibre push-outs and less pronounced BN delamination.

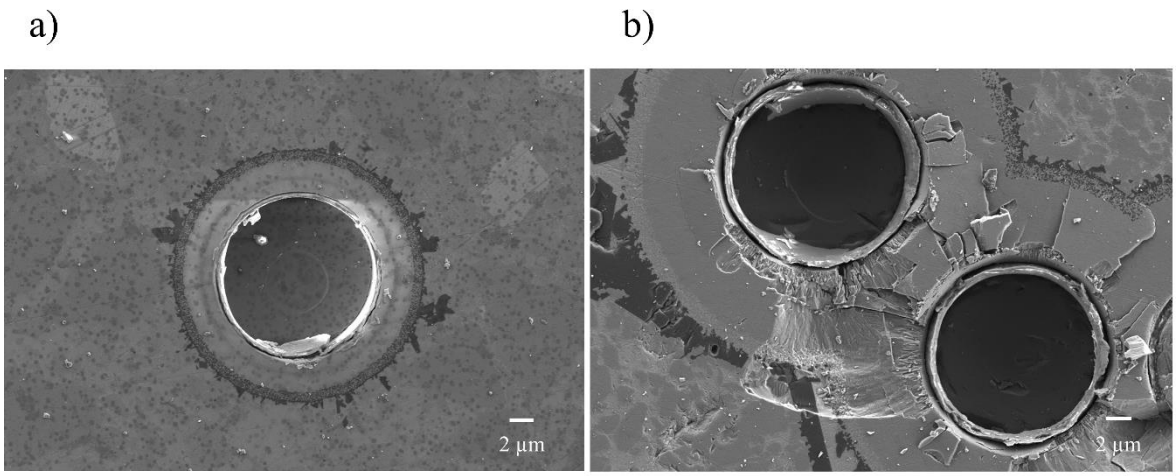


Figure 31: SEM micrographs of a Hi-Nicalon type S sample with a thick BN interlayer of different thicknesses (a) 87 µm and (b) 199.5 µm, showing different behaviour from push-outs, including pronounced BN delamination for thicker samples

As can be seen on Figure 31.b, the thicker sample resulted in more crack spallation and radial crack development when contrasted to a thinner sample of the same type (Figure 31.a). This can be partially explained by the fact that the BN interlayer might be in residual tensile stress from processing. Upon frictional heating during micromechanical testing, the interlayer therefore buckles as the fibre scrapes through and subsequently debonds, causing delamination. Thinner samples overcome the shear stress with more ease, as there is little room for elastic recovery. Thicker samples might additionally require higher loads to generate the same ISS as thin samples – thus inducing larger Poisson expansions in the fibre.

In order to verify if the spallation cracks were not due to tip contamination or tip contact, the tip was additionally mounted on a SEM stub for imaging and quality-check.

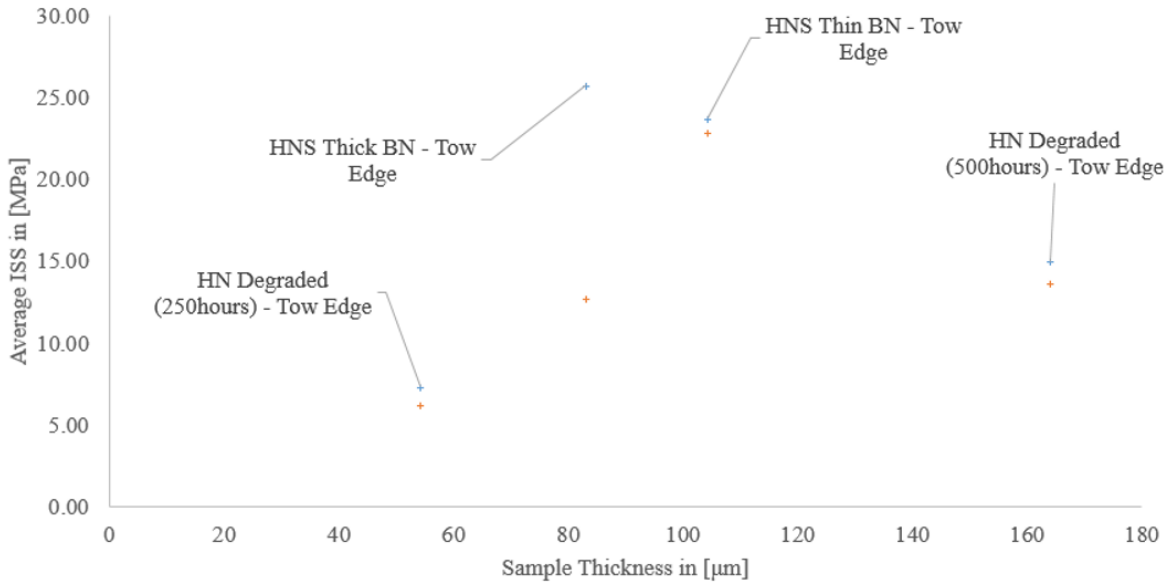


Figure 32: Average ISS as a function of sample thickness. Each data point corresponds to 100 fibre push-outs.

The mean ISS for a series of 8 populations of 100 push-outs each (Hi-Nicalon type S both thick and thin, as well as Hi-Nicalon degraded for 250 and 500 hours) were plotted as a function of sample thickness (Figure 32) to check if the ISS was normalised by sample thickness. Both non-degraded samples displayed higher mean ISS than their degraded counterparts, confirming a significant impact of humidity on the mechanical performance of the interlayer. Additionally, the only significant difference between the mean ISS of tow edge populations (in blue) and the tow middles (in orange) was on the thick BN sample. This confirmed that the thinning of the BN (on the non-degraded sample) had the same effect as degrading the BN and exposing it to humidity – thereby rendering the interphase inefficient in both cases.

3.3.3 Effect of Tip Size

In order to investigate the effect of tip size on both the ISS and push-out success rates, 100 push-outs were repeated using a 3 µm and a 7 µm diameter tips on the same sample made with Tyranno type SA3 fibres and a thin BN interphase.

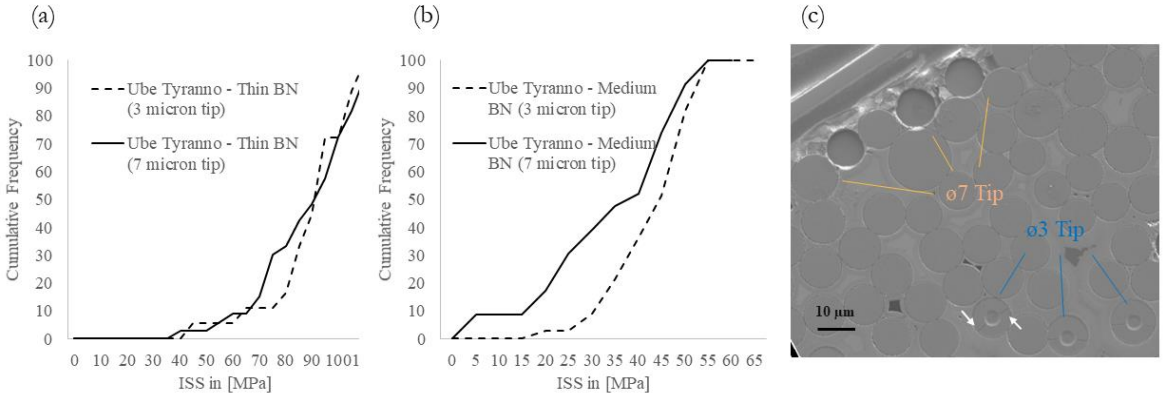


Figure 33: Cumulative distributions functions comparing the effect of using different nanoindenter tips of diameters 3 µm (dashed lines) and 7 µm (continuous lines) on the measured ISS in a (a) Tyranno type SA3 sample with a thin BN interlayer and a (b) Tyranno type SA3 sample with a medium BN interlayer. Push-out success rates of the push-out batches were 51% (thin BN, 3 µm tip), 50% (thin BN, 7 µm tip), 48% (medium BN, 3 µm tip) and 26% (medium BN, 7 µm tip). c) SEM micrograph showing fibre cracking (white arrows) with the 3 µm tip in contrast to successful push-outs with the 7 µm tip.

Firstly, it was observed that Tyranno type SA3 fibres were more prone to cracking (Figure 33.c) compared to Hi-Nicalon type S when indented with the same flat-punch tip – this may have resulted from either the slightly smaller average diameters of the Tyranno fibres or the increased porosity (and therefore crack initiation sites density) in the middle of the Tyranno fibres. Comparing the ISS cumulative frequencies on Figure 33.a and Figure 33.b, it was found that the 3 µm tip ISS were on average greater than those from the 7 µm counterpart (e.g. the median ISS values were 91.06 and 44.05 MPa for the 3 µm contrasted to 90.91 and 40.40 MPa for the 7 µm tip). The push-out success rate was higher with the 3 µm tip despite the majority of the fibres breaking due to the high stress intensity factor located at the sharper nanoindenter tip. Conversely, push-outs completed with the 7 µm tip displayed lower success rates and were also harder to calibrate in terms of lateral stage positioning, as indents created prior to fibre push-outs were less distinctive and less shallow than the 3 µm tip. Using a larger tip – such as the 7 µm tip – on fibres with an average diameter of 10 µm also significantly increased the chances of the tip indenting the BN interphase at the edge of the fibres. For Tyranno type SA3 and Hi-Nicalon type S fibres it is therefore recommended that a ratio of 1:2 is maintained for tip/fibre average diameters.

3.3.4 Effect of Tip-Induced Plastic Deformation

Most pushed-out samples showed a 400 nm ± 61 nm thick plastic indent the size of the tip – as shown on Figure 34. 400 nm on the load/displacement curves for push-outs therefore have to be omitted from the fibre displacement measured by the G200 instrument, when comparing to the measured fibre displacement on the SEM post-analysis.

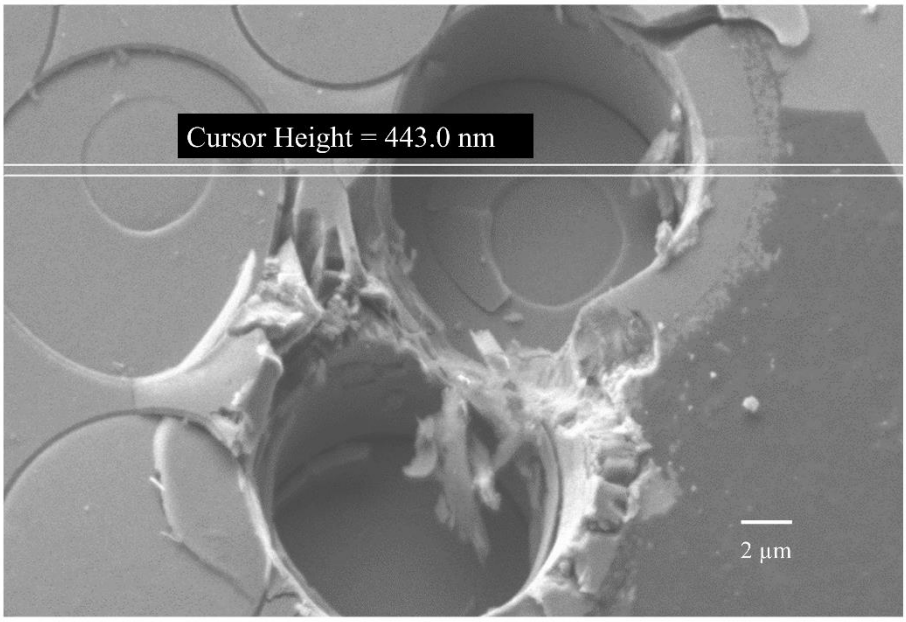


Figure 34: Micrograph of a post-push-out analysis of a Hi-Nicalon S fibre with medium BN sample showing plastic deformation from the tip on the fibre surface

3.3.5 Effect of Strain Rate

The effect of modifying the load rate on push-outs was conducted on a Tyranno type SA3 fibre with a thin BN interlayer, in order to investigate high push-out rates (and draw closer to mimicking ballistic impact on the fibre[123]). Three iterations of the experiment were completed before the 4th and 5th iteration results highlighted below but omitted from this thesis for length purposes (the previous iterations showed no concrete trends and/or were performed at strain rates too elevated for the instrument to record loading data).

All push-outs completed up to Section 3.3.5 used a default loading rate of 5 mN.s^{-1} in load-control. Iteration 4 contained 10 push-outs at each of 5 different load rates, performed on a Tyranno type SA3 fibre with a thin BN – the load / time segments recorded by the Agilent G200 instrument were plotted in Figure 35, and the resulting load / displacement curves from the push-outs plotted in Figure 36.

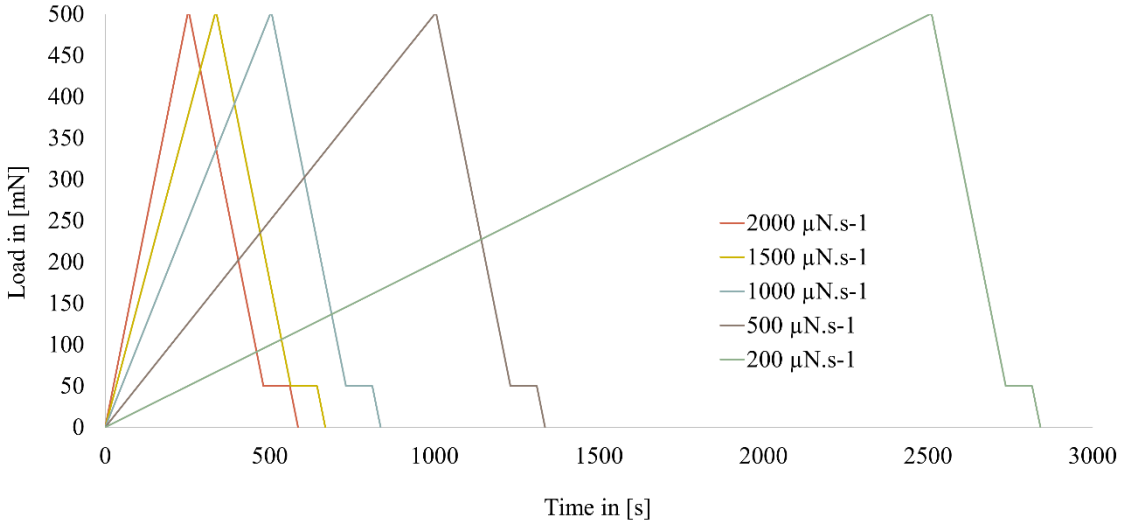


Figure 35: Load rate conditions as measured by the Agilent G200 instrument

The curves on Figure 36 show that there is an increasing number of successful push-out events (presence of load plateau) as the load rate increases from 200 to 1000 µN.s^{-1}, higher load rates showed instability in some of the load / displacement data.

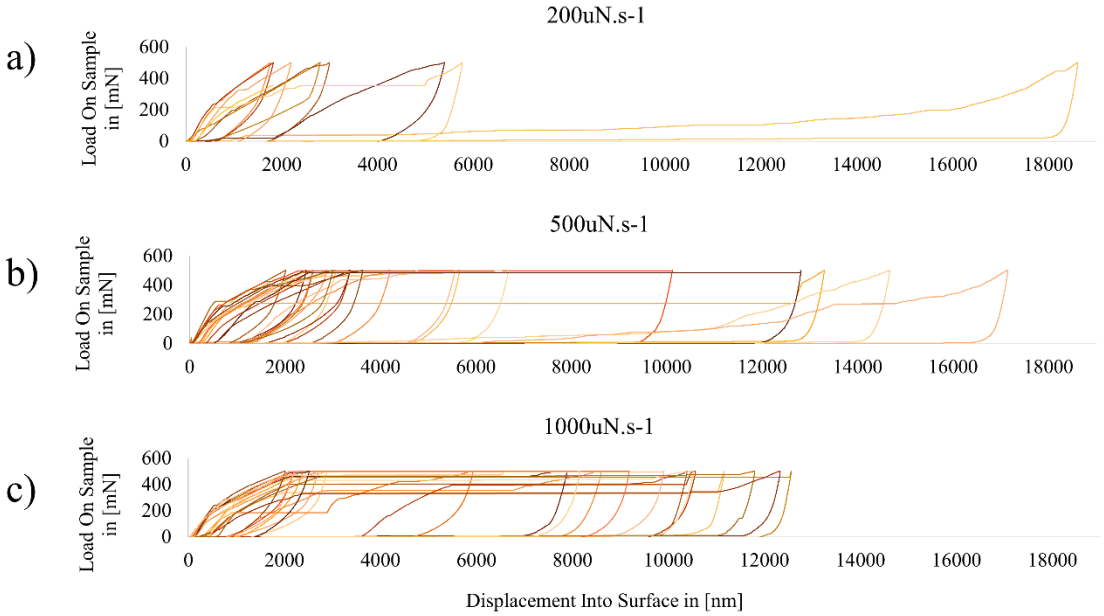


Figure 36: Series of 10 push-outs performed at (a) 200, (b) 500 and (c) 1000 µN.s^{-1} on a Tyranno type SA3 fibre with a thin BN sample showing increasing number of successful push-outs (displayed in load pop-ins)

The latter effect was further shown during microscopy analysis where it was made clear on Figure 37.a that lower load rates did not result in push-outs. This might have been due to the tip having more time to plastically deform the fibre itself and create an imprint akin to those in section 0. This could be verified by means of quantifying indent depth for a given maximum load as a function of loading rate. Conversely, higher load rates resulted in push-outs and BN delamination (Figure 37.b). Slower strain rates resulted in improved discernibility between debonding and fibre sliding events. As such,

slow strain rates yielded more information in segmenting micro-events but were found to be less representative of mechanical in-service applications (where fibres would pull-out at higher rates).

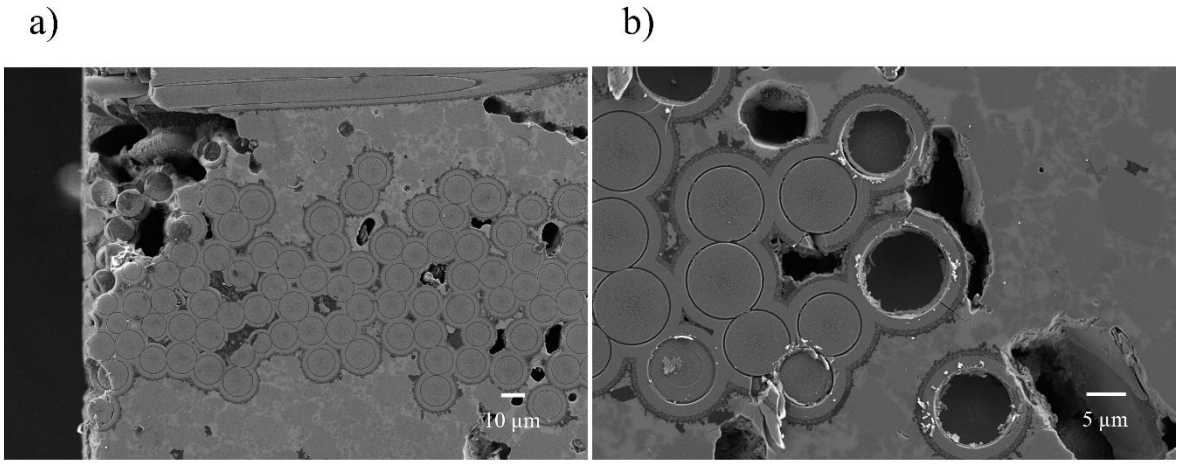


Figure 37: SEM micrographs on a Tyranno type SA3 fibre with a thin BN sample showing (a) shallow push-outs for low load rates and (b) successful push-outs for higher load rates

High load rates also resulted in the smoothing of load/displacement curves, due to the decrease in time for feedback loops to activate, and the reduction in pop-in events during both loading and unloading. Indeed, in prior iterations of these experiments, load/displacement curves displayed a pre-mature plateau in load value before the main push-out event. The latter could have corresponded to either a crack having fully propagated (from which a $\sigma_{DEBONDING}$ could be calculated), a secondary event from the gradual load increase from the fibre Poisson expansion, or the onset of the BN delaminating as the push-out initiates. By improving separation of micro-events, the error bars in ISS calculations were reduced at slower rates.

The fifth iteration of the experiment investigated varying loading rates on fibres in a single tow within a single sample (Tyranno type SA3 with a thin BN interphase) with only one fibre being pushed per loading rate and up to 20 $mN.s^{-1}$) as highlighted in Figure 38.

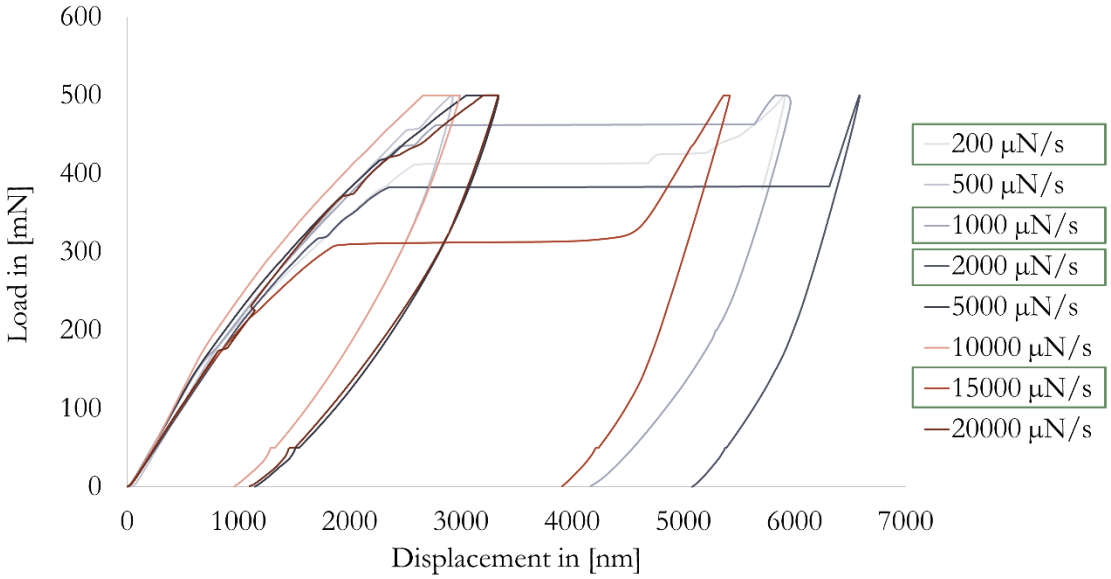


Figure 38: Load displacement curves from the loading rate push-outs of iteration 5 - successful push-outs are highlighted in green boxes

Iteration 5 showed that even within a single tow, the success factor of the fibre push-out seemed to be uncorrelated to how fast the micromechanical test was performed. Figure 38 also shows the rise in load from the indenter making contact with the matrix at the edge of the fibre socket.

Additionally, the shear compliance from push-outs can be analysed by looking at spring backs during unloading of the fibre at the end of the push-out (when retracting the flat-punch tip). However, this type of analysis has only been performed on displacement-controlled instruments, due to the need for tracking tip travel distances[187].

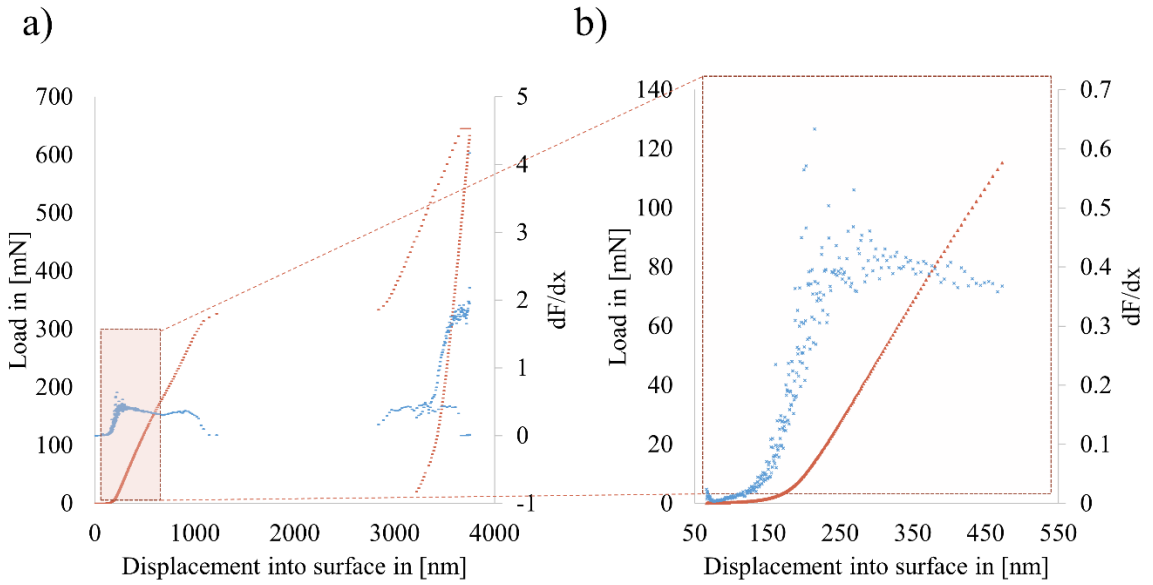


Figure 39: Investigating the crack initiation event on a high-load (20 mN.s^{-1}) rate push-out performed on a Tyranno type SA3 sample with a medium BN with a 3 µm ⌀ tip by performing a first derivative (in blue).

High load rates additionally enable clearer detection of a crack initiation event during the fibre push-out. This was investigated on a (successfully cracked) Tyranno type SA3 fibre with a medium BN pushed out with a 3 µm diameter tip, in order to clearly dissimilate the crack initiation event and the fibre cracking event on the load / displacement curve. The detection was performed by simply taking the 1st derivative of the measured load with respect to raw displacement - where a peak was detected corresponding to the load and displacement of crack initiation during push-out (Figure 39.b).
At higher loading rates (> 20 mN.s^{-1}), the dissipation of energy from crack propagation often resulted in a dual delamination of the interphase from both of its walls (i.e. inside and outside debonding occur concurrently), observed on Figure 40.b – although this was previously observed at lower strain rates (5 mN.s^{-1}) on Figure 31.a.

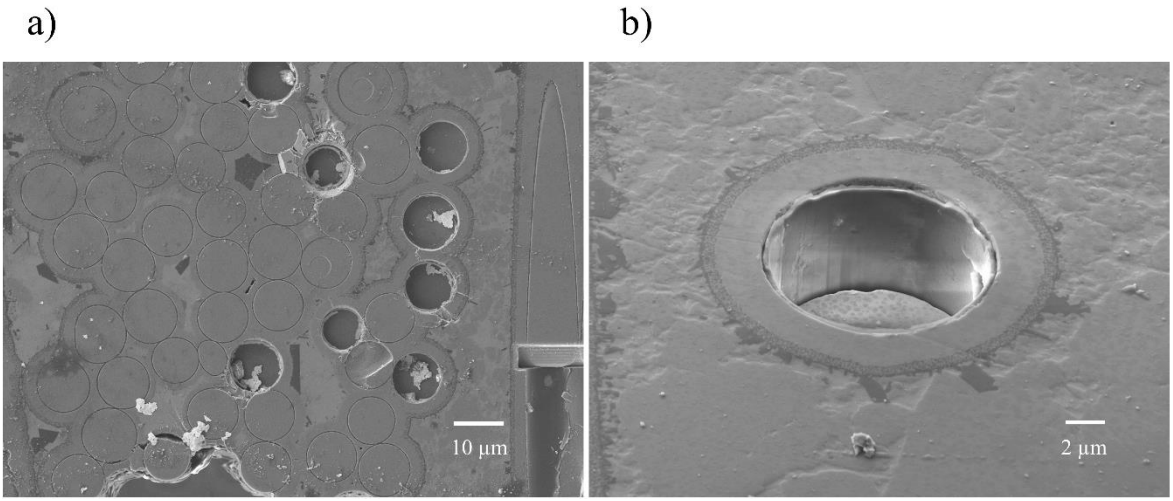


Figure 40: High loading rate push-outs showing BN delamination on both sides (inside and outside debonding) of the interphase on a Hi-Nicalon type S sample with a medium BN interphase

When looking at the SEM images included in Figure 40, it was found that push-outs performed close to the tows running parallel to sample surface were more likely to be successful than those performed away from the parallel tows. This suggests that higher loading rates had a stronger impact at 'weave' points in the fibre bundles, where two perpendicular tows intersect. Thereafter, strain-rate sensitivity studies focused on the fibres in the middle of the tow. The interfacial shear stress and the success rate from ten push-outs in the middle of tows from each loading rate was plotted against corresponding load rate in Figure 41; the success rate approached 100% at higher testing rates whilst the mean ISS decreased.

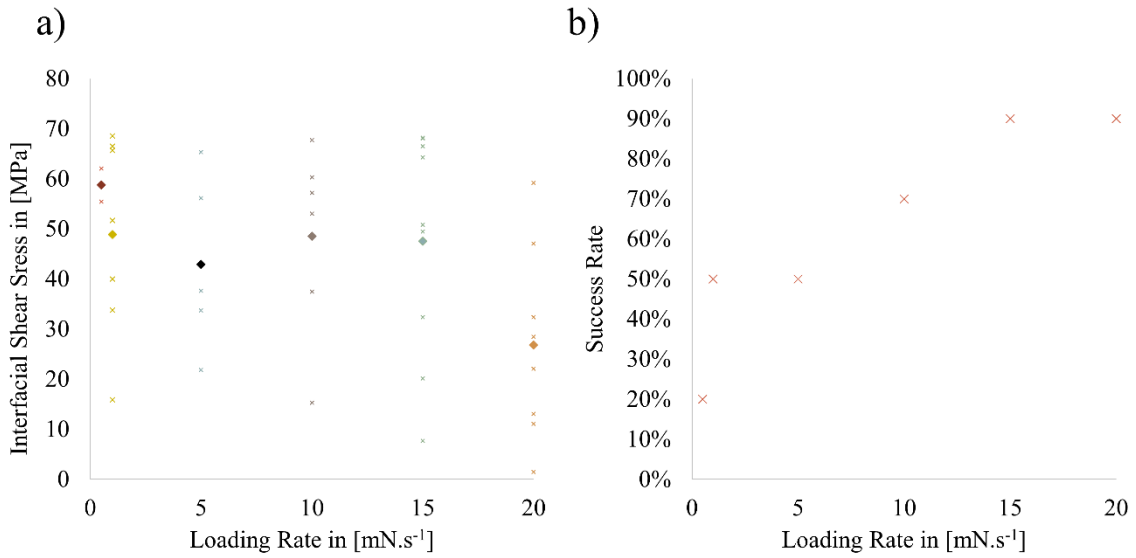


Figure 41:ISS and success rate of middle-of-the-tow fibre push-outs as a function of loading rate on a Hi-Nicalon type S sample with a medium BN interphase

Despite higher rates of detectable push-outs for faster testing rates, the default 5 $mN.s^{-1}$ displacement rate was used for the rest of this work, as slower rates resulted in more pronounced tip-induced plastic deformation on fibres surfaces (despite a clearer segregation in micro-events) whilst faster rates (greater than 20 $mN.s^{-1}$) resulted in a decrease of micro-events separation (e.g. one could not dissociate when a crack initiated or propagated). One consideration not addressed in this work is the size/width of the sample holder slit when performing push-outs, indeed the latter could induce secondary beam-bending effects on the sample.

3.4 Investigating Local Fibre Environment Effects[2]

3.4.1 Inter-Tow Variations

Due to the stochastic nature of fibre push-outs, all push-out data was presented probabilistically using cumulative frequencies, in order to yield best and worse-case design scenarios for performance envelope libraries. These cumulative distribution functions enable comparisons between samples – the ISS were ranked, binned in 2 MPa increments and counted, before being plotted against normalized frequency. Samples were initially compared to one another with respect to fibre type (Tyranno type SA3 / Hi-Nicalon type S) and interphase thickness (200 / 600 nm). At least 200 push-outs were performed on each of the three samples highlighted in Table 4. Half of the push-outs were performed on an outer tow whilst the other half performed on inner tows as illustrated on Figure 42. The effects of intra-tow variability were concurrently investigated and described in section 0.

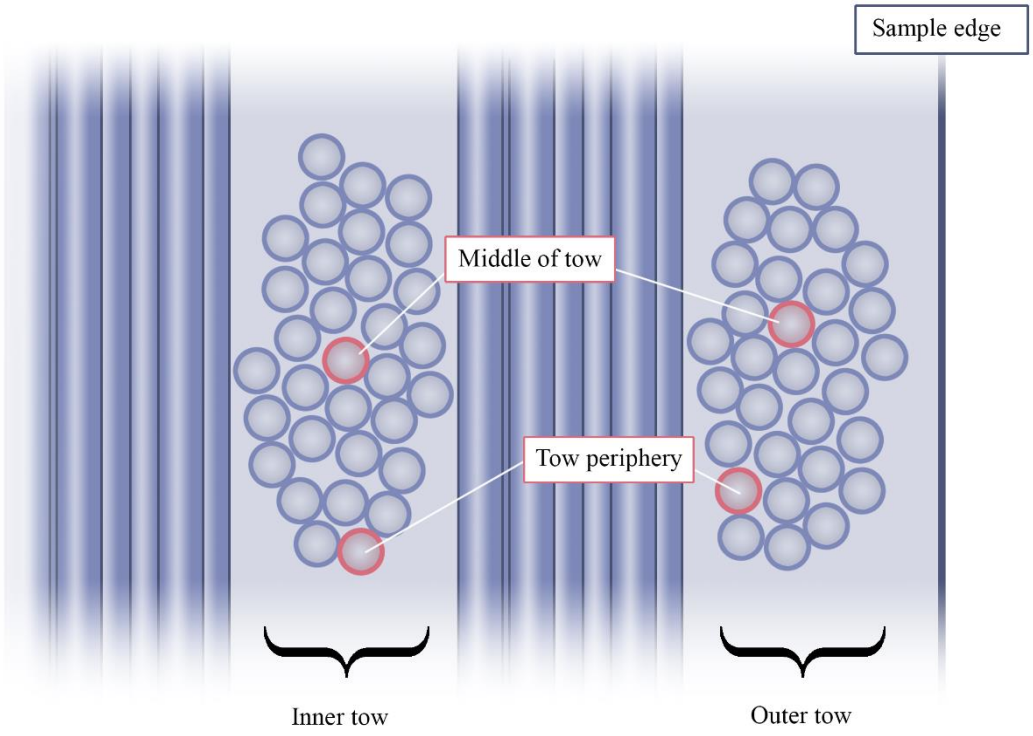


Figure 42: Investigating the effect of fibre local environment by analysing ISS intra-tow (middle of tow and tow periphery) and inter-tow (inner and outer tow) variations

[2] *Results from section 0 are located in Chapter 4 as they discuss material-dependent variables as opposed to technique-dependent variables – the techniques are however introduced in this methods chapter.*

3.4.2 Intra-Tow Variations

The heterogeneity in load/displacement behaviour of push-outs could have partially been due to the difference in local fibre environment - as some fibres are present inside tows (surrounded by other fibres) whilst others are segregated in the matrix (at tow periphery) and surrounded by all CVI SiC. More fibre push-outs on a single sample (Tyranno type SA3 with thick BN) were therefore performed to look at the performance of the interlayer inside and at the periphery of a fibre tow, highlighted in Figure 42. As fibres have a differing number of neighbours, this might have affected the strength of the interlayer being pushed out. It is also worth noting that the CVI thickness of both BN and SiC layers slightly varied – both within a tow and between tows – thus influencing results.

3.4.3 Cascade Push-outs

The intra-tow variability in measurement was further investigated using 'cascade' push-outs on a sample with Tyranno type SA3 fibres with a medium-sized BN interphase. Several fibres were pushed out around a target fibre which was subsequently pushed out – for example in Figure 43, the central fibre was pushed out after pushing out of its first 3 neighbours (Figure 43.a) or 5-6 neighbours (Figure 43.b).

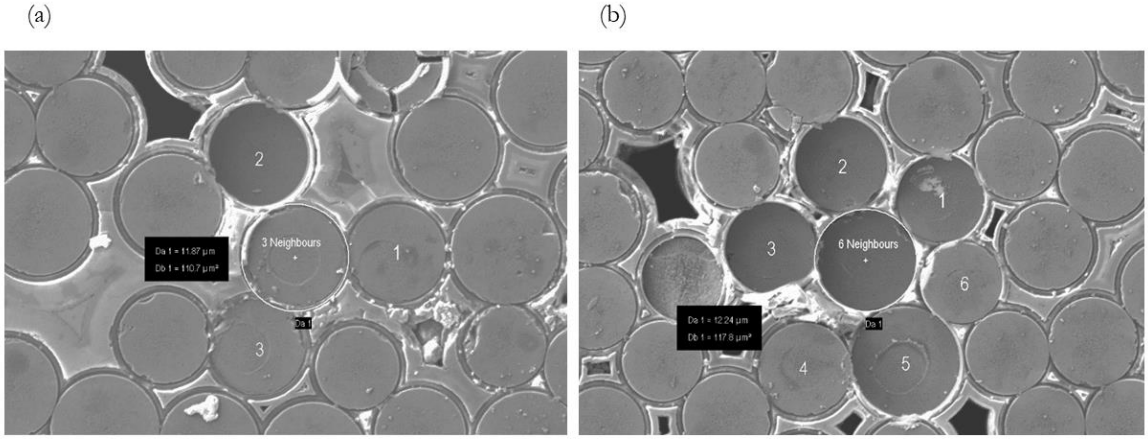


Figure 43: SEM Micrographs showing post-portem analysis of the cascade push-outs on a Tyranno type SA3 fibre with medium BN. Cascade push-outs with (a) 3 neighbours and (b) 5-6 neighbours

3.5 Fibre Push-Ins & Push-Backs

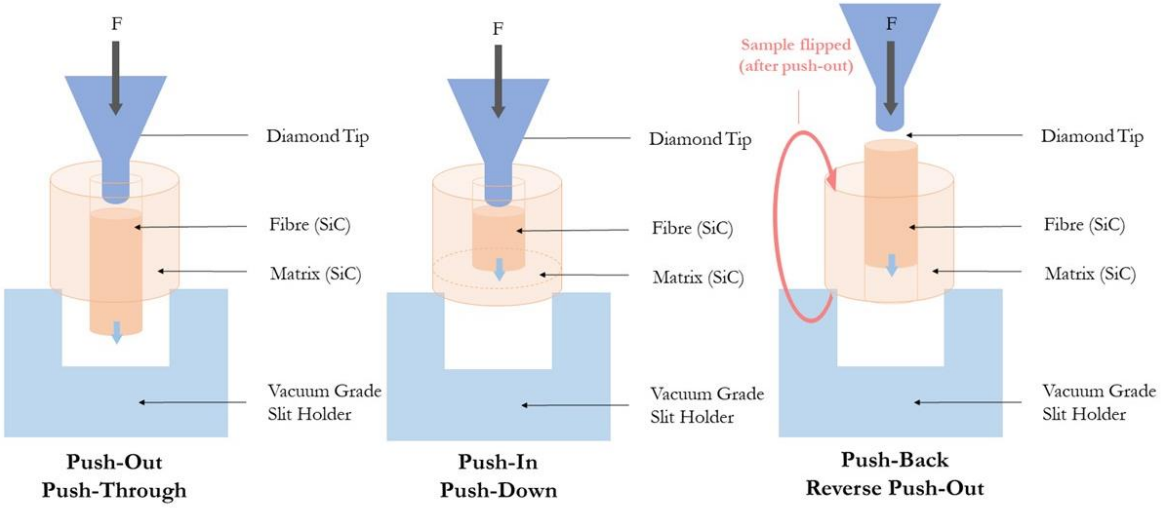


Figure 44: The differences in micro-mechanical methods between fibre push-outs, push-ins and push-backs.

Fibre push-ins and push-backs were performed at the same displacement rates and using the same tips as fibre push-outs; however, the samples were not ground to specific thicknesses below 100 µm. The subtle differences between all three techniques are illustrated in Figure 44 and were previously summarised in Chapter 2, Section 2.2: the fibre push-out provides an overview of the mechanical strength of the interphase. The fibre push-in can provide a numerical value for the interfacial shear strength and the fracture toughness of the fibre, the interphase or the underlying material, depending on which of the above fails first. However, the fibre push-in required data fitting to models for any desired property. The fibre push-back yields insights on friction-only components of the fibre push-outs, these were first performed on the Tyranno type SA3 (thin BN) sample with a depth limit double that of initial push-outs (6 µm) and a 0.2 $nm.s^{-1}$ allowable drift rate.
The push-out and push-in behaviours were performed on single samples in a row. This was to directly compare cracking behaviour to push-out behaviour as seen on work by Medina et al.[105] whom performed similar analysis. The equation used to calculate the ISS for push-out is equation [25] whereas both equations [26] and [27] were used to calculate the push-in ISS:

$$\tau_{Push-Out} = \frac{F_c}{2\pi r t} \quad [25]$$

$$\tau_{Push-In} = \frac{nF_c}{2\pi r^2} \quad [26]$$

$$n = \frac{S_0}{\pi r E_f} \quad [27]$$

With F_c the critical load from the indenter, r the fibre radius, E_f the fibre elastic modulus and S_0 the slope of the indenter load-displacement signal as it pushes in before reaching critical load. All ISS were calculated for 100 tests per test type (push-out or push-in) per sample (3 samples including Hi-

Nicalon type S thin BN, Tyranno type SA3 thin and thick BN) and per tow location (edge or middle). It is noted that there is a human-dependent tendency to select bigger fibres for push-ins[48], as there is a higher factor of the experimentalist being weary of the indenter tip crashing in the matrix. Fibre push-backs have a re-seating stress which can be directly correlated to the coefficient of friction, however (and similarly to data analysis on the unloading portion of the indentation curve as previously highlighted), this is mostly observable on displacement-controlled instruments. Model traces of load/displacement data comparing fibre push-out and respective fibre push-back were illustrated in the first figure of Parthasarathy[188] describing extracting properties from the micro-mechanical technique in 1991 – with a noticeable drop in load with friction for the push-out but a constant load plateau for the push-back.

3.6 Advanced Methods

More advanced methods including in-situ trench push-outs, high-temperature indentation & X-ray tomography (both micro and nano-scale) were utilised in chapter 5– more detail on the methodology involved was included in said chapter.

3.7 Chapter Conclusions

This chapter provided an overview of the elastic properties of the materials as well as descriptions of the various micromechanical and characterisation techniques employed in the main body of this work. It was found that the BN interphase displayed significantly weaker elastic properties when compared to other composite constituents with a modulus of 25.9 ± 5.4 GPa and a hardness of 1.3 ± 0.1 GPa at room temperature. The express mapping of elastic properties also gave insights on which type of fibre was indented as fibre porosity was highlighted.

The non-material dependent parameters of the fibre push-out technique were investigated in this chapter. Firstly, it was confirmed that an optimum 100 µm for the total sample thickness was needed for a maximum technique success rate, and to minimise sample bending and/or other sample geometry artefacts. Secondly, a ratio of 1:2 for the tip:fibre diameter is recommended for optimized flat-punch tip push-outs, as a higher ratio resulted in higher chances of indenting neighbouring fibres/environment and a lower ratio resulted in an increased stress intensity factor at the tip edges, rendering the fibre more prone to cracking. In this case, a tip diameter of 5 µm supersedes expectations and can push both 2nd and 3rd generation fibres for Hi-Nicalon and Tyranno fibres. Thirdly, a tip-induced plastic deformation of 400 nm ± 61 nm on the fibre surface was found and therefore needed to be omitted during depth calculations of the actual push-out displacement. Finally, the default 5 mN.s^{-1} displacement rate was used for the rest of this work as slower rates resulted in more pronounced tip-induced plastic deformation on fibres surfaces (despite a clearer segregation in micro-events) whilst faster rates resulted in a decrease of micro-events separation (e.g. one could not dissociate when a crack initiated or propagated).

Introductions to techniques used in investigating material-dependent variables, alternative micromechanical tests (push-ins and push-backs) as well as more advanced techniques (in-situ via push-outs, high-temperature indentation and the use of x-ray tomography) were provided.

Chapter 4 • Material Variables

4.1 Material Database

This thesis makes use of 13 different sample types – the nature of each is highlighted below:

1. Hi-Nicalon, 2nd Generation Fibres from *NGS Advanced Fibers Co*. as:
    a. Pristine
    b. Degraded for 50 hours at 600°C and 95% Relative Humidity
    c. Degraded for 250 hours at 600°C and 95% Relative Humidity
    d. Degraded for 500 hours at 600°C and 95% Relative Humidity

2. Hi-Nicalon Type S, 3rd Generation Fibres from *NGS Advanced Fibers Co*. with a:
    a. Thin BN (~ 200 nm)
    b. Medium BN (~ 400 nm)
    c. Thick BN (~ 600 nm)
    d. Si-doped interlayer (6 different types with multilayers & different levels of doping)
    e. Medium BN (~ 400 nm) and an all CVI SiC Matrix

3. Tyranno Type SA grade 3, 3rd Generation Fibres from *Ube Industries Ltd*. with a:
    a. Thin BN (~ 300 nm)
    b. Medium BN (~ 400 nm)
    c. Thick BN (~ 600 nm)
    d. Single bundle of fibres as micro- or mini-composites (BN thickness ~ 3 μm)

With the exception of II.e and III.d, all samples have fibre tows woven into balanced 2D 5HS fabrics (woven under every 5th weft thread) and stacked to form a preform, which is subsequently CVI-coated with both a BN interphase and a SiC-layer. The quality of the CVD process means that the BN interphase is of average quality, with crystallinity levels reaching 50% at maximum, and whereby crystallite pockets of differently-oriented aromatic BN planes are scattered in a sea of glassy (amorphous) BN. The crystallinity is further investigated by means of TEM (with diffraction and HR) in Chapter 6. The porous preforms are finally densified with SiC slurry and a Si melt infiltration to complete the composite matrices. In contrast, sample II.e has been fully densified by CVI without any SiC slurry or Si infiltration whilst sample III.d consists of a single fibre tow of roughly 800 fibres coated with a thick (3 μm) BN interlayer, adorned with a CVI SiC layer. Commercially-available constitutive dimensions of some of the samples are highlighted in Table 7.

Table 7: Fibre type, roughness, diameter and interphase thicknesses

Sample	Fibre Type	Fibre Diameter	BN Interphase Thickness	Root-Mean Square Fibre Roughness
HN – Thin BN (I)	Hi-Nicalon	14 ± 2 µm	200 ± 50 nm	5.42 nm[182]
HNS – Thin BN (II.a)	Hi-Nicalon Type S	12 ± 3 µm	200 ± 50 nm	2.33[65], 3.0[189] nm
HNS – Medium BN (II.b)	Hi-Nicalon Type S	12 ± 3 µm	400 ± 50 nm	2.33[65], 3.0[189] nm
HNS – Thick BN (II.c)	Hi-Nicalon Type S	12 ± 3 µm	600 ± 50 nm	2.33[65], 3.0[189] nm
TSA3 – Thin BN (III.a)	Tyranno Type SA3	8 ± 2 µm	200 ± 50 nm	8.04[65], 9.0[189] nm
TSA3 – Medium BN (III.b)	Tyranno Type SA3	8 ± 2 µm	400 ± 50 nm	8.04[65], 9.0[189] nm
TSA3 – Thick BN (III.c)	Tyranno Type SA3	8 ± 2 µm	600 ± 50 nm	8.04[65], 9.0[189] nm

4.2 Composite Characterisation (Geometric Variables)

The use of simple SEM imaging on all samples gave morphological insights. The Hi-Nicalon fibre sample had a large variation in CVI layer thickness, where the edge of the tows displayed significantly thicker CVI layers. Fibre radii were homogeneous. The samples with thinner BN interlayers (Figure 45.c) displayed less porosity and signs of more homogeneous infiltrations. The all-CVI SiC sample in Figure 45.a showed extremely large porosity, as no melt infiltration filled the pores after CVI. Porosity was investigated in a more quantitative setting in chapter 6, section 6.4.

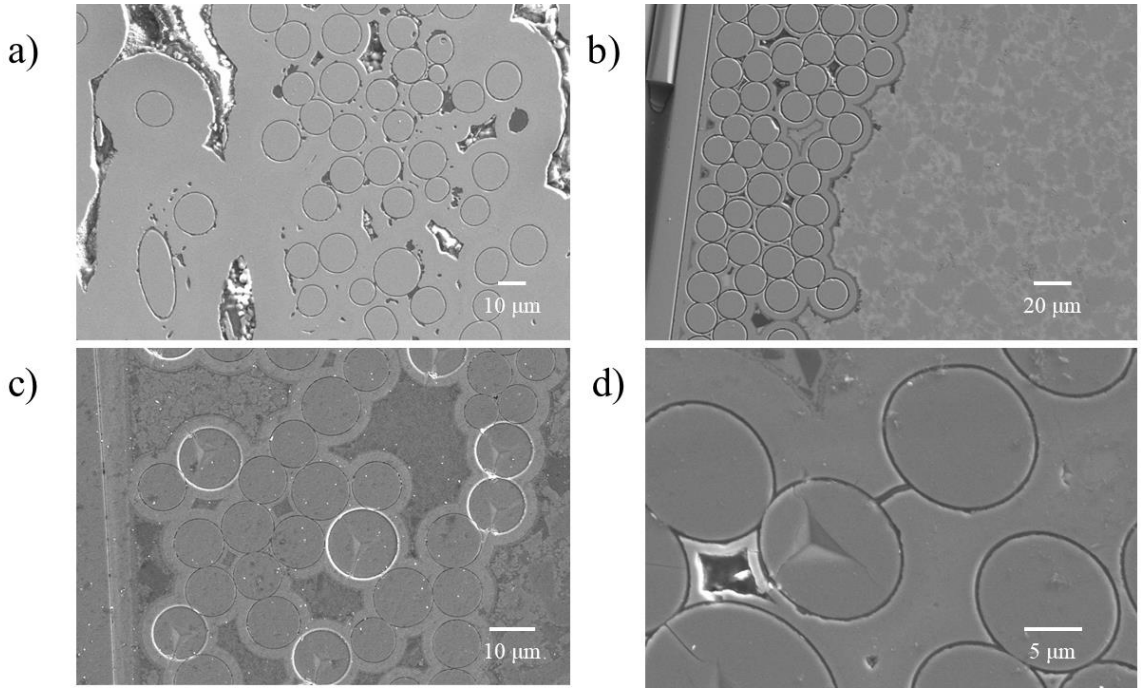


Figure 45: Initial SEM characterisation of the samples showing a) porous Hi-Nicalon type S with an all CVI SiC matrix, b) a Hi-Nicalon Type S thick BN sample pre-indentation, c) a Hi-Nicalon type S thin BN sample after fibre Berkovitch indentation, and d) crack bridging after fibre indentation on a Hi-Nicalon thin BN sample

Overall, samples with Tyranno type SA3 fibres had thicker BN interlayers. SEM analysis post-indentation (same tests as experiments in section 3.2.1.1) revealed clear indents on thinner BN interlayers. Indeed, fibres were pushed out despite indenting in bulk-like (cold-set epoxy mounted) samples, as seen on Figure 45.c. [redacted] Crack bridging between fibres – as seen on Figure 45.d – suggest indenting fibres with a Berkovich tip resulted in a release of stress accumulation in fibre surroundings, inducing cracks which propagated on the outskirts of indented fibres. These qualitative observations indicate that composite structural integrity before and after testing is suitable for indentation (and micromechanical testing in general), as little debris was created, even at panel edges where cutting damage was more significant.

An approximation of average fibre diameters and interlayer thicknesses was given for each sample (and constituents) after 10 high-resolution SEM measurements on a Zeiss Merlin instrument. The results of which are given in Table 8

Table 8: Average fibre diameters and interlayer thicknesses for the BN and CVI SiC layers

Sample	Fibre Diameter	±	BN Interlayer	±	SiC CVI Interlayer
-	**µm**	µm	**nm**	nm	**µm**
HN – Thin BN (I)	**11.83**	2	**231**	30	**1.51**
HNS – Thin BN (II.a)	**13.01**	2	**223**	20	**2.23**
HNS – Medium BN (II.b)	**12.16**	1	**430**	56	**2.95**
HNS – Thick BN (II.c)	**13.51**	0	**662**	69	**3.47**
TSA3 – Thin BN (III.a)	**9.97**	1	**322**	56	**1.77**
TSA3 – Medium BN (III.b)	**10.34**	0	**431**	45	**1.79**
TSA3 – Thick BN (III.c)	**9.36**	2	**658**	33	**0.99**
HNS - All CVI SiC (II.e)	**14.66**	1	**488**	80	-

From Table 8, it is clear that the all-CVI SiC sample presented the widest fibre average. BN interlayers were 200 nm thin for the thinner samples and 650 nm thick for the thicker samples. The SiC CVI interlayers were much thinner for the Tyranno type SA3 fibres (which have an industrial-reported average of 8 to 10 µm) than the Hi-Nicalon type S fibres. The SiC CVD interlayers presented a wide variation in thickness. Measurements of all these geometries could be improved by the use of an automated analysis tool from imaging data, both tomography or AI with machine learning (to correctly identify and measure fibres and interphases from a database of micrographs). When contrasting these measurements to those in literature, some sources categorise BN interphases from 100 to 500 nm in thickness as "thin"[48].

4.3 Intertow Variations

Push-outs were completed in batches at different locations within the Tyranno type SA3 with thick BN sample to investigate the effect of fibre local environment on the ISS measured. Results were summarised in Figure 46.

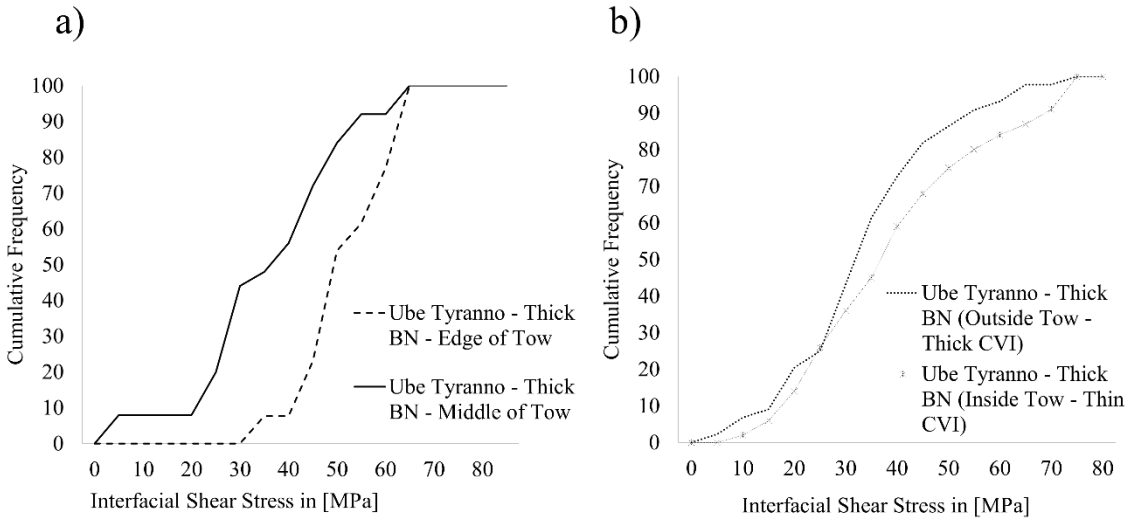


Figure 46: Cumulative Distributions Functions (a) contrasting fibre push-outs at the periphery of tows (dashed) and in the centre of tows (continuous) in a Tyranno type SA3 with a thick BN sample; and (b) contrasting fibre push-outs in outer tows (dotted) and in centre tows (dashed and crossed) on the same sample.

Firstly, push-outs - of random location within a tow - were completed in different fibre tows on Figure 46.b. Push-outs completed in tows at the edge of the sample, as illustrated in Figure 42) (with thicker CVI SiC interlayers surrounding the tows), were found to be statistically easier to push out (with a lower mean and median ISS of 33.2 and 31.7 MPa respectively) than fibres pushed out in tows close to the centre of the sample (with a mean and median ISS of 39.0 and 36.1 MPa respectively). However, as the cumulative distributions overlap, the statistical significance of this result is ambiguous without further analysis (discussed below).
Secondly, it was found that for samples with a thick BN interphase, fibres at the edge of a tow were statistically harder to push out than fibres in the centre of a tow (surrounded by numerous neighbouring fibres – up to 6 in a hexagonal stacking configuration – and therefore with more shared interphase contact area) as shown more clearly on Figure 46.a (no overlap of the cumulative distribution functions).

Performing an unequal variance two-tail t-test (with $\alpha = 0.05$ and a hypothesized mean difference of 0) comparing intratow (Figure 46.a) and intertow (Figure 46.b) populations results in the t stat for the intratow populations (2.73) sitting above the positive t critical for two-tailed analysis (2.03), and the t stat for the intertow populations (-2.27) sitting below the negative t critical for two-tailed analysis (-1.98); both of which confirm the hypothesis (the populations share the same mean) can be rejected. This is also reflected in the P-values obtained (2-tailed) of 0.009 (intratow) and 0.025 (intertow) both being lower than α, reinstating that in both cases (intratow or intertow), all populations are significantly different.

4.4 Intratow Variations

4.4.1 Effect of Fibre Type

Cumulative distribution functions of the interfacial shear stresses for different types of samples were plotted below in Figure 47:

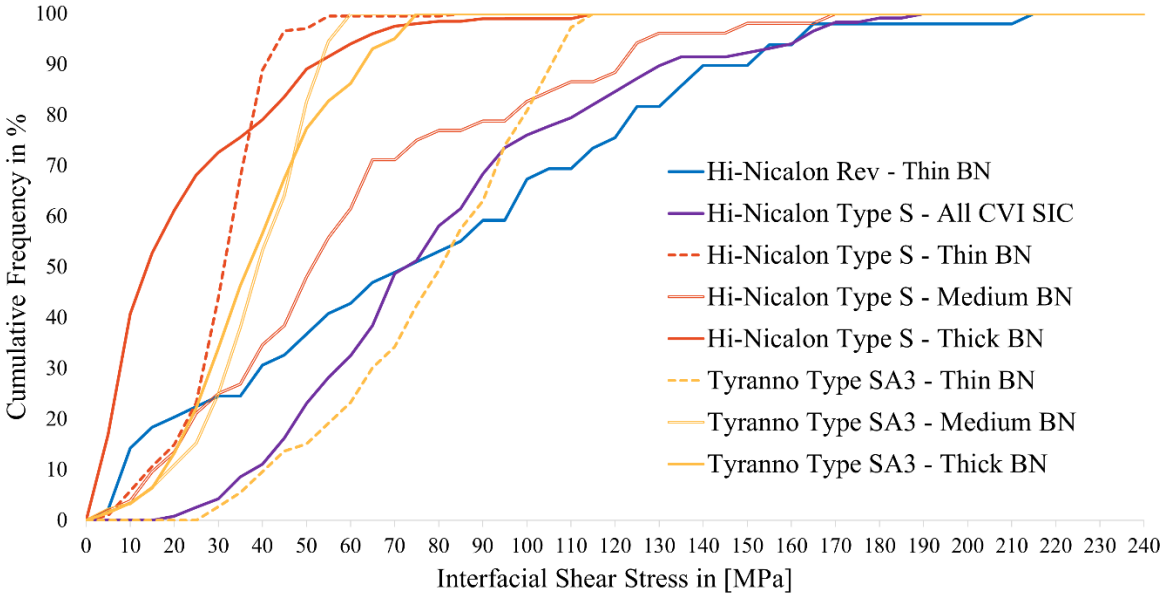


Figure 47: Cumulative Distribution Functions (CDF) of the Interfacial Shear Stresses (ISS) for different types of fibres

Trends from Figure 47 seem to indicate that Tyranno type SA3 fibres and Hi-Nicalon type S fibres show dissimilar spreads in interfacial shear stresses even if the differences in BN thicknesses are the same. Comparing fibre types with similar interphase thicknesses (e.g. both with a thin BN) results in the Tyranno type SA3 fibre sample displaying the highest interfacial shear stresses on statistical average. The latter may be due to the larger fibre dimensions, differences in fibre thermal expansions from processing and the smoother fibre surface (or fibre surface chemistry). This effect is further investigated in Section 4.6.

The sample with the second-generation Hi-Nicalon fibres and the sample with the third-generation Hi-Nicalon type S fibres (but imbedded in an all-CVI SiC matrix) displayed the highest interfacial shear stresses on statistical average. In the first case, this may be due to the rougher surfaces of second-generation fibres. In the second case, only the presence of a melt-infiltrated matrix differs from other samples with same fibre types. Since the all-CVI SiC matrix has a similar interphase thickness to that of medium BN samples (Table 8) the blue line can be compared directly to the hollow red line. The higher mechanical stresses from the all-CVI SiC may hint that there are either non-negligible tensile stresses in the melt-infiltrated matrix (with residual Silicon), or compressive stresses in the SiC produced through chemical vapour deposition, both of which significantly influence how much shear the interphase can absorb. CVD has been known to show increased residual compressive stresses with thicker coating, as the deposition process creates columnar grains which induce a mechanical anisotropy in the response[190]. The range of ISS values per sample led to the investigation of parameters which affect this variability.

4.4.2 Effect of Test Location Within a Tow

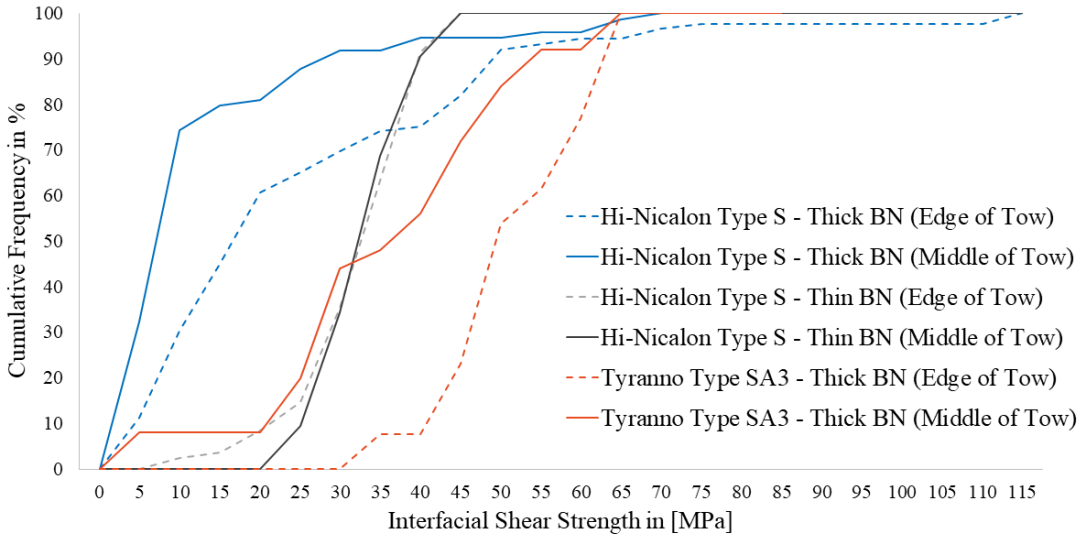


Figure 48: Cumulative distributions of the ISS obtained for two Hi-Nicalon type S fibre-samples (one with a thin BN and one with a thick BN) and a Tyranno type SA3 fibre-sample. The dashed lines represent fibres pushed out at the periphery of a tow.

Figure 48 and Figure 49 plot the same data under two different formats (cumulative distribution functions and box-and-whiskers plot). Comparing fibre types in the first instance, the Tyranno type SA3 sample (in red on Figure 48) seems to have the highest interfacial shear stresses (with a mean and median of 50.6 MPa and 48.5 MPa respectively, summarised in Table 9). The thickness of the BN interlayer has a significant effect on the distribution of the ISS with respect to fibre location within a tow. Indeed, fibres pushed on the sample with the thinner interlayer (in dark grey on Figure 48) displayed no bias with respect to intra-tow location (this is further investigated in Section 4.5 - Discussion (Material Variables)). When looking at the effect of the thickness of the interphase, comparing the Hi-Nicalon type S samples with a thin (dark grey) and a thick (blue) BN layer – it is clear that in the lower end of the ISS spectrum, fibres were harder to push-out if only a thin BN was coating the fibre. This is reflected in the values in Table 9 where all mean and median values for the thin interphase (columns 2 & 3) are greater than the respective values of the thicker interphase (columns 4 & 5), therefore a thinner interlayer resulted in higher shear stresses.

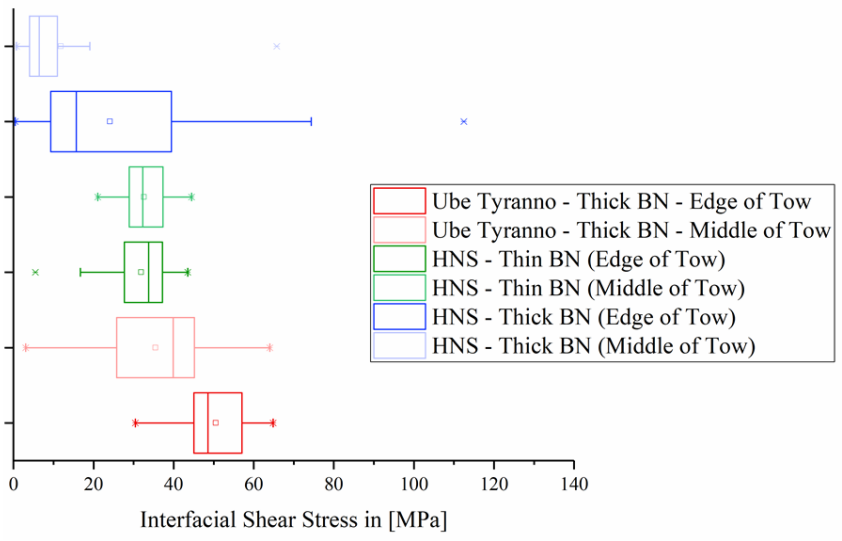


Figure 49:Box-and-whisker plots of the ISS obtained for two Hi-Nicalon type S fibre-samples (one with a thin BN and one with a thick BN) and a Tyranno type SA3 fibre-sample. The darker colour represents fibres pushed out at the periphery of a tow.

The interfacial shear strength found from the same fibre push-outs as Figure 48 were also plotted in box-and-whisker plot format - which includes the median and 1st/3rd quartiles – to visualise the data differently. Data on Figure 49 suggests that when compared to Hi-Nicalon type S fibres, Tyranno type SA3 fibres displayed rougher interfacial properties, an observation which aligns with fibre roughness properties in Section 4.6. However, the Tyranno type SA3 fibres are also smaller on average than their Hi-Nicalon counterparts, and whilst the ISS was normalized to fibre diameter, there was an experimental bias when selecting fibres for push-out. Indeed, human selection of fibres was performed so as to ensure fibres were big enough to not affect tip diameter (i.e. if a fibre was too small, there was a greater chance of the tip hitting the BN directly), resulting in only bigger fibre sizes being probed in the distributions.

Table 9: Mean and median values for the ISS in the three focus samples when investigating intra-tow variations of fibre push-outs

Sample	**Hi-Nicalon type S – Thin BN**		**Hi-Nicalon type S – Thick BN**		**Tyranno type SA3 – Thick BN**	
Location	Tow Edge	Tow Middle	Tow Edge	Tow Middle	Tow Edge	Tow Middle
Mean	**31.9**	**32.6**	**24.1**	**11.9**	**50.6**	**35.5**
Standard Deviation	*± 7.0*	*± 5.0*	*± 17.5*	*± 7.0*	*± 10.0*	*± 15.0*
Median	**33.7**	**32.2**	**15.6**	**6.4**	**48.5**	**39.9**
1st Quartile	*27.7*	*28.8*	*9.2*	*4.0*	*44.5*	*25.6*
3rd Quartile	*37.2*	*37.3*	*39.7*	*10.9*	*60.9*	*46.1*

4.4.3 Effect of BN Interphase Thickness

One of the fundamental properties investigated on the SiC_f/SiC composites is interlayer thickness. Over 200 push-outs were performed on each of two Hi-Nicalon type S samples (one with thin and one with thick interlayer) to look at intratow variations. It was found that – as highlighted on Figure 50 – for thinner BN samples (yellow), there was very limited effect on intratow variations when compared to the thicker BN (red). This result is somewhat intuitive as for thinner BN layers, the effect of the BN (and therefore its thickness) was reduced (more fibre bridging/connectivity), resulting in the fibre push-outs probing the fibre/CVI SiC interface contact more than the fibre/BN or BN/CVI SiC interfaces. Thinner BN interlayers seemed to result in more matrix compressive stresses acting to slow down crack propagation and fibre sliding – this hypothesis can be verified by carrying out these tests in-situ (c.f. Chapter 6).

Please note that the CDF's of ISS on Figure 50 were calculated from Hi-Nicalon type S fibres, yet still show similar trends to the Tyranno type SA3 fibres highlighted on Figure 48 (fibres on tow edges being harder to push out on statistical average than those in the middle of tows). The trend on Figure 50 also serves to explain the fact that the deposition process of the BN creates inhomogeneities in thickness within a tow. These are more prevalent on samples with a thicker BN, where a greater difference in behaviour (a.k.a. cumulative frequencies which are futher apart) is therefore noted when compared to samples with a thin interlayer. When contrasting the data at 25 MPa cut-off, it is evident that the majority of the push-outs were weaker than that threshold for the thicker interphase whereas the majority of the push-outs were stronger than that threshold for the thinner interphase – since both samples have similar "exposure" to water in storage conditions, this effect might be attributed to interphase thickness alone.

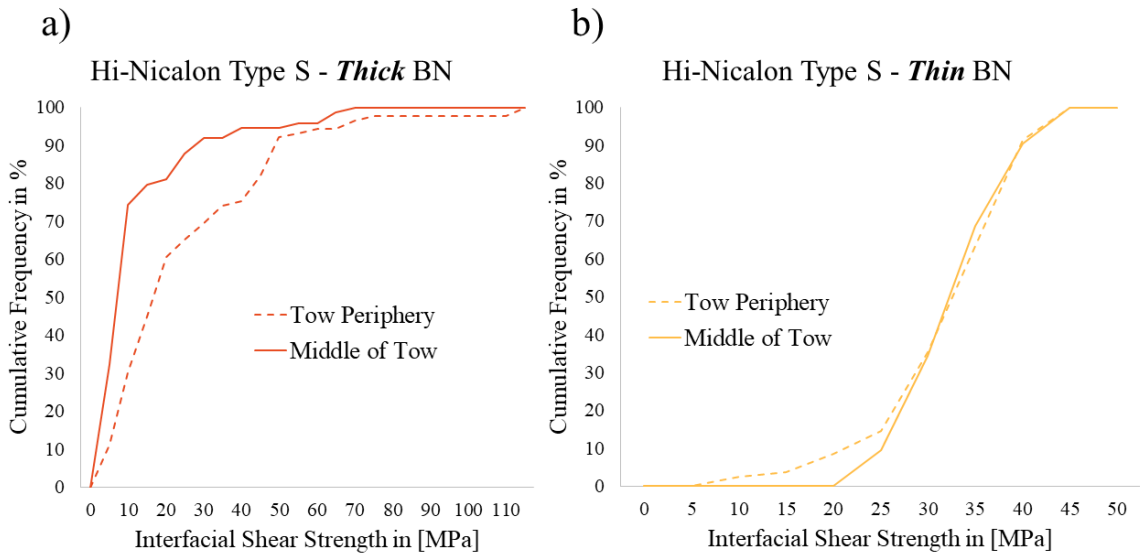


Figure 50: CDF's for two Hi-Nicalon type S samples with a) thick and b) thin interlayer, showing no intratow variations in the thin sample and strong intratow variations in the thick sample

Another variable to consider is the thickness of the BN interphases within a tow. Indeed, CVD induces differences in the variable outlined as fibres in the tow middle will have thinner coatings than fibres at tow peripheries. This means that if the logic comparing BN thickness between samples held true (that thinner interphases resulted in higher ISS) within a tow as well, one would see the

opposite trend of Figure 50.a. Since the observations contradict such thought, one can come up with a 'ranking' of prioritised variable and the magnitude of their effects on measured ISS:

Intertow BN thickness > Intratow Location > Intertow Location > Intratow BN thickness

Another interpretation of the offset in the magnitude of the ISS (when looking at the 90th percentile for example) seen in Figure 50 could lie in the sample preparation, whereby thicker interphases are more easily damaged during transport or storage of samples.

4.4.4 Effect of Neighbouring Fibres ('*Cascade*' Push-Outs)

The ISS measured from cascade push-outs introduced in Chapter 3 were plotted (Figure 51.a) as function of the undamaged 'leftover' BN surface area coating the fibre. This area assumes a perfectly cylindrical fibre and a minimum of 2 µm in cross sectional arc length of contact length (BN interlayer) connecting two fibres. The ISS increases as more BN is left pristine (Figure 51.a). Plotting the ISS as a function of the area metric enabled direct correlation between the surface area / the theoretical amount of BN deformed and the measured interfacial shear stress.

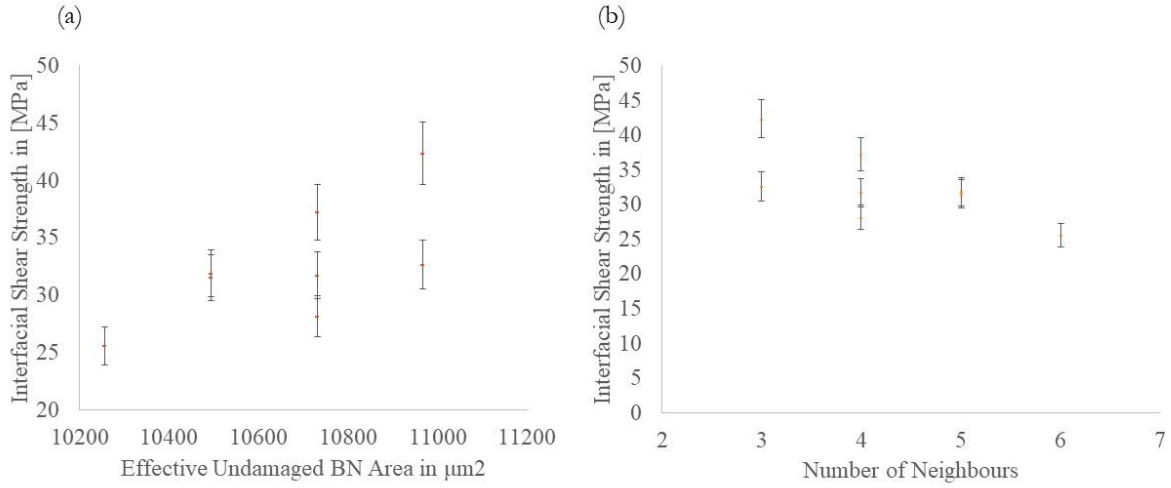


Figure 51: Spread of the ISS with respect to a) the empirical effective undamaged BN area surrounding the fibre and b) the number of neighbours previously tested.

4.5 Discussion (Material Variables)

Fibre push-outs which displayed higher interfacial shear strengths in all the results may be due to the larger fibre dimensions, which enhanced differences in fibre thermal expansions from processing and the rougher fibre surface (or fibre surface chemistry). Results from section 4.4.2 investigating the effect of interphase thickness – compared a Hi-Nicalon S sample with both thin and thick BN interlayers on Figure 48 and found that the thickness of the BN influences either the amount of (compressive) load sharing from the matrix to the fibre and/or the work required to fully propagate the crack at the interphase. A thinner interlayer resulted in higher shear stresses due the higher possiblity of the interlayer being damaged along the fibre and/or accentuating the effect of fibre nano-asperities from surface roughness (in thicker interphases, this effect is reduced). The distribution of ISS values (Figure 48) in the lower end (1st quartile) and on thicker BN samples was narrower. This was most probably due to the smaller influence of fibre tapering, tilting and offset, as well as the influence of the fibre volume fraction and eccentricity (i.e. the thicker interphase annuls the effects of all of the above). Figure 48 also showed no distinction between pushing fibres at the edge or in the middle of tows in samples with a thinner interphase (as opposed to those with a thicker interphase, where the difference was more than noticeable), suggesting there is a threshold interphase thickness which neutralises the effects of fibre location within a tow. Thinner interphases may result in more inherent defects from manufacturing and a higher probability of the interlayer not coating the fibre fully before the fibre push-out begins – thus influencing push-outs and resulting in little difference between pushing a fibre with a thin interphase and no interphase at all. However, no SEM observation as of yet showed non-coated sections on a pristine interphase to support this hypothesis.

'Cascade' push-outs on a sample with a medium-sized BN interphase in Figure 51 add to this picture. Damaging the BN connecting 2 neighbours showed strong correlation with the ease at which a fibre can be pushed out. Indeed – pushing a fibre neighbouring one which has already been pushed out enhances the cascade effect by which neighbouring fibres will effectively push each other out, because the interlayer lying between them is already damaged[141]. A damaged BN is therefore easier to push-out if the BN has reached a threshold thickness (below which the ISS measured is the same as testing a nude fibre). The modelling of the cascade push-outs as well as the testing of fibre with no known neighbours (isolated outside of a traditional tow) could provide a reference value for the trends observed in Figure 51.

The strong correlation between number of direct neighbours during push-out and push-in has been both observed and modelled by Molina-Aldareguía[124], whom has found that a constraining factor (R_e/r) ratio included in their analytical model accounts for fibre packing density within a tow, and notes that a small constraining factor (high number of neighbours, high packing density) induced disparities between observed load and measured displacement during push-in tests[124]. A symmetric hexagonal arrangement of neighbours around a target fibre can be related to the fibre packing/volume fraction of fibre as follows:

$$\ln\left(\frac{R_e}{r}\right) = \frac{1}{2}\ln\left(\frac{2\pi}{\sqrt{3}V_f}\right) \;\therefore\; V_f = 74\%\,; \frac{R_e}{r} \approx 8.08 \qquad [28]$$

Where R_e is the outer radius encompassing the BN interphase (the radius of equivalent environment), and r is the small radius of the bare fibre alone. Therefore, for a hexagonal neighbouring configuration (corresponding to a 74% packing density and a 8.08 constraining factor), cascade push-outs on the CMC's were measured to induce 26.4 MPa in ISS, as shown on Figure 51.b. At lower constraining factors (higher number of neighbours), Molina-Aldareguía[124] also found that the stiffness was over-predicted by 30% when using the shear-lag model, and therefore recommended

that the constraining factor always be taken into account for fibre push-ins as a parameter during linear-slope fitting of mechanical data. Fibre push-ins were therefore performed in the next section.

4.6 Push-Ins

All ISS were calculated for 100 tests per test type (push-out or push-in) per sample (three samples including Hi-Nicalon type S with a thin BN, Tyranno type SA3 with thin and thick BN) and per tow location (edge or middle) using equations [25], [26] and [27] outlined in section 3.5, finally plotted as mean – with population standard deviations – in Figure 52.

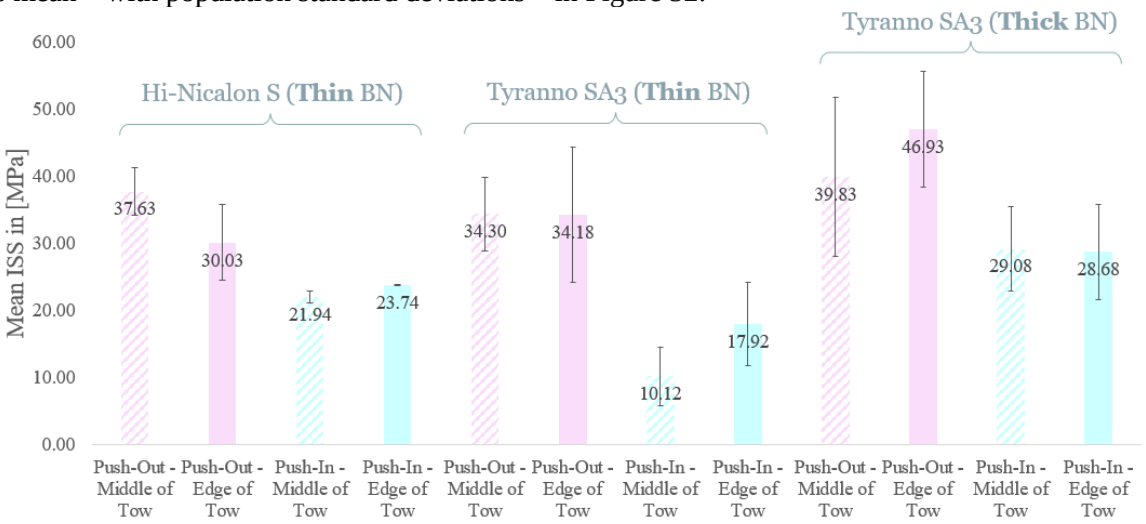


Figure 52: Push-out (pink) and push-in (blue) behaviours on three samples. Each column corresponds to 100 tests.

For each sample plotted in Figure 52, the mean ISS calculated from simple shear force balance were significantly higher than their fitted push-in ISS counterparts. The analysis of the ISS through the push-in behaviour was therefore skewed so that either the push-out overestimated the ISS (failing to take into account any cracking of the fibre or neighbours) or the push-in underestimated the ISS (by contributing too much energy to debonding and crack propagation). Callaway et al. found no correlation between ISS measured and BN interphase thickness when testing with fibre push-ins[4848].

A surface topography of both fibre types was measured by scanning with a Berkovich tip using a Hysitron TI Premier nanoindenter in contact mode (small constant force)[3]. The maps spanned an area of 10 x 10 µm with a step size of 20 nm. The root-mean squared fibre roughness was obtained on sub-maps of 1.5 x 4 µm areas by a Root-Mean Square analysis with the scanning probe software Gwyddion (Version 2.56). Two further maps of a fibre push-in and a fibre push-out on Figure 53 showed that the depth of indenting could be measured with high accuracy using the indenter on AFM mode. The push-in imprint (Figure 53 – top) showed a maximum indentation depth of 200 nm whereas the push-out imprint (middle) showed tip artefact geometries, as the tip could not probe depth lower than 350 nm. The measured roughnesses for the Hi-Nicalon (35.5 nm) and Tyranno type SA3 (100.6 nm) fibres can be compared to values for Hi-Nicalon type S (20 nm) and Tyranno type SA3 (24 nm) found by Kabel et al.[141], in their magnitude and ratios. The discrepancy might have been due to the lack of accountancy of the fibre curvature, instead assuming a perfectly flat scanning surface. In the case of push-ins performed in Figure 52, the rougher fibre type nevertheless resulted

[3] Data acquisition was performed by Kay Song

in smaller ISS, perhaps from fibre roughness playing a lesser role in push-ins, compared to push-outs. This conclusion might be inconsistent due to the data fit limitations highlighted above.
With more measurements of other fibre types and surfaces, the relationship between fibre roughness, ISS and BN thickness could be correlated in a full multivariate model in future work. Trends observed in the model can then be useful in selecting the appropriate fibre type and interphase thickness to manufacture.

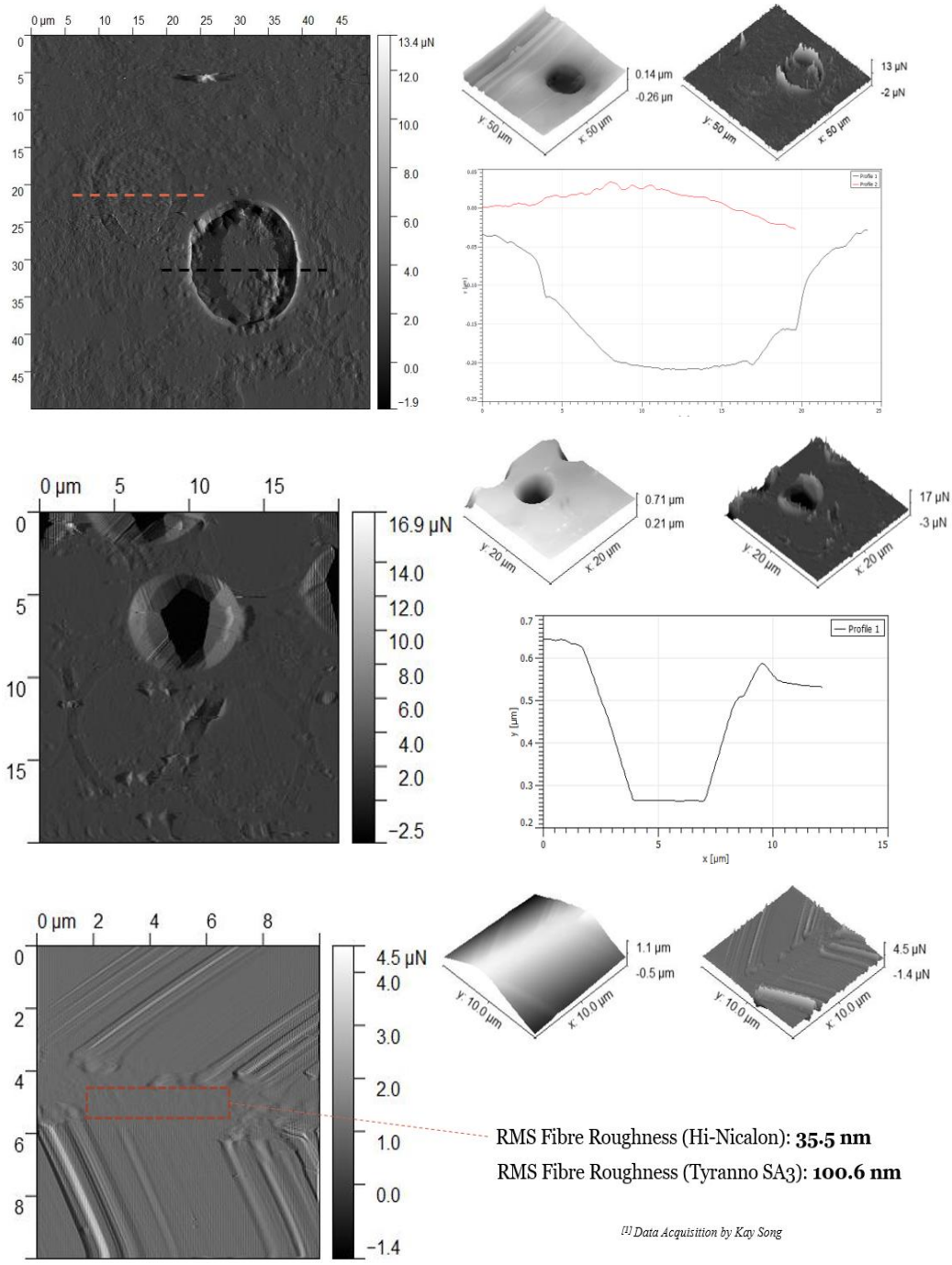


Figure 53: Fibre push-in (top), push-out (middle) and fibre roughness (bottom) imprint analyses performed using a nanoindenter on contact AFM mode. Load and depth maps as well as depth line profiles across imprints were included.

4.7 Push-Backs & Frictional Studies

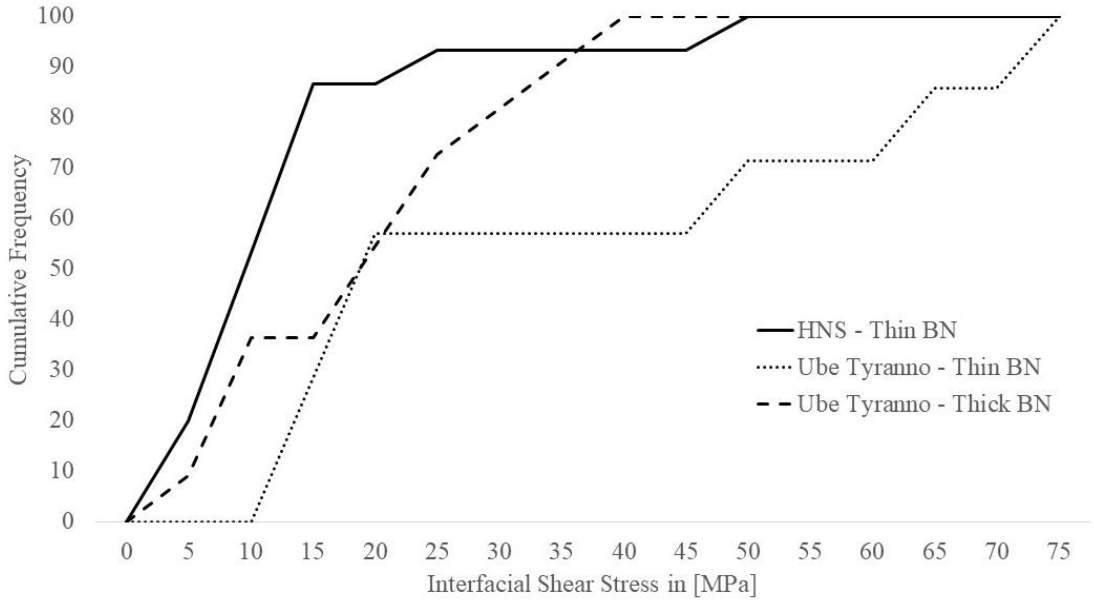


Figure 54: Cumulative distribution functions of the ISS in fibre push-backs showing harder push-backs on average for the Tyranno type SA3 sample with a thinner BN (dotted line) when compared to the same sample with a thick BN interlayer (dashed line). The Hi-Nicalon type S (bold line) shows the weakest/most degraded interphase of all three upon push-backs

Sample push-backs resulted in a 30% success rate due to the uncertainty in misalignment angle when mounting the sample upside down (the same means of optical microscopy as the fibre push-outs were used to check for fibre roundness in combination with ImageJ). Fibres and interphases were also prone to early onset of failure, as previous damage from the push-out might have subsisted. The raw load/displacement data for fibre push-backs showed very few plateaus. Pushing fibres back on samples with thinner BN resulted in higher stresses, as seen on Figure 54. When comparing fibre types, the Tyranno type SA3 (dashed and dotted lines) showed larger ISS and were therefore significantly rougher than the Hi-Nicalon Type S fibre (continuous line) – consistent with known roughness data on the fibres previously highlighted in Table 4 (Section 4.1) and literature[66, 67].

A single fibre push-back was compared to its push-out equivalent in Figure 55.

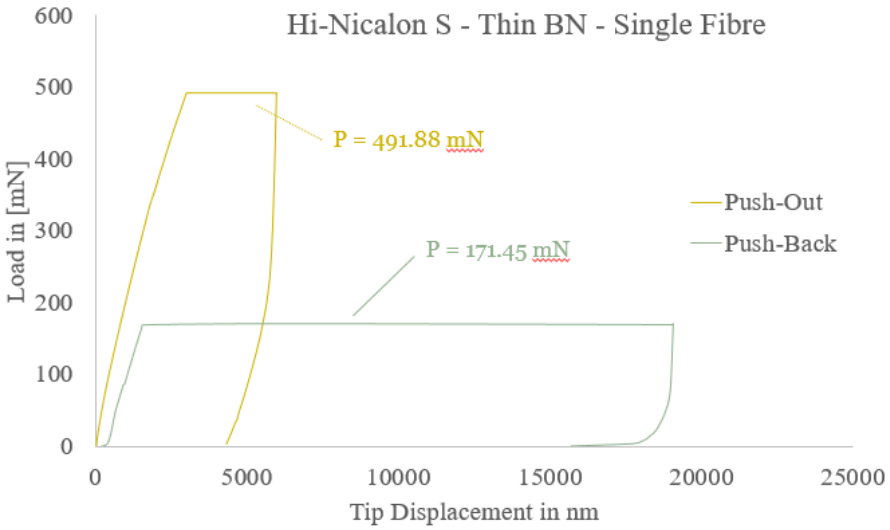


Figure 55: Load/displacement curve with superimposed push-out and push-back curves

Figure 55 showed that for the same fibre, pushing the fibre back from the sample flip side resulted in a 65.2% decrease of frictional load (i.e. the load retention ratio was 2.87). Similar load retention (of 2.5 ± 1.8) was observed by Rebillat[21], however since their instrument was displacement-controlled, Rebillat et al.[21] were able to further detect a re-seating stress (where the fibre sits exactly in its original position) on the load-displacement data – not visible on our data. The re-seating stress is key to calculating the surface roughness (in amplitude and wavelength) from wear behaviour.
'Self' fibre push-backs were observed on samples which were thinned to below-tow dimensions (such as 40 ± 5 µm sample thicknesses in Figure 56) showing that once de-bonded, the load retention of the matrix surrounding the fibres was not sufficient to hold the fibres in place when further handling the samples. 'Self' fibre push-backs specifically refer to un-tested fibres whereby the ISS and bonding were weak enough for the fibre to unsheathe itself (by means of sample transporting or otherwise) uncontrollably without making use of the indenter.

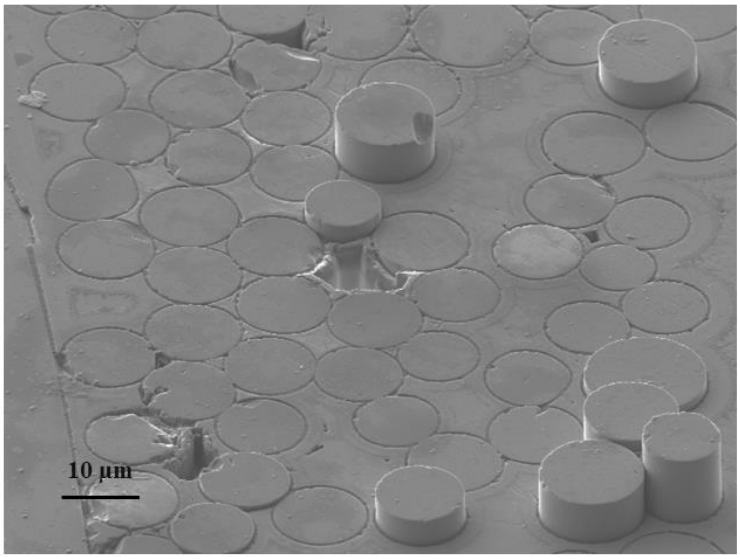


Figure 56: SEM micrograph of several fibre push-backs on a Hi-Nicalon type S sample with a thin BN interphase (Working distance of 5 mm, accelerating voltage of 5 keV, probe size of 100 nA).The micrograph looks at the original plane where the indenter was performing the push-outs.

The smooth fibre surface of the Hi-Nicalon type S fibres can be seen under SEM (Figure 56), even after subsequent fibre push-out and push-back tests. Due to the lack of plateau load bursts during fibre push-backs – it is suggested that the Poisson effect observed in push-outs is much more prominent during push-backs. Pushing fibres back on samples with thinner BN resulted in higher stresses, as seen on Figure 54. This was most probably due to the disintegration of the BN interlayer upon initial push-out, resulting in the fibre being pushed back against the surrounding SiC matrix (and BN debris) rather than a BN interlayer. This was implied by the smooth Hi-Nicalon type S fibre surface seen on Figure 56.

The ISS obtained from fibre push-backs for the three fibre types were further subjected to a Marshall analysis for determination of the frictional sliding resistance[25], the results of which are summarised in Table 10:

Table 10: ISS and frictional sliding resistances obtained from a Marshall analysis on fibre push-backs. All values in MPa.

Sample		**Hi-Nicalon type S – Thin BN**	**Tyranno type SA3 – Thin BN**	**Tyranno type SA3 – Thick BN**
Interfacial Shear Stress	Mean	**10.8**	**33.7**	**18.1**
	Standard Deviation	*± 0.6*	*± 3.3*	*± 1.2*
Frictional Sliding Resistance	Mean	**4**	**11**	**9**
	Standard Deviation	*± 1*	*± 7*	*± 7*

The frictional sliding resistances – herein termed τ_S – were obtained from the equation [29]:

$$\tau_S = \frac{F^2/\Delta u}{8\pi^2 R^3 E_f} \quad [29]$$

Where $F^2/\Delta u$ is the slope of the reloading curve obtained from Marshall[25], whom performed similar experiments using cyclic loading and a Berkovich tip. In our case, the push-back loading curve is contrasted to that of the initial push-out loading curve, this was mirrored in other studies comparing push-out and push-backs by Cherouali et al.[187], whom also used the cyclic method to compare. The cyclic studies are needed to investigate fibre roughness and coefficient of friction. Data in Table 10 show that the sliding resistance is more pronounced for the Tyranno type SA3 fibres when contrasted to Hi-Nicalon type S fibres, in agreement with results from fibre push-ins. When comparing the thick and thin interphases, the thinner interphase yielded larger frictional sliding resistances and higher stresses, further confirming that there was a minimum threshold below which the interphase had little to no effect on toughening of the composite.

The results from the fibre push-out, push-in and push-back techniques comparing fibre types and interphase thickness all highlight the importance of radial gripping[112] in the presence of rough surfaces (Tyranno type SA3 fibres) and an increasingly brittle, erratic behaviour when thinning interphases down[65]. In a similar fashion to PyC-based coatings[191], the ISS decreased with increasing thickness.

4.8 Statistical Approach & Shear-Lag Model

Due to the large amount of data obtained from all micromechanical methods, more statistical tools were used to enable comparison and assess the importance of the various material and experimental-dependent variables. Additionally, the load-displacement data was fitted to shear-lag models found in literature, to give an estimate of model-derived properties (such as the coefficient of friction and G_{IIC}).

4.8.1 Maximum Likelihood Estimates (MLE's)

An MLE approach was utilised on a single sample type to assess whether a deterministic value of the ISS could be calculated. The MLE's were used against three different distributions to look at best fit of the ISS population using a MatLAB code[4].
A set of 201 push-outs performed on a Hi-Nicalon type S sample with a thick BN interphase and the respective cumulative frequency were used to plot the histograms. Bins of ISS were made in steps of 5 MPa. The data was plotted as histograms and contrasted to standard types of distributions (Rayleigh, Lognormal and Normal distributions) in Figure 57. Results show that the Lognormal distribution best describes the measured ISS populations with a mean ISS of 7.15 ± 2.79 MPa. These populations already have an optimised quality of fit, as the ISS values have been censored towards the positive skewed tail (with 'unsuccessful' push-outs accounting for the majority of censored values).

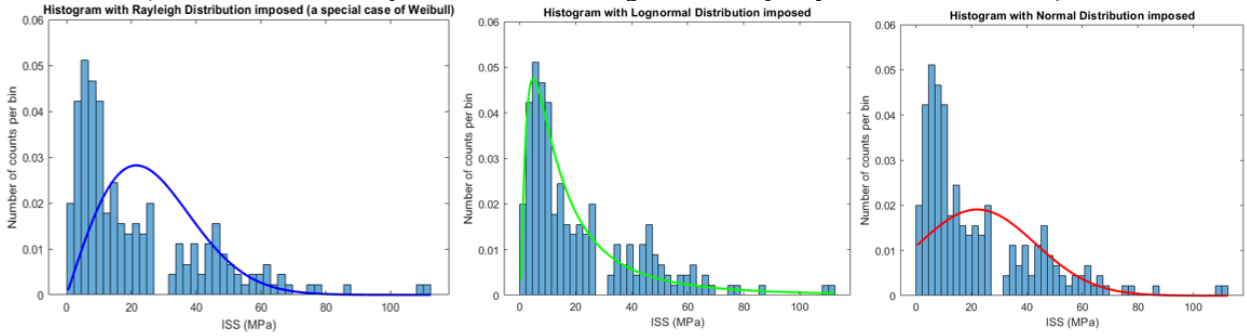


Figure 57: Maximum Likelihood Estimates to fit data to three different distributions

These distributions could be implemented into wider models, looking at how this variability in ISS affects the macro-scale properties of the CMC.

[4] *The author would like to thank Michael Goode for their contribution to this work*

4.8.2 Welch Unequal Variance T-Test

In order to assess which material-dependent variable was significant – a probabilistic approach was adopted. Firstly, Welch's unequal variance t-test was performed using the *'ttest2'* tool in MatLAB (v.2019a). The heteroscedastic technique is more robust than traditional ANOVA and is better for populations of different numbers and variance. The Welch's unequal t-test is also robust enough to use for data with a non-underlying Gaussian distribution, including Weibull-type distributions.

Table 11: Welch's unequal variance t-tests performed on different material-dependent parameters of the fibre push-outs. A higher variance meant there was a higher chance of the two populations being compared having the same means

Comparing:	*Two-sample unequal variance (heteroscedastic)*	*%*
Intratow location in TSA3 Thick BN	0.0011	0.11%
Intratow location in HNS Thin BN	**0.4985**	**49.85%**
Intratow location in HNS Thick BN	0.0000	0.00%
Fibre type (both thick and edge BN)	0.0000	0.00%
Fibres type (both thick and middle BN)	0.0000	0.00%
BN thickness (both HNS and Edge)	0.0000	0.00%
BN thickness (both HNS and middle)	**0.3688**	**36.88%**
Intertow location in TSA3 Thick BN	0.0503	5.03%

From Table 11, it is clear that the intratow location of the fibre push-out is insignificant in affecting the mean ISS measured, when performed either on a sample with a thin interphase (49.85%) and/or when modifying the interphase thickness and testing in the middle of the tow (36.87%). This implies that all other comparisons were significant, as populations were likely to display dissimilar means (resulting in relatively poor t stats).

This was further investigated looking at the P values obtained for the Tyranno type SA3 sample (with a thick BN interphase):

Table 12: P values for a Welch unequal variance t-test on a Tyranno type SA3 fibre with a thick BN

Comparing:	*Intratow location*	*Intertow location*
Mean ISS in [MPa]	46.57	33.05
t Stat	2.73	-2.27
P(T<=t) one-tail	0.00	0.01
t Critical one-tail	1.69	1.66
P(T<=t) two-tail	0.01	0.03
t Critical two-tail	2.03	1.98

In both intratow and intertow cases, the absolute t Stat value was greater than the t Critical two-tail magnitude. All P values (one or two-tailed) were also less than the set alpha = 0.05 – all of which

implied that our initial hypothesis of the populations sharing the same means was void, and therefore that both intertow and intratow location of the fibre push-out can statistically deviate the ISS.

4.8.3 Weibull Statistics

The ISS measured during ex-situ push-outs calculated were also subject to ranking, and fitting to an assumed Weibull distribution. Results in Figure 58 showed that the thicker BN (Figure 58.b and Figure 58.d) resulted in a much lower modulus than the thinner BN (Figure 58.a and Figure 58.c) – regardless of fibre intra-tow location. The higher Weibull modulus for the thin interlayers suggests that the thin BN showed little variation in failure stress – resulting in the possibility of a single strength value being a good descriptor of mechanical performance. Conversely, the low Weibull modulus for the thicker BN interphases suggests the larger volume of BN increases the chance of flaws being clustered inconsistently – resulting in a weaker interphase with a highly variable magnitude.

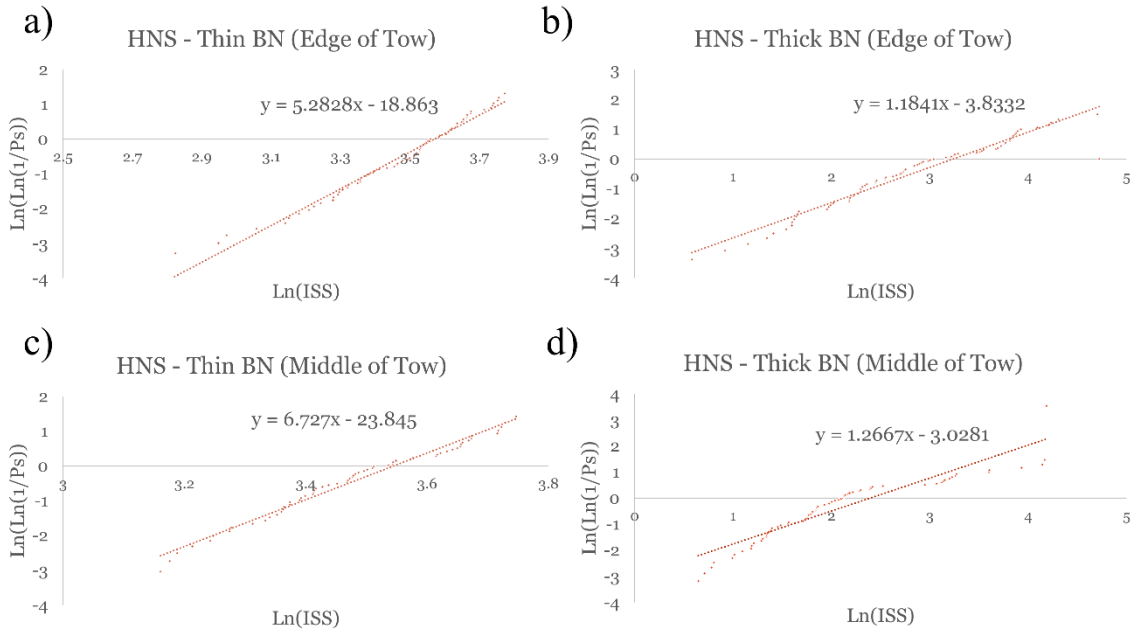


Figure 58: Weibull statistics on several populations of ex-situ push-outs - all on Hi-Nicalon type S fibres – with (a + c) thin BN and (b + d) thick BN.

Ways to improve on the fitting of the data to Weibull distributions include using different ranking methods, such as using median-ranking or MLE-ranking. MLE analyses have indeed superseded linear regression interpolations for calculating Weibull moduli[192]. Linear regression nevertheless remains the more common method, despite being heavily influenced by extreme data points (which could be censored). Examples of authors whom have used Weibull statistics on SiC_f/BN/SiC CMC's include Callaway and Zok, whom have asserted that over 1000 individual tests (or fibre bundle tests) need to be performed for the Weibull modulus to be accurately calculated with respect to fibre area [192]. Callaway also found in parallel that the fibre strength itself did not follow a Weibull distribution, and that the combined Weibull and maximum likelihood estimates methods estimate the SiC fibres Weibull modulus to be in the range of 0.79 – 1.45.

4.8.4 Shear-Lag Model Fittings

Raw load/displacement from fibre push-outs were fitted to various models in order to gain approximate values of the coefficient of friction, debond stress and the residual compressive stresses (both fibre axially and radially) by non-linear regression. One limitation to shear-lag models resides in the fact that very few thermal effects are taken into account, which renders fitting parameters less reliable.

An overview of the models used for data fitting was given below:

I) For the ISS (all from Shear-Lag):

i. Taking into account residual compressive stresses from the matrix component (like residual silicon): Equation 9 from Rebillat[21]
ii. Taking into account residual compressive stresses + Poisson effect from fibre expansion: Lawrence[111]
iii. Taking into account residual compressive stresses + Poisson effect from fibre expansion + mismatch strains between fibre and matrix (in both radial and axial directions) using the modified Hsueh model[40]

II) For other parameters:

i. Coefficient of Friction using the Shetty model[35]
ii. Debond Stress using Equation 9 from Rebillat[21] (equal to ISS in that case) or Kalton[193]
iii. Residual Compressive Stresses from any of the Hsueh models[111, 40]
iv. Interfacial Fracture Energy from Crack Propagation from Kalton[193]

Two sets of results were presented below. The first was a distribution of G_{1C}, obtained from plateau loads during push-outs when fitted to an energy-based model derived by Kalton[193] on Figure 59. The model assumed constant friction, but failed to take into account both Poisson expansion and back-face debonding during fibre push-out. Due to these assumptions the best sample to fit the model to was sample II.e (with Hi-Nicalon type S fibres but an all CVI-SiC matrix with no infiltration) so as to annul the potential effects of residual compressive stresses on the fibre Poisson effect.
The Kalton[193] equation used to calculate G_{IC} from fibre push-out data was the following:

$$G_{1C} = \frac{r}{4E_f}\left\{(\sigma_{max} - \sigma_z) - \frac{2\tau l}{r}\right\}^2 \quad [30]$$

With σ_{max} the maximum normal stress measured, r the fibre radius, σ_z the radial stress fitted from debond stress (Rebillat[21]) and τ the ISS. Equation [30] is only valid assuming constant friction, other expressions are available when taking into account Poisson expansion and back-face debonding.

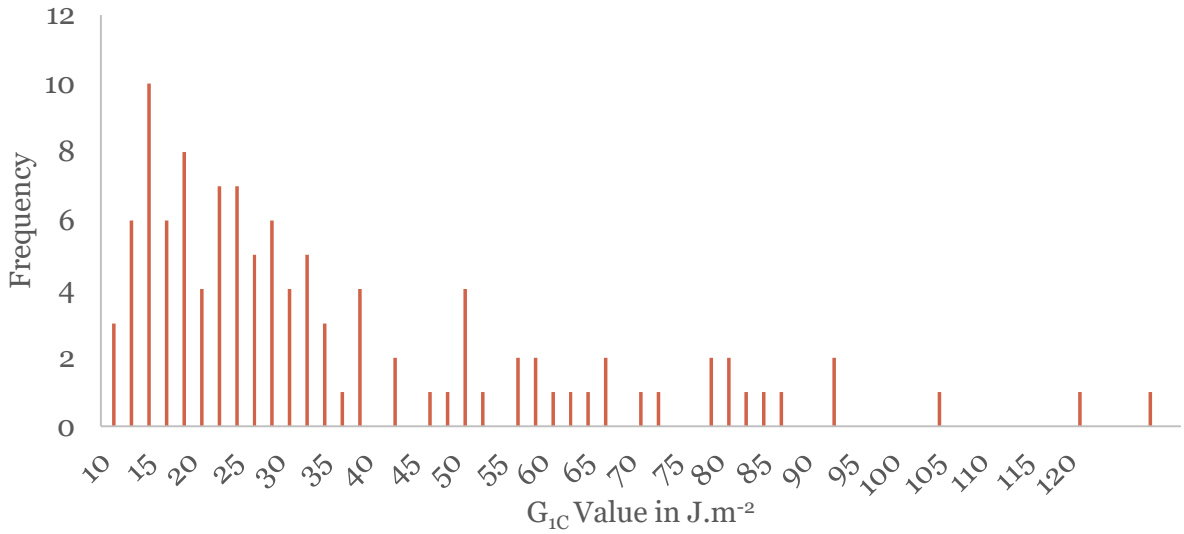


Figure 59: Distribution of G_{1C} values obtained from fitting push-out loads on a Hi-Nicalon type S with an all CVI matrix to the Kalton model.

From Figure 59, a maximum frequency value of G_{1C} of 16 $J.m^{-2}$ could be deduced, however a right-censoring method would increase tailor fit.

The second set of results made a direct comparison of data fitting for a sample which had distinct push-outs on the edge and in the middle of fibre tows - found below on Table 13.

Table 13: Data fitting of fibre push-outs on a Tyranno type SA3 with a thick BN interlayer filtered by intratow variations, showing clear differences in interfacial mechanical properties for fibres on the edge of a tow.

Tyranno type SA3 (with Thick BN)	Unit	Edge of Tow	±	Middle of Tow	±
Coefficient of Friction	-	**0.21**	0.04	**0.19**	0.04
Mean ISS (no fit)	MPa	**50.12**	15	**32.50**	13
Mean ISS (I.i • Rebillat)	MPa	**26.58**	4	**27.10**	2
Mean ISS (I.iii • Lawrence + Hsueh) - includes Poisson's expansion	MPa	**108.74**	57	**59.24**	31
Interfacial Fracture Energy from Crack Propagation (II.iv • Kalton)	$J.m^{-2}$	**159.36**	43	**60.17**	37

It was clear from Table 13 that fibres at tow peripheries displayed superior mechanical properties, even when fitted to shear-lag models. The fitting to the Rebillat model[21] (I.i) reduced the magnitude of the ISS whilst the Hsueh model[40] (I.iii) increased the magnitude when compared to the baseline (unfitted) ISS. This suggests that the taking into account all of the residual stresses, the Poisson effect from fibre expansion and the mismatch strains between the fibre and matrix may result in an

overestimation of the mechanical properties. Therefore, it is recommended that fitting to models be limited, only to scenarios where there is a lack of data points of unfitted ISS from push-out tests.

4.9 Fatigue & Cyclic Testing of the Interphase

The number of cycles which the interphase can withstand before debonding effectively gives an indication as to which type of debonding mechanism dominated (Li Longbiao[194,28] has highlighted four-combinations of cases: whether complete or partial debonding occurred and whether fibre sliding or the interface debonding occurred). Jennifer Pierce from AFRL[195,196,197] showed that this type of experiment can be used to analyse sequential peak loads – both at the micro and macro scale – to better life components. Finally, cyclically testing a fibre in push-in mode – as performed by Kawanishi Ken[17] and Frank Zok at UCSB – can yield a hysteresis loop on the load/displacement response, the value can be used to calculate an initial reference sliding stress for data analysis of monocyclic push-outs. The push-in hysteresis loop can also change in shape depending on whether CMC mechanical response is dominated by a rigid-brittle BN interface or an 'elastic-plastic rupture' response[48].

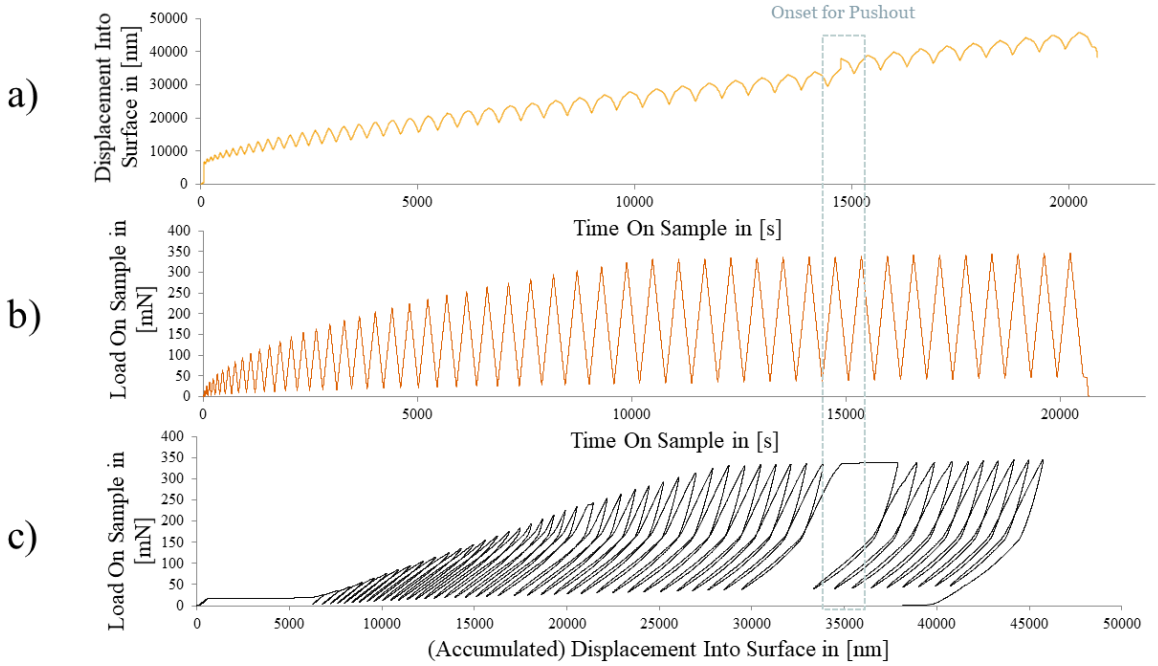


Figure 60: Graphs from a single cyclic push-out test performed on a Hi-Nicalon type S sample with a thick BN showing the onset for full crack propagation and sliding initiation on (a) the displacement as a function of time and (c) load as a function of displacement plots. The event is not detectable on (b) the load as a function of time plot since the instrument is load-controlled

Cyclic push-outs were performed on single Hi-Nicalon type S fibres (coated with a thick BN) loaded up to 500 mN in force increments of 10 mN (total number of cycles: 50). Bottom and peak hold times were 5 s with a total time to load of 10 s (bringing the loading and unloading rates to values of 1 $mN.s^{-1}$), unloading to 90% of maximum load value at the same rate. The onset of full crack propagation (and corresponding sliding initiation) was detected when plotting either displacement as a function of time or plotting load as a function of displacement, as illustrated on Figure 60. Cyclic

push-outs investigated the effect of slow crack propagation in the interphase, and probed the fatigue life of the BN.

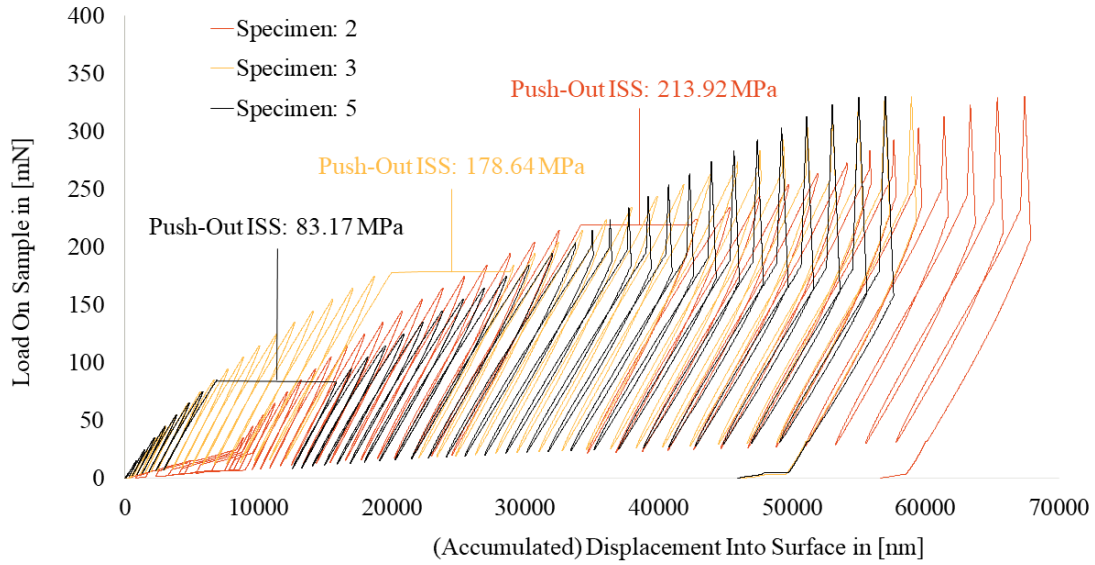


Figure 61: Load displacement curves from three cyclic push-outs performed on a Hi-Nicalon type S with a thick BN sample, showing the exact cycle at which push-out was detected in each case.

The onset of push-out was noted at different cycles in the same sample for three different fibres (Figure 61), this showed that cyclic push-outs depended on a more robust statistical analysis, analogous to monocyclic fibre push-outs. The number of cycles before push-out therefore varied from 7 cycles (specimen 5) to 17 cycles (specimen 3) and 23 cycles (specimen 2). Most hysteresis loops between the unloading of a cycle and the subsequent loading in the next cycle were too small to detect on a load-controlled instrument. The non-normalised load-displacement curves could not be used for our analysis, as those accrued additional damage during each cycle (with increasing maximum exposure stress). Therefore, displacement was first normalised so that loops were more apparent and clear. The displacement loops Δ were used to compute a mean re-seating displacement Δ^* for Specimen 2 alone, which comprises the sum of Hertzian contact and displacement for elastic compression of the fibre before full interface fracture[48]. The Δ^* parameter – alongside corresponding sliding load F_s and critical debonding force F_c (found upon full fracture / push-out) – were used to calculate a debonding toughness Γ and an interfacial sliding stress τ from the cyclic push-out:

$$\Gamma = \left(\frac{F_c}{2\pi}\right)^2 \frac{1}{R^3 E_f} \quad [31]$$

$$\tau = \frac{F_s^2}{4\pi^2 R^3 E_f \Delta^*} \quad [32]$$

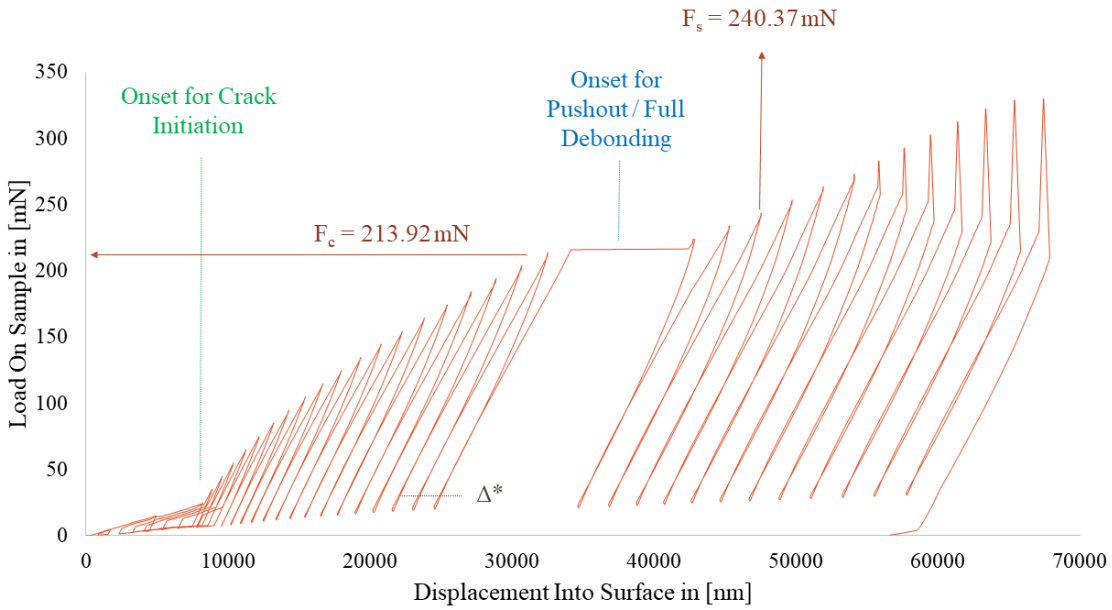


Figure 62: Load displacement response of a single cyclic push-out (specimen 2) on a Hi-Nicalon type S sample with a thick BN showing selection of parameters for use in the Callaway analysis of the cyclic hysteresis, the displacement was accumulated (no normalisation) in this figure.

The change in stiffness at higher loads seen on Figure 60, Figure 61 and Figure 62 could be due to the conical tip making contact with the neighbouring CVI SiC or matrix at deeper penetrations. Analysis from Figure 62 showed that an interfacial sliding stress τ of 17.1 MPa and a debonding toughness Γ of 13.3 $J.m^{-2}$ for specimen 2 were estimated through the Callaway[48] analysis. Comparing this cyclic ISS to our monotonic ISS measured during push-outs (24.1 MPa on outside tows and 11.9 MPa in tow middle) on the same sample, the magnitudes are analogous – suggesting the cracks propagated in a controlled manner during both monotonic and cyclic loading. The debonding toughness is more elevated than the debonding toughness found in Callaway's[48] work (3 – 10 $J.m^{-2}$) however this may be due to their use of dissimilar Tyranno ZMI fibres (which are not to high-temperature standard, have lower tensile modulus and higher elongation at break than Hi-Nicalon type S).

4.10 Doping the Interphase

The effect of lightly doping the BN interphase with Silicon and its effect on the mechanical properties was investigated by means of fibre push-out tests. Doped samples comprised of Hi-Nicalon type S fibres with interphase thicknesses of 449 ± 23 µm (comparable to a medium BN undoped sample). The cumulative frequency of ISS in the sample with the highest amount of doping (#1244) was contrasted to those of un-doped samples with the same fibres in Figure 63 below:

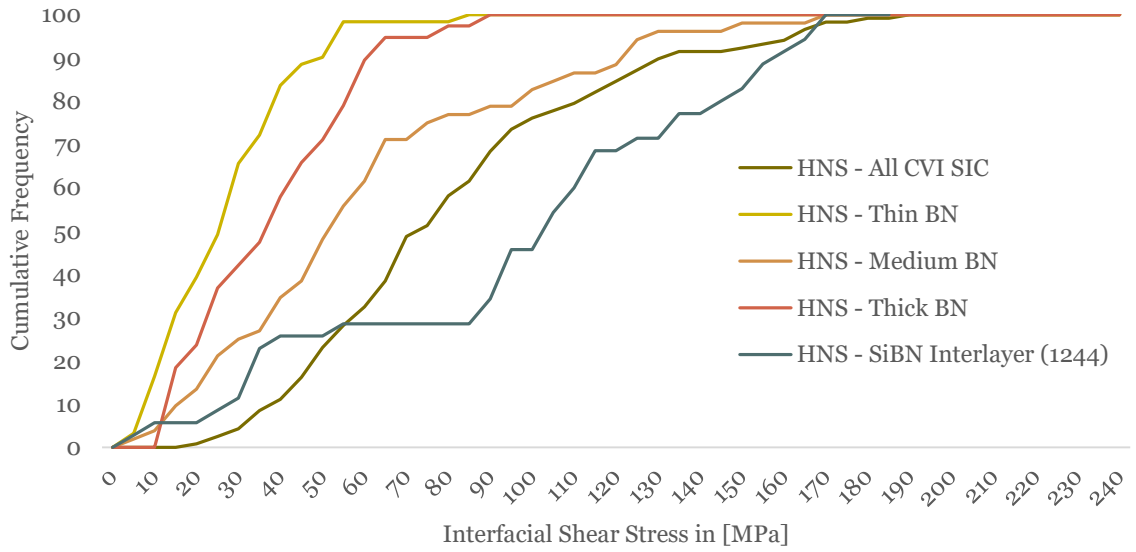


Figure 63: Cumulative frequencies of all samples with Hi-Nicalon type S fibres showing stronger ISS in interlayers when doped with Si

Figure 63 showed that when comparing doped and undoped samples of same fibre type, the doped samples statistically exhibited higher interfacial shear stresses (with a cumulative distribution function on the higher end of the ISS magnitude scale), irrespective of interphase thickness. Post-fractography analysis on Figure 64 revealed push-outs, push-ins and push-backs on doped-interphase samples were clean, with little to no interlayer delamination or fibre breakage.

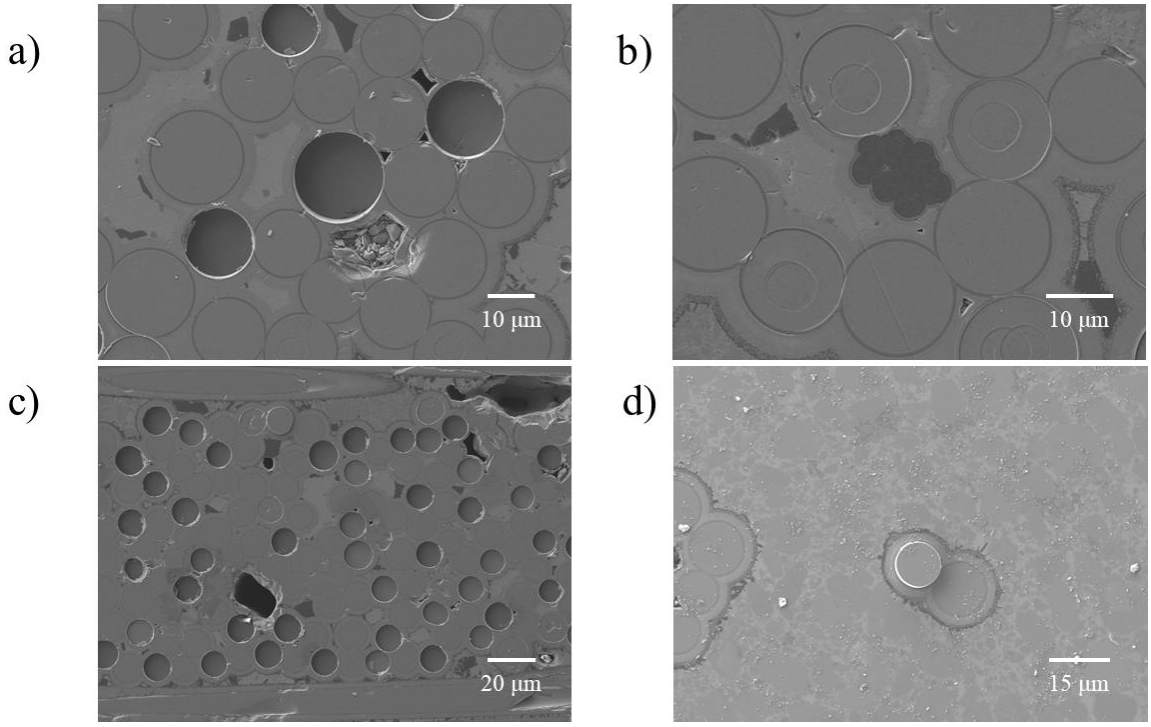


Figure 64: SEM micrographs of SiBN interphase samples with Hi-Nicalon type S fibres showing (a) fibre push-outs (b) fibre push-ins with a bundle of carbonised fibre in the centre, (c) a tow subject to push-out testing and (d) a fibre push-back.

Completely carbonised fibres were found on some SiBN samples, which were otherwise not present in undoped samples (Figure 64.b). An EDX analysis was performed on one of those fibres – alongside neighbouring Hi-Nicalon S fibres – in Figure 65, where Si was also detected in the doped interlayer. The carbonised fibres (Figure 64.b) seemed to have had traces of boron (Figure 65.b), making them susceptible to be B_4C in nature.

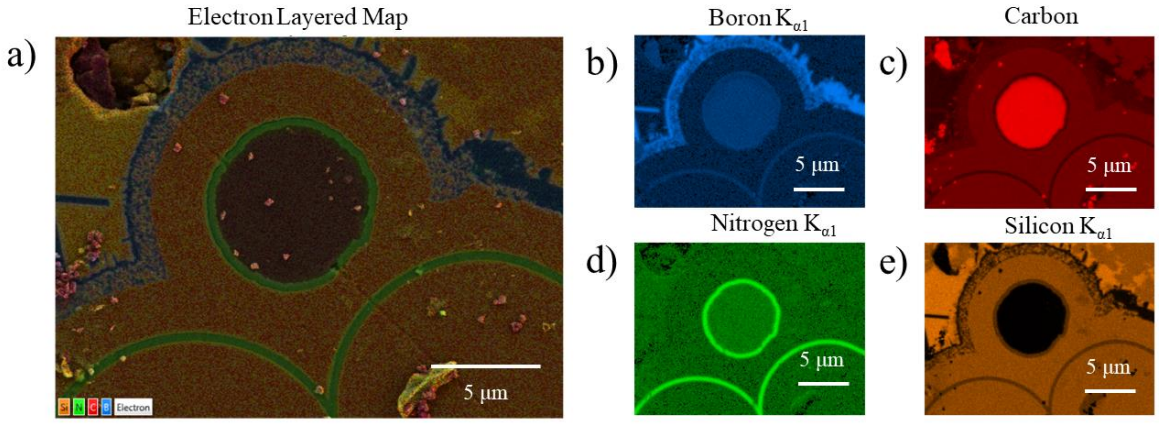


Figure 65: SEM EDX analysis on the doped interlayer highlighting a carbonised fibre and the presence of Si inside the BN interphase

SEM EDX point analysis was also performed on the SiBN interlayer #1244 close to the interface of the carbonised fibre, to get a better understanding of the phases present.

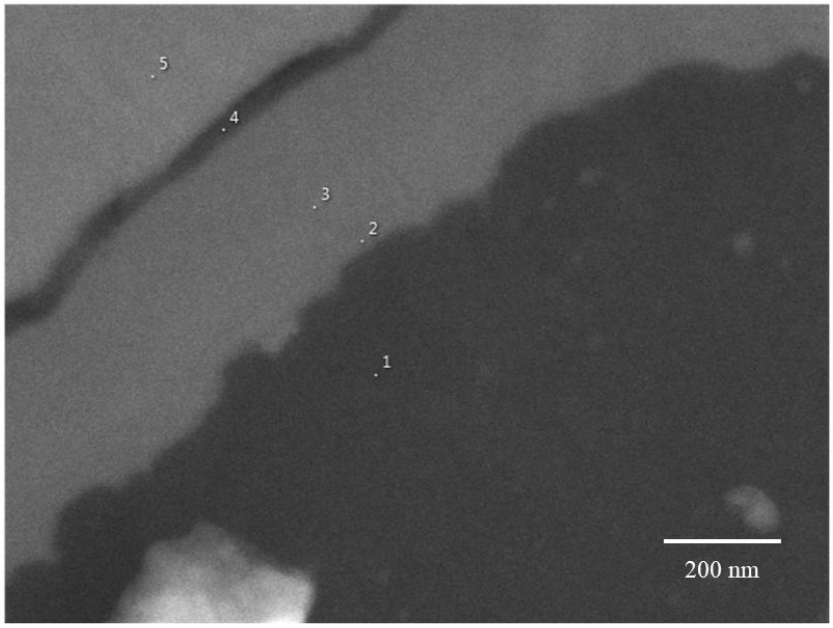


Figure 66: Point SEM EDX analyses on the interface of the carbonised fibre found on the SiBN interlayers

Points 1 to 5 on Figure 66 corresponded to the following: 1) a carbon fibre (87.1% C with 7.0% N), 2) a faint boron carbide interface right outside the fibre (36.6% B, 26.9% C, 19.1% N), 3) the 1:4 Si-doped BN interphase (38.6% B, 22.2% N, 19.8% Si), 4) the Si migration layer (42.3% B, 21.4% C) and 5) the CVI SiC matrix (53.6% Si, 39.8% C).

Additional point EDX analyses were performed on all interphases to yield more quantitative results with regards to chemistry. EDX analysis was performed using the Aztec software at an 8.5 mm working distance, using a 400 pA probe size, 5 keV accelerating voltage, 10 keV energy range, 10 µs pixel dwell time and 2048 channels (for the map).

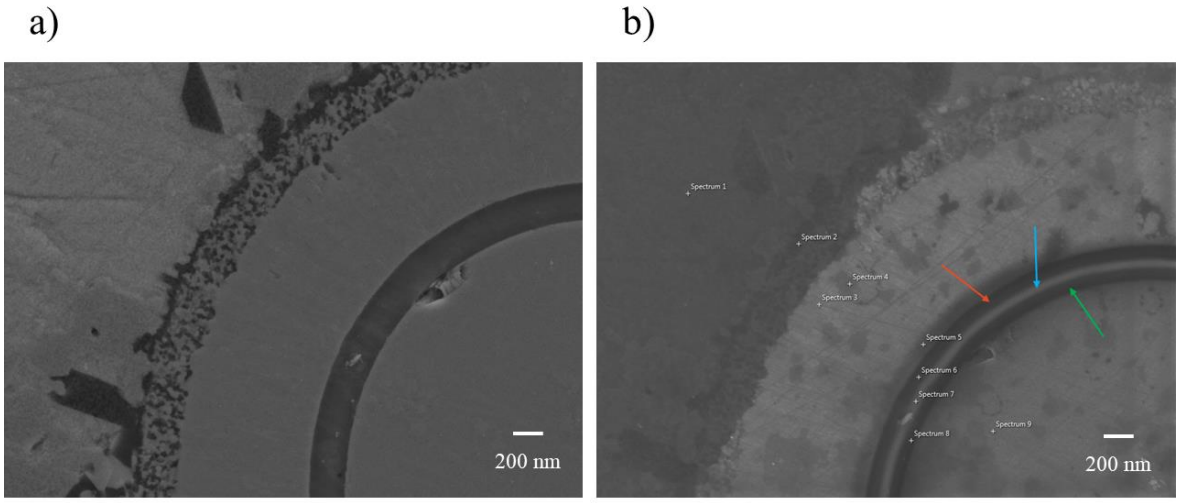


Figure 67: (a) Secondary electron image prior to point EDX analysis of a Hi-Nicalon type S sample with a Si-doped interphase (#1243), and (b) a back-scattered electron image showing the location of all points taken per sample with additional arrows pointing to three sub-layers within the BN interphase

Figure 67.b showed that upon initial SEM inspection in backscattered contrast, the doped BN interphase split into three distinct sub-layers: one close to the CVI SiC layer coating the fibre (red arrow), one 'middle' phase where the BN is more predominant (blue arrow) and a third layer close to the fibre (green arrow). This multi-layer system could have stemmed from either processing or from sample preparation. The results from the point EDX analyses were summarized in Table 14, where all three sub-layers inside the BN interphase were considered. The high levels of dopant found during this analysis led to estimation of the interaction volume, in the event that the latter was smaller than interphase dimension. Equation [33] from basic Monte Carlo simulations was used to estimate the radius of the electron range hemisphere R_{ER} on surface contact

$$R_{ER} = \frac{0.0276 \times A}{Z^{0.89} \times \rho} E_0^{1.67} \qquad [33]$$

Where A is the atomic weight in $g.mol^{-1}$, Z is the atomic number, ρ is the density in $g.cm^{-3}$ and E_0 is the beam energy in keV. Taking an atomic weight of 10.811 g.mol-1, a density of 2.37 g.cm-3 for pure Boron and an accelerating voltage of 5 keV yields an estimate interaction hemisphere radius of 442 nm. This suggests that there was a high probability of the detector collecting data from much further away (the CVI SiC) from the 400 pA probe diameter, and that repeat measurements would be more adequate to measuring doping levels.

Table 14: Point EDX analysis on all doped interphases. All numbers expressed as wt%. Percent Si-doping of the middle of the BN interlayer are in bold font

Sample	**SiBN 1243**					**SiBN 1244**					**SiBN 1245**					**SiBN 031011**				
Element	Si	C	B	N	O	Si	C	B	N	O	Si	C	B	N	O	Si	C	B	N	O
MI Matrix (SiC)	64.1	35.2	-	-	-	64.8	34.5	-	-	-	63.8	35.7	-	-	-	64.3	34.4	-	-	-
MI Matrix (Si)	92.4	6.3	-	-	1.2	94.1	5.3	-	-	-	95.2	4.1	-	-	0.7	95.7	3.8	-	-	-
Silicon Migration	16.2	19.6	62.2	-	1.4	50.5	25.9	22.9	-	-	33.9	26.2	39.3	-	-	7.3	18.1	73.3	0.4	0.7
CVI SiC	63.9	35.7	-	-	-	58.9	38.3	-	-	1.6	62.7	36.8	-	-	-	64.4	35.0	-	-	-
Interphase (Between CVI & BN)	62.3	34.2	1.5	1.5	-	60.9	38.7	-	-	-	-	-	-	-	-	62.7	33.9	0.9	1.9	0.6
Interlayer (BN – close to CVI) - Red	13.3	3.6	44.5	34.9	1.1	-	-	-	-	-	-	-	-	-	-	31.7	8.4	29.3	27.5	1.6
Interlayer (BN - Centre) - Blue	**11.9**	2.6	45.3	36.9	1.0	**30.0**	31.6	31.5	6.9	-	**26.7**	8.2	30.9	31.7	-	**28.7**	8.0	32.6	27.1	2.1
Interlayer (BN – close to fibre) - Green	15.3	6.4	42.2	32.0	2.0	-	-	-	-	-	-	-	-	-	-	-	-	-	-	-
Hi-Nicalon type S Fibre (SiC)	61.1	37.2	0.6	-	1.1	57.4	31.3	3.4	6.9	1.0	61.0	37.7	0.5	-	0.9	60.9	37.9	-	-	1.3

From findings in Table 14, the effect of doping percentage on the micromechanical performance was investigated. Repeating over 100 push-outs on each of the Si-doped interlayers in both the tow peripheries and centres, it was found (on Figure 68) that all samples obeyed the same observations found on non-doped samples. Fibres pushed on the edge of tow (dashed lines) were statistically harder to push out, regardless of Si doping levels. Fractography analysis showed clean push-outs with very few events of Si-doped BN delamination (Figure 64.a), however most samples displayed an increased presence of carbonized fibre bundles (Figure 64.b). The amount of doping (from 11.9% to 30.0%, as reported in Table 14) did not seem to significantly affect the mechanical properties. Indeed, all doped samples displayed statistically similar push-out behaviours (cumulative frequency curves were close to one another in Figure 68), although the lowest doped sample (SiBN 1243 at 11.9%) displayed the highest stresses when comparing both intra-tow and inter-tow variations. From a more theoretical perspective, one could suggest that a higher crystallinity in the interphase is achieved by doping, resulting in an increased chance of cracks arresting and propagating between the BN crystallites, and thus higher stresses are required to fully propagate the cracks.

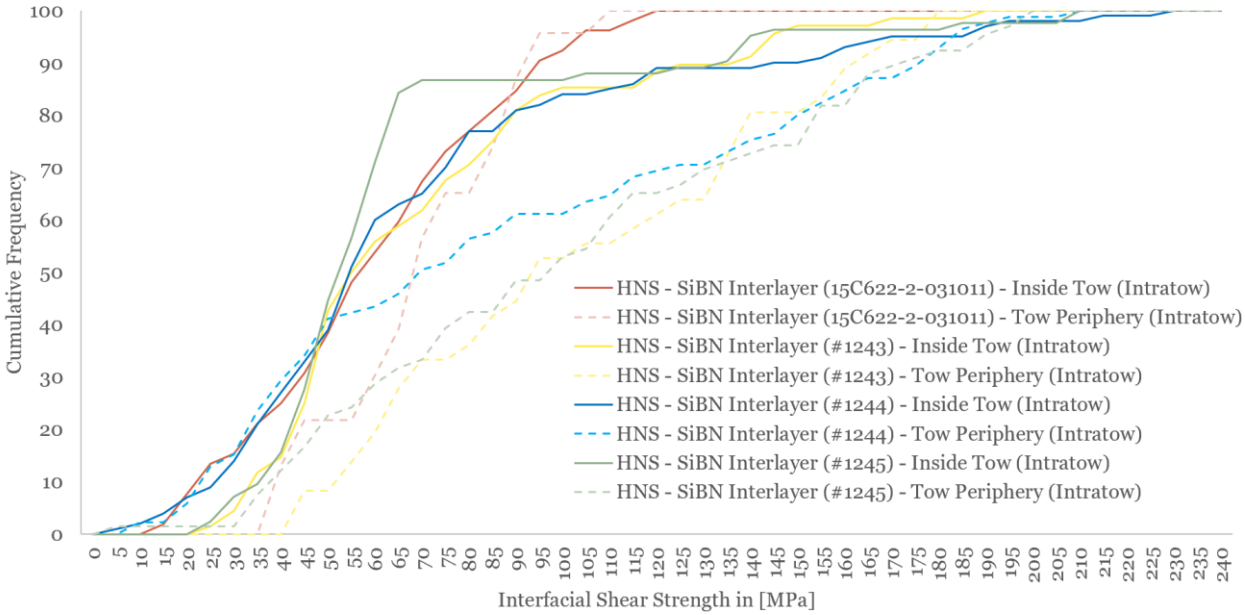


Figure 68: CDF's of intratow push-out studies in all Si-doped interphases.

SEM EDX analysis was performed on a push-out cross-section by trench milling. It was found that the failure was adhesive with inside debonding (crack propagating between the fibre and the interphase), since the nitrogen signal on the outer rim in Figure 69.d was strongly present.

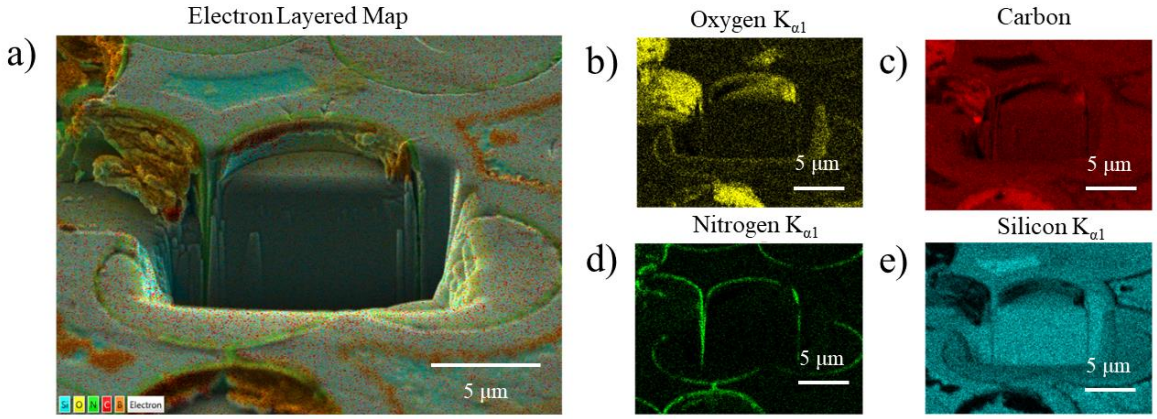


Figure 69: SEM EDX analysis on a siliconised interlayer after push-out and trench milling.

Additionally, a TEM lamella liftout (Figure 70) was thinned to look at the difference between undoped and doped interphases at a more atomic scale.

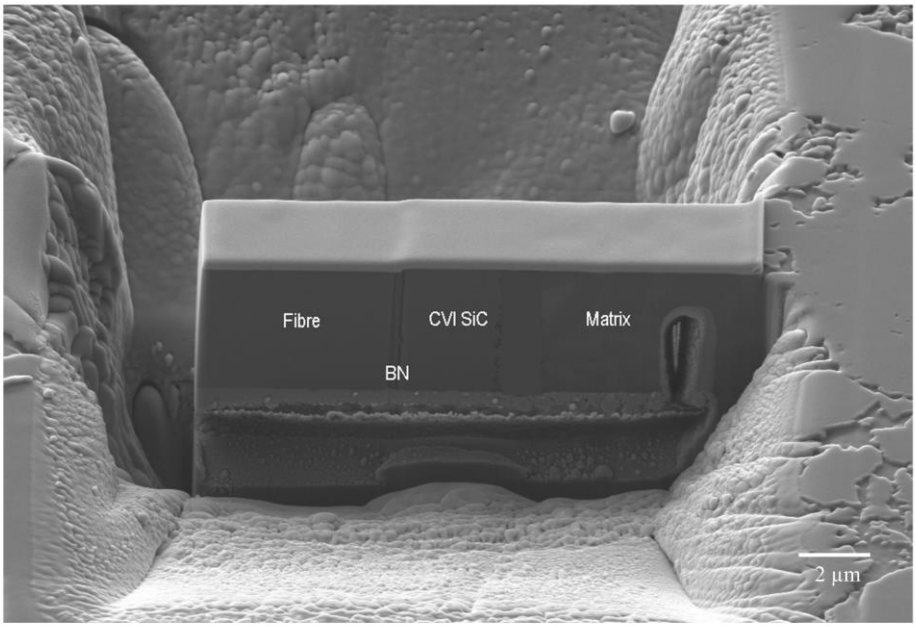


Figure 70: TEM Lamella before liftout on a SiBN Interlayer (#15C622-2-031011) sample showing all composite components

TEM results[5] from the lamella in Figure 70 were included in Figure 71. It can be observed from such Figure that the Si-doped BN interphase is crystalline, with turbostratic crystallites imbedded in an amorphous sea in Figure 71.b. No quantitative measurement of the degree of crystallinity was made, but the micrograph suggest the density of crystallites compared to amorphous material sits at 50%. This hypothesis is supported by the equal brightness of the amorphous rings and the diffuse turbostratic rings in the BN diffraction signal in Figure 71.d. Conversely, the diffraction signals of the SiC fibre and CVI SiC show clear crystallinity with well-defined rings on the one hand (Figure 71.c and strong orientation of the columnar grains (diffuse spots, Figure 71.e) on the other hand.

[5] Data acquisition performed by Dr. Lisa Töller-Nordstrom

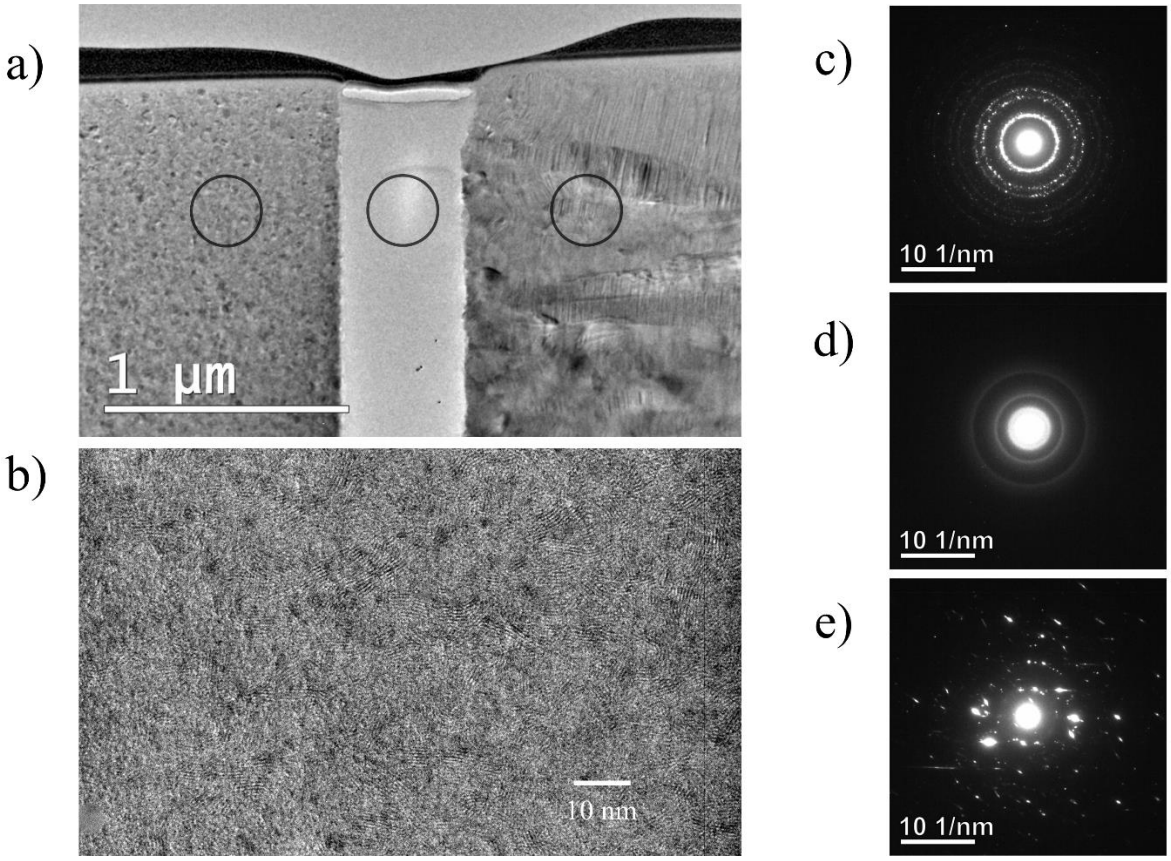


Figure 71: TEM micrographs showing a) the SiC fibre, BN interphase and CVI SiC spot sizes, b) the turbostratic BN, and diffraction patterns of c) the SiC fibre, d) the BN interphase and e) the CVI SiC

4.11 Chapter Summary

Following presentation of technique- and system- dependent variables on the measurements of SiC_f/SiC composites tribological properties, the material-dependent variables of the CMC's and their constituents were investigated. Indeed, the toughness and desired micromechanical behaviour of the composites can be achieved through tailoring of interphase properties, best probed through various micro-mechanical tests including the fibre push-out. A parametric study was therefore needed to give insights on the variables affecting the mechanical performance.

Firstly, an overview of the different sample types was given. This was followed by initial qualitative characterisation and a more detailed analysis of constituent geometries. In a second instance, the variability in measurements of mechanical properties was investigated by means of t-tests with respect to tow location at weave-architecture level (inter-tow), where it was found that despite some overlap in the cumulative frequency of ISS populations in inter-tow studies, both cases (intratow or intertow) had statistically different populations. The larger difference in cumulative frequencies in the intra-tow case led to more work on the variables affecting testing fibres within a single tow.

Thirdly, variations of the mechanical performance within a tow (intra-tow) were scrutinised. This included several sub-variables such as (i) the edge or central location of the fibre within the tow (ii) the nature of fibre type, (iii) the thickness of the BN interphase and (iv) the number of direct neighbours in contact with the target fibre. When looking at (ii) fibre type, Tyranno type SA3 fibres displayed higher interfacial shear strengths on statistical average when compared to Hi-Nicalon type S fibres, confirming the dependence of ISS on fibre roughness (and suggesting limited effects of fibre failure on micromechanical tests). (iii) A thinner interlayer resulted in higher shear stresses due to the higher possiblity of the interlayer being damaged along the fibre or accentuating the effect of fibre nano-asperities from surface roughness (in thicker interphases, this effect is reduced). Thinner BN interlayers seemed to result in more matrix compressive stresses acting to slow down crack propagation and fibre sliding. Combining (i) and (iii), the thickness of the BN interlayer had a significant effect on the distribution of the ISS with respect to fibre location within a tow. For thinner BN interlayers, the location of the fibre within the tow (at its periphery or in the middle) had no effect on the cumulative frequency of the Interfacial Shear Strength found. Conversely for thicker BN interlayers, fibres pushed at the periphery of tows were statistically harder to push out when compared to fibres pushed in the middle of tows. When contrasting fibre location alone (inside a tow and between tows), evidence showed that models taking into account fibre environment should place more emphasis on intra-tows variations rather than inter-tows variations. Finally following cascade push-outs tests, a correlation was found between the interfacial shear strength measured on a fibre with respect to the number of neighbours pushed out around the central fibre. This correlation could be fitted and/or used for modelling purposes.

Once the interfacial shear stresses and the general stress / strain response of the fibre push-out were investigated, other micromechanical techniques including the fibre push-in and the fibre push-back were used to extract more parameters such as the coefficient of friction. It was found that push-ins underestimated the ISS when compared to push-outs, but were adequate for performing post-mortem AFM-type analysis. Conversely, stresses found during push-backs on samples with thinner interphases were more elevated than thicker interphases, with a 65.2% decrease in frictional load (i.e. a load retention ratio of 2.87) when pushing a fibre back after push-out. In both push-in and push-back cases, the rougher Tyranno type SA3 fibre surfaces were detected, and this was reflected in the results.

From the large amount of data obtained, the ISS results were subjected to statistical, stochastic approaches including fittings to obtain maximum likelihood estimates, Welch unequal variance T-tests, and Shear-lag models available in literature. Only two cases of comparing populations were found to have high t-stats and therefore concluded to have little to no effect on affecting the mechanical performance: (i) the intratow location of the fibre push-out when performed on a sample with a thin interphase and (ii) modifying the interphase thickness whilst testing in the middle of the tow. Fitting to shear-lag models resulted in under or over-estimation of the ISS, but yielded an estimate of plastic energy release rate G_{1C} (16 $J.m^{-2}$ for the Hi-Nicalon type S with an all CVI SiC matrix case).

Moving past monotonic loading and failure, the cyclic nature of testing the interphase was investigated with increasing-load step cyclic push-outs. The results gave insights on the amount of energy absorbed during testing and enabled an estimate of the load hysteresis (recovered) between cycles. Estimates of initial sliding stress and debonding toughness Γ (13.3 $J.m^{-2}$) were computed, however the number of cycles to 'failure' and the loads measured were inconsistent even if testing the same material with next to no deviation (i.e. all tests performed on tow periphery, on the same tow, with the same method within the same experiment).

Finally, the last variable tested was the chemical effect of doping the BN interphase with silicon. It was found that doped interphase increased interfacial stresses when compared to un-doped samples. Fibres pushed on the edge of tows were found to be statistically harder to push out, regardless of Si doping level. For SiC_f/SiC with BN interlayers, the most prominent problem to date remains pest oxidation - excessive degradation at intermediate temperatures (600 – 800 ºC) in humid engine exhaust environments. One solution proposed by literature to improve the oxidative performance includes doping the interphase with silicon. The effects of humidity and elevated temperature on the composites were investigated in the following Chapter (5).

Chapter 5 • Degradation

5.1 Abstract

SiC_f/BN/SiC Ceramic-Matrix Composites are candidate materials for aero-engines, but their interphase stability after potential low-temperature water-vapour exposures during flight cycles is not well known. The examination of these composites exposed for 50, 250 and 500 hours at low temperature (65 °C) and 95% relative humidity was therefore performed, in order to understand if resulting oxidation products affected the mechanical properties at the micro-scale. Tests were additionally performed at elevated temperature up to 650°C in vacuum, to look at the effect of intermediate temperature exposure on the shear interphase properties. After confirmation of oxidation by EDX and Raman spectroscopy studies, the composites were subject to fibre push-out tests to compare pristine from degraded composites. It was found that whilst the sample exposed for 50 hours had little change from pristine, the samples exposed for 250 and 500 hours had a clear decrease in interfacial shear strengths measured. Parallel studies also revealed that whilst damage was strongly localised, the diffusion of water within the composite was not fully complete at exposure times between 50 and 250 hours. The permeability of the CMC was shown to be affected at longer exposure times, where differences in mechanical performances – both between and within tows – were noted.

5.2 Introduction

The principal issue faced by SiC-based composites lies in its degradation in corrosive environments and its current inadequacy in adopting performance life models[4]. Any specified environment (temperature, stress applied and time exposed) might induce deleterious and non-reversible damage at the micro-mechanical scale. In an engine environment, the water can stem from all following sources: (i) the inlet air humidity (particularly elevated in more tropical countries), (ii) the aircraft washing cycles, (iii) the hydrocarbon fuel exhaust, (iv) rain, (v) the combustor hot gas steam, but also (vi) during storage, taxi and ground-based humid environments - totalling over 10 vol% of water in high-saturation cases[53].

5.2.1 SiC Oxidation

Silicon carbide and silicon adopt similar behaviour when oxidising[70]. SiC_f/SiC composites have excellent high-temperature oxidation resistance in dry air (owing to the slow growth rate of SiO_2 in dry air) however SiC_f/SiC composites are subject to silica volatilisation in steam environments (low p_{O_2}). When moisture is present in the exhaust, $Si(OH)_4$ becomes the principal volatile species created[199] at intermediate conditions - a layer of silica is produced in temperatures as low as 600 °C[2] or 650 °C[200], which strengthens the fibre/matrix bond, thus preventing crack deflection and antithetically embrittling the overall composite. Oxidation of bulk SiC in steam has resulted in the formation of cristobalite and significant porosity[73] potentially from reaction by-products including CO and H_2. The presence of water vapour was shown to only increase cristobalite crystallisation rate, but not nucleation rate[201].

5.2.2 Fibre Oxidation

The fibres themselves oxidise – with the concentration of impurity, the presence of alkali elements and the oxidation atmosphere all controlling the oxidation rate[70]. The linear-parabolic kinetics of the oxidation are best described by the Deal & Grove model[202] (general SiC) and by the Parthasarathy model[203] (SiC_f/SiC) for Hi-Nicalon & Hi-Nicalon type S fibres, which postulate that SiC fibre oxidation is linear at first when the oxide layer is thin. The reaction is subsequently parabolic (with a rate constant commensurate with the partial pressures of dioxygen and water) once oxygen permeation through the oxide film becomes the limiting factor.

SiC corrosion rates are similar for the fibre and the matrix[55] but are further decupled when water is introduced in the environment (at partial pressures of around 20 kPa) due to the weakening of Si-O bonds[205]. Oxidation of the fibres results in a lowering of their complex permittivity due to SiC grain growth[45] and a clear oxidation activation energy has yet to be found[206]. The activation energy however differs depending on the environment conditions: higher when dry (108 $kJ.mole^{-1}$), lower when wet (60 $kJ.mole^{-1}$) in the parabolic regime[202].

Fibre and matrix oxidation usually lead to surface recession (the SiC surfaces oxidises to silica and/or releases gaseous by-products) in relatively localised surface damage (where both interphase and mechanical hysteresis response are unaffected). However, if the interlayer is attacked, oxidation can reach the 'bulk' interior of the composite – usually at intermediate temperatures (500ºC - 1000ºC).

5.2.3 BN Interphase Oxidation

Even with fibre and matrix oxidations, CMC embrittling is mainly due to fibre/matrix interlayer degradation in steam environments. Indeed, due to their elastic-like loading behaviour – and the corresponding debonding of matrix and fibres – CMC's are subject to oxygen diffusion inside formed cracks[52]. Despite silica being thermodynamically more stable than boria under most regimes[55] and even if BN interlayers constitute as little as 5 vol% of the composites[175], they are nevertheless subject to 'pest' oxidation whereby oxidation nurtures environmentally-assisted cracking at intermediate temperatures (500ºC – 800 °C) and high stresses (Over 100 MPa)[5,6]. Pest corrosion is a major ongoing problem to be solved for BN interlayers. It was identified to potentially be due to a carbon sub-layer left from the sizing steps underneath the BN, which affected the oxidation resistance of the latter[61]. Indeed, the carbon layer burned off and opened up new airways for oxygen to reach the BN – however this claim is only supported by observational evidence[17] and research into the phenomenon continues. Fracture surfaces of pest-corroded material resemble a frame with brittle facets on the outskirts and regular fibre pull-outs inside the core, as reported by Ogbuji[61].

BN coatings are preferred to pyC coatings, due to the formation of a less volatile component (borosilicate glass) in 48 hours under 1400ºC[210]. Thermodynamically, BN oxidises at higher oxygen activities when compared to SiC or residual carbon[162]. Oxidation-damage depth is also correlated to the modulus of the fibres (a lower modulus induces greater depth) and the interfacial shear strength (a lower shear strength also induces greater depth)[4].

The oxidation (in air or low water-vapour content at high temperatures from 1000 to 1450ºC) of the hex-BN interlayer in SiC_f/SiC composites is described by Sheldon et al.[214] in 4 stages:

1. $SiC_{(s)} + O_{2_{(g)}} \rightarrow SiO_{2_{(s)}} + C_{(s)}$
2. $C_{(s)} + {}^{1}/_{2}\, O_{2_{(g)}} \rightarrow CO_{(g)}$
3. $2BN_{(s)} + \frac{3}{2} O_{2_{(g)}} \rightarrow B_2O_{3_{(l)}} + N_{2_{(g)}}$ (favourable at temperatures above 450ºC)
4. $SiC_{(s)} + \frac{3}{2} O_{2_{(g)}} \rightarrow SiO_{2_{(s)}} + CO_{(g)}$
   (favourable at temperatures above 900ºC)

Each stage is successive, and therefore boron only oxidises once SiC and excess C is consumed. The formation of silica is favoured over boria initially, partially due to the difference in oxygen potential between SiC and BN[214] (this oxygen segregation in the silica was also observed by Dugne[47]). Low vapour content prevents boria from volatilising instantly[90]. At higher water contents, some sources[160] suggest SiC oxidation and B_2O_3 volatilisation happen at the same time. The three most stable thermodynamic species created from the reaction of water with the interlayer are HBO_2, H_3BO_3 and $H_3B_3O_6$, the last of which is the heaviest and most detectable[178]. Opila[55] & Jacobson[215] agreed that the dominating reaction in the presence of water is the following:

$$B_2O_{3_{(l)}} + H_2O_{(g)} \rightarrow 2HBO_{2_{(g)}}$$

The initial formation of borosilicate glass (with 5-20 mol% boria[216]) enhances SiC oxidation since diffusivity of oxygen and water in borosilicate augments[217] (boron diffuses through the glass network and oxygen also diffuses more rapidly), however the vitreous boria glass enables the composite to self-heal (as the glass formation seals pores and cracks) at elevated temperatures[93, 218]. The silica and boria glass can form an oxidation diffusion barrier to limit oxygen and water ingress to the middle of the material. A SiO_2-B_2O_3 eutectic is however reached at 372ºC which causes formation of borosilicate glass and faster oxygen diffusion[176] – Boria dissolves all SiC (fibre and CVI coatings) to form borosilicate liquid, which is in turn hydrolysed to release $B(OH)_3$ gas.

The reactivity to oxidation is directly correlated to the synthesis (and therefore crystalline quality amongst other parameters) of the hex-BN film[53]. The more crystalline the layer, the higher the temperature of operation of the composite. Hex-BN interlayers on SiC_f/SiC are usually processed at intermediate temperatures greater than 1000ºC: processing at slightly lower temperatures would hinder the quality of the film[161] due to the formation of ammonium borate hydrates and nanocrystalline BN at the SiC densification stage[221]. Conversely, higher deposition temperatures might induce early onset of fibre oxidation during the coating process. Therefore, a balance must be struck[222]. Five-hour long heat treatments at 1200ºC in argon have been applied to further increase film quality and moisture resistance[30], due to the creation of a carbon-rich interlayer (from the decomposition of fibre sizing agents), which improves load transfer[89]. Wing in his dissertation adds a new dimension to the problem – clearly stating that even under the same processing conditions, BN interlayers display dissimilar oxidisation rates and properties[90].

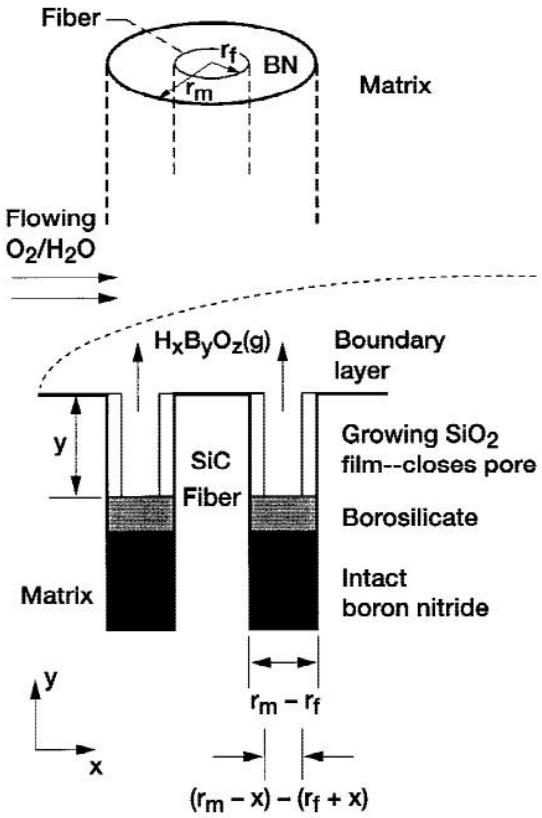


Figure 72: Modelling BN recession & volatilisation in a composite, figure from Jacobson et al.[160]

On a bigger scale, oxidation of monolithic BN was shown to be dependent on porosity (due to faster pore diffusion rates) and crystallographic orientation[160,215] , however these parameters might have a less significant effect when dimensions are reduced to films and fibre coatings.

Oxidation is accentuated in humid environments, where water (strongest oxidant for Si[175]) pressures greater than 0.003 atm are sufficient to trigger boria volatilisation under gaseous forms (mostly HBO_2, but also with traces of H_3BO_3 and $H_3B_3O_6$)[53]. Boria indeed pertains high chemical activity in a borosilicate liquid – thus making it susceptible to volatilisation[223]. Boron volatilisation creates a Boron-free silica layer[160], mirroring carbon interface pyrolysis in SiC_f/pyC/SiC composites[160]. If at room temperature, ambient moisture can trigger boria to dissolve to boric acid[53].

Whilst the mechanisms above investigate high and intermediate temperature exposure, data acquisition of low temperature, relatively high humidity exposure is needed to model full flight cycles. Very few publications look at this regime, bar Gaválda-Diaz et al. [222] whom have found that low water vapour pressures lead to an oxoborinic acid (BHO_2) protection-layer formation whilst high water vapour pressures may lead to increased formation of aqueous boric acid ($B(OH)_3$) – leading to reaction kinetics being controlled by BO_2^- and $B(OH)_3$ convection. Additionally, Matsuda[221] has found that the reaction of CVD-BN plates with moisture resulted in the formation of ammonium borate hydrates.

This effect has important consequences on the fatigue life of SiC_f/SiC composites, reducing the life to a few thousand cycles[225] and creating an oxide layer made of borosilicate glass - analysable by

fractography[26] (appearing as brittle-like flat surfaces). Fatigue is affected at temperatures of 600ºC but loses impact at temperatures above 800ºC. Even with pyrolytic carbon interphases, the cristobalite oxide layer created spalls and cracks after one cooling cycle to room temperature[73], severely reducing composite cyclic life. Furthermore, oxidation requires matrix cracks for it to have a significant effect on the bulk mechanical properties of the composite[226] (cracks drive oxidants to the fibre core). Elsewise, oxidation does not damage surfaces deeper than 300µm[175] (although cristobalite has been shown to form at high temperature and high water-pressure exposures[175]). Matrix cracks saturate at densities of 2 mm^{-1} and are usually accompanied by plastic behaviour and acoustic wave emissions[227]. Care should be taken when analysing and distinguishing between accumulated damaged depth (from machining/grinding/polishing) and recession depth (from oxidation). The thickness of the coatings also varies inside a fibre tow – with coating thickness usually reaching its maximum at tow edges[90] and therefore being more vulnerable to ends-on-oxidation. The interlayer recession can be measured from the push-in technique and can give an estimate of the effective compliance of the fibre after the BN oxidises[128]

5.3 Surface Degradation

Due to the significant effects of water vapour, the Hi-Nicalon samples (I) were degraded at 65°C in 95% relative humidity for a) 500 hours, b) 250 hours and c) 50 hours to investigate the oxidation of the amorphous BN and its deleterious effects on the mechanical properties of the composite at the micro scale. These conditions were chosen so as to mimic the most common of water vapour sources (i - inlet air humidity, iii - hydrocarbon fuel exhaust & vi - during storage, taxi and ground-based humid environments respectively) as listed at the end of Section 5.2.1.

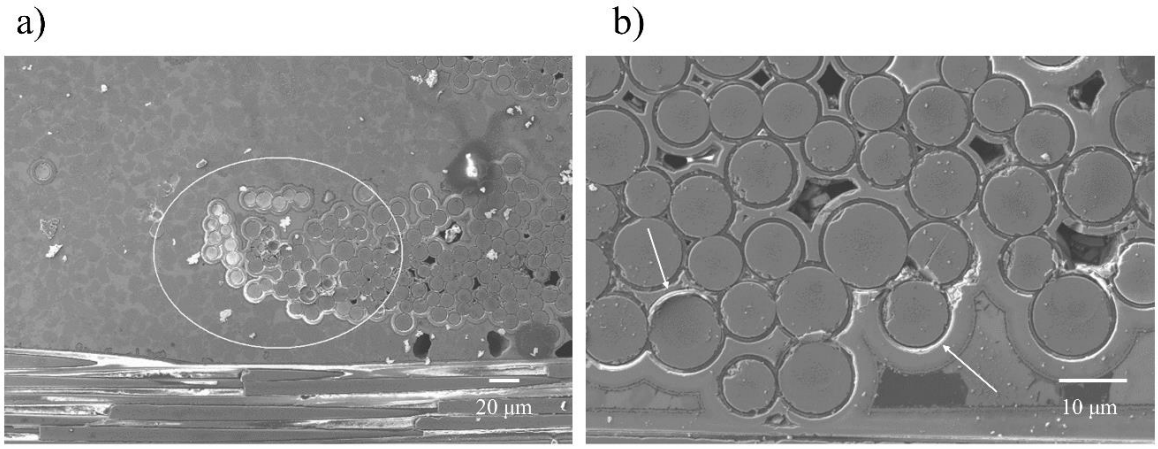


Figure 73: SEM micrographs of a Tyranno type SA3 sample with a medium BN imaged a year after initial polishing, showing degradation of the BN into secondary glassy phases – (a) circled and (b) pointed by arrows – which charge more and appear brighter

The first signs of degradation were present on non-degraded samples stored for a year after polishing, where non-conductive boria and silica phases charge more at higher probe currents under the SEM (as seen in Figure 73).

Raman spectroscopy was performed with an inVia™ confocal Raman microscope (Renishaw, UK) on both the pristine and the longest degraded Hi-Nicalon samples (exposed for 500 hours) at laser spot sizes of 17 µm and wavelength of 798 nm (resulting in a lateral resolution of 300 nm, and depth resolution of less than a micron), to see if any clear difference could be observed. Green laser light

(≈ 514.n nm) could not be used as SiC is transparent under that light[229]. A total of 6 scans were performed in total, comparing three different types of location (matrix, normal fibre tow and transverse fibre tow) highlighted in circles 1 (red), 2 (blue) and 3 (green) respectively on Figure 74.

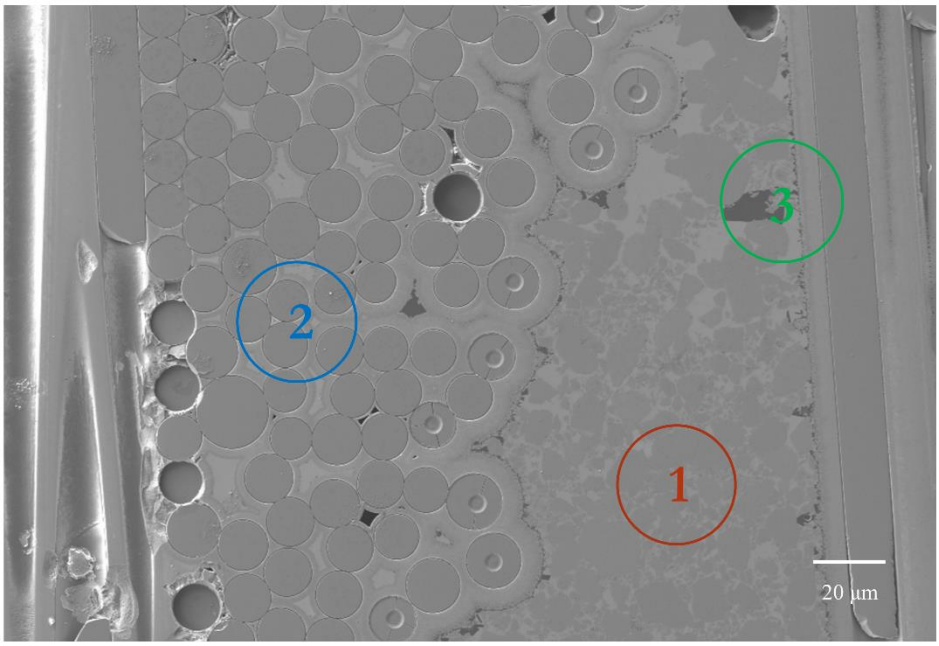


Figure 74: SEM micrograph on a Hi-Nicalon fibre sample exposed for 500 hours at 65°C and 95% relative humidity, showing the three locations and indicative laser probe size for Raman spectroscopy studies

Four standout peaks in the signals were identified (numbered 1-4 on Figure 75) corresponding to the 1) Si-Si triply degenerate peak at 520.5 cm^{-1}, 2) the Si-C transverse optical phonon (TO mode) at 796 cm^{-1}, 3) the Si-C longitudinal optical phonon (LO mode) at 972 cm^{-1} and 4) the wide amorphous B-N band coating fluorescence at Raman shifts exceeding 1250 cm^{-1}. All signals in Figure 75 show on the first hand that the Si-Si bonds and the B-N fluorescence overshadow the Si-C signals in their amplitude and peak width.

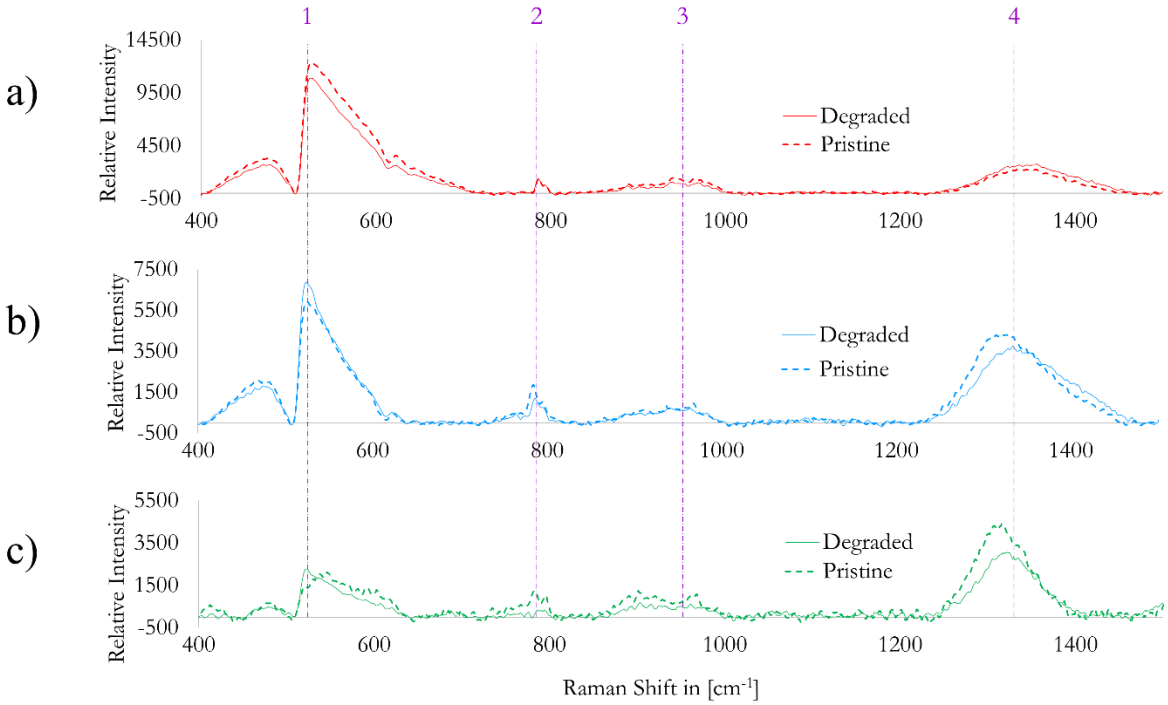


Figure 75: Raman signals comparing the pristine (dashed) and degraded (continuous) states in (a) the melt-infiltrated matrix, (b) a normal fibre tow, (c) a transverse fibre tow comprising a B_4C particle

Figure 75 showed that the Raman scattering efficiency of the longitudinal and transverse SiC optical phonons was much lower than the Si-Si bonds found in the residual Si in the matrix or the amorphous BN fluorescence. A significant peak shift was found on the Si-Si band at 520.5 cm^{-1} previously highlighted by Wing[90,75]. For the silicon peak, the hydrostatic component alone from the stress tensor can be estimated, due to its constant triple degeneracy even with applied stress[229]. The Si-Si intensity shift from degradation is largest in the matrix (case a) – and was previously found by Knauf et al. to reach (compressive) 300 MPa in magnitude in the matrix and 180 MPa within a tow, on the same material[229]. The Si-Si peak shift in Figure 75.a is equal to $\Delta\Omega$ = 525.21 – 526.44 = -1.23 cm^{-1} which can be converted to the hydrostatic component of the stress tensor $\Delta\sigma_h$ via equation [33][229]:

$$\Delta\sigma_h = \Delta\omega \times C \qquad [33]$$

Where C is equal to -0.177 GPa.cm^{-1} for silicon[230] and -0.283 GPa.cm^{-1} for the 6H SiC polytype[231]. Using this equation, we can estimate our degradation-induced stress to be $\Delta\sigma_h$ = - 1.23 x - 0.177 = 218 MPa, of comparable magnitude than that found by Knauf. Knauf also found that the Si stresses are lessened if the Si is present within a tow (as opposed to being in the melt-infiltrated matrix), which is our case here as the peak shift in Figure 75.b is negligible – confirming that the Si majorly induced residual stresses in the matrix.

The stress from peak shift at the Si-C TO peak at 789 cm^{-1} is harder to estimate, as the absorption coefficient of SiC makes the laser light penetrate deeply into the material, inducing a volumetric response (which cannot simply be calculated using surface-level analysis)[229].

Lastly, the BN fluorescence signal analysis is complicated by FR (Fano Resonance), a signature asymmetric profile shape induced by any groups IIIA and VA silicon dopants[229], which must be

removed prior to stress analysis. The BN signal at 1250 cm^{-1} nevertheless had a significant decrease in its intensity for the degraded sample, corresponding to a change in chemistry at the microscopic level. The degradation (continuous lines) has had an effect in both shifting the normal amorphous peak of B-N at the higher end of the spectrum (4) and decreasing the intensity when compared to the pristine (dashed lines) state of the composite in cases b and c.

5.4 Mechanical Performance

The fibre push-out ISS cumulative distribution functions for exposure times of 50, 250 & 500 hours were plotted alongside cumulative distribution functions of the ISS measured on pristine samples – all with Hi-Nicalon fibres – in Figure 76. Each distribution corresponds to 100 successful push-out tests.

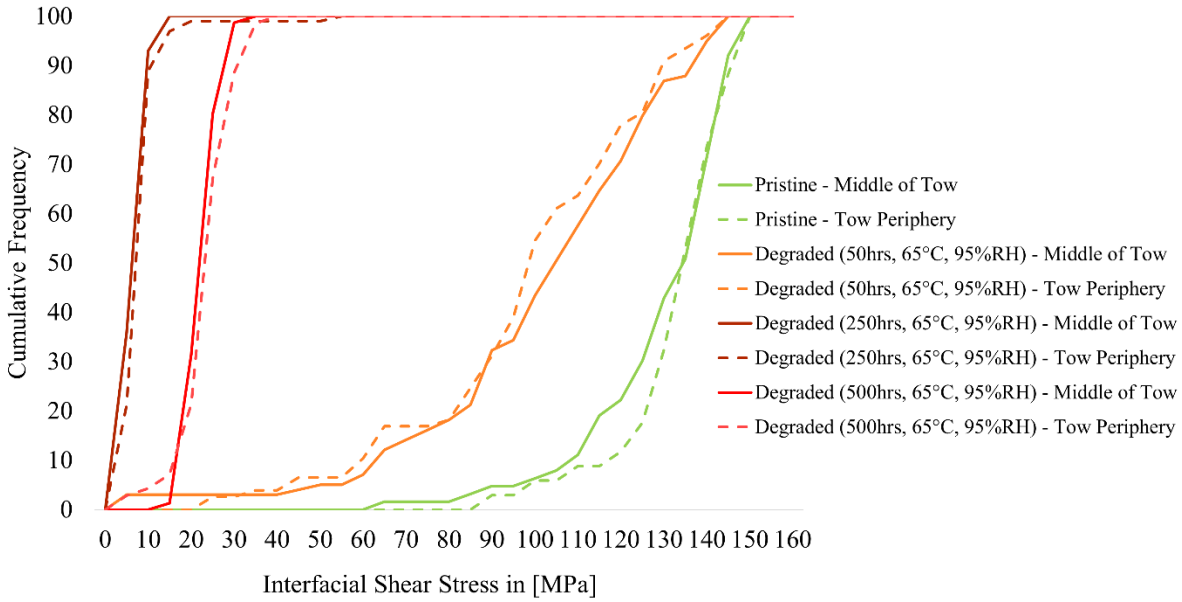


Figure 76: Cumulative Distribution Functions of the ISS obtained on four samples made of Hi-Nicalon exposed at 65°C and 95% relative humidity for varying exposure times

Figure 76 indicated that the widest gap (and decrease) in mechanical performance was observed for samples exposed at times greater than 250 hours. Samples degraded for 50 hours showed some decrease in mechanical performance, but showed similar ISS distribution profiles to those of pristine samples. The sample degraded for 250 hours however showed weaker interphases when compared to the one exposed for 500 hours. This inconsistency in conclusions might be due to the location of the push-outs at weave-level – where exposures might have not reached the centre of the samples (despite macro-cuts made in similar areas: with a first off-cut from the bulk sample – right on Figure 77 – and then push-outs performed in a middle tow).

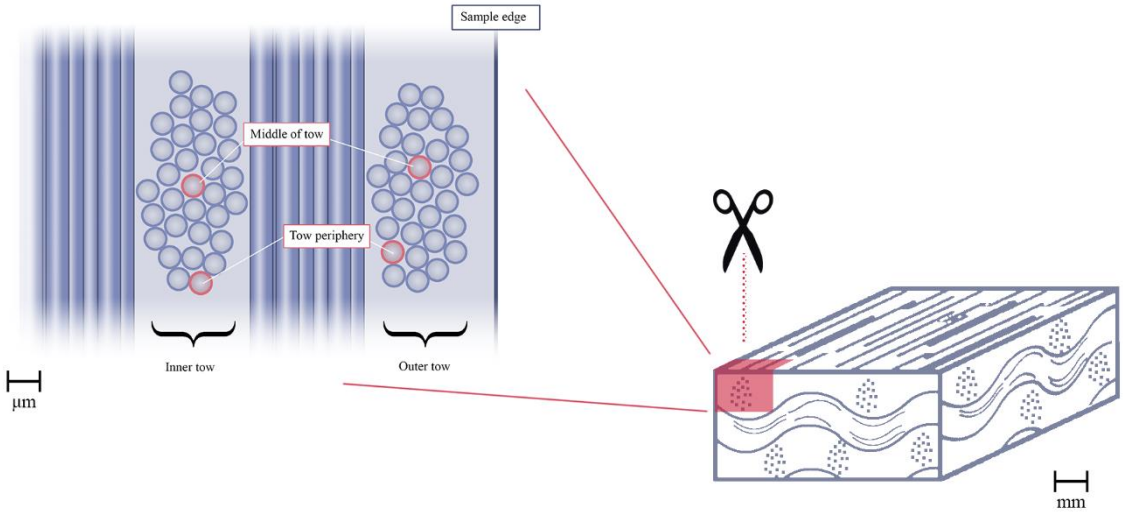


Figure 77: Illustration showing location of the cuts made at the macro-level before micro-mechanical testing

When looking at the micrographs after push-outs, the micromechanical tests on the sample degraded at 250 hours (Figure 78) showed clean push-through with no to little BN surface recession and/or resurfacing for both tow edge (left) and tow middle (right).

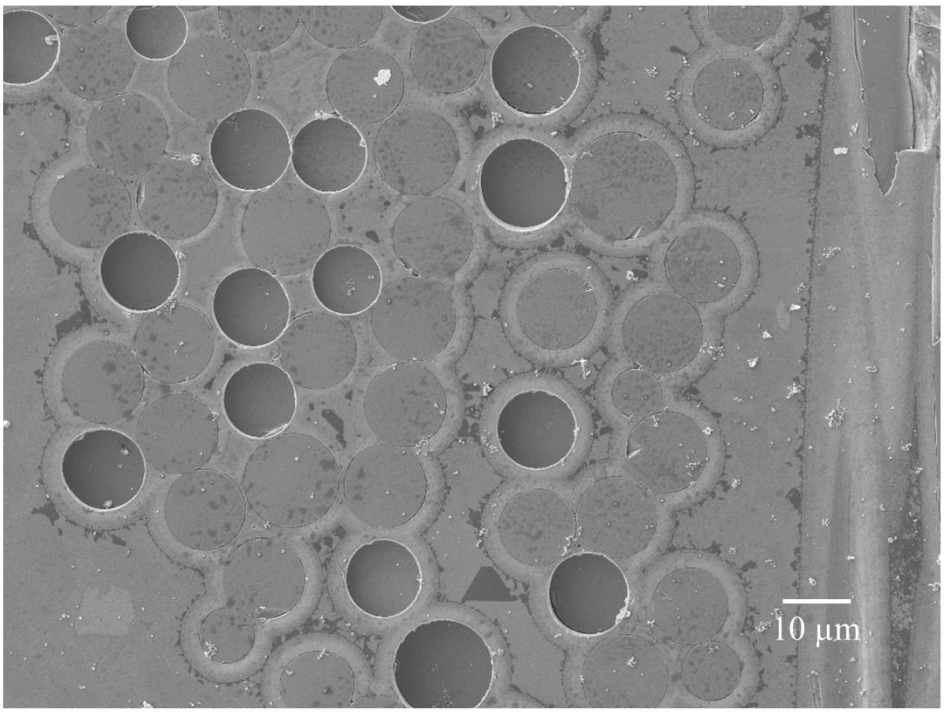


Figure 78: SEM micrograph from a Hi-Nicalon fibre sample exposed to 95% relative humidity and 65°C for 250 hours, showing fibres after push-out testing

The microscopy of all samples after testing was further investigated in the series of micrographs found in Figure 79.

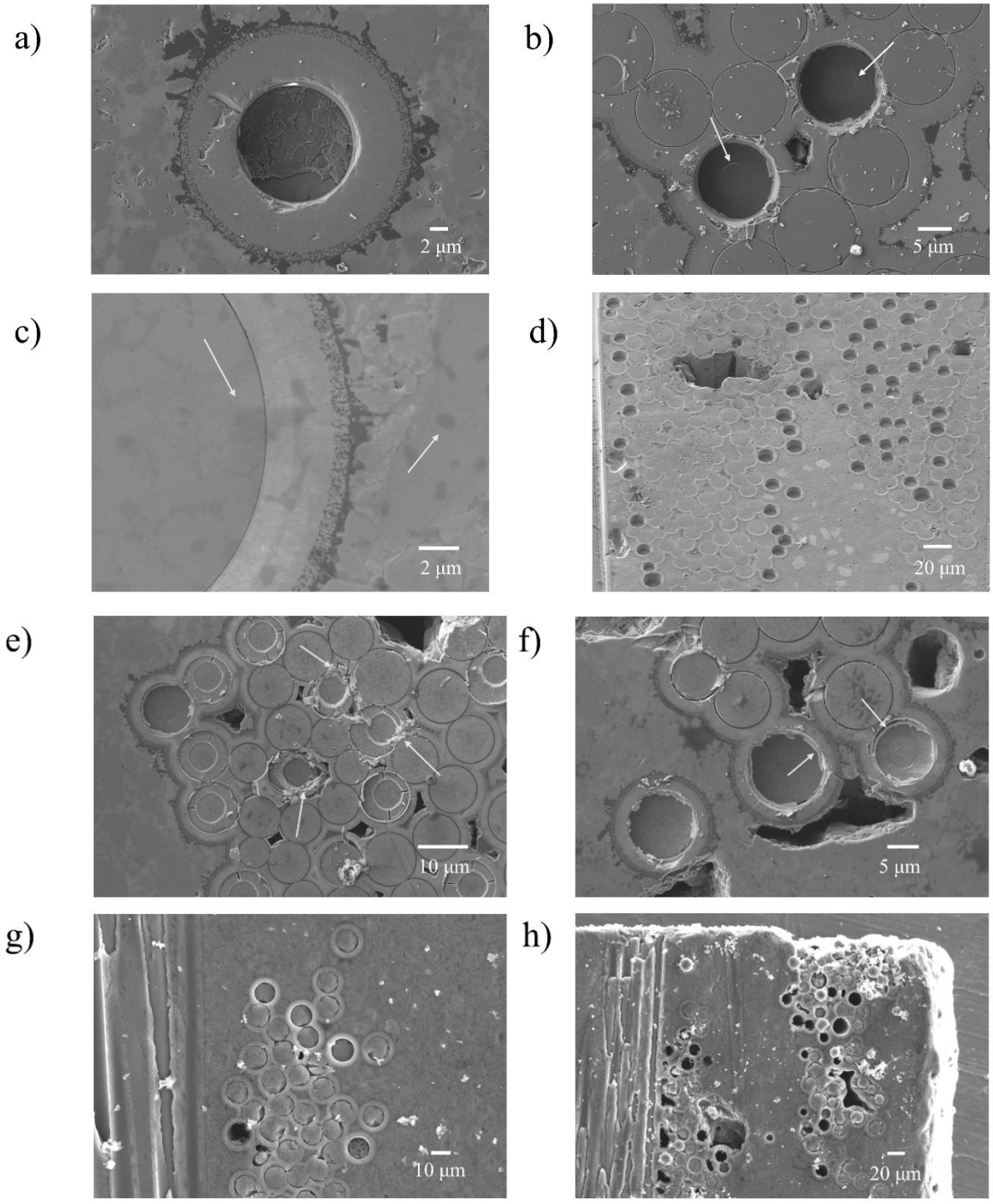


Figure 79: SEM micrographs from (push-out) post-mortem analyses on Hi-Nicalon fibre samples exposed to 95% relative humidity and 65°C for (a + b) 50, (c + d) 250 and (e – h) 500 hours respectively. (a) Push-out surface of a rough fibre in the middle of the matrix, (b) slip bands (white arrows) from tip slip on fibre surface, (c) hydro-damage on un-tested sample surface (samples were cleaned prior to testing), (d) fibre push-outs on tow periphery (left) and tow middle (right), (e) embrittlement (white arrows) of fibre surfaces from fibre push-ins, (f) dual-BN delamination (white arrows) of the degraded boria, (g) push-outs on an edge-tow subjected to higher environmental damage showing pre-mature signs of charging, (h) 'self' fibre push-outs on an untested edge-tow on the sample with the longest degradation time.

When comparing samples exposed for various times, samples exposed for 50 hours showed rough fibre surfaces (Figure 79.a) and 'plastic' slip bands (Figure 79.b) from tip contact on the fibre surface, suggesting the initial contact (between the tip and fibre) before testing was not flat/aligned with the flat-punch. Samples exposed for 250 hours showed the least damage as illustrated in both Figure 78 and Figure 79.d, where push-outs on both tow periphery and tow middle were undistinguishable in behaviour; however the presence of darker spots on the surface (Figure 79.c) despite sample cleaning were signs of early onset of the sample's degradation.

When increasing the exposure time to 500 hours, damage was more prominent. In fibre push-ins, fibre cracking showed clear signs of embrittlement (Figure 79.e) whilst successful push-outs showed delamination (i.e. a combination of inside and outside debonding) of the boria layer (Figure 79.f). On an outer tow in the same sample (cuts illustrated in Figure 77), the surface ingress of oxygen was more prominent, as sample surface was charging (Figure 79.g) and some 'self' fibre push-outs (Figure 79.g) were observed at the very edge of the sample, where degradation was most significant. The sample degraded at 500 hours also showed oxidised CVI SiC interlayers as well as gaps between fibres and silica by-products, showing the BN interphases had volatilised.

5.5 Intertow & Intratow Variations

The sample degraded with the longest exposure time was tested in ex-situ push-outs with 100 performed at edge and 100 in the middle of a tow (200 additional push-outs were performed on another tow at the edge of the sample, where the degradation was more significant to investigate intertow variations). Tests performed for inter-tow variations (Figure 80 in blue) were taken at random with respect to intra-tow location (i.e. tests include both fibres at tow periphery and in the middle of the tow).

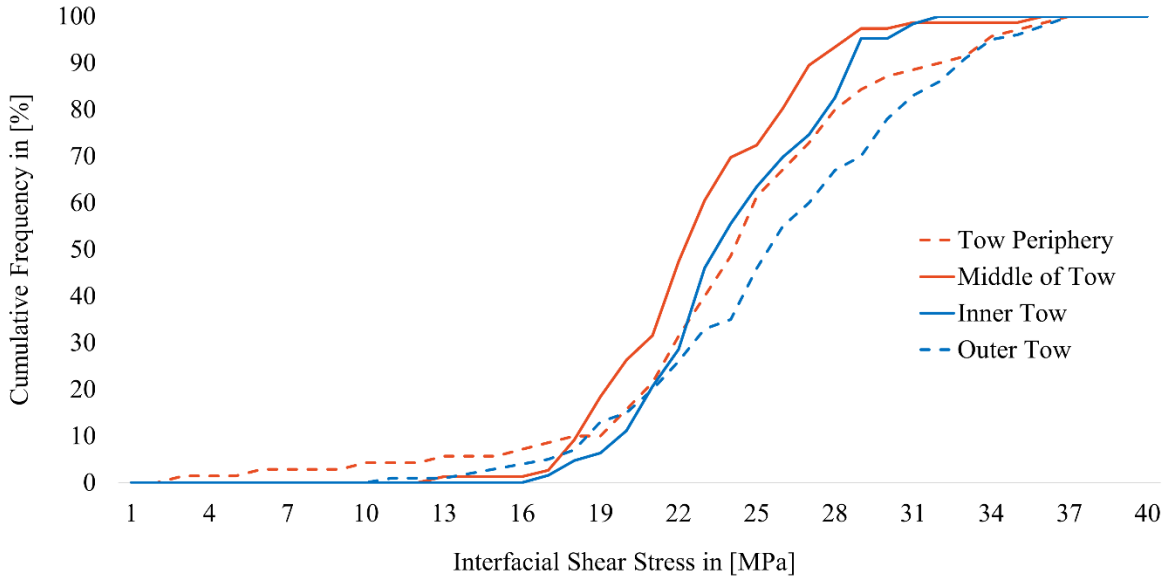


Figure 80: CDF's of the ISS measured during fibre push-outs on the Hi-Nicalon sample degraded for 500 hours at 65°C and 95% relative humidity showing little intratow (red) or intertow (blue) variation

Results from Figure 80 show that the degradation of the BN interphase at these conditions 'normalised' the average values of ISS obtained, resulting in very little intratow and intertow variations. This is also highlighted in Table 9 where means, medians and quartiles of all 4 populations were found to be similar.

Table 15: Mean & median values for the ISS measured on the Hi-Nicalon sample degraded for 500 hours at 65°C and 95% relative humidity when investigating intra-tow (red) and inter-tow (blue) variations during fibre push-outs. All values in MPa

Location	Tow Periphery	Tow Middle	Inner Tow	Outer Tow
Mean	**22.3**	**21.6**	**22.9**	**24.6**
Standard Deviation	*± 6.0*	*± 3.7*	*± 3.5*	*± 5.3*
Median	**23.1**	**21.2**	**22.7**	**24.2**
1st Quartile	*20.28*	*18.86*	*20.71*	*20.83*
3rd Quartile	*26.27*	*24.51*	*26.02*	*28.80*

Due to similarities in magnitudes of the ISS found in Table 9, the significance between differences in intratow (red) and intertow (blue) variations on Figure 80 was further tested by means of the Welch unequal variance t-test, results from which are included in Table 11.

Table 16: Welch's unequal variance t-tests performed on the Hi-Nicalon sample degraded for 500 hours at 65°C and 95% relative humidity contrasting the intertow and intratow ISS populations of the fibre push-outs. A higher variance meant there was a higher chance of the two populations being compared having the same means

Comparing:	*Two-sample unequal variance (heteroscedastic)*	*%*
Intertow location in degraded samples	0.1083	10.83%
Intratow location in degraded samples	0.0220	2.20%

Table 11 showed that the probabilities for both intertow or intratow populations having the same mean were low, therefore both parameters were investigated by means of cascade push-outs in Sections 0 and 0.

5.6 Intratow Variations

In a first instance, cascade push-outs within a single tow were reproduced on the sample exposed for 500 hours at 95% relative humidity and 65°C. The results from which are presented in Figure 81.

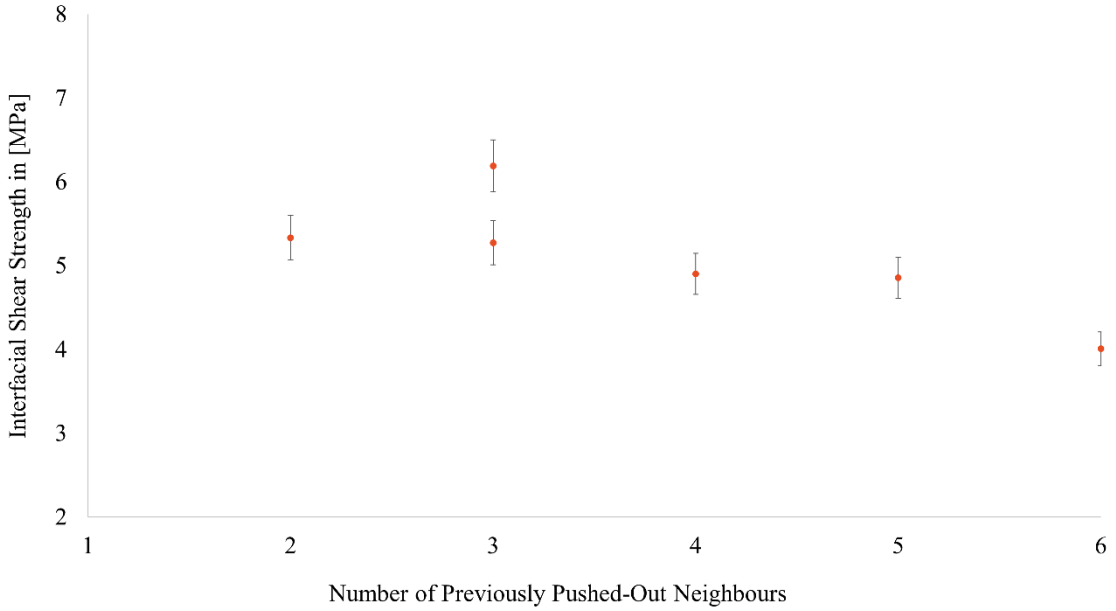


Figure 81: ISS as a function of number of direct fibre neighbours from cascade push-outs on a Hi-Nicalon sample exposed for 500 hours

Figure 81 suggests the same trend found in previous cascade push-outs on different fibre types and exposure conditions from Chapter 4 and previous studies[232,140] remained the same: the number of direct fibre neighbours in contact with the primary fibre affected the strength of the BN interphase in inverse proportionality. However, it is worthwhile noting that cascade push-outs assumed fibre contact (or lack thereof) only at the fibre surface visible to the optical microscope before indentation, thereby failing to take into account sub-surface damage or contact(s) between fibres.

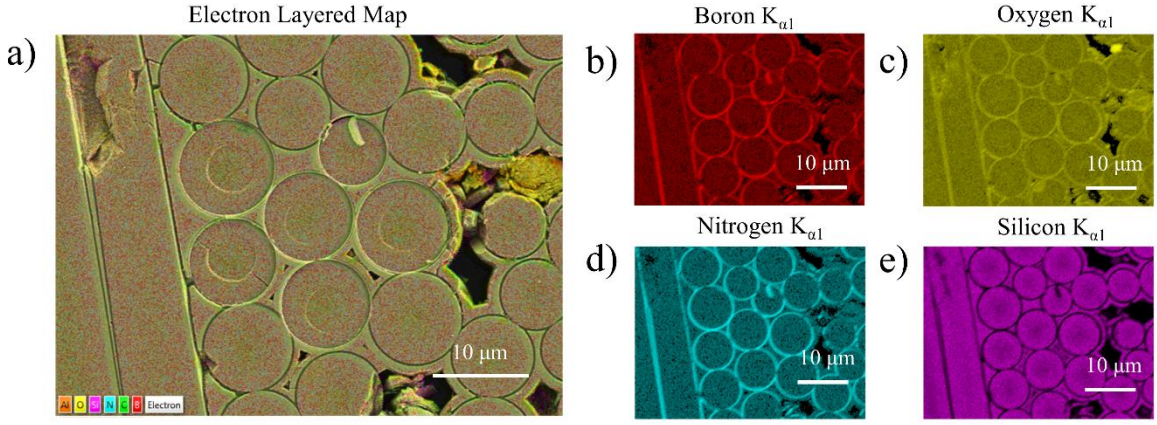


Figure 82: EDX elemental maps of post-push-out tests on an outside tow of a Hi-Nicalon sample exposed for 500 hours at 65C and 95% relative humidity, showing clear segregation of the Oxygen inside the interphase

When performing EDX maps shown in Figure 82 (working distance of 8.5 mm, probe size of 200 pA, accelerating voltage of 5 keV) on the sample after testing, it was shown that after 500-hours exposure, the oxygen had preferentially segregated to the BN-rich regions (i.e. the interphase), as highlighted on the oxygen map in Figure 82. Additionally, fibre centres were depleted in silicon, yet enriched in oxygen signals.

SEM EDX analysis on a trench milled after a push-out showed strong nitrogen & oxygen signals from the edge of the push-out. As such, adhesive failure can be assumed to have been the dominating failure mechanism. Figure 83.c helped confirm oxygen ingress within the sample, however no specific depth was measured, as the trenches dug were not deep enough for imaging.

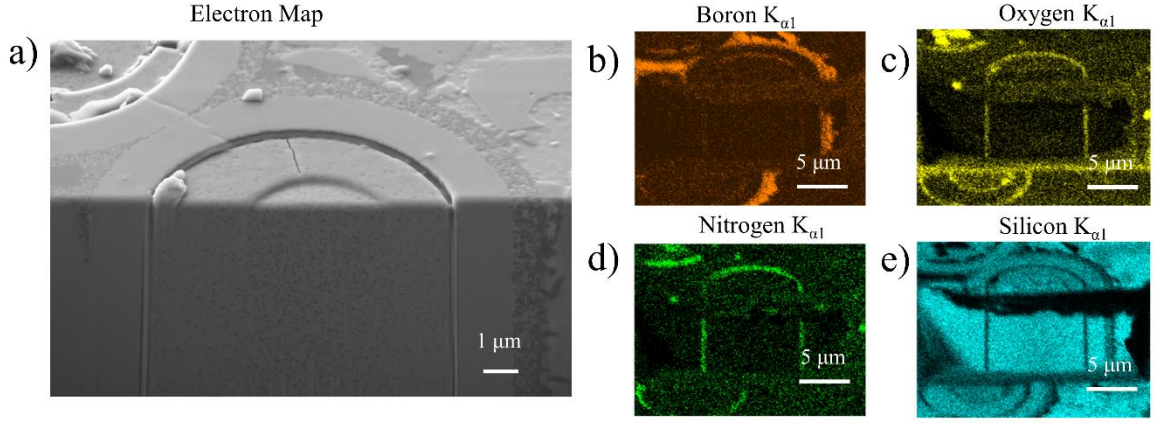


Figure 83: SEM EDX analysis on a cross section milled after a push-out on a Hi-Nicalon fibre sample exposed for 500 hours at 65°C and 95% relative humidity. The elemental map experienced surface contamination of unknown nature during data acquisition.

5.7 Intertow Variations

The cascade push-out methodology highlighted in Chapters 3 and 4 was reproduced on the degraded samples (500 hours) in two locations – one in an inner tow and one in an outer tow (on the outskirts of the sample where the degradation would have been more significant) to investigate the variability in inter-tow measurements.

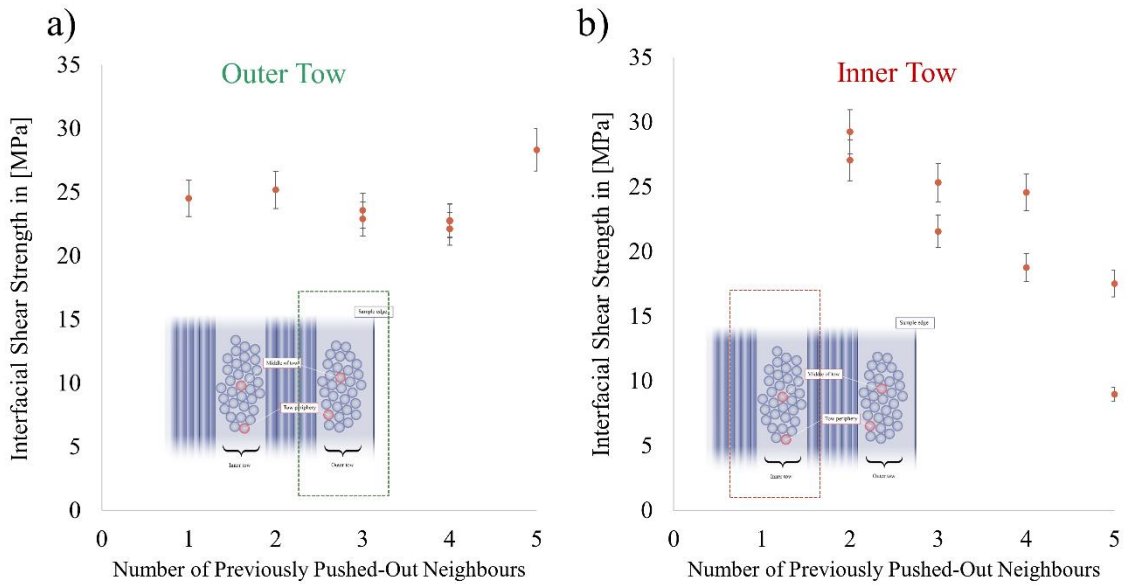


Figure 84: ISS VS number of previously pushed out neighbours on a Hi-Nicalon sample exposed for 500 hours at 65°C and 95% relative humidity, performed in (a) an outer tow and (b) an inner tow where degradation would have been less noticeable.

Results from the cascade push-outs on Figure 84.a showed that there was little difference in ISS variation with respect to number of neighbours in an outer tow, where degradation was more significant. Conversely, tows inside the sample (Figure 84.b) showed the same trends as pristine samples (the results of which are included elsewhere[232]). The cascade push-outs performed on pristine samples in Chapter 4 Section 4.4 were however performed on Tyranno type SA3 fibres with a medium BN, despite showing similar behaviour to Hi-Nicalon fibres. These observations suggest that the degradation on the outer tows had a significant impact in creating defects in the BN, resulting in a strong dependence of the push-out stress to interphase quality. When looking at the fractography under SEM after testing, cascade push-outs on fibres in an inner tow (Figure 85.a) were cleaner with limited BN delamination and fibre breakage. By contrast, push-outs in an outer tow (Figure 85.b) showed lower rates of success and significant BN damage.

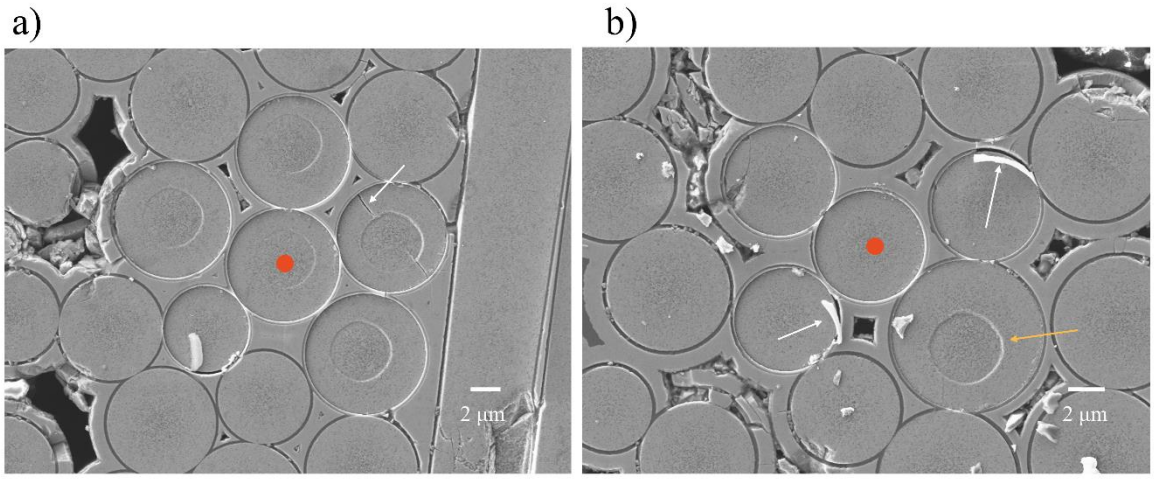


Figure 85: SEM micrographs of the cascade push-outs (a) on a fibre with 5 direct neighbours in an inner tow and (b) on a fibre with 4 direct neighbours in an outer tow. In both micrographs, the red spots denote the central 'target' fibre of the cascade. Fibre cracking (white arrow on (a)) was more frequent on inner tows whereas BN delamination (white arrows in (b)) was more prominent in outer tows. A gold arrow on (b) is noted to draw attention to fibre surface damage induced by the tip.

Micrographs in Figure 85 show that fibre cracking from push-out (white arrow on Figure 85.a) was more prominent on inner tows whereas BN delamination (white arrows on Figure 85.b) was more frequent on outer tows. The latter may be due to degradation of the composite on the outer tow embrittling the interphase and making it more prone to expansion when converting to boria. Damage from the nanoindentation tips on the fibre surface (highlighted by the gold arrow in Figure 85.b) was frequently noted for larger-diameter fibres only (as seen on both Figure 85.a and b) with smaller-diameter fibres presenting little to no damage from the tip.

5.8 Push-Backs & Friction Studies

Fibre push-backs were also performed on the degraded sample to compare and contrast with the pristine sample push-backs.

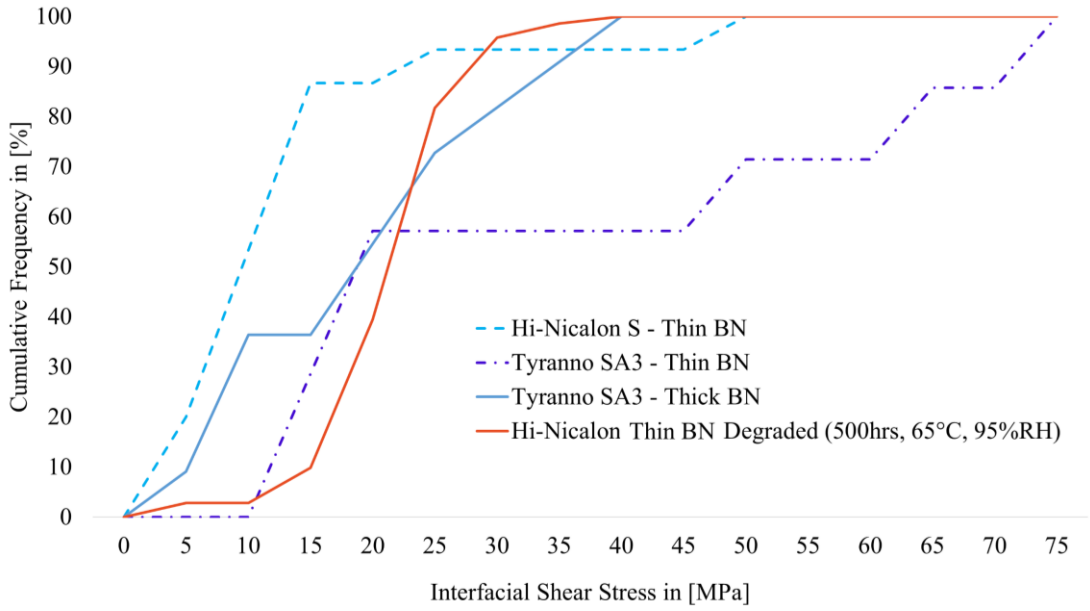


Figure 86: CDF of the frictional stresses obtained from fibre push-backs on various samples.

The sample push-backs on the degraded sample showed negligible difference with respect to other pristine samples of different fibre types, as shown in results on Figure 86. The stresses upon pushing the Tyranno type SA3 fibres back were slightly higher due to the rougher surfaces.

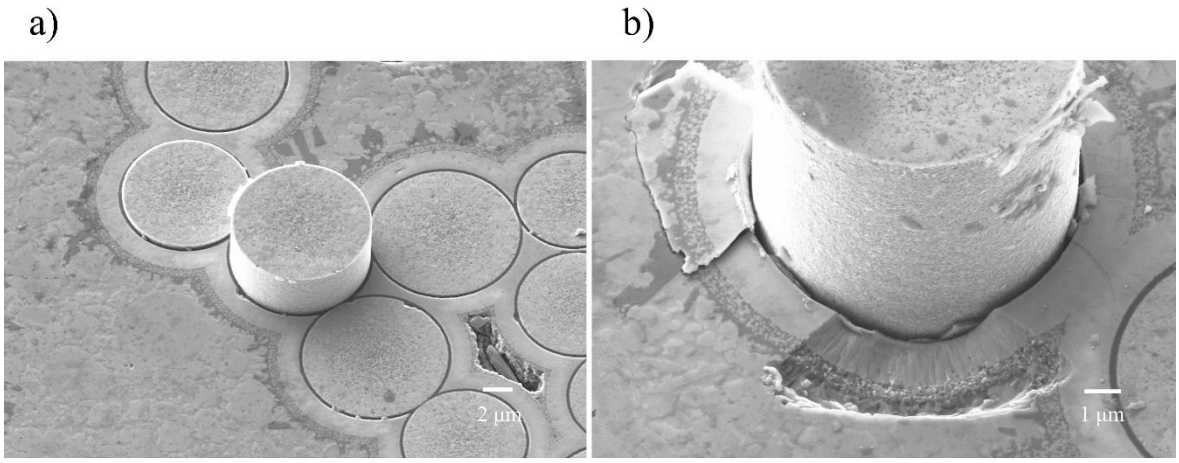


Figure 87: SEM micrographs on the Hi-Nicalon sample degraded for 500 hours at 65°C and 95% relative humidity showcasing (a) a fibre that has been pushed back with (b) spallation from surrounding CVI SiC.

Analysing the fractography after mechanical test showed fibres – which were pushed back – often displayed edge cracks which spalled off the surface (Figure 87.b). These might have been induced by the release of compressive stresses during initial push-out.

When performing the same Marshall[33] analysis on the fibre push-back ISS for the degraded Hi-Nicalon fibre sample, the frictional sliding resistance averages at 16.6 ± 7.3 MPa, a much higher stress than pristine samples with resistances below 11 MPa.

5.9 Discussion

Firstly, a study was performed on the as-exposed sample surface, following exposures of 50, 250 and 500 hours at low temperature (65°C) and 95% relative humidity. Raman spectroscopy showed that the decrease in Si-Si bond signal intensity was most significant in the melt-infiltrated matrix, suggesting the matrix residual Silicon had reacted with water vapour on the first instance. Whilst both optical phonon modes (longitudinal and transverse) of the Si-C bonds displayed little to no change following exposure, the amorphous BN fluorescence displayed a strong shift in both intensity and wavelength. This effect is particularly pronounced in the presence of borides and carbides in the matrix. This is consistent with observations from More et al.[175] as well as Opila et al.[213], whom found that BN oxidation was quicker than CVI SiC or SiC fibre oxidation. The oxidation was also confirmed by EDX studies on Figure 82 and Figure 83 showing the oxygen had segregated to BN-rich regions.

Secondly, the micro-mechanical performance of the degraded SiC_f/BN/SiC composites was compared to that of pristine samples. It was found that whilst the sample exposed for 50 hours had little change from the pristine state, the samples exposed for 250 and 500 hours had a clear decrease in overall ISS measured. This suggests that oxygen ingress inside the BN changed the bonding strength of either BN/fibre or BN/CVI SiC interfaces. This could be due to the formation of the more likely oxidation by-product[178] $H_3B_3O_6$ (BHO_2) replacing the BN/fibre interface and weakening the push-out behaviour for exposure times greater or equal to 250 hours. Similarly, Gavalda-Diaz et al.[222] – working on the same material and similar exposure times – computed a reaction function yielding a likely solid BHO_2 stabilised phase formed at the 95 % humidity saturation and 65 °C temperature exposure. They have found a similar change in micro-mechanical behaviour during fibre push-out from stick-slip to even-friction after 500 hours exposure times. For samples exposed for 50 hours or less to the degradation conditions, the rate of diffusion by convection of the BO_2^- and $B(OH)_3$ gas in steam[222] might have not allowed enough time for the majority of the BN interphase to degrade and display a drop in mechanical response. From another perspective, one can argue that 500 hours (the maximum exposure time) might not have been enough time for any species to diffuse through, and therefore the mechanism might have been dominated by more local oxidation or dissolution (internal) mechanisms.

Post-mortem analysis showed that the fibre push-outs at 50 and 250 hours were similar in nature to pristine push-outs on Hi-Nicalon fibres, however the sample exposed at 500 hours had significantly more damage both from tip insertion inside the fibre and from 'self' push-outs on its outskirts. The tip insertion damage inside the fibre suggests that the SiC Hi-Nicalon fibre oxidation might have been limited to the surface (since this was not observed on the tests exposed for fewer hours). A softer thin SiO_2 layer likely formed – an evidence also claimed by Hay et al.[70] and Opila et al.[55], however latter sources operated at higher temperatures showing that the silica layers were only 8 monolayers-thick whereas the boria layers can reach thicknesses of 400 nm. Future work making use of XPS could help in identifying the nature of the surface formations. This observation then led to testing the inter and intra-tow variability, which resulted in no distinguishable difference on that same sample (exposed for 500 hours). When performing Welch's unequal t-test to confirm findings, it was however noted that the probabilities for both intertow or intratow populations having the same mean were low. Therefore, both variabilities were statistically significant. This conclusion resulted in the testing of cascade push-outs on the same sample. The cascade push-outs showed that outer tows had a similar dependence on the number of neighbouring fibres to pristine samples. Fibre cracking was more prominent on inner tows whilst BN delamination was more frequent on outer

tows. All the above suggest that the oxidation within the naked (unprotected[217]) composite is oxygen diffusion limited, as such high humidity and low temperature exposures resulted in significant differences in testing both between and within tows (initially observed on pristine samples).

5.10 High-Temperature Fibre Push-Outs

5.10.1 Background

High-temperature measurements of these SiC_f/SiC components is essential. Indeed, some mechanism such as crack bridging toughening (enabled by the BN) are only dominant at elevated temperatures[212]. High temperature micromechanics have been pioneered recently with a multitude of in-situ laser heating systems. The majority of the ex-situ hot temperature indenter instrument challenges are highlighted in the Wheeler et Armstrong review[98] – these include diamond tip oxidation, measuring an accurate temperature at testing site, and the challenges in obtaining stable thermal drift measurements (with contributions from both the stage frame and the sample to indenter contact). Solutions to address this problem include testing for shorter times and increasing indentation size whilst also taking into account potential high temperature radiation from materials when imaging and calibrating. High-temperature observations during measurement is further limited by thermal noise and drift.
High-temperature testing of SiC_f/BN/SiC has been attempted in the past – albeit relatively recently and usually at the macro-scale – whereby testing by Mazars et al.[233] with xCT at 1250°C revealed a prevalence of fibre/matrix debonding in longitudinal tows. The same study acknowledged the limitations in detecting crack openings similar in size to voxel dimensions by phase contrast – further stressing the need for more targeted micro-mechanical evaluations of failure mechanisms. High-temperature indentation of SiC_f/BN/SiC composites has been performed up to 800°C, and showed lower strain rate sensitivity when compared to monolithic counterparts[234]. The study also found that the contact radius disproportionally decreased with increasing temperature for the composites. Furthermore, the study model showed that the zone of influence/plasticity at high temperature extended to 36.5 µm around the indent, with the Young's modulus experiencing a slight decrease of 20 GPa between room temperature and 800°C.

5.10.2 Methods

High temperature indentation and push-outs were performed in high-vacuum (2×10^{-6} mbar) on a NanoTest Xtreme instrument (MicroMaterials©) to measure the evolution of the elastic properties of the CMC constituents with respect to temperature. The instrument had a lateral spatial resolution of less than 0.1 nm and a heating rate of 1.6 °C.min^{-1}. The temperature was controlled by heating the stage and the indenter separately (the output power of the tip was utilised to match the stage temperature at higher temperatures, as the indenter was smaller in mass and therefore faster to adjust) – however three thermocouples were used during the experiment to measure (i) tip temperature, (ii) stage temperature and (iii) sample temperature respectively. Both depth signal & pendulum load calibrations were performed at each held temperature for indentation, with the power adjusted on the heating elements to minimise thermal drift.
An AlNi sample holder (with an in-built slit and hole for the thermocouple) as well as a high-temperature flat-punch tip were custom manufactured to perform the high-temperature push-out tests. Push-outs were performed on a Hi-Nicalon (thin BN) sample in a MicroMaterials© Xtreme system,

in displacement-control mode. Tests were halted at a limit stop load of 0.1 mN, using a 0.02 µm.s^{-1} indenter contact velocity, a 50 µN initial detection load, a 10 nm.s^{-1} displacement rate and a 1.5 mN.s^{-1} unloading rate for a maximum indentation depth of 2 µm.

A minimum of three fibre push-outs were performed per temperature regime, up to 650°C measured on sample surface. Push-outs were performed on inner tows (aligned with the custom slit) and within tows only (i.e. no tow periphery fibres were probed). The ISS was calculated in the same manner as room temperature measurements (c.f. Chapters 3 and 4).

5.10.3 Results

The load/displacement data from the high-temperature fibre push-outs was converted to ISS using the standard load-displacement equation [5] found in Chapter 4 (with no prior data fitting). Results were plotted on Figure 88 as a function of the temperature measured on the sample surface thermocouple. Two sets of push-out data were plotted for the room-temperature (25 °C) measurements (during heating and cooling), the lighter set corresponded to the cooling data. All other data points were collected during heating only.

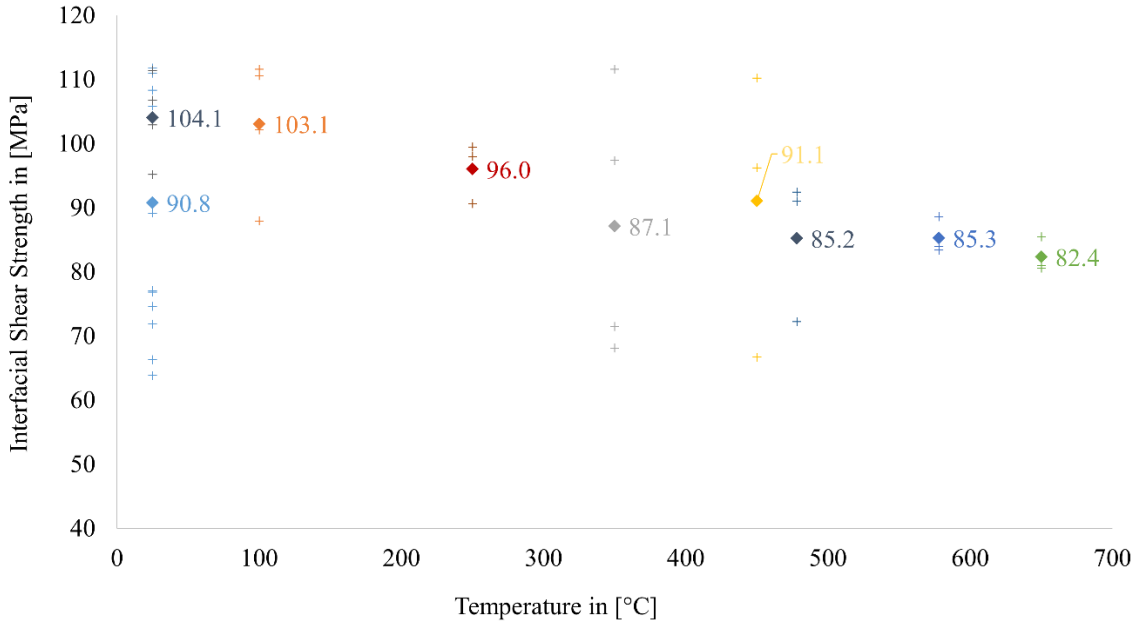


Figure 88: Interfacial Shear Strength (ISS) as a function of temperature from fibre push-outs

Figure 88 showed that there was a wide spread in the values measured at room temperature, but that the spread of values decreased with increasing temperature. A notable event between 350 °C and 450 °C in the thermodynamics might have induced a change in the microstructure, which resulted in a wider spread of ISS values between those temperatures. The ISS nevertheless steadily decreased from averaging 104.1 MPa to 82.4 MPa, from room temperature to 650 °C respectively. However, these fibre push-outs tests were performed on a Hi-Nicalon-fibre sample with a thin BN, where the role of the interphase at this scale can be questioned, even at room temperature (when compared to thicker interphases).

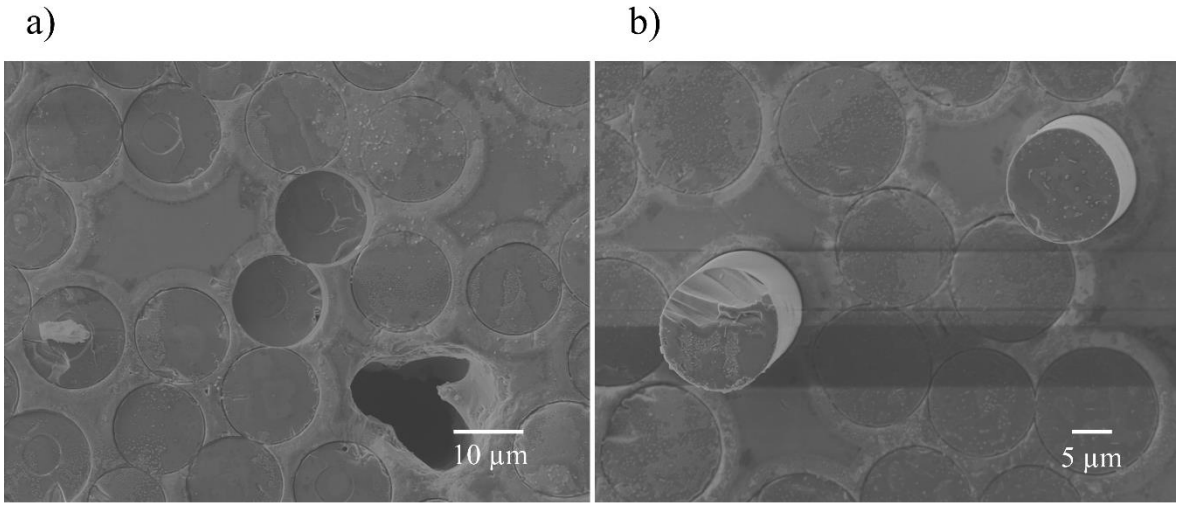


Figure 89: SEM micrographs of the CMC showing a) two fibres pushed out on the inside of the tow, and b) fibre surface showing surface-level degradation of the fibre

When observed under microscope after testing[6], the sample showed similar behaviour to room-temperature measurements for the majority of the push-outs (Figure 89.a). Only superficial change in the polished surface was noted (Figure 89.b). Overall, the effect of high-temperature (in vacuum) seemed to have less effect than the introduction of water vapour in the system.

[6] Data acquisition by Dr. Lisa Toller-Nordström

5.11 Chapter Summary

Having investigated both technique-dependent and material-dependent variables at room-temperature, this chapter probed the effects of humidity exposure and high-temperature on the samples, and its subsequent effect on the mechanical performance of the composite.

SiC_f/BN/SiC composites were exposed for 50, 250 and 500 hours at low temperature (65 °C) and 95% relative humidity to understand how the resulting oxidation products would affect mechanical properties at the micro-scale. Superficial studies revealed that the BN interphase coating the fibre and the residual silicon in the matrix had preferentially oxidised. When comparing the micro-mechanical properties of all composites, it was found that whilst the sample exposed for 50 hours had little change from the pristine state, the samples exposed for 250 and 500 hours had a clear decrease in overall ISS measured. This was in line with observations of mechanical behavioural changes seen elsewere[222]. Parallel studies also revealed the damage was strongly localised, and the diffusion of water within the composite was not fully complete at exposure times between 50 and 250 hours. The permeability of the CMC was however shown to be affected at longer exposure times where differences in mechanical performances between – and within – tows were noted.

Finally, push-back studies highlighted that the frictional sliding resistance for exposed samples (16.6 ± 7.3 MPa) was higher than pristine samples, suggesting the change in chemistry roughened the interfaces, and caused higher energies to be dissipated during fibre sliding. High-temperature vacuum push-outs showed gradual decay in the micromechanical performance of the BN interphase (interfacial shear strength retention ratio of 79.1%), from which it was inferred that the effect of high temperature was less pronounced than the effect of introducing water vapour in the system.

Having investigated the effects of humidity exposure and high-temperature on the composite, we now turn to separately looking at any change in performance from testing in-situ in Chapter 6.

Chapter 6 • Visualising Failure

6.1 Introduction

A need for in-situ techniques in the context of CMC's has already been highlighted by Callaway et al.[48] whom have stated that a need to recognise local plasticity prior to coating rupture is fundamental to models. When combined with chemistry-based detectors like EDX, mechanical and chemical components of in-situ micro-tests can also be further explored. Imaging failure on the composites due to the statistical nature of crack initiation has continuously proven to be a challenge. 3D X-ray tomography has already been used on CMC's to investigate porosity[235]. Pores should be at least ten times bigger than the voxel size for segmentation and detection to be accurate[227].

Crack propagation however requires a much higher resolution in synchrotron tomography, as crack opening displacements are restricted to dimensions of a few microns. Cracks in SiC_f/SiC minicomposites tested in tensile conditions have also been found to be segregated to microcracks in most parts – with very few cracks developing to clearly identifiable full size helixes around fibres cracks[236,237,238]. Estimations of the ISS from minicomposite tensile tests have been performed in the past but require complex deconvolution[239]. Synchrotron tomography has enabled Chateau et al. to find that cracks break fibres after having fully cracked the surrounding matrix[236], and that as a result, fibres can fail in 2 different locations.

Other experiments attempting to visualise failure made use of 3D DIC to measure strains[106] however the results showed optical distortion on the edges, limited depth of field, and a level of resolution which fails to distinguish whether interphase failure was chemical or mechanical (frictional) in nature.

6.2 In-Situ Trench Push-outs

6.2.1 Abstract

Traditional fibre push-outs for the evaluation of interfacial properties in long fibre ceramic-matrix composites present numerous limitations – some of which are addressed in this work by the introduction of the novel trench push-out test. The trench push-out makes use of a FIB milling system and an in-situ nanoindenter to probe a fibre of a few microns in length, which is pushed into a trench underneath, allowing in-situ observations to be directly correlated with micromechanical events. Both full and half fibres were tested; in comparison of Hi-Nicalon SiC fibres and Tyranno type SA3 fibres: both fibres were coated with BN interphases and mean interfacial shear stresses of 14 ± 7 MPa and 20 ± 2 MPa respectively were measured during fibre sliding in SiC_f/BN/SiC composites - candidate material for turbine engines. The micromechanical technique enabled visualisation of how defects in the interphase (voids, inclusions & milled notches) or in the fibre (surface asperities, non-uniform coatings, pre-mature oxidation) affected the variability of interfacial property measurement. The trench push-out generated reliable and reproducible results, monitored in real-time.

6.2.2 Introduction

Micro-scale techniques have helped bridge the gap between explaining atomic and molecular scale events and macro/meso scale mechanics. The micropillar compression technique applied to SiC_f/PyC/SiC was investigated by Kabel et al.[24] extensively but that study presented its limitations, as pillars can often be too fragile and experience instant debonding. Furthermore, Kabel et al. iterate that no kinetic properties (e.g. load rate effects) can be obtained reliably from the stage after debonding and cracks cannot be propagated in a stable manner. On the other hand, fibre push-outs - first theorised by Marshall in 1985 and performed in 1987 by Marshall & Oliver[107] - best mimic the mechanisms of CMC failure and can provide a measurement of the interfacial shear stress (ISS) τ experienced at the interphase, which is estimated by Equation [34][193]:

$$\tau = \frac{F}{2\pi RH} \quad [34]$$

Where F is the push out load, R is the fibre radius and H the sample thickness. Sample thinning to appropriate dimensions (where the tow architecture influence is reduced and where push-out load is lower than the load-cell limit of the mechanical device) is required – usually to sample thicknesses not exceeding 100 µm[63]. Sample thinning is challenging due to the hardness and brittleness of the ceramic composites.

The difficulty of sample preparation for the fibre push-out was illustrated by both works of Boakye et al.[118] making use of a tripod polisher and a light microscope to manually correct for fibre alignment with respect to the polished surface, and works by Herbreteau et al.[113] whom used wedge designs and ion slicers. The loading during fibre push-out can have further effects such as bending of the specimen or the holder, which can prevent accurate measurements. Ideally, a flat-punch nanoindentation tip is used to prevent fibre damage[99] however even flat-punch tips have been known to leave an impression on the fibre surface due to the large force needed[96]. It was shown by Mueller et al[96] that load/displacement curves are significantly different from Berkovich push-out and that a parallel alignment of the tip and fibres surface is necessary to minimise the impact of sharper indenters. Moreover, Kabel et al.[24] highlighted that poor calibration of the microscope-to-indenter positioning can result in lower throughput and technique yields, as the experimental acquisition is slowed down.

A major limitation of the fibre push-out method lies in the lack of information regarding in-situ observations as the fibre is fully imbedded in the matrix. This results in little knowledge on how defects in the matrix (voids, inclusions, chemical segregations) or in the fibre (surface asperities, non-uniform coatings, pre-mature oxidation) affect the variability of interfacial property measurements. Even if tested in-situ, there is no direct visualisation of either crack(s) propagating or the dominating failure mechanism. Simultaneous observations of artefacts at the top and bottom of the fibre and the nature of failure (inside or outside debonding) are needed for a full understanding of the test results. Furthermore, the mechanical data obtained from traditional fibre push-outs shows a high degree of variability which can be alleviated and better understood with the use of in-situ techniques. When developing new micromechanical techniques, the following criteria must be taken into account: the complexity of equipment/set-up, set-up and acquisition times, stability of the micromechanical loading, consistency of results and data analysis, data validation or the use of alternative experiments. Another key concern lies in how the technique can be representative by replicating material behaviour in its proposed application. The data analysis for fibre push-out is

particularly challenging as it is usually performed post-mortem as opposed to in-situ, which can lead to potential errors in data matching (associating a specific fibre to a load/displacement curve and an SEM micrograph of failure for example). There is a need to develop a micromechanical technique that can extract the micromechanical properties of the composite interphase reliably and in a reproducible manner. The trench push-out technique introduced in this work aims to address some of these issues for a future better understanding of how processing, degradation or other factors affect composite performance[222].

6.2.3 Methods

Due to the uncertainties surrounding fibre push-outs performed ex-situ, an in-situ technique that enabled visualisation of small-scale events needed to be created. A novel 'trench push-out' method depicted in Figure 90 has been adapted from the similar trench micropillars by Wu et al.[139] whom performed tests on electrical VIA's (Vertical Interconnect Access).

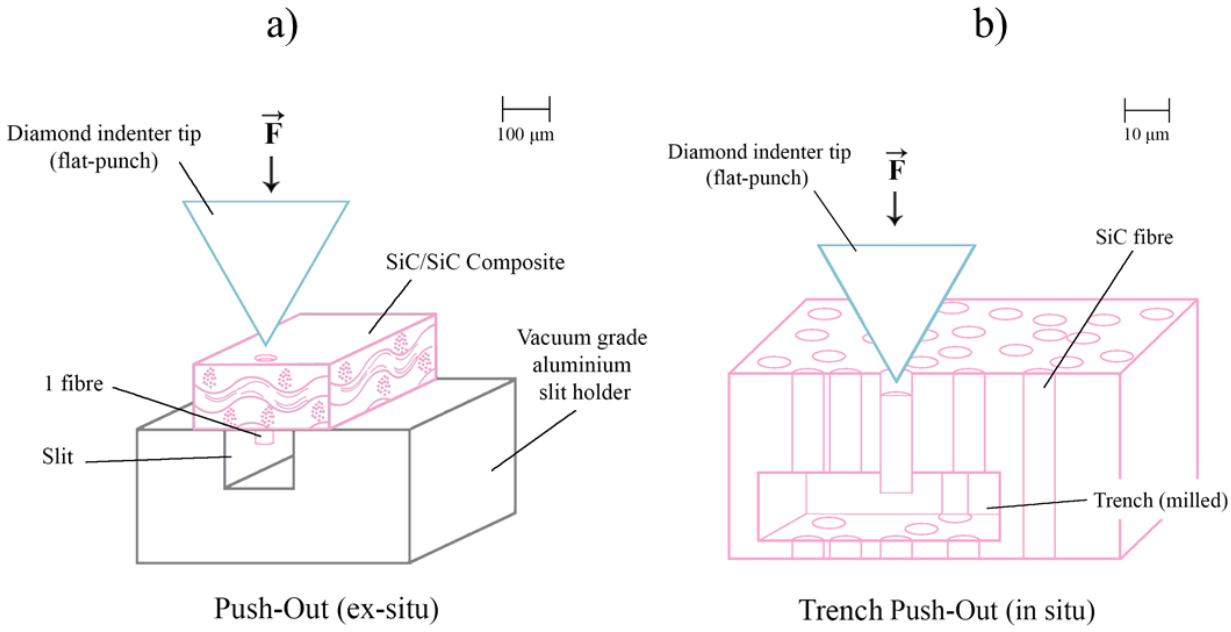


Figure 90: (a) Ex-situ push-outs and (b) novel in-situ trench push-outs. The SiC/SiC composite (and fibre) in a) have been enhanced for clarity and are not to scale with the corresponding scale bar

Two SiC_f/BN/SiC composites akin to those in previous chapters, and manufactured by Rolls-Royce High Temperature Composites (Cypress, CA) through a combination of Chemical Vapour Infiltration (CVI) & Melt Infiltration (MI) processes were used as model materials. The two composites differed in their fibre types: Hi-Nicalon™ (NGS Advanced Fibers & Co.) and Tyranno SA grade 3 ® (Ube Industries Ltd.) of dissimilar fibre radii (7 µm and 5 µm), and CVI-deposited interphases (200 ± 50 nm and 600 ± 50 nm thicknesses respectively).

Sample preparation of the trench push-out was performed on the dual SEM-FIB column Zeiss Auriga using milling currents of 4 nA for cutting of the 20-µm-deep trenches, 2 nA for surface 'polish' and 240 pA for surface finish. Micromechanical testing with the trench push-outs was performed both ex-situ and in-situ on a Tyranno type SA3 fibre sample. Ex-situ tests were performed on the ~~a~~

Keysight Nanosuite G200 instrument – used in Chapters 3-5 – as a control experiment to test whether the techniques produced similar results. There was a clear load plateau during fibre sliding inside the trench which enabled calculation of the ISS with minimal error. The ex-situ trench push-out also showed no fibre cracking.

During in-situ testing, a displacement-controlled speed of 0.1 μm.s^{-1} was used on an Alemnis / FEI Quanta FEGSEM column system; images were acquired at 500 ns per frame and a 1024 x 884 resolution. Test were performed on both full Hi-Nicalon fibres and half Hi-Nicalon fibres on the cross section. The full fibres tests allow tracking of the displacements of the top and bottom fibre surfaces, whereas the half-fibre tests allow investigation of cracking along the fibre interfaces. The ISS at peak load (maximum load) and plateau load (purely frictional) were calculated with equation [34] for full fibres and equation [35] for half-fibres.

$$\tau = \frac{F}{\pi R H} \quad [35]$$

The energies required for debonding $\Gamma_{debonding}$ and friction $\Gamma_{friction}$ were obtained by integrating the load (F) / displacement (t) responses with respect to their corresponding displacement ranges as detailed in equations [36] and [37].

$$\Gamma_{debonding} = \frac{\int_{t_{initial}}^{t_{debonding}} F dt * \left(t_{debonding} - t_{initial}\right)}{\pi R H} \quad [36]$$

$$\Gamma_{friction} = \frac{\int_{t_{debonding}}^{t_{max}} F dt * \left(t_{max} - t_{debonding}\right)}{\pi R \left(H - \left(t_{max} - t_{debonding}\right)\right)} \quad [37]$$

EDX analysis was performed on a Zeiss Merlin instrument using a 200 pA probe size, 5 keV accelerating voltage and an 8.5 mm working distance – each map was drift corrected and acquired over periods of 30 minutes each. The surface topography was measured by scanning with a Berkovich tip using a Hysitron TI Premier nanoindenter in contact mode. The maps spanned an area of 10 x 10 μm with a step size of 20 nm. Root mean squared fibre roughness was obtained on sub-maps of 1.5 x 4 μm areas by a Root-Mean Square analysis with the scanning probe software Gwyddion (Version 2.56).

6.2.4 Results

A standard load/displacement curve and corresponding SEM frame from a half-fibre trench push-out is shown in Figure 91.a. The load displacement curve is similar to traditional push-out responses in displacement-control with a peak in load until full crack propagation[240,222], after which the plateau load shows the fibre sliding into the trench. A plateau load observed during fibre sliding is consistent with friction models developed by Callaway at al.[48], showing no dependence on any Coulomb-type law.

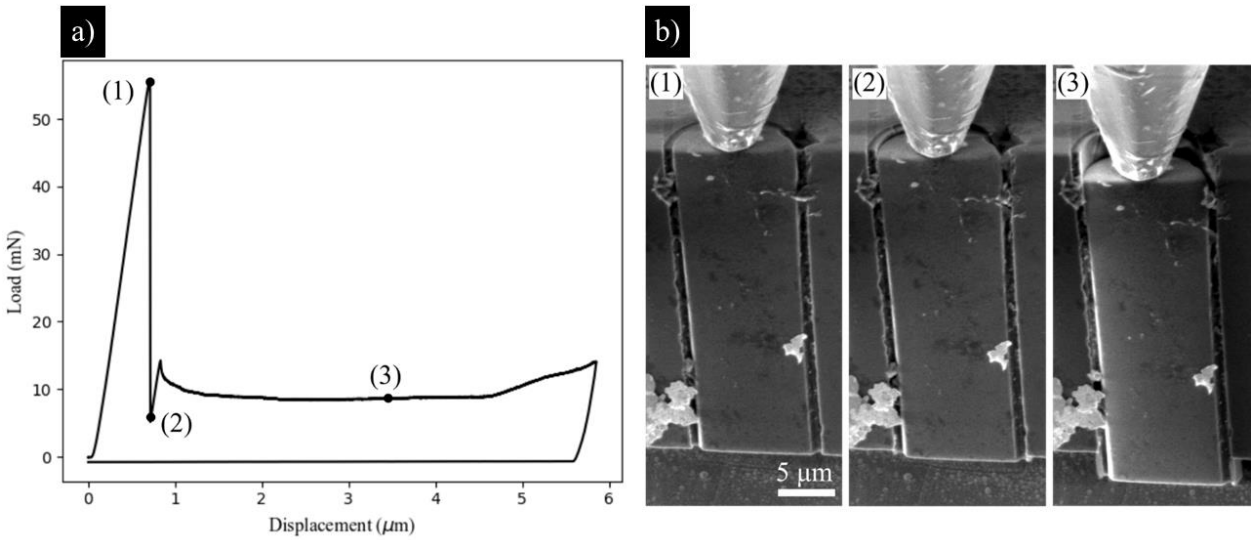


Figure 91: SEM frame from an in-situ trench push-out experiment conducted on a Hi-Nicalon fibre showing corresponding load-displacement on the left.

Testing of fibres at the edge of tows or closer to the edge of the trench – as seen in Figure 91.b – results in a tendency for the load to increase at the end of the plateau (past point (3) on Figure 91.a, where the tip cone starts making contact with the top outskirts of the fibre). The sharp load-drop from point (1) to point (2) in displacement-controlled experiments corresponds to crack(s) fully propagating and leading to fibre sliding. Looking in more detail at a sequence of SEM images from a trench push-out test of a half-fibre (Figure 92) shows that transverse radial cracks first propagate in the CVI SiC surrounding the fibre (3.b, c). Thereafter, coils of BN interphase emerge at the surface (3.b). Radial cracks in the CVI SiC propagate until the fibre - alongside the BN and part of the CVI SiC – is pushed inside the trench towards the end of the test (3.d).

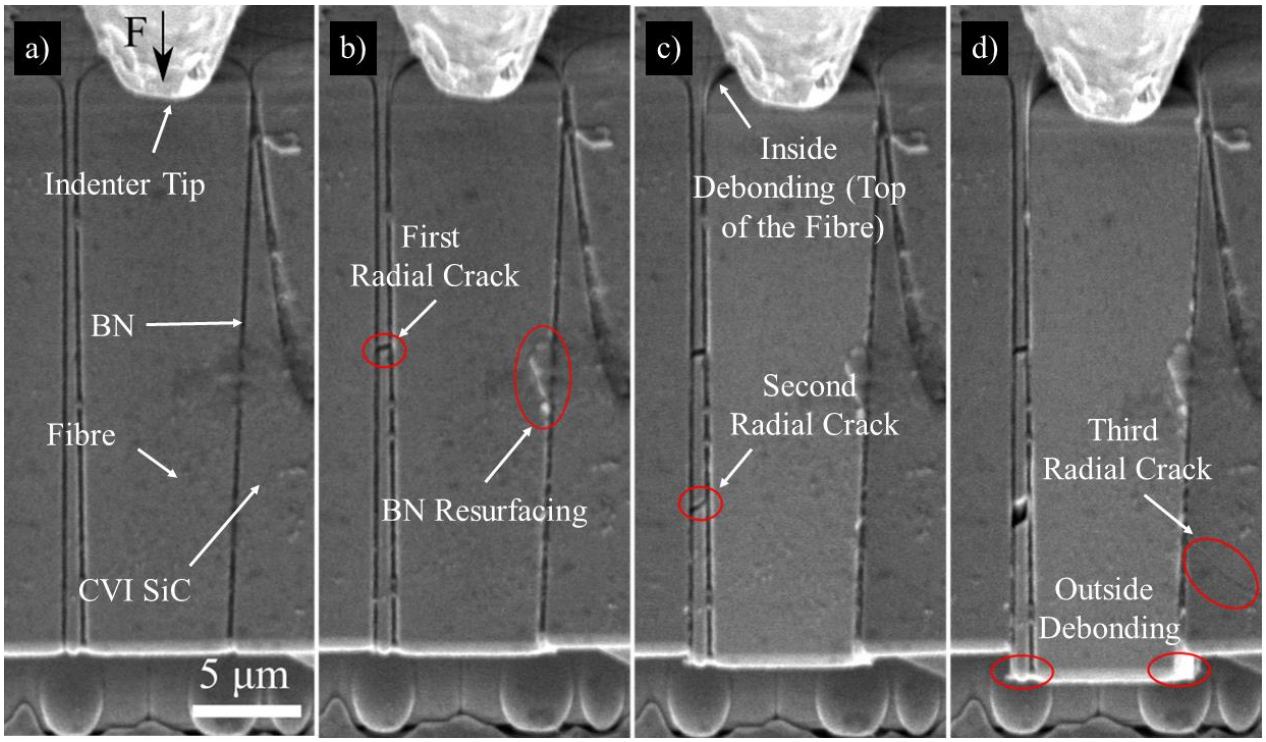


Figure 92: SEM frames from an in-situ trench push-out experiment on the SiC$_f$/BN/SiC sample with Hi-Nicalon fibres showing progressive cracks in the surrounding CVI SiC, the BN coiling and resurfacing, and both the BN and the CVI SiC pushing out at the bottom of the sample inside the trench

The frictional degradation with the BN interphase coils and subsequent resurfacing is visible on Figure 92.b. Cracks have also propagated to neighbouring fibres and neighbouring interphases in the transverse direction as shown in Figure 92.d. One could deduce from observations that radial cracks induced inside debonding of the interphase in the neighbouring fibre, which resulted in inside debonding being the dominated mechanism, as opposed to outside debonding highlighted in Figure 92.d.

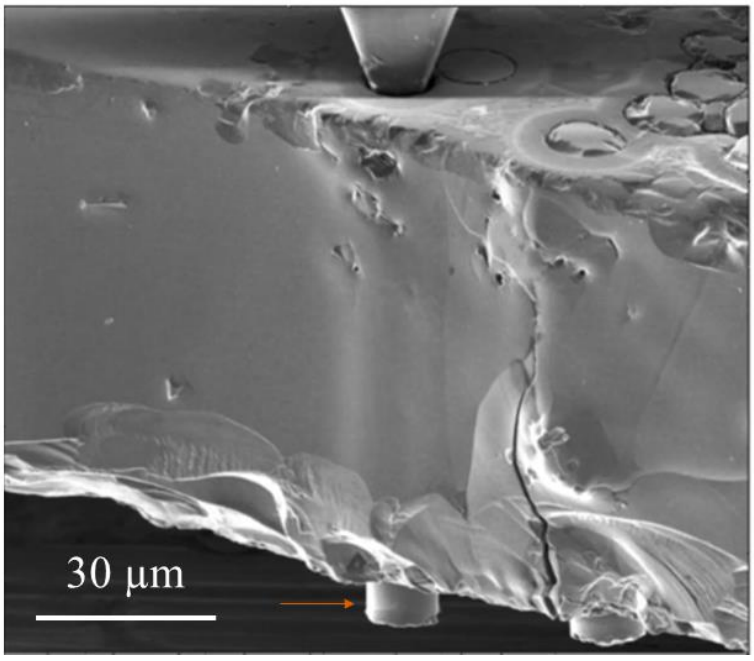


Figure 93: SEM frame from an in-situ push-out experiment on the SiC$_f$/BN/SiC sample with Hi-Nicalon fibres showing a loading of a traditional push-out with the fibre sticking out at the bottom (orange arrow) but no visual information on the micromechanical events is given

When testing full fibres directly beneath the trench or with no trench on fully pushed out samples (Figure 93), an increase in the load response towards the end of the test akin to that of past point (3) in Figure 91.a was observed.

Looking at the magnitude of plateau loads obtained during the trench push-outs in Table 17 – loads found on half fibres were almost half those found on full fibres. When calculating shear stresses using Equation [34] comparing the half and full fibres, similar stresses were obtained on the same sample. The accuracy and error on these measurements are taken into consideration in the discussion.

Table 17: Comparing the interfacial frictional stresses obtained from a half-fibre and a full fibre trench push-out experiment in the SiC/BN/SiC composite with Hi-Nicalon fibres

	Units	Half Fibre	Full Fibre
Plateau Load	mN	7.5 ± 0.3	13.5 ± 0.2
Fibre Radius	µm	4.0 ± 0.1	3.5 ± 0.1
Interfacial (Frictional) Shear Stress	**MPa**	**23.8** ± 0.3	**24.6** ± 0.3

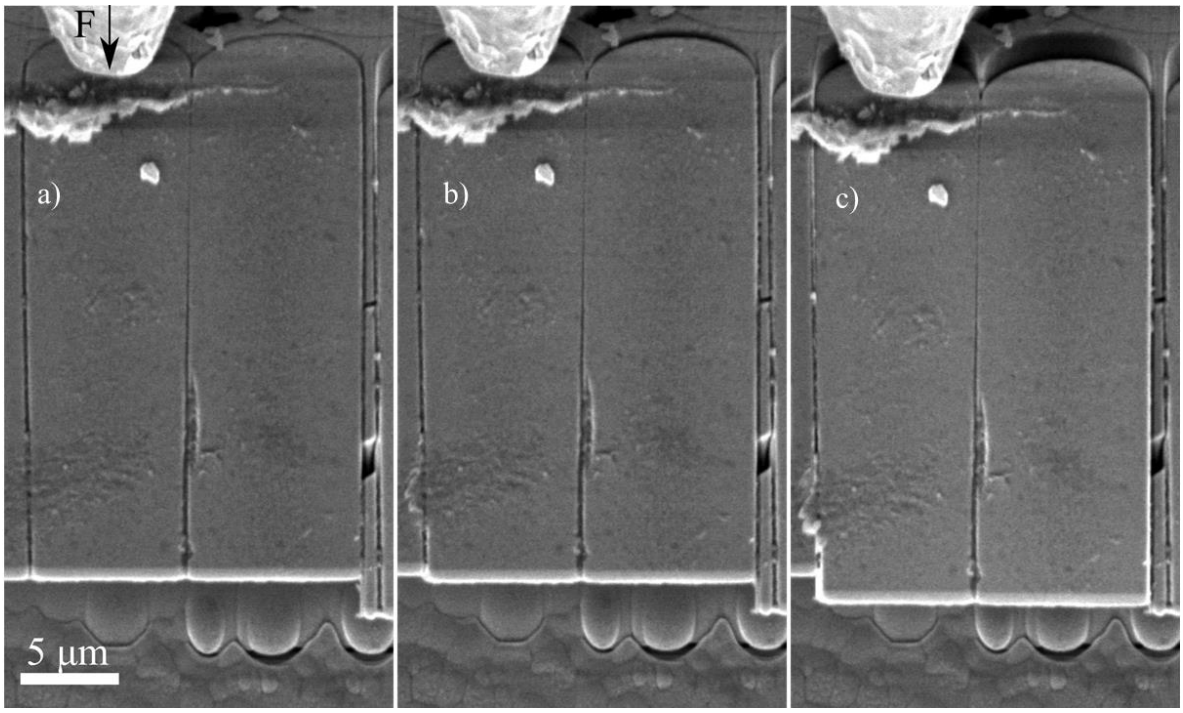


Figure 94: SEM frames from in-situ trench push-out experiments on the SiC$_f$/BN/SiC sample with Hi-Nicalon fibres showing loading of 2 half-fibres simultaneously.

The pushing out of two neighbouring Hi-Nicalon fibres on Figure 94 suggests there was strong adhesion between fibres and that the adhesive strength between fibres was greater than the fibre/matrix bonding. There are two possible explanations for this phenomenon. The BN interphase might have been damaged from grinding, polishing and trench milling with gallium ions (at currents quoted in the experimental section), resulting in the fibres touching. Elsewise, this can suggest the interphase bond between fibres is not homogeneous, with some fibres touching each other and transferring load between one another.

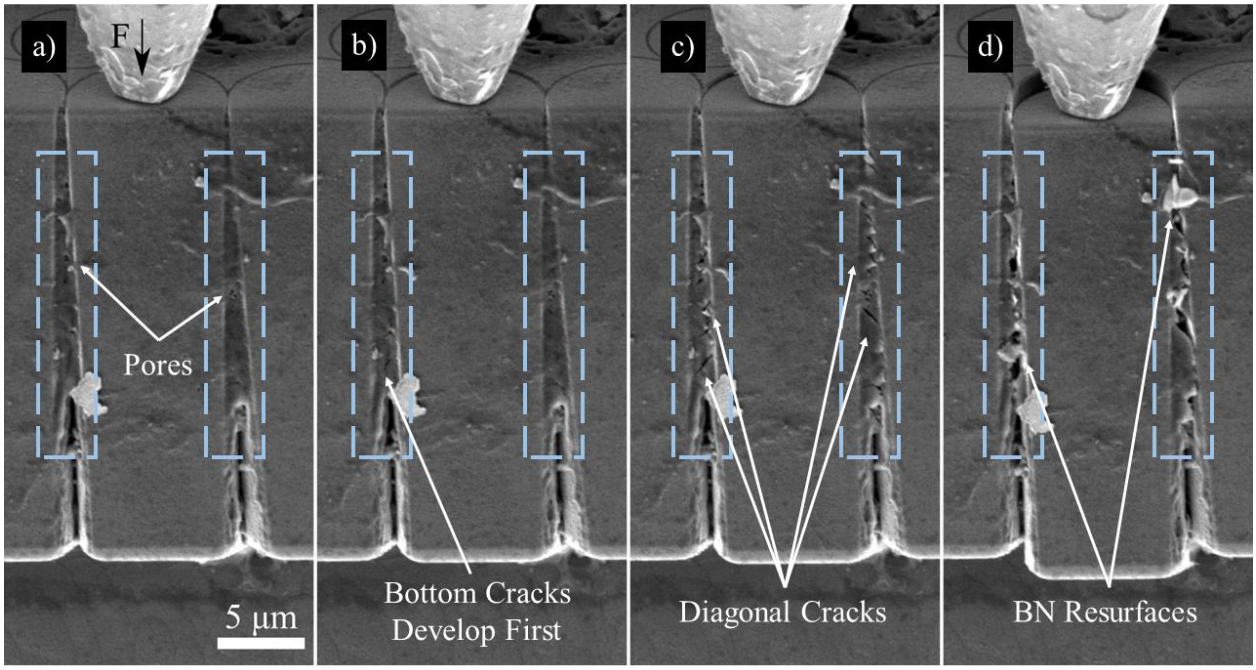


Figure 95: SEM frames from an in-situ trench push-out experiment on the SiC$_f$/BN/SiC sample with Hi-Nicalon fibres showing gradual formation of diagonal tracks from bottom to top inside the BN as cracks connect pre-existing pores and defects in the interphase.

It was observed that sample preparation induced defects in the interphase: for example, different trench-milling rates for the SiC and BN might have resulted in preferential milling and notched areas in the SiC and BN at the bottom of the fibre. Diagonal cracks with respect to loading direction were observed to have propagated from the bottom and connected pre-existing pores, as seen on Figure 95. Similar observations were made in samples with pre-existing defects from manufacturing (e.g. non-homogeneous coatings). In this context, the SEM frames on Figure 95 show that (i) cracks initiate towards the bottom half of the fibre (close to the trench) and propagate upwards to the tip, and (ii) cracks have propagated between the fibres and the interphases as remnants of both boron and nitrogen are visible on EDX on the bare top section of the push-out highlighted in Figure 96. The visualisation of pre-existing defects in the BN interphase and how they interact with the cracks help explain any outlier values in the loads recorded, whilst reducing variability in the stresses recorded.

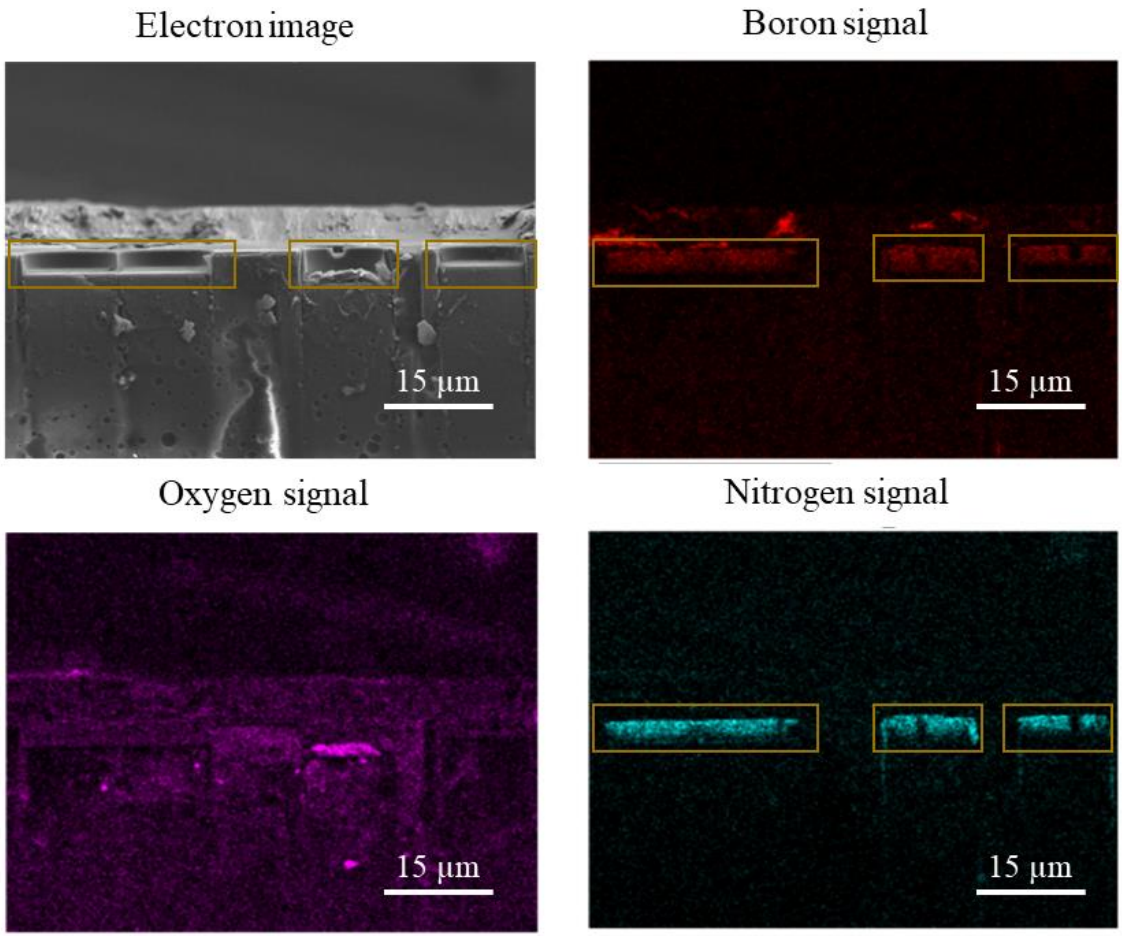


Figure 96: SEM EDX analysis of tested half-fibres showing BN signals (inside the squares) on the denuded top edges of Hi-Nicalon fibres. Circular defects on the fibre surface stem from sample cleaning after testing.

When comparing the different fibre types, the Tyranno type SA3 fibres exhibited the same behaviour: a mix of both inside and outside debonding illustrated in Figure 97. Simultaneous failures occurred, the BN was left untouched at the fibre top close to the tip (inside debonding), whilst concurrently adhering to the bottom of the fibre being pushed in the trench (outside debonding). The crack propagation behaviour is investigated in the discussion.

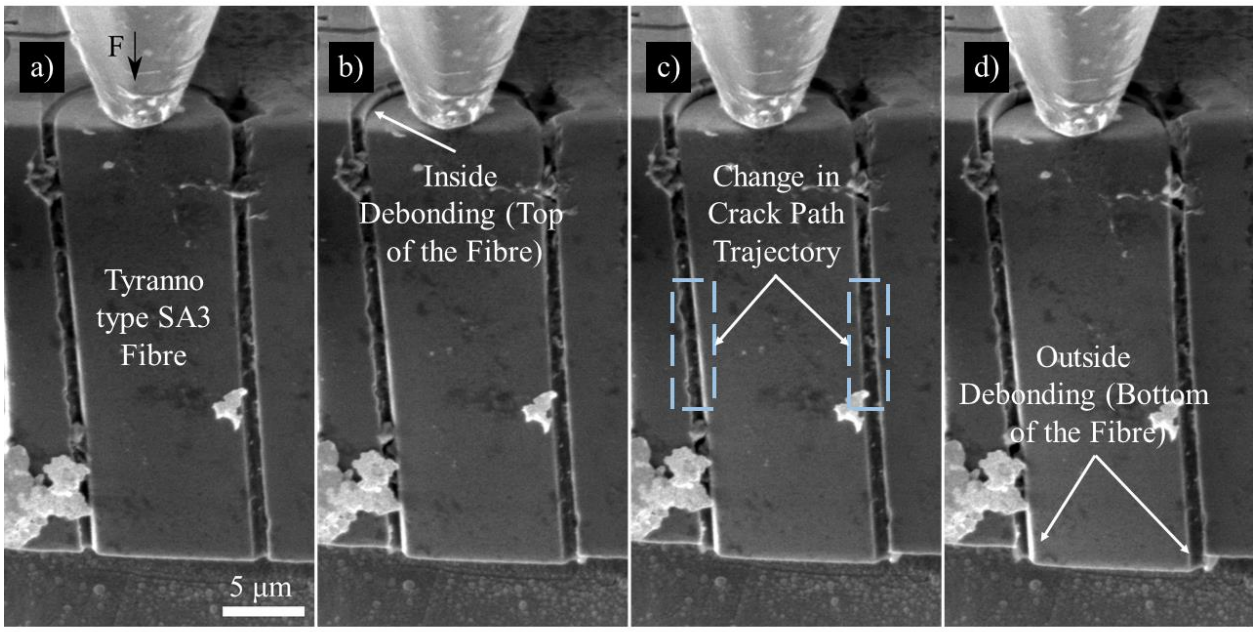


Figure 97: SEM frames from an in-situ trench push-out experiment on the SiC_f/BN/SiC sample with Tyranno type SA3 fibres showing simultaneous inside debonding (top) and outside debonding (bottom as BN is pulled out) suggesting there are two changes in crack propagation modes after the crack(s) initiate(s).

The loads obtained from the frictional section of the tests (as the fibres were sliding) were used to calculate ISS. The remaining data was used to integrate energies from crack propagation and friction using Equations [36] and [37], and compared to the fibre roughness data acquired with the triboindenter in Table 18.

Table 18: Mean values for loads, computed stresses and energies for all successful half-fibres trench push-outs (6 Hi-Nicalon and 3 Tyranno SA3 tests). All sliding distances on the displacement-controlled instrument were set to be the same. RMS roughnesses of the fibre surface were obtained from the nanoindenter surface topography analysis; all errors stem from standard deviations in the populations and express a minimum, as artefacts such as crack formation in the CVI were not included.

Fibre Type	Units	Hi-Nicalon	Tyranno Type SA3
Plateau Load	mN	5 ± 4	7 ± 1
Maximum Load	mN	22 ± 12	35 ± 20
Plateau Shear Stress	MPa	14 ± 7	20 ± 2
Maximum Shear Stress	MPa	200 ± 80	70 ± 25
Energy required to 'debond'/fracture $\Gamma_{debonding}$	$kJ.m^{-2}$	3.6 ± 2.0	4.2 ± 2.3
Energy from friction $\Gamma_{friction}$	$kJ.m^{-2}$	15.1 ± 7.0	22.5 ± 6.5
R_{RMS} *Fibre Roughness*	nm	35 ± 5	100 ± 5

The debonding load and shear stresses refer to the max loading point before catastrophic crack propagation and initiation of fibre sliding (the maximum loading point on Figure 91). Table 18 mean values gave insights to compare the two fibre types tested. The higher roughness of the Tyranno type SA3 fibres (100 ± 5 nm) resulted in stronger mechanical properties overall. A significantly larger energy from fibre sliding for the Tyranno type SA3 fibre once the crack fully propagated was observed. Similarly, the energy required to debond the fibre was more significant as the BN interphase might have had additional mechanical keying when deposited on a rougher fibre surface. This energy should also not be the main constitutive property, as we are considering brittle failures in these CMC's. It is worthwhile noting that the maximum shear stress before fibre sliding was much higher for the Hi-Nicalon fibres despite the rougher Tyranno SA3 fibres. During sliding of half-fibres, only half of the surface could contribute to resisting the push-out, suggesting the interphase friction coefficient was the biggest contributor to slowing crack propagation at the later stages of the micromechanical test.

6.2.5 Discussion

From an experimental point-of-view, the half fibres show promise as model material geometry for micromechanical testing. Half-fibres (or any partial fibre in general) are indeed easier to mill (as milling depths for the trenches are reduced to only half fibre radii), and can display clear crack trajectories when tested in-situ. The comparison between half and full fibre tests showed similar values (23.8 ± 0.4 and 24.6 ± 0.4 MPa respectively) for the frictional ISS measured – thus demonstrating the viability in pushing half-fibres on the surface near the edge of the trench on the polished side. These values are further comparable to ISS measurements of 28 ± 7 MPa made using more traditional push-outs (through thickness) performed on the same material[232]. In the context of half (or incomplete) fibres, the residual stresses released from the 'free boundary' at the sample edge may have had no visible effects on the remaining BN interphase coating the half fibre. This phenomenon could also have been explained by an effective cancelling of residual stresses with respect to fibre Poisson expansion. Limitations of testing the half-fibre geometry are outlined towards the end of the discussion.

Fibre types and their adherence to coatings were compared with the use of trench push-outs. The EDX studies (Figure 96) showed the BN on the top Hi-Nicalon fibre surface after push-out. This suggested inside debonding (and a cohesive type of failure) dominated, with the crack propagating between the BN interphase and the fibre. The inside debonding on the top surface of the fibres was also observed by other works on traditional push-outs[19,99,66], however limited to no events on the bottom half of the fibres were reported with traditional push-outs (i.e. samples were not flipped and examined post-mortem in other works – most of the push-back tests in this thesis suggest an inside debonding mechanism dominated because very few fibres were still coated with BN on the bottom plane). Since orthogonal cracks – perpendicular to the axial direction of the fibres – also propagated (Figure 95 and Figure 92), both inside debonding and a subsequent relaxation of residual hoop stresses in the fibre environment was likely to have occurred. It was also observed that for both Hi-Nicalon and Tyranno type SA3 fibres, a significant portion of the BN interphase remained attached to the fibre during push-out (Figure 97.d). A possible explanation lies in the interphase oxidising through oxygen ingress during fabrication or sample preparation, thereby increasing the strength of the fibre/BN interface bonding. Alternatively, increased mechanical keying (especially if the fibres were attached together) can be observed as a result of a heterogeneous defect distribution in the interphase prior to testing. Tyranno type SA3 fibres also showed a mixture of failure modes during the same test as shown on Figure 97 where both inside and outside debonding mechanisms occurred.

Despite the ratio of roughnesses of the two fibre types, the Hi-Nicalon fibres on average displayed significantly higher shear stresses at maximum load only as seen in Table 18. This may be due to the thinner BN coating on the Hi-Nicalon samples having better adhesion, as the driving force for cracking and delamination increases with thickness[241]. The fibre roughness measurements are in line with both these results and literature [242,65,243] where Tyranno fibres are rougher – regardless of their generation – on the surface than their Hi-Nicalon counterparts resulting in higher interfacial shear stresses measured.

One of the key advantages of the trench push-out is the possible visualisation, explanation and correlation of the crack path to corresponding micromechanical events. In Hi-Nicalon fibre tests such as the one shown in Figure 92, cracks seemed to initiate in the neighbouring CVI SiC and/or SiC matrix, radially propagating from the loading direction. These secondary cracks may be induced due to the relaxation of stresses neighbouring the fibre being tested as highlighted by Hull et al.[107], their direction can be attributed to the columnar microstructure of the CVI SiC with grains aligned radially from the fibres, observations of which can be found in the works of Gavaldà-Diaz et al[222, 244]. In a more realistic context for gas turbine engines, fibre pull-out (as opposed to push-out) would induce a slight fibre shrinkage from Poisson contraction, thus decreasing the radial force acting on the BN/fibre bond, resulting in less damage on the surrounding CVI SiC. The porosity and quality of the BN interphase induced diagonal cracks (Figure 95) within the interphase which then interconnected to enable a larger longitudinal (alongside fibre direction) crack to fully propagate and the fibre to push-out. The BN porosity has previously been linked to increased rate of oxidation in both its monolithic[215] and composite form[160]. Experiments with a higher density of fibres in the tow (Figure 95) show that cracks had a tendency to propagate at the fibre BN interface whilst those with a lower density (Figure 92) show cracks propagating in the CVI SiC between fibres. This shows that fibre packing has a strong influence on crack path trajectory and this can be investigated using this technique. Even if the fibre packing density is too elevated, testing of full fibres can be followed by a milling to half-fibre geometry to visualise cracks post-mortem. The crack path mechanism during the test was touched upon in Figure 96 and Figure 97, multiple scenarios can be outlined. (i) A change in failure mode suggests the cracks propagate in mode II, (deflection or) change to a mixed-mode fracture in the middle of the fibres before reconverting to mode II on the outskirts of the fibre-and-interphase system. (ii) A crack propagating along the fibre/BN interface was arrested at a strongly bonded area, inducing secondary cracks along the BN/matrix interface to propagate next. (iii) Multiple cracks formed simultaneously in weakly-bonded zones.

In addition to being able to relate failure-mode to microstructure, the trench push-outs present multiple advantages: the thickness or exact testing length of the fibre can be controlled, the top and bottom of the fibres can be concurrently tracked, the tests can be stopped and/or resumed at any point, and the FIB surface finish surpasses that of the mechanical polishing in quality. The trench push-outs are easy to fabricate, re-producible, and provide clearer visualisation of micro-scale events during the fibre push-out. Trench push-outs also enable further analysis of the effect of thickness/total push-out length on the measured ISS. When compared to traditional fibre push-outs, the new technique inherently transposes multiple dependencies on the number of artefacts around – and in – the fibre (including its unbroken length), to a somewhat unique dependency on unbroken fibre length (because artefacts can be visualised). The problem thus transforms from being both defect-controlled and load-controlled, to only load-controlled (reducing the need for Weibull statistics). By virtue of being performed in-situ, the trench push-out ensures monitoring of tip damage, which can occur without being detected during traditional push-out testing of ceramic fibres.

Despite resolving some assumptions of the traditional fibre push-out, trench push-outs present several limitations including the continuing lack of full 3D information, the access to specialised equipment, and the time of milling which can take longer than grinding. Another limitation lies in the uncertainty in milling depth in the trenches as any inhomogeneity in milling can result in the fibre being pushed out to touch the underlying redeposition material, however this can be noticed before starting tests. An additional artefact in performing tests on half-fibres is limiting the FIB damage. Indeed, by modifying the original fibre geometry, preferential milling of the BN over the SiC can occur, thus changing the desired geometry to a more complex system. Testing on half-fibres results in the BN being able to resurface towards the free boundary – a phenomenon unique to half-fibres, which induces a release of compressive stresses which would otherwise accumulate in the interphase with testing time. Finally, half-fibre trench push-outs are limited by the precision to which one can section half a fibre; this can be alleviated by measuring the top-surface arc length and modifying equation [35] to account for any custom geometry (as the perimeter of the half fibre may in practise be slightly higher or lower than πR). An FEM model in future work would help validate any hypothesis outlined herein.

6.2.6 Summary (Trench Push-Out)

A novel trench fibre push-out was introduced for SEM in-situ investigation of interfacial properties in CMCs. The FIB preparation of samples was relatively simple and required no thinning of the samples. The new method further enabled live monitoring of the push-out mechanism, thus explaining the stochastic nature of its results. The numerical data from calculating frictional interfacial shear stresses on half and full fibres showed reliability and the mechanical properties matched expected trends when comparing the rougher Tyranno type SA3 fibres to the Hi-Nicalon fibres. Failure mechanisms during the fibre push-out were investigated with most fibres showing mixed-mode failure (with simultaneous inside and outside debonding, although this may be an artefact of trench testing half fibres) and some fibres with defective interphases showing linking of smaller cracks before push-out. Transverse cracks in the neighbouring CVI SiC were seen to have propagated before fibre sliding, accompanied by a coiling and resurfacing of the damaged BN interphase. All these micromechanical events were observed leading to potential explanations in the scatter of data acquire from more traditional push-outs. Finally, the benefits and limitations of the trench push-out technique were discussed.

6.3 DIC

The use of digital image correlation (DIC) was used to gain insights on the micro-scale displacements during trench push-out testing. DIC testing of micro-tensile specimens on a carbon-based CMC has been attempted[106] but shown to be highly challenging for fibre diameters ranging from 1 to 50 µm. Two different types of in-situ speckle patterning were used. Firstly, a layer of 8 nm of Au was sputtered on the surface of a Hi-Nicalon type S with a thick BN sample using a Leica ACE600 Coating instrument; the sample was subsequently imaged at high ionic (Ga^+) currents on a Zeiss dual FIB-SEM column to create a random speckling of the Au layer on the surface. This resulted in 200-nm round-like features (Figure 98.a and b) which were not homogeneous in size between fibres on a same trench. The use of a Pt or Au coating by means of the Gas Injection System (GIS) inside the dual FIB-SEM column might resolve this, as the deposition could have been more targeted and homogeneous. In order to increase resolution and homogeneity, the SEM column itself was used at

high electron currents to replicate patterns made using the FIB column; the result of which yielded a finer and more distinct (less bridging) speckle pattern imaged on Figure 98.d.

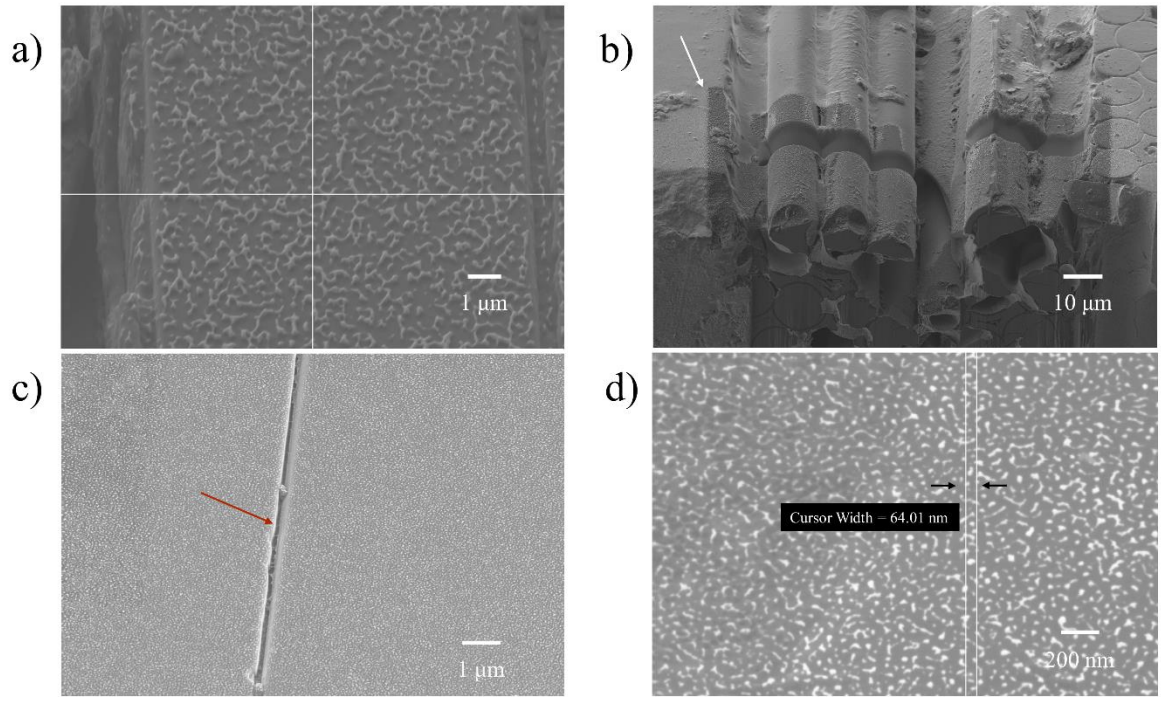


Figure 98: SEM micrographs showing in-situ DIC speckle patterns by (a, b) Au deposition on a Hi-Nicalon type S with a thick BN sample after trench milling with a white arrow on (b) showing the delimitation of the ion beam sputtering for the speckle pattern, and (c, d) by high-current electron sputtering on a Tyranno type SA3 with a thick BN sample showing a BN interphase with a red arrow on (c) and a measurement of speckle size on (d)

The heterogeneity in speckle size has somewhat helped in performing image correlation, as the bigger surface defects and impurities have provided greater contrast on the field of view scale[7]. Two regions of interest (ROI) on a trench push-out were interrogated. Region 1 consisted of a square region underneath the indenter tip, whilst Region 2 covered the entire lateral region of the trench push-out visible cross-section, thus spanning multiple fibres. ROI 1 was pre-processed with a 3 x 3 pixels Gaussian Filter, interrogated a 29 pixels-size, 3 pixels-step window using a GOM-Aramis software, and yielded a correlation value above 0.95. Results from DIC on ROI 1 revealed the magnitude of the strains observed near the tip on the upper-end of the fibre were negligible, even right before fracture (Figure 99.a). This suggested that load shedding across the fibre was homogeneous and that fracture before sliding was mainly dominated by interphase defects.
ROI 2 was pre-processed with a 4 x 4 pixels Gaussian sliding average filter, interrogated a 69 pixels-size, 4 pixels-step window, and yielded a correlation value of 0.7.

[7] *The analysis in this section was performed with the help of Thomas Zillhardt*

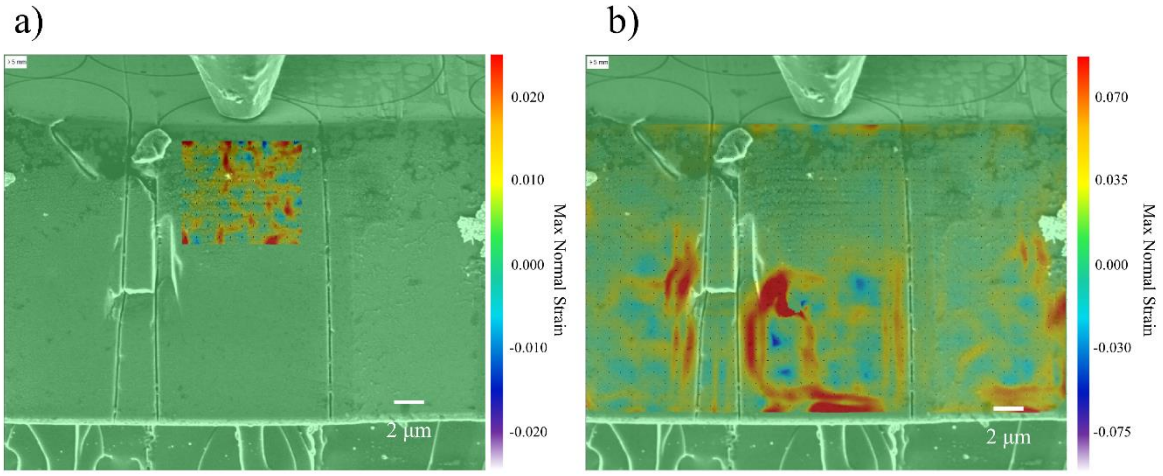


Figure 99: DIC analysis showing two interrogation windows on the same trench push-out fibre with a) maximum normal strain below the nano-indenter tip before fracture and b) a large interrogation window to focus on the fibre interaction

DIC results from Figure 99.b show that there was interaction with the central fibre's nearest neighbour, increasingly so around the defect connecting the fibres. Maximum strains measured reached 7% with minimal compressive strains, owing to the Poisson expansion of the fibre as it is pushed through. DIC thus provides complementary information as to the nature of fibre/matrix interactions, the effects of defects on strain distribution, and yield quantitative information on the strains involved. Since DIC is limited to surface information (when compared to DVC), one cannot extract information on out-of-plane tunnelling and comprehensive crack growth behaviour.

Noise levels on the DIC maps were significant. This may be resolved by increasing speckle size to ensure each speckle is 10 times the size of a pixel. In the case of maps on Figure 99, this magnitude stood at 50 nm for an average pixel size of 42.7 nm, thus increasing the chances of a speckle being mistaken for a microstructural feature and inducing heightened noise signal when analysing displacements.

6.4 Micro-Tomography of Composites

Thus far, the analysis of the crack mechanism and micro-scale strains has been limited to the 2D in-plane information provided by secondary electron imaging. Micro- and nano-scale X-ray tomography were thus performed on a Zeiss X-Radia microscope whilst nanotomography (Section 6.5) was performed on a Xradia nanoXCT instrument at Manchester Imaging Facilities (MIF)[8] – both techniques enabling more 3D information to be extracted.

Cracks in SiC_f/SiC minicomposites tested in tensile conditions have been found to be segregated to microcracks in most parts – with very few cracks developing to clearly identifiable full size helixes around fibres[236,237,238]. Synchrotron tomography has enabled Chateau et al. to find that cracks break fibres after having fully cracked the surrounding matrix[236], and that as a result, fibres can fail in 2 different locations.

[8] Funding to cover instrument cost was provided by the Royce Institute under the *Royce Student Equipment Access Scheme* university consortium.

The strains induced at the microscale can also be deduced from testing minicomposites using tomography techniques. Indeed, fibre centroids can be identified from reconstructed data, and the centroids can be traced back to look at fibre movement, as well as packing and twisting at tow-level. X-ray Computed Tomography (X-CT) scans were performed on a Zeiss X-Radia microscope with an accelerating voltage of 80 keV, 7 W power, 88 µA current, a 40x objective and a 28 s exposure time per frame collecting 1601 projections for a final voxel size of 0.74 μm^3. Segmentation of the fibre, BN coating and CVI SiC interphase was achieved using Avizo (v.2019.2) with a combination of the magic wand (255 threshold), locking, watershed and filling tools.

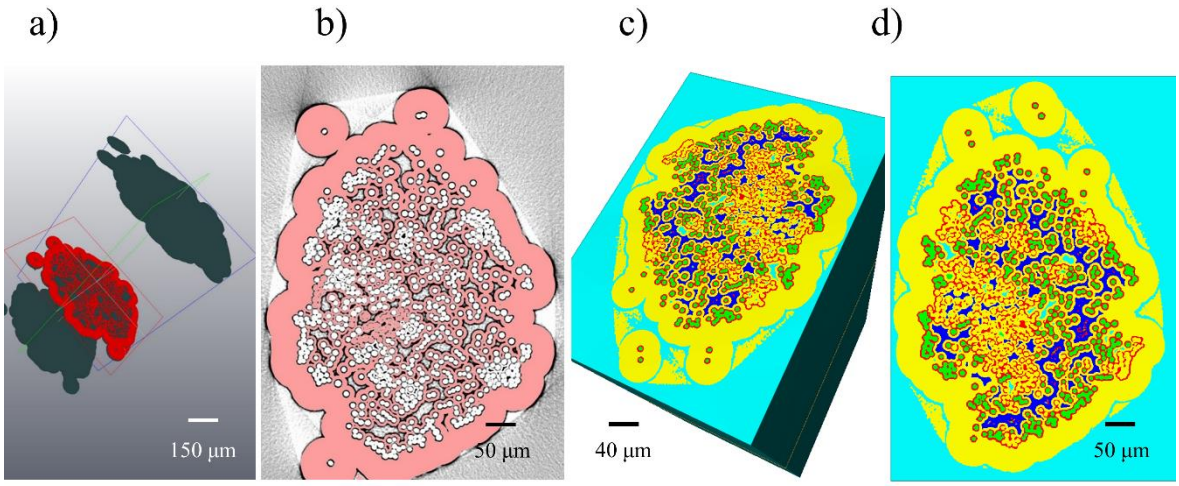


Figure 100: microCT scans of a SiC microcomposite single fibre-bundle using Avizo (2019.2) to perform (b) a segmentation of the CVI SiC in coral red and, (c) + (d) segmentations of the CVI SiC in yellow, the pores in blue, the fibres in green and the BN in red.

From segmentation of the tomography data seen in Figure 100, the CVI BN thickness was found to be homogeneous (3.0 ± 0.4 µm) but the CVI SiC thickness varied from 1.3 ± 0.4 µm to 7.2 ± 2.0 µm linearly from the middle of the tow to the edge of the tow. The smaller CVI SiC thickness value is comparable to values found in bulk materials under SEM measurements in Chapter 4 Section 4.2. The CVI SiC thickness on the fibres at the very edge of the tow were found to have an outer casing CVI thickness of 50 ± 7 µm.

The volume of voids was determined from segmentation and averaging values over all sections as 17.4 ± 11.1 %. No detectable (larger than the voxel size) cracks were found in the pre-tensile test, as-manufactured state.

6.5 Nanotomography

In order to visualise cracks propagating along the interphase/fibre region as well as any buckling and delamination of the interlayer in the trench during push-out – an experiment involving a microcomposite scanned under nanotomography was attempted. Minicomposites were used as smaller sample sizes allow easier rotation within tomography instruments[27]. Prior to scanning, minicomposites were mounted vertically using a combination of wax, cold-set epoxy and silver electrodag, subsequently laser ablated to 70 µm diameter needles and milled using a dual SEM-FIB column Zeiss Auriga instrument. The experimental steps (and associated locations) were outlined as a flowchart (Figure 101) and as follows:

1. Vertical mounting of minicomposites (Oxford)
2. Laser ablation of specimens to 70 µm ⌀ needles (Manchester)
3. Trench milling using FIB (Oxford)
4. Quality control and specimen selection by means of micro-XCT (Oxford)
5. Initial nano-XCT scan, prior to mechanical testing (Manchester)
6. Mechanical testing of the ex-situ trench push-out (Oxford)
7. Final nano-XCT scan post-indentation (Manchester)

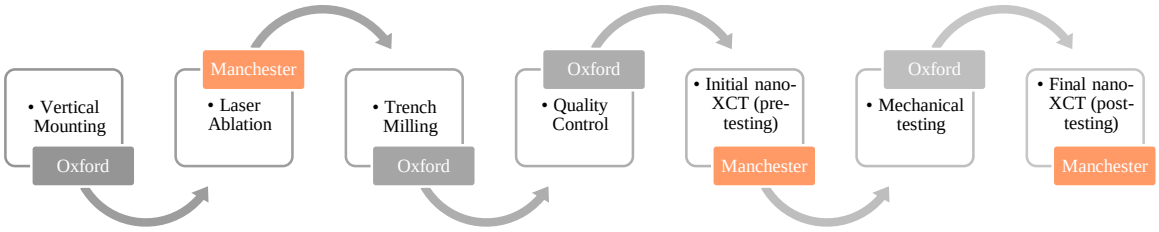


Figure 101: Flow chart for the nanoXCT minicomposite experiment

Step 1 involved five methods including wax, silver electrodag, high-temperature cement, cold-set epoxy and tape. A combination of wax, cold-set epoxy and dag worked the most successfully, leading to minicomposite sections standing upright (Figure 102.a).

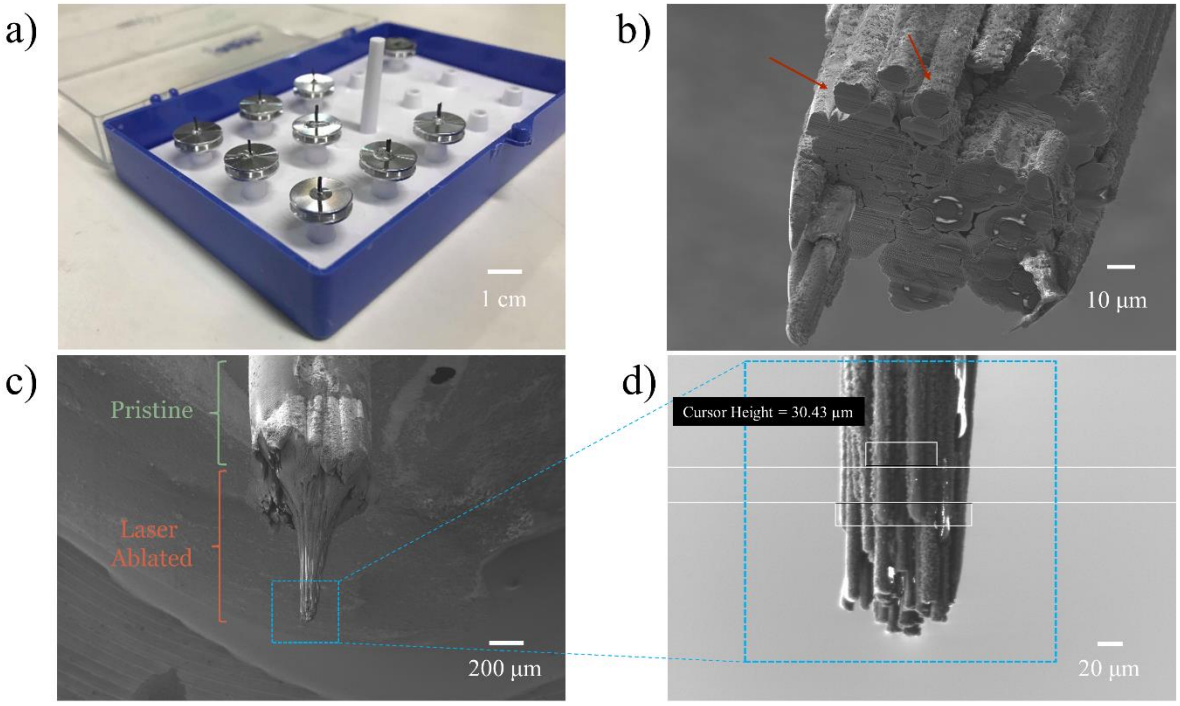


Figure 102: Sample preparation steps of the nanoXCT minicomposite experiment showing a) minicomposite needles standing upright before laser ablation, b) needle cross-section after step 3 (laser ablation and FIB milling) showing complete BN disintegration on the outskirts of the needle from laser ablation (red arrows), c) millimetre-scale view of the minicomposite after step 2 - laser ablation, and d) cross-sectioning and trench milling by focused ion beam to create a trench 30.43 µm away from the milled surface.

Step 2 involved performing the laser ablation, which made use of a long pillar recipe sending 7.6 pulses per second to 200 µm depth in two layers on a microPREP 3D Specimen Preparation System (LA)-ICP-MS at the XMIF (Manchester Imaging Facilities). The laser ablation struck the balance between power W and area dose[245]:

$$\frac{W \times 10}{Number\ of\ Layers\ \times Number\ of\ Pulses} \approx 0.2 \qquad [38]$$

Equation [38] is valid for silicon (the usual reference material in laser ablation) whilst the rate ratio is less than 0.2 for softer materials and greater than 0.2 for harder materials, including CMC's. Resulting geometries (after laser ablation) of the needles were illustrated in Figure 102.c.

Step 3 involved the milling of a trench by a Zeiss Auriga dual SEM-FIB instrument, using high 16 nA and 20 nA currents for blunt cuts, and smaller 2 nA current for finer finishes.

Figure 102.c and Figure 102.b were testaments to the quality of the needle and the trench after both laser ablation and focused ion beam Ga^+ milling respectively. Figure 102.b also highlighted the fact that the BN was consumed on the outer edges of the minicomposite close to the laser source (red arrows). The remaining BN seemed to have charged (in white in the centre), and therefore most probably degraded to a boria state. The attempted mechanical testing was performed on non-charged fibres. Following milling of the trenches, the quality of the needles was assessed in step 4 through the use of micro xCT before the first nanotomography scans, the milled surface (Figure 103.a) showed clean BN interphases whilst the trench (Figure 103.b) showed redeposition material, which

was subsequently removed. The clean trench could be seen in the radiographs (Figure 103.c) taken before nanotomography during step 5.

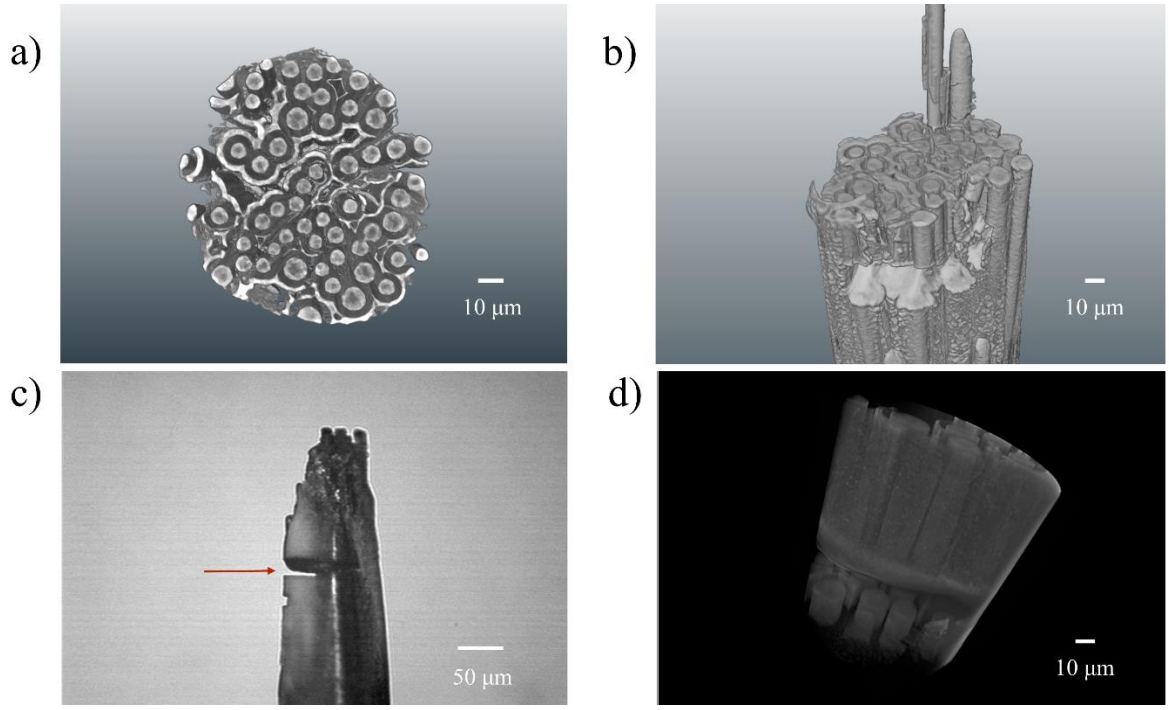


Figure 103: Step 4 and 5 of the nanotomography experiment involving (a) top and (b) diagonal views of the minicomposite needle with the milled trench, and (c) + (d) radiographs before nanotomography showing the trench from the side (red arrow)

Scans on the Zeiss XRadia microscope were performed with an accelerating voltage of 110 keV, 10 W power, 90.7 µA current, a 40x objective, a 342 µm field of view and a 20 s exposure time per frame for a final voxel size of 0.7 μm^3. The nano X-ray source ran at 35 kV and 25 mA, with the characteristic peak from the Chromium anode - Cr-kα at 5.4 keV. The nanoCT scans had a voxel size of 0.129 µm and a FoV of 64 x 64 microns (x2 detector binning) - performed in phase contrast mode (using Zernicke optics) with a 60s exposure time per projection and 801 projections in total (over 180 degrees).

Step 6 was the limiting factor of the experiment. Micromechanical testing of singular fibres within the minicomposites were not plausible, most probably due to rod buckling. A repeat experiment of the above would make use of bulk materials (other than minicomposites), and the mounting of the composites in step 1 would make use of both a stronger resin and a higher "imbed" ratio of fixed/free material (i.e. less material would protrude from the mounting in Figure 102.a).

The experiment – if successful – could determine the maximum a-length for stable crack growth. The nature of the sub-micron resolution of nanoCT on minicomposite can in theory create sufficient contrast in defects for digital volume correlation to then be applied, and measure fibre movement relative to one another during testing. The technique can further track changes in trench size from testing, and detect micro-cracking from neighbouring fibre movements. The observed failure behaviour can be compared to that of tensile tests also performed on Tyranno type SA3 minicomposites, which displayed relatively long pull-out lengths, fibre/interphase debonding and matrix crack formation[65]. The inside debonding at the micro-scale was also observed on Hi-Nicalon type S fibre-based minicomposites in the same study.

It has been observed by Hilmas et al. that X-ray attenuation of the BN is too low for it to be discernible with any crack[27], rendering tomography alone inadequate, and DVC the only method to capture cracks propagating within or around the BN interphase. The same study found that fibre breaks were not correlated with any microstructural component, and that cracks propagating within the matrix had complex trajectories (highly tortuous in nature), bifurcated and merged – thus rendering the chance of capturing a specific crack within the interphase very limited. This then helps confirm that a repeat experiment would make use of a more traditional CMC architecture.

6.6 Lamellae, TKD & TEM

In-situ experiments in this chapter helped elucidate which mechanism dominated, however it was uncertain which factors at the finer microscale had effects on the majority of the observations made so far. TKD & TEM measurements were therefore performed on CMC surfaces. A lamella of a Hi-Nicalon type S sample with a thick BN was prepared using an Auriga © Dual FIB/SEM column and made 15 µm wide, 6 µm tall and less than 93 nm thin for electron transparency. The lamella was dug from a location where a fibre push-out from Chapter 4 had been produced, as seen on Figure 104.a. During lamella thinning, a noticeable bend in the specimen occurred as residual stresses were released, but the overall lamella thickness could still be measured (Figure 104.b). These stresses were either introduced during fabrication or during the push-out. Pattern quality maps were reported to be better than grain orientation maps for TKD on SiC_f/SiC composites (with 82 % cubic and 18 % HCP SiC) however the drift during map acquisition meant that pattern quality was not sufficient enough to look at grain orientation – grain size however averaged 200 nm in diameter inside the fibres.

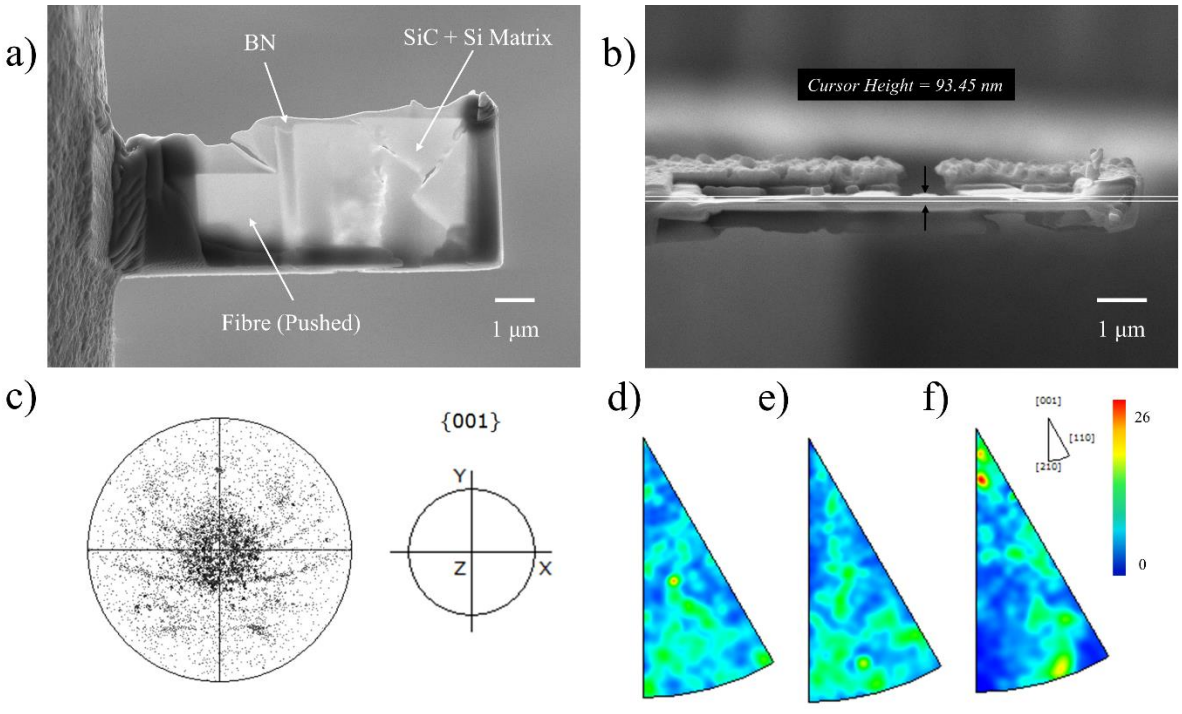
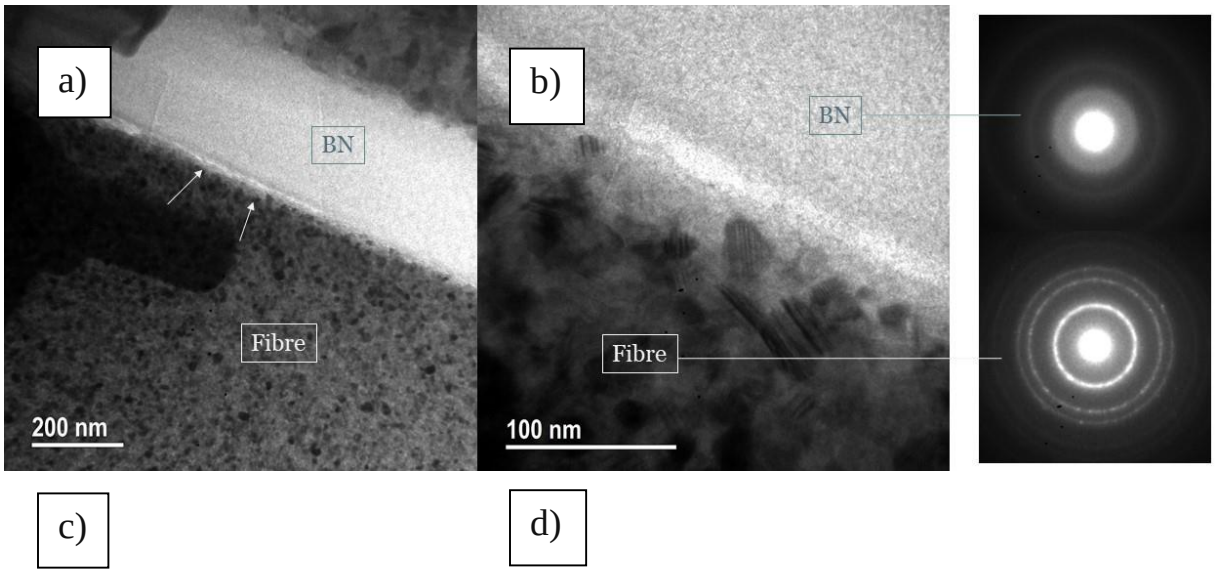


Figure 104: Lamella thinning after push-out showing (a) a cross-section after lift-out with the target fibre, the BN interphase and the matrix, (b) measuring the thickness of the lamella, (c) Wulff sphere of the BN from Transmission Kikuchi Diffraction (TKD) showing {001} texture and (d – f) inverse pole figures from stereographic projections for the x, y and z directions respectively

The TKD patterns obtained from the BN interlayer were convoluted at 5° with 72.4 % zero solutions but showed a slight texture in {001} on the non-negative solutions, suggesting the BN interlayer remained largely amorphous (only 27% crystalline). The BN can thus be assumed to have been turbostratic in nature but only with short range order (nano-scale grains oriented in different directions, imbedded in an amorphous BN structure) as was previously imaged in Figure 71.

Some TEM work was performed on the same lamella to get a better grasp of where the crack had propagated during the push-out. Bright field images on Figure 105 were obtained on an JEOL 3000F TEM instrument and showed the crack had propagated between the fibre and the BN interlayer (Figure 105.a and b) – similar observations to those made by Gavalda-Diaz[222]. Diffraction rings obtained from the different composite components showed [redacted] clear SiC crystalline rings for the matrix from which volumetric strains could be extracted (Figure 105.e and Figure 105.f). Assuming an unstrained interplanar {111} d-spacing of 2.51 Å in 3C-SiC – the rings from the diffraction patterns yield an interplanar spacing of 2.65 Å (equivalent to a strain of 5.57 % from unstrained) and 2.54 Å (equivalent to a strain of 1.19 % from unstrained) in spacing further away and close to the crack respectively. Assuming an elastic modulus of 380 GPa for Hi-Nicalon type S fibres (quoted from *NGS Advanced Fibers Co., Ltd* data at the beginning of Chapter 4) one can estimate the residual stresses (in plane-stress condition only) to values of 23 MPa and 8 MPa away and close to the crack respectively. These values are further increased if a reduced modulus of 360 GPa measured on the fibres (Chapter 3) is used.



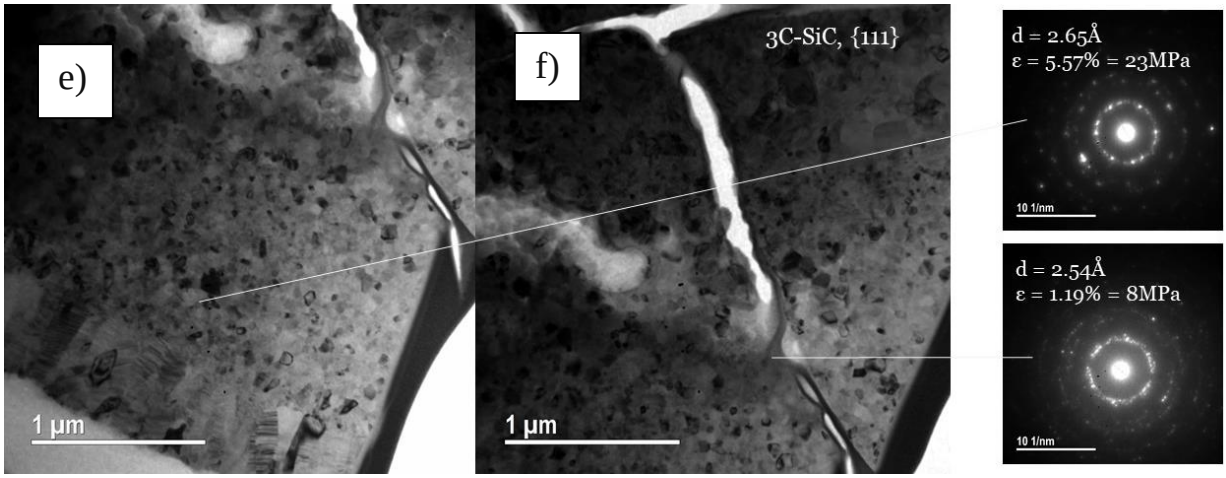


Figure 105: TEM bright field images of the lamella after push-out showing (a) + (b) a crack propagating between the BN and the fibre, [redacted], (e) + (f) diffraction rings from the matrix far and close to a crack.

6.7 K_C Fracture Toughness Measurements

6.7.1 Micro-Cantilevers on BN

The final micro-mechanical tests involved micro-cantilevers to estimate a fracture toughness for the interphase. Cantilevers with equilateral-triangle cross-sections, approximately 2 µm in width and 6-7 µm long were milled with trenches at 4 nA currents (polished with 120 pA currents) on samples with Hi-Nicalon type S fibres and a medium-sized BN interphase. The fracture toughness of the BN interlayer was measured by positioning the cantilevers on fibres parallel to the polished surface, with the BN interlayer acting as a notch 2 µm away from the cantilever edge (Figure 106.a). The advantage of performing micro-cantilevers on CMC's was not having to pre-mill notches, the crack was guaranteed to propagate in the weaker interphase.

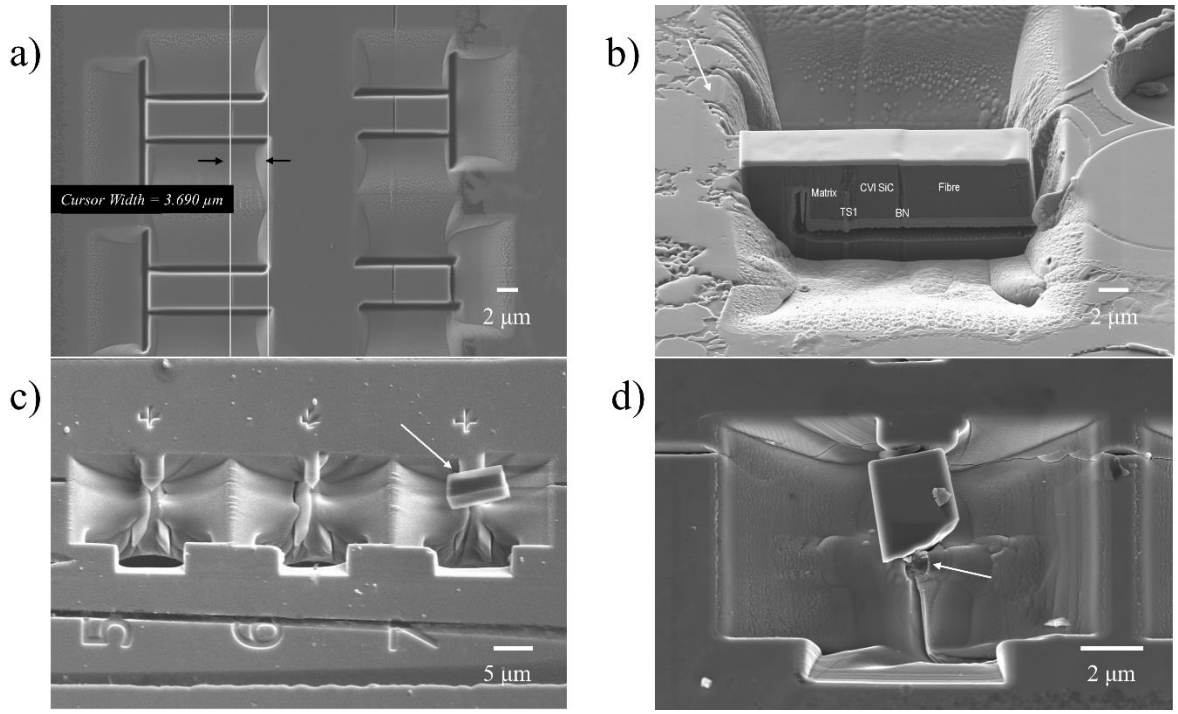


Figure 106: SEM micrographs of (a) micro-cantilever pre-cut sample preparation, (b) cantilever before finishing cuts showing all CMC constituents, (c) micro-cantilevers after testing showing a fractured cantilever on re-attachment by electrostatic attraction, (d) micro-cantilever fracture at loading point.

Twelve micro-cantilevers were tested on a G200 nanoindenter instrument (MicroMaterials) using a Berkovitch tip, a single load-point and the Nanovision Interactive Scan method. A tip displacement rate of 10 $nm.s^{-1}$ and a surface approach detection stiffness criterion of 100 $N.m^{-1}$ up to interphase failure (a maximum depth limit of 1 µm was additionally set in the direction of tip approach) were used.

Behaviour of the cantilevers during and after testing was varied, with some tests resulting in the cantilever detaching and re-attaching on the fractured end by electrostatic van der Waals attraction (Figure 106.c). The majority (7) of the cantilevers fractured at the BN interphase; some cantilevers fractured at load point after BN interphase failure (Figure 106.d).

EDX was performed on the cantilevers surfaces after testing using a Zeiss Merlin EDX instrument with a current of 5 keV and a working distance of 8.5 mm. It was found that some BN was still present on the fracture surface (Figure 107.b and Figure 107.d) – suggesting the crack had propagated inside the interphase itself, or at the fibre/BN interface. Oxygen was also prevalent on the fracture surface (Figure 107.c), suggesting preferential oxidation of the interphase might have affected the brittleness and the interfacial properties of the BN. However, since EDX studies were not performed immediately after testing, it cannot be determined whether Oxygen ingress in the cantilever had occurred prior, or after mechanical testing. The EDX Gallium map on Figure 107.e suggested that despite using high currents for cuts during sample preparation, little to no Gallium ion damage (implantation) was observed on the micro-cantilever itself.

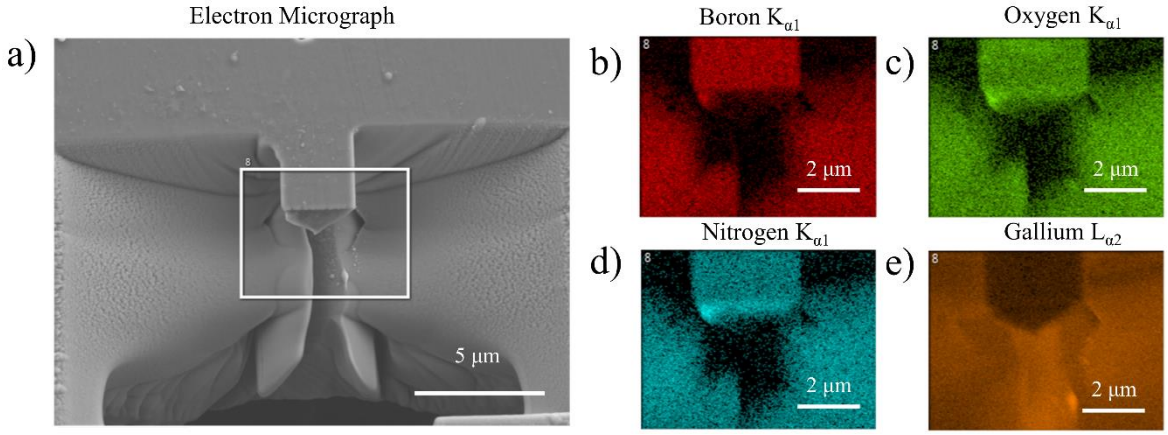


Figure 107: SEM EDX studies on the cross-section of a fractured micro-cantilever at the BN interphase

From the load-displacement data during micro-cantilever testing (Figure 108) added to the milled-cantilever dimensions measured during sample preparation, an estimate of the fracture toughness of the BN interphase could be calculated using equation [39][246]

$$K_{IC} = \frac{6PL}{bh^2}\sqrt{\pi a}.F\left(\frac{a}{h}\right) \qquad [39]$$

where P is the load at fracture, L is the distance between the notch (e.g. the BN interphase) and the point of application of load, b is the beam width, h is the beam height and a is the depth of the notch; the first half of the equation is the fracture stress calculated by beam theory; $F_{(a/h)}$ is a scaling factor dependent on microcantilever geometry and can be assumed by the first 4 terms of a Taylor Expansion[246] to be:

$$F\left(\frac{a}{h}\right) = 1.12 - 1.39\left(\frac{a}{h}\right) + 7.32\left(\frac{a}{h}\right)^2 - 13.1\left(\frac{a}{h}\right)^3 + 14.0\left(\frac{a}{h}\right)^4 \qquad [40]$$

The "a" notch depth was measured as the surface damage induced on the BN by the FIB gun (when compared to the SiC surface recession), estimated at 120 ± 10 nm. The estimate remains within the 80 nm depth used to map the indents in section 3.2.2 (from which indents managed to reach the deeper end of the BN) and therefore constitutes a maximum notch depth. This FIB damage also implies that other micromechanical test geometries on SiC_f/BN/SiC composites (including those highlighted in previous chapters) will be faced with surface implications.

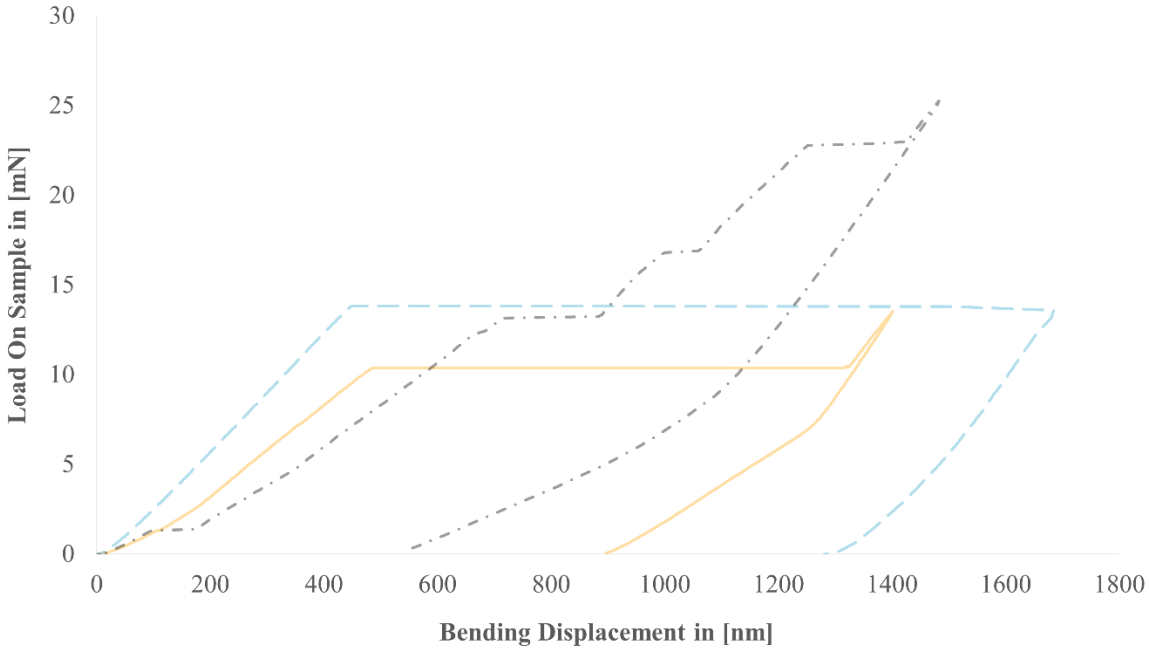


Figure 108: Load displacement data from three micro-cantilever tests in bending performed on Hi-Nicalon type S fibre with a medium-sized BN

Of the cantilevers which had a clear, discernible maximum load at fracture, as well as no cantilever fracture or failure outside of the interphase, three of the tests were used for further analysis. The measurements and results for and from K_{IC} calculations are included in Table 19:

Table 19: Fracture toughness estimates of the BN from micro-cantilever testing of SiC_f/SiC composites

Parameter	-	Units	Beam 1	Beam 2	Beam 3
Maximum Load	P	mN	15.7 ± 0.1	10.3 ± 0.1	13.8 ± 0.1
Beam Height	h	µm	2.7 ± 0.1	2.7 ± 0.1	2.7 ± 0.1
Beam Width	b	µm	2.9 ± 0.1	2.7 ± 0.1	2.8 ± 0.1
Notch Depth	a	nm	120 ± 10	120 ± 10	120 ± 10
Notch – Load Point Distance	L	µm	3.1 ± 0.2	3.0 ± 0.2	3.1 ± 0.2
Geometry Scale Factor	$F_{(a/h)}$	-	1.078	1.078	1.078
Fracture Toughness	**K_{IC}**	**MPa.m$^{0.5}$**	**7.6 ± 2.4**	**5.5 ± 2.3**	**6.9 ± 2.0**

The average fracture toughness of the BN interphase by micro-cantilever testing was therefore calculated at 6.7 ± 2.4 MPa.m$^{1/2}$. This value can be contrasted both to the macro-level measurements in CMC's with Nicalon/SiC composites[247] having reached fracture toughness of 5-9.5 MPa.m$^{1/2}$ and to Hi-Nicalon fibres alone[248] manifesting a fracture toughness of 1.1 ± 0.2 MPa.m$^{1/2}$. These values are also on par in magnitude when compared to values found in models, such as Callaway[48] (3.7 – 6.3 MPa.m$^{1/2}$ for minicomposites with Hi-Nicalon type S fibres). The same source cites that this finding induced a severe constraint on allowable interphase thickness. Overall, FIB machining (whether testing micro-cantilevers, micro-pillars or other geometries) is believed to induce Ga^+ damage and overestimate the measured toughness[138].

6.7.2 Indent Crack Measurements for the MI Matrix

Concurrently, the fracture toughness of the melt-infiltrated (MI) matrix was obtained after nanoindentation (performed in Chapter 3) on constituents using the fitted experimental Dukino method[249] from nano-indent dimensions:

$$K_C = 0.015 \times \frac{\sqrt{\frac{2}{1+\frac{2}{\pi}}}}{\sqrt{\frac{\frac{n}{2}}{1+\frac{n}{2\pi}\times sin\frac{2\pi}{n}}}} \left(\frac{a}{l}\right)^{\frac{1}{2}} \left(\frac{E}{H}\right)^{\frac{2}{3}} \frac{P}{c^{\frac{3}{2}}} \quad [41]$$

where n is the number of radial cracks surrounding the indent, E and H are the elastic modulus and hardness measured from the indent, respectively, P is the maximum indenter load, and a, c, and l are geometric properties (a, c & l being the indent, crack and total lengths respectively). The complexity of the equation stems from the alpha coefficient in the original LEM Lawn-Evans-Marshall equation adapted to Berkovich geometry[138] and lower indentation depths (the original equation was only valid for single-phase ceramics with radial cracks much larger than indent dimension). The crack lengths from the indentation tip c were measured thrice individually after testing under SEM. Figure 109 showed that the crack length from indent tip varied considerably with cracks being arrested at longitudinal fibre tows when propagating from the matrix, and cracks arresting at tow edge or neighbouring fibre BN when propagating from within the fibre tow. Figure 109 further showed that cracks propagating intragranularly within the matrix, regardless of whether traversing β-SiC grains or residual silicon.

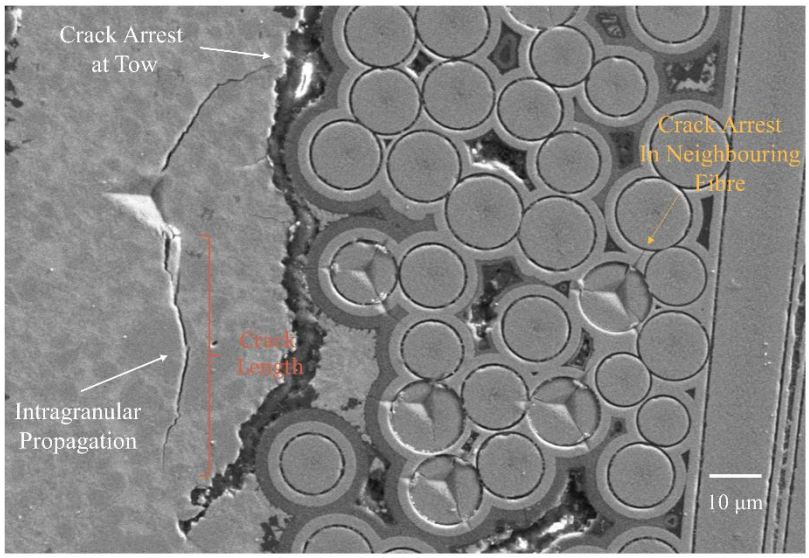


Figure 109: SEM micrograph of a CMC with Tyranno type SA3 fibres and a thin BN interphase after indentation, showing intragranular cracks propagating in the melt infiltrated matrix from the indentation tips, and crack arrests at tow entries or neighbouring fibres when indenting fibres directly.

Experimentally, only a fraction of the indents performed at 600 nm in depth had cracks radiating from the prints left on the sample surface. This could imply that higher toughness values are being censored from the dataset, as cracks might have propagated inside the material instead, or that there was a lack of nucleation fracture from blunting of the indenter tip. Indents performed at greater depths (of 1000 nm or more) and inside fibres were restricted by the fibre edges and the BN interlayer. Indents for fracture toughness measurements should therefore be performed at shallower depths (with a limit of 500 nm) and inside fibres oriented parallel to the polished surface. These conditions would allow cracks to propagate further, however fibre anisotropy in microstructure should be taken into account.

Table 20: Fracture toughness inputs and calculations from nanoindentation crack measurements

Geometric Constraint	**Young's Modulus**	**Hardness**	**-**	**Maximum Load**	**Fracture Toughness**
	GPa	*GPa*		*mN*	***MPa.m$^{1/2}$***
a/l	E	H	E/H	P_{max}	**K_{IC}**
0.67	145.1	18.3	7.91	576	**12.3**
0.58	219.1	23.9	9.15	576	**9.4**
0.62	155.3	20.1	7.71	576	**9.6**
0.65	161.2	20.6	7.82	576	**10.8**
0.62	142.5	21.5	6.62	576	**8.7**
0.67	157.5	22.5	7.00	576	**11.9**

The variation in crack length contributed heavily to the variation in fracture toughness estimations. Data from Table 20 yielded an average fracture toughness K_{IC} of 10.4 ± 1.3 MPa.m$^{1/2}$ for cracks propagating in the melt-infiltrated matrix. This was on the higher end of the fracture toughnesses given in the previous section (5-9.5 MPa.m$^{1/2}$ range reached in Nicalon/SiC composites[247]). When compared to the BN interphase fracture toughness (6.7 ± 2.4 MPa.m$^{1/2}$), the result showed that cracks dissipated more energy propagating in the melt-infiltrated matrix than when arrested at a BN interphase. The main limitation of the Dukino method lay in the lack of consideration of any residual stresses[138].

6.8 Chapter Summary

Several techniques were investigated to tackle the ongoing limitations of ex-situ technique of damage development observations in CMC's. Firstly, a novel trench fibre push-out was introduced for SEM in-situ investigation of the failure mechanism during fibre push-out. Said mechanisms were found to lie in fibres showing mixed-mode failure (with simultaneous inside and outside debonding) and some fibres with defective interphases showing linking of smaller cracks before push-out. Transverse cracks in the neighbouring CVI SiC were seen to have propagated before fibre sliding, accompanied by a coiling and resurfacing of the damaged BN interphase. Damage accumulation was more quantitatively assessed with the use of in-situ DIC, where it was observed that in-plane strain measurements developed in neighbouring fibres, but that no significant strain was noticed adjacent to tip/fibre contact. Secondly, a trench push-out was attempted on a minicomposite needle with quality assessment of laser ablation and FIB milling changes achieved through nano-XCT; it was found that the complexity of the experimental set-up made it challenging to draw any conclusion from the data. The use of TEM & TKD techniques from a thinned lamella lift-out after ex-situ push-out gave insights on both the microstructure and texture of the material. Finally, micro-mechanical techniques were used to assess the fracture toughness of the BN interphase by means of micro-cantilever testing (6.7 ± 2.4 $MPa.m^{1/2}$), and the fracture toughness of the melt-infiltrated SiC-Si matrix by means of crack measurements post-Berkovitch indentation (10.4 ± 1.3 $MPa.m^{1/2}$).

Chapter 7 • Conclusions

Mechanical testing of the BN interphase in SiC_f/BN/SiC composites for lifing models remains a challenging endeavour. The body of this work attempted to give an overview of its mechanical performance at the micro-scale, which were contrasted to existing macro-scale properties. Microscale data gave more precise inputs for lifing models, without needing to resort to data fitting of macro-testing results.

The composites were on the first hand subjected to room-temperature characterisation by means of nano-indentation of all constituents in Chapter 3. This was followed by descriptions of the development of several micro-mechanical techniques, including the fibre push-out, push-in and push-back in the same chapter; the goal of which was the probing of the BN interphase alone. The experimental steps and variables considered – prior to testing the CMC material itself – attested to the micro-mechanical technique's complexity.

The techniques developed in Chapter 3 were then used to investigate material-dependent variables and their effects on the change in micro-mechanical behaviour measured in Chapter 4. The parameters tackled included the variability in measurements from tow location at weave-architecture level (inter-tow), and tow-level (intra-tow), where it was found that both cases (intratow or intertow) had statistically different populations by means of t-tests. The variables investigated also included the thickness of the BN interphase, the nature of the fibre type, cyclic testing, interphase doping levels and the number of neighbouring fibres (which could be directly correlated to tow denier).

The wealth of parameters considered in both Chapters 3 and 4 demonstrated that the experimental simplification of the fibre push-out method – amongst its sister techniques – often performed in literature[21,34,66], is inadequate. Prior to this work, authors resolved to testing a few dozen fibres[96,99,112,120], whilst performing highly complex data fitting. Conversely, the information in this thesis included well above 3,000 fibre push-out tests alone, thus apprising which variables should be considered over others. The micromechanical contribution from the interlayer was most pronounced when its thickness was modified, or when it was doped. The reproducibility of the measurements after statistical analyses showed that thicker interphases helped narrow the spread of ISS measured, but at the expense of a more pronounced degradation in oxidation resistance.

As such, experiments in Chapters 3 and 4 were then reproduced in Chapter 5 on ceramic-matrix composite samples exposed to high relative humidity and high temperatures respectively. It was found that the added presence of water had more noticeable repercussions on the micro-mechanical performance, when contrasted to heightened temperature exposure in vacuum. This suggested that future tests on the CMC for lifing purposes should be performed with steam-exposure, in-situ. Indeed, despite results from these chapters, the dominating failure mechanism still needs to be observed. This led to the development of miscellaneous micro-mechanical techniques performed in-situ (both in SEM, micro and nano-XCT for full internal visualisation and characterisation), including the fibre trench push-out – with and without DIC – and micro-cantilever testing in Chapter 6.

Main concluding remarks for CMC lifing from this thesis include:

- Measured properties of the BN interphase at room temperature including, but not limited to:
  - Modulus: 25.9 ± 5.4 GPa
  - Hardness: 1.3 ± 0.1 GPa
  - Fracture Toughness: 6.7 ± 2.4 $MPa.m^{1/2}$
  - Mean Interfacial Shear Strength: Varies significantly (dependent on fibre type, interphase thickness, all parameters highlighted above, also dependent on micro-mechanical test employed)
  - Frictional Sliding Resistance: 4 ± 1 MPa (Hi-Nicalon type S only)
  - Plastic Energy Release Rate: 16 $J.m^{-2}$ (Hi-Nicalon type S only)
  - Debonding Toughness Γ: 13.3 $J.m^{-2}$

- Optimised experimental parameters for testing of CMC interphases by fibre push-out including details on the tip:fibre size ratio, sample thickness and displacement rate to maximise testing success rate and minimise tip damage on the fibre itself.

- A need for intra-tow variability to be stressed over the importance of inter-tow variability in measurements of mechanical properties, although both were found to be statistically relevant.

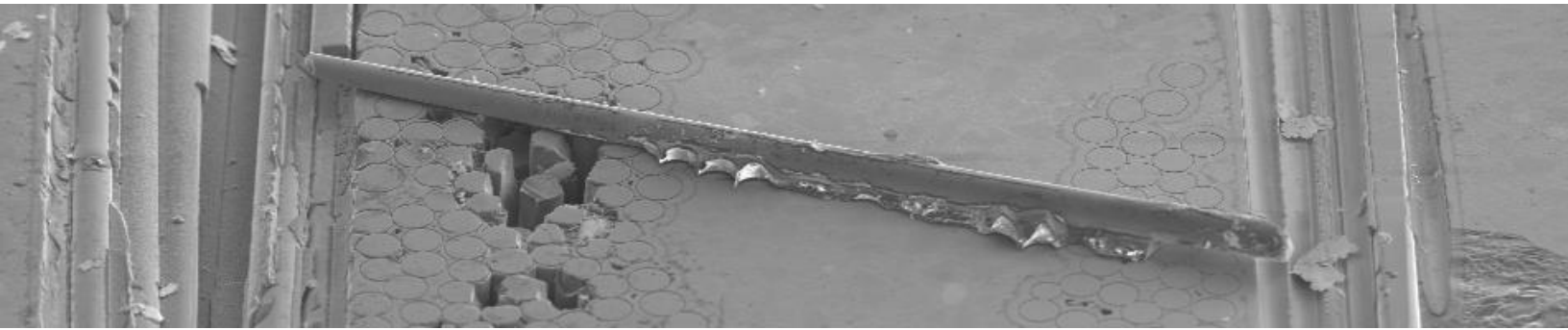
- A strong correlation of number of direct neighbouring fibres and measurements of micro-mechanical properties was found, leading to a relation with tow denier.

- Degradation of the composites by exposure to 95 % relative humidity resulted in a significant decrease in mechanical performance, wherein the permeability of the CMC was shown to be affected at longer exposure times, and differences in mechanical performances between – and within tows – were noted.

- Degradation of the composites via intermediate-to-high temperatures (up to 650 °C) in vacuum showed little to no change in micromechanical performance, with an interfacial strength retention ratio of 79.1% measured.

- In-situ tests by means of trench fibre push-outs and x-ray based computed tomography resulted in an appreciation for the complexity of failure mechanism(s) and its(/their) dependency on variables highlighted in preceding chapters.

In the context of work by Rolls-Royce plc, the body of results yield both quantitative and qualitative information which can be incorporated in both coupon and component lifing models. The academic merit of this work lies in the investigation of variability in measurements of composite interphase properties, as well as the development of micromechanical testing techniques for a clearer understanding and visualisation of the damage mechanisms at hand. The latter helped confirm which theories behind fibre push-outs best fitted observed experiments.



Chapter 8 • References

1. DiCarlo A., J. Advances in SiC/SiC Composites for Aero-Propulsion. *NASA Technical Report TM-2013-217889* (2013).
2. Zishan, C., Hejun, L., Qiangang, F. & Xinfa, Q. Tribological behaviors of SiC/h-BN composite coating at elevated temperatures. *Tribol. Int.* **56,** 58–65 (2012).
3. Rice, R. W. BN Coating of Ceramic Fibers for Ceramic Fiber Composites. *BN Coat. Ceram. Fibers Ceram. Fiber Compos.* (1987).
4. Bansal, N. P. & Lamon, J. Recent NASA Advancements in SiC/SiC Materials and Processes *Ceramic matrix composites : materials, modeling and technology*. **4**(7) 221-230
5. Hay, R. S. & Petry, D. Fiber strength with coatings from sols and solutions. in *Proceedings of the 20th Annual Conference on Composites, Advanced Ceramics, Materials, and Structures-B: Ceramic Engineering and Science Proceedings, Volume 17, Issue 4* 43–52 (John Wiley & Sons, Inc., 2009).
6. Evans, A. G., Zok, F. W., McMeeking, R. M. & Du, Z. Z. Models of High-Temperature, Environmentally Assisted Embrittlement in Ceramic-Matrix Composites. *J. Am. Ceram. Soc.* **79,** 2345–2352 (1996).
7. Spendley, P. R. Design Allowables for Composite Aerospace Structures. *Doctoral Dissertation, University of Surrey* (2012).
8. Krenkel, W. Cost effective processing of CMC composites by melt infiltration (LSI-process). in *Ceramic Engineering and Science Proceedings* (2009).
9. Zok, F. W. Ceramic-matrix composites enable revolutionary gains in turbine engine efficiency. *Am. Ceram. Soc. Bull.* (2016).
10. Rebillat, F. Advances in self-healing ceramic matrix composites. *Adv. Ceram. Matrix Compos.* 475–514 (2014). doi:10.1016/B978-0-08-102166-8.00020-7
11. DiCarlo, J. A., Yun, H.-M., Morscher, G. N. & Bhatt, R. T. SiC/SiC Composites for 1200°C and Above. in *Handbook of Ceramic Composites* 77–98 (Springer US, 2005). doi:10.1007/0-387-23986-3_4
12. Naslain, R. *et al.* Boron-bearing species in ceramic matrix composites for long-term aerospace applications. *J. Solid State Chem.* **177,** 449–456 (2004).
13. Christin, F. Design, Fabrication, and Application of Thermostructural Composites (TSC) like C/C, C/SiC, and SiC/SiC Composites. *Adv. Eng. Mater.* **4,** 903–912 (2002).
14. Krenkel, W. *Ceramic Matrix Composites: Fiber Reinforced Ceramics and their Applications*. *Ceramic Matrix Composites: Fiber Reinforced Ceramics and their Applications* (John Wiley and Sons, 2008). doi:10.1002/9783527622412
15. Bunk, W. J. G. Aerospace Materials, Situation and Perspectives. in *Advanced Aerospace Materials* 1–20 (Springer Berlin Heidelberg, 1992). doi:10.1007/978-3-642-50159-3_1
16. Padture, N. P. Advanced structural ceramics in aerospace propulsion. *Nat. Mater.* **15,** 804–809 (2016).
17. Zok, F. W., Maxwell, P. T., Kawanishi, K. & Callaway, E. B. Degradation of a SiC-SiC

Composite in Water Vapor Environments. *J. Am. Ceram. Soc.* jace.16838 (2019). doi:10.1111/jace.16838

18. Mackerle, J. Finite element modelling of ceramics and glass, an addendum – a bibliography (1998-2004). *Eng. Comput.* **22,** 297–373 (2005).
19. Rebillat, F., Lamon, J. & Guette, A. The concept of a strong interface applied to SiC/SiC composites with a BN interphase. *Acta Mater.* **48,** 4609–4618 (2000).
20. Yu, H., Zhou, X., Zhang, W., Peng, H. & Zhang, C. Mechanical behavior of SiCf/SiC composites with alternating PyC/SiC multilayer interphases. *Mater. Des.* **44,** 320–324 (2013).
21. Rebillat, F. *et al.* Interfacial Bond Strength in SiC/C/SiC Composite Materials, As Studied by Single-Fiber Push-Out Tests. *J. Am. Ceram. Soc.* **81,** 965–978 (2005).
22. Hinoki, T. *et al.* Improvement of mechanical properties of SiC/SiC composites by various surface treatments of fibers. *J. Nucl. Mater.* **289,** 23–29 (2001).
23. Yang, B., Zhou, X. & Chai, Y. Mechanical properties of SiCf/SiC composites with PyC and the BN interface. *Ceram. Int.* **41,** 7185–7190 (2015).
24. Kabel, J. *et al.* Ceramic composites: A review of toughening mechanisms and demonstration of micropillar compression for interface property extraction. *J. Mater. Res.* **33,** 424–439 (2018).
25. Marshall, D. B. & Oliver, W. C. Measurement of Interfacial Mechanical Properties in Fiber-Reinforced Ceramic Composites. *J. Am. Ceram. Soc.* **70,** 542–548 (1987).
26. Kim, T. T., Mall, S. & Zawada, L. P. Fatigue Characterization of a Melt-Infiltrated Woven HI-NIC-S/BN/SIC Ceramic Matrix Composite (CMC) Using a Unique Combustion Test Facility. in *Mechanical Properties and Performance of Engineering Ceramics and Composites IV* 103–115 (John Wiley & Sons, Inc., 2009). doi:10.1002/9780470584262.ch9
27. Hilmas, A. M., Sevener, K. M. & Halloran, J. W. Damage evolution in SiC/SiC unidirectional composites by X-ray tomography. *J. Am. Ceram. Soc.* **103,** 3436–3447 (2020).
28. Longbiao, L. Modeling first matrix cracking stress of fiber-reinforced ceramic-matrix composites considering fiber fracture. *Theor. Appl. Fract. Mech.* **92,** 24–32 (2017).
29. Morscher, G. N., Yun, H. M. & DiCarlo, J. A. In-Plane Cracking Behavior and Ultimate Strength for 2D Woven and Braided Melt-Infiltrated SiC/SiC Composites Tensile Loaded in Off-Axis Fiber Directions. *J. Am. Ceram. Soc.* **90,** 3185–3193 (2007).
30. Udayakumar, A., Stalin, M., Abhayalakshmi, M. B., Hariharan, R. & Balasubramanian, M. Effect of thermal cycling of SiCf/SiC composites on their mechanical properties. *J. Nucl. Mater.* **442,** S384–S389 (2013).
31. Curtin, W. A. Theory of Mechanical Properties of Ceramic-Matrix Composites. *J. Am. Ceram. Soc.* **74,** 2837–2845 (1991).
32. Budiansky, B., Hutchinson, J. W. & Evans, A. G. Matrix fracture in fiber-reinforced ceramics. *J. Mech. Phys. Solids* **34,** 167–189 (1986).
33. Marshall, D. B., Cox, B. N. & Evans, A. G. The Mechanics of Matrix Cracking in Brittle-Matrix Fibre Composites. *Acta Metall.* **33,** 2013–2021 (1985).
34. Hsueh, C. H., Rebillat, F., Lamon, J. & Lara-Curzio, E. Analyses of fiber push-out tests

performed on Nicalon/SiC composites with tailored interfaces. *Compos. Eng.* **5,** 1387–1401 (1995).

35. Shetty, D. K. Shear-Lag Analysis of Fiber Push-Out (Indentation) Tests for Estimating Interfacial Friction Stress in Ceramic-Matrix Composites. *J. Am. Ceram. Soc.* **71,** C-107-C-109 (1988).
36. Kerans, R. J. & Parthasarathy, T. A. Theoretical Analysis of the Fiber Pullout and Pushout Tests. *J. Am. Ceram. Soc.* **74,** 1585–1596 (1991).
37. Pompidou, S. & Lamon, J. Analysis of crack deviation in ceramic matrix composites and multilayers based on the Cook and Gordon mechanism. *Compos. Sci. Technol.* **67,** 2052–2060 (2007).
38. He, M. Y., Evans, A. G. & Hutchinson, J. W. Crack deflection at an interface between dissimilar elastic materials: Role of residual stresses. *Int. J. Solids Struct.* **31,** 3443–3455 (1994).
39. Sun, X. *et al.* Oxidation resistance of SiC/SiC composites containing SiBC matrix fabricated by liquid silicon infiltration. *J. Eur. Ceram. Soc.* **38,** 479–485 (2018).
40. Hsueh, C.-H. Interfacial debonding and fiber pull-out stresses of fiber-reinforced composites VII:improved analyses for bonded interfaces. *Mater. Sci. Eng. A* **154,** 125–132 (1992).
41. Carrère, N., Martin, E. & Lamon, J. The influence of the interphase and associated interfaces on the deflection of matrix cracks in ceramic matrix composites. *Compos. Part A Appl. Sci. Manuf.* **31,** 1179–1190 (2000).
42. Brennan, J. J. Interfacial Chemistry and Bonding in Fiber Reinforced Glass and Glass-Ceramic Matrix Composites. in *Ceramic Microstructures '86* 387–399 (Springer US, 1987). doi:10.1007/978-1-4613-1933-7_40
43. Sun, E. Y., Nutt, S. R. & Brennan, J. J. Interfacial Microstructure and Chemistry of SiC/BN Dual-Coated Nicalon-Fiber-Reinforced Glass-Ceramic Matrix Composites. *J. Am. Ceram. Soc.* **77,** 1329–1339 (1994).
44. Brunner, A. J. & Williams, J. G. Mode II fracture testing of composites: a new look at an old problem. *Eng. Fract. Mech.* **73,** 2443–2455 (2006).
45. Yin, X. W., Cheng, L. F., Zhang, L. T., Travitzky, N. & Greil, P. Fibre-reinforced multifunctional SiC matrix composite materials. *Int. Mater. Rev.* **62,** 117–172 (2017).
46. Zhao, S. *et al.* Design, Fabrication, Characterization and Simulation of PIP-SiC/SiC Composites. *Mater. Contin.* **42,** 103–124 (2014).
47. Dugne, O. *et al.* Interface characterization by TEM, AES and SIMS in tough SiC (ex-PCS) fibre-SiC (CVI) matrix composites with a BN interphase. *J. Mater. Sci.* **28,** 3409–3422 (1993).
48. Callaway, E. B., Christodoulou, P. G. & Zok, F. W. Deformation, rupture and sliding of fiber coatings in ceramic composites. *J. Mech. Phys. Solids* **132,** 103673 (2019).
49. Baste, S. Inelastic behaviour of ceramic-matrix composites. *Compos. Sci. Technol.* **61,** 2285–2297 (2001).
50. Calomino, A. & Verrilli, M. Ceramic Matrix Composite Vane Subelement Fabrication. in *Volume 2: Turbo Expo 2004* 401–407 (ASME, 2004). doi:10.1115/GT2004-53974

51. Wang, P., Liu, F., Wang, H., Li, H. & Gou, Y. A review of third generation SiC fibers and SiCf/SiC composites. *J. Mater. Sci. Technol.* **35,** 2743–2750 (2019).

52. Naslain, R. Design, preparation and properties of non-oxide CMCs for application in engines and nuclear reactors: an overview. *Compos. Sci. Technol.* **64,** 155–170 (2004).

53. Zawada, L. P., Staehler, J. & Steel, S. Consequence of Intermittent Exposure to Moisture and Salt Fog on the High-Temperature Fatigue Durability of Several Ceramic-Matrix Composites. *J. Am. Ceram. Soc.* **86,** 1282–1291 (2003).

54. Schubert, U. Making and Breaking of Si□E(E= C, Si) Bonds by Oxidative Addition and Reductive Elimination Reactions. *Angew. Chemie Int. Ed. English* **33,** 419–421 (1994).

55. Opila, E. J., Robinson, R. C. & Verrilli, M. J. Borosilicate Glass-Induced Fiber Degradation of SiC/BN/SiC Composites Exposed in Combustion Environments. *Int. J. Appl. Ceram. Technol.* **13,** 434–442 (2016).

56. Wang, H. *et al.* KD-S SiCf/SiC composites with BN interface fabricated by polymer infiltration and pyrolysis process. *J. Adv. Ceram.* **7,** 169–177 (2018).

57. Simon, C., Rebillat, F., Herb, V. & Camus, G. Monitoring damage evolution of SiCf/[SiBC]m composites using electrical resistivity: Crack density-based electromechanical modeling. *Acta Mater.* **124,** 579–587 (2017).

58. Zinkle, S. J., Terrani, K. A., Gehin, J. C., Ott, L. J. & Snead, L. L. Accident tolerant fuels for LWRs: A perspective. *J. Nucl. Mater.* **448,** 374–379 (2014).

59. Jimenez, O., Bagheri, H., McClain, J., Ridler, K. & Bornemisza, T. CSGT: Final Design and Test of a Ceramic Hot Section. in *Volume 1: Turbo Expo 2003* 685–692 (ASME, 2003). doi:10.1115/GT2003-38978

60. Corman, G. S., Brun, M. K. & Luthra, K. L. SiC Fiber Reinforced SiC-Si Matrix Composites Prepared by Melt Infiltration (MI) for Gas Turbine Engine Applications. in *Volume 4: Manufacturing Materials and Metallurgy; Ceramics; Structures and Dynamics; Controls, Diagnostics and Instrumentation; Education; IGTI Scholar Award; General* V004T02A004 (ASME, 1999). doi:10.1115/99-GT-234

61. Ogbuji, L. U. J. . Pest-resistance in SiC/BN/SiC composites. *J. Eur. Ceram. Soc.* **23,** 613–617 (2003).

62. Prewo, K. M. Tension and flexural strength of silicon carbide fibre-reinforced glass ceramics. *J. Mater. Sci.* **21,** 3590–3600 (1986).

63. Rebillat, F. *et al.* Properties of Multilayered Interphases in SiC/SiC Chemical-Vapor-Infiltrated Composites with “Weak” and “Strong” Interfaces. *J. Am. Ceram. Soc.* **81,** 2315–2326 (2005).

64. Bouillon, E. *et al.* Conversion mechanisms of a polycarbosilane precursor into an SiC-based ceramic material. *J. Mater. Sci.* **26,** 1333–1345 (1991).

65. Sauder, C., Brusson, A. & Lamon, J. Influence of Interface Characteristics on the Mechanical Properties of Hi-Nicalon type-S or Tyranno-SA3 Fiber-Reinforced SiC/SiC Minicomposites. *Int. J. Appl. Ceram. Technol.* **7,** 291–303 (2010).

66. Yang, W. *et al.* Interfacial characterization of CVI-SiC/SiC composites. *J. Nucl. Mater.* **307–311,** 1088–1092 (2002).

67. Cabet. Review: Oxidation of SiC/SiC Composites in Low Oxidising and High Temperature Environment. *Mater. Issues Gener. IV Syst.* (2008). doi:10.1007/978-1-4020-8422-5

68. Frazer, D. *et al.* Localized mechanical property assessment of SiC/SiC composite materials. *Compos. Part A Appl. Sci. Manuf.* **70,** 93–101 (2015).

69. Huguet-Garcia, J. *et al.* In situ TEM annealing of ion-amorphized Hi Nicalon S and Tyranno SA3 SiC fibers. *Nucl. Instruments Methods Phys. Res. Sect. B Beam Interact. with Mater. Atoms* **374,** 76–81 (2016).

70. Hay, R. S. *et al.* Hi-NicalonTM-SSiC Fiber Oxidation and Scale Crystallization Kinetics. *J. Am. Ceram. Soc.* **94,** 3983–3991 (2011).

71. Kim, H.-E. & Moorhead, A. J. Strength of Nicalon Silicon Carbide Fibers Exposed to High-Temperature Gaseous Environments. *J. Am. Ceram. Soc.* **74,** 666–669 (1991).

72. Bender, B. A., Wallace, J. S. & Schrodt, D. J. Effect of thermochemical treatments on the strength and microstructure of SiC fibres. *J. Mater. Sci.* **26,** 970–976 (1991).

73. Terrani, K. A. *et al.* Silicon Carbide Oxidation in Steam up to 2 MPa. *J. Am. Ceram. Soc.* **97,** 2331–2352 (2014).

74. Gauthier, W. & Lamon, J. Fatigue statique de monofilaments et de fils SiC Hi-Nicalon à 500 °C et 800 °C. *Rev. des Compos. des Matériaux Avancés* **16,** 221 (2006).

75. Wing, B. L. & Halloran, J. W. Microstress in the matrix of a melt-infiltrated SiC/SiC ceramic matrix composite. *J. Am. Ceram. Soc.* **100,** 5286–5294 (2017).

76. Shin, D.-W., Park, S. S., Choa, Y.-H. & Niihara, K. Silicon/Silicon Carbide Composites Fabricated by Infiltration of a Silicon Melt into Charcoal. *J. Am. Ceram. Soc.* **82,** 3251–3253 (2004).

77. Morscher, G. N., Yun, H. M., DiCarlo, J. A. & Thomas-Ogbuji, L. Effect of a Boron Nitride Interphase That Debonds between the Interphase and the Matrix in SiC/SiC Composites. *J. Am. Ceram. Soc.* **87,** 104–112 (2004).

78. Kollins, K., Przybyla, C. & Amer, M. S. Residual stress measurements in melt infiltrated SiC/SiC ceramic matrix composites using Raman spectroscopy. *J. Eur. Ceram. Soc.* **38,** 2784–2791 (2018).

79. Kingery, W. D. Note on Thermal Expansion and Microstresses in Two-Phase Compositions. *J. Am. Ceram. Soc.* **40,** 351–352 (1957).

80. Reich, S. *et al.* Resonant Raman scattering in cubic and hexagonal boron nitride. *Phys. Rev. B* **71,** (2005).

81. Carminati, P., Jacques, S. & Rebillat, F. Oxidation/corrosion of BN-based coatings as prospective interphases for SiC/SiC composites. *J. Eur. Ceram. Soc.* **41,** 3120–3131 (2021).

82. Wu, H., Chen, M., Wei, X., Ge, M. & Zhang, W. Deposition of BN interphase coatings from B-trichloroborazine and its effects on the mechanical properties of SiC/SiC composites. *Appl. Surf. Sci.* **257,** 1276–1281 (2010).

83. Lowden, R. A. & More, K. L. The Effect of Fiber Coatings on Interfacial Shear Strength and the Mechanical Behavior of Ceramic Composites. *MRS Proc.* **170,** 205 (1989).

84. Yun, H. M., Dicarlo, J. A., Ogbuji, L. T. & Chen, Y. L. Tensile Behavior of As-Fabricated

and Burner-Rig Exposed SiC/SiC Composites with Hi-Nicalon Type-S Fibers. in *Ceramic Engineering and Science Proceedings* 571–580 (John Wiley & Sons, Inc., 2002). doi:10.1002/9780470294741.ch67

85. Windisch, C. F., Henager, C. H., Springer, G. D. & Jones, R. H. Oxidation of the Carbon Interface in Nicalon-Fiber-Reinforced Silicon Carbide Composite. *J. Am. Ceram. Soc.* **80,** 569–574 (1997).

86. Filipuzzi, L., Camus, G., Naslain, R. & Thebault, J. Oxidation Mechanisms and Kinetics of 1D-SiC/C/SiC Composite Materials: I, An Experimental Approach. *J. Am. Ceram. Soc.* **77,** 459–466 (1994).

87. Pippel, E. *et al.* CVD-coated boron nitride on continuous silicon carbide fibres: structure and nanocomposition. *Journal of the European Ceramic Society* **20,** 1837–1844 (2000).

88. Wang, S. & Zheng, Y. Effect of different thickness h-BN coatings on interface shear strength of quartz fiber reinforced SiOCN composite. *Appl. Surf. Sci.* **292,** 876–879 (2014).

89. Udayakumar, A., Sri Ganesh, A., Raja, S. & Balasubramanian, M. Effect of intermediate heat treatment on mechanical properties of SiCf/SiC composites with BN interphase prepared by ICVI. *J. Eur. Ceram. Soc.* **31,** 1145–1153 (2011).

90. Wing, B. Residual Stresses and Oxidation of Silicon Carbide Fiber Reinforced Silicon Carbide Composites. *Doctoral Dissertation* (University of Michigan, 2016).

91. Corman, G. S. & Luthra, K. L. Silicon Melt Infiltrated Ceramic Composites (HiPerComp^{TM}). in *Handbook of Ceramic Composites* 99–115 (Springer US, 2005). doi:10.1007/0-387-23986-3_5

92. Jones, R. H. & Henager, C. H. Subcritical crack growth processes in SiC/SiC ceramic matrix composites. *J. Eur. Ceram. Soc.* **25,** 1717–1722 (2005).

93. Cofer, C. G. & Economy, J. Oxidative and hydrolytic stability of boron nitride — A new approach to improving the oxidation resistance of carbonaceous structures. *Carbon* **33,** 389–395 (1995).

94. Shaffer, P. T. B. Solubility of boron in alpha silicon carbide. *Mater. Res. Bull.* **5,** 519–521 (1970).

95. Newsome, G., Snead, L. L., Hinoki, T., Katoh, Y. & Peters, D. Evaluation of neutron irradiated silicon carbide and silicon carbide composites. *J. Nucl. Mater.* **371,** 76–89 (2007).

96. Mueller, W. M., Moosburger-Will, J., Sause, M. G. R. & Horn, S. Microscopic analysis of single-fiber push-out tests on ceramic matrix composites performed with Berkovich and flat-end indenter and evaluation of interfacial fracture toughness. *J. Eur. Ceram. Soc.* **33,** 441–451 (2013).

97. Bertrand, S., Forio, P., Pailler, R. & Lamon, J. Hi-Nicalon/SiC Minicomposites with (Pyrocarbon/SiC) $_n$ Nanoscale Multilayered Interphases. *J. Am. Ceram. Soc.* **82,** 2465–2473 (1999).

98. Wheeler, J. M., Armstrong, D. E. J., Heinz, W. & Schwaiger, R. High temperature nanoindentation: The state of the art and future challenges. *Curr. Opin. Solid State Mater. Sci.* **19,** 354–366 (2015).

99. Desaeger, M. & Verpoest, I. On the use of the micro-indentation test technique to measure

the interfacial shear strength of fibre-reinforced polymer composites. *Compos. Sci. Technol.* **48,** 215–226 (1993).

100. Karch, J., Birringer, R. & Gleiter, H. Ceramics ductile at low temperature. *Nature* **330,** 556–558 (1987).

101. Rodríguez, M., Molina-Aldareguía, J. M., González, C. & LLorca, J. A methodology to measure the interface shear strength by means of the fiber push-in test. *Compos. Sci. Technol.* **72,** 1924–1932 (2012).

102. Nanoindentation - Nanohardness Testers NanoScan. Available at: http://nanoscan.info/eng/methods/nanoindentation. (Accessed: 31st May 2021)

103. Oliver, W. C. & Pharr, G. M. Measurement of hardness and elastic modulus by instrumented indentation: Advances in understanding and refinements to methodology. *J. Mater. Res.* (2004).

104. Field, J. S. & Swain, M. V. Determining the mechanical properties of small volumes of material from submicrometer spherical indentations. *J. Mater. Res.* **10,** 101–112 (1995).

105. Medina M, C. *et al.* Comparison of push-in and push-out tests for measuring interfacial shear strength in nano-reinforced composite materials. *J. Compos. Mater.* **50,** 1651–1659 (2016).

106. Tabiai, I., Delorme, R., Therriault, D. & Levesque, M. In-situ Full Field Measurements During Inter-Facial Debonding in Single Fiber Composite Under Transverse Load. *Exp. Mech.* **58,** 1451–1467 (2018).

107. Hull, D. & Clyne, T. W. *An Introduction to Composite Materials*. (Cambridge University Press, 1996). doi:10.1017/CBO9781139170130

108. Lawrence, P. Some theoretical considerations of fibre pull-out from an elastic matrix. *J. Mater. Sci.* **7,** 1–6 (1972).

109. Bechel, V. T. & Sottos, N. R. Application of debond length measurements to examine the mechanics of fiber pushout. *J. Mech. Phys. Solids* **46,** 1675–1697 (1998).

110. Oliver, W. C. & Pharr, G. M. An improved technique for determining hardness and elastic modulus using load and displacement sensing indentation experiments. *J. Mater. Res.* **7,** 1564–1583 (1992).

111. Hsueh, C.-H. Evaluation of Interfacial Properties of Fiber-Reinforced Ceramic Composites Using a Mechanical Properties Microprobe. *J. Am. Ceram. Soc.* **76,** 3041–3050 (1993).

112. Parthasarathy, T. A., Barlage, D. R., Jero, P. D. & Kerans, R. J. Effect of Interfacial Roughness Parameters on the Fiber Pushout Behavior of a Model Composite. *J. Am. Ceram. Soc.* **77,** 3232–3236 (1994).

113. Herbreteau, M., Jouannigot, S., Weisbecker, P., Coradi, A. & Martin, E. A New Push-Out Procedure for the Evaluation of Interfacial Properties of SiC/SiC Composites. in *ECCM15 - 15TH European Conference On Composite Materials, Venice, Italy* 2–4 (2012).

114. Lamon, J., Rebillat, F. & Evans, A. G. Microcomposite Test Procedure for Evaluating the Interface Properties of Ceramic Matrix Composites. *J. Am. Ceram. Soc.* **78,** 401–405 (1995).

115. Mandell, J., Grande, D., Tsiang, T.-H. & McGarry, F. Modified Mircodebonding Test for Direct In Situ Fiber/Matrix Bond Strength Determination in Fiber Composites. in *Composite Materials: Testing and Design (Seventh Conference)* 87-87–22 (ASTM International, 1986).

doi:10.1520/STP35343S

116. Morscher, G. N. & Cawley, J. D. Intermediate temperature strength degradation in SiC/SiC composites. *J. Eur. Ceram. Soc.* **22,** 2777–2787 (2002).

117. Kerans, R. J., Hay, R. S., Parthasarathy, T. A. & Cinibulk, M. K. Interface Design for Oxidation-Resistant Ceramic Composites. *J. Am. Ceram. Soc.* **85,** 2599–2632 (2004).

118. Boakye, E. E. *et al.* Processing and Testing of RE2Si2O7 Fiber-Matrix Interphases for SiC-SiC Composites. *J. Am. Ceram. Soc.* **99,** 415–423 (2016).

119. Zhang, L., Ren, C., Zhou, C., Xu, H. & Jin, X. Single fiber push-out characterization of interfacial mechanical properties in unidirectional CVI-C/SiC composites by the nano-indentation technique. *Applied Surface Science* **357,** 1427–1433 (2015).

120. Rollin, M., Jouannigot, S. & Pailler, R. Characterization of fibre/matrix interfaces in carbon/carbon composites. *Compos. Sci. Technol.* **69,** 1442–1446 (2009).

121. Kallas, M. N., Koss, D. A., Hahn, H. T. & Hellmann, J. R. Interfacial stress state present in a 'thin-slice' fibre push-out test. *J. Mater. Sci.* **27,** 3821–3826 (1992).

122. Bechel, V. T. & Sottos, N. R. The effect of residual stresses and sample preparation on progressive debonding during the fiber push-out test. *Compos. Sci. Technol.* **58,** 1741–1751 (1998).

123. Tanoglu, M., McKnight, S. ., Palmese, G. . & Gillespie Jr, J. . The effects of glass-fiber sizings on the strength and energy absorption of the fiber/matrix interphase under high loading rates. *Compos. Sci. Technol.* **61,** 205–220 (2001).

124. Molina-Aldareguía, J. M., Rodríguez, M., González, C. & LLorca, J. An experimental and numerical study of the influence of local effects on the application of the fibre push-in test. *Philos. Mag.* **91,** 1293–1307 (2011).

125. Xu, T. *et al.* Evaluation of the Effect of Thermal Oxidation and Moisture on the Interfacial Shear Strength of Unidirectional IM7/BMI Composite by Fiber Push-in Nanoindentation. *Exp. Mech.* **58,** 111–123 (2018).

126. Hsueh, C.-H. Slice Compression Tests Versus Fiber Push-In Tests. *J. Compos. Mater.* **28,** 638–655 (1994).

127. Weihs, T. P. & Nix, W. D. Experimental Examination of the Push-Down Technique for Measuring the Sliding Resistance of Silicon Carbide Fibers in a Ceramic Matrix. *J. Am. Ceram. Soc.* **74,** 524–534 (1991).

128. Lewinsohn, C. A., Henager, C. H., Jones, R. H. & Eldridge, J. I. Measuring Interphase Recession by Fiber Push-In Testing. *J. Am. Ceram. Soc.* **84,** 866–868 (2001).

129. Bhushan, B. & Ko, P. L. Introduction to Tribology. *Appl. Mech. Rev.* **56,** B6–B7 (2003).

130. Kim, K.-S. & Tsai, K.-H. Study of stick slip behavior in interface friction using optical fiber pull-out experiment. in *Second International Conference on Photomechanics and Speckle Metrology: Speckle Techniques, Birefringence Methods, and Applications to Solid Mechanics; Moiré Techniques, Holographic Interferometry, Optical NDT, and Applications to Fluid Mechanics* **1554,** 49 (SPIE, 1991).

131. Matoy, K. *et al.* A comparative micro-cantilever study of the mechanical behavior of silicon based passivation films. *Thin Solid Films* **518,** 247–256 (2009).

132. Jaya B, N., Jayaram, V. & Biswas, S. K. A new method for fracture toughness determination of graded (Pt,Ni)Al bond coats by microbeam bend tests. *Philos. Mag.* **92,** 3326–3345 (2012).

133. Liu, S. *et al.* Measuring the fracture resistance of hard coatings. *Appl. Phys. Lett.* **102,** 171907 (2013).

134. Sebastiani, M., Johanns, K. E., Herbert, E. G., Carassiti, F. & Pharr, G. M. A novel pillar indentation splitting test for measuring fracture toughness of thin ceramic coatings. *Philos. Mag.* **95,** 1928–1944 (2015).

135. Shih, C., Katoh, Y., Leonard, K. J., Bei, H. & Lara-Curzio, E. Determination of interfacial mechanical properties of ceramic composites by the compression of micro-pillar test specimens. *J. Mater. Sci.* **48,** 5219–5224 (2013).

136. Kabel, J. *et al.* Micro-mechanical evaluation of SiC-SiC composite interphase properties and debond mechanisms. *Compos. Part B Eng.* **131,** 173–183 (2017).

137. Sebastiani, M., Johanns, K. E., Herbert, E. G. & Pharr, G. M. Measurement of fracture toughness by nanoindentation methods: Recent advances and future challenges. *Current Opinion in Solid State and Materials Science* **19,** 324–333 (2015).

138. Ast, J. *et al.* A review of experimental approaches to fracture toughness evaluation at the micro-scale. *Mater. Des.* **173,** 107762 (2019).

139. Wu, C., Huang, R. & Liechti, K. M. Characterizing Interfacial Sliding of Through-Silicon-Via by Nano-Indentation. *IEEE Trans. Device Mater. Reliab.* **17,** 355–363 (2017).

140. De Meyere, R. M. G. *et al.* A novel trench fibre push-out method to evaluate interfacial failure in long fibre composites. *J. Mater. Res.* 1–10 (2021). doi:10.1557/s43578-021-00153-1

141. Kabel, J. *et al.* A novel fiber-fretting test for tribological characterization of the fiber/matrix interface. *Compos. Part B Eng.* **206,** 108535 (2021).

142. Bowden, F., Bowden, F. & Tabor, D. *The friction and lubrication of solids*. **1** (2001).

143. Kheradmand, N., Dake, J., Barnoush, A. & Vehoff, H. Novel methods for micromechanical examination of hydrogen and grain boundary effects on dislocations. in *Philosophical Magazine* **92,** 3216–3230 (Taylor & Francis Group , 2012).

144. Kato, N. I. Reducing focused ion beam damage to transmission electron microscopy samples. *Journal of Electron Microscopy* **53,** 451–458 (2004).

145. Ghoniem, N. M., Busso, E. P., Kioussis, N. & Huang, H. Multiscale modelling of nanomechanics and micromechanics: An overview. in *Philosophical Magazine* **83,** 3475–3528 (Taylor & Francis Group , 2003).

146. Hall, D. A., Steuwer, A., Cherdhirunkorn, B., Withers, P. J. & Mori, T. Micromechanics of residual stress and texture development due to poling in polycrystalline ferroelectric ceramics. *J. Mech. Phys. Solids* **53,** 249–260 (2005).

147. Nieto, A., Bisht, A., Lahiri, D., Zhang, C. & Agarwal, A. Graphene reinforced metal and ceramic matrix composites: a review. *International Materials Reviews* **62,** 241–302 (2017).

148. Edwards, T. E. J., Maeder, X., Michler, J. & Ast, J. Correlative in situ total and elastic strain mapping on micromechanical test pieces by DIC and HR-EBSD. *Nanomechanical Test. Mater. Res. Dev. VII* (2019).

149. Sabaté, N. *et al.* Measurement of residual stress by slot milling with focused ion-beam equipment. *J. Micromechanics Microengineering* **16,** 254–259 (2006).

150. Zhao, L. G., Warrior, N. A. & Long, A. C. A micromechanical study of residual stress and its effect on transverse failure in polymer-matrix composites. *Int. J. Solids Struct.* **43,** 5449–5467 (2006).

151. Song, X. *et al.* Residual stress measurement in thin films using the semi-destructive ring-core drilling method using Focused Ion Beam. in *Procedia Engineering* **10,** 2190–2195 (Elsevier Ltd, 2011).

152. Zayachuk, Y., Karamched, P., Deck, C., Hosemann, P. & Armstrong, D. E. J. Linking microstructure and local mechanical properties in SiC-SiC fiber composite using micromechanical testing. *Acta Mater.* **168,** 178–189 (2019).

153. Lunt, A. J. G. *et al.* Full in-plane strain tensor analysis using the microscale ring-core FIB milling and DIC approach. *J. Mech. Phys. Solids* **94,** 47–67 (2016).

154. Candler, R. N. *et al.* Impact of geometry on thermoelastic dissipation in micromechanical resonant beams. *J. Microelectromechanical Syst.* **15,** 927–934 (2006).

155. Rueschhoff, L. M., Carney, C. M., Apostolov, Z. D. & Cinibulk, M. K. Processing of fiber-reinforced ultra-high temperature ceramic composites: A review. *Int. J. Ceram. Eng. Sci.* **2,** 22–37 (2020).

156. Chen, H.-F. *et al.* Recent progress in thermal/environmental barrier coatings and their corrosion resistance. *Rare Met. 2019 395* **39,** 498–512 (2019).

157. Min, J., Harris, D. & Ting, J. Advances in Ceramic Matrix Composite Blade Damping Characteristics for Aerospace Turbomachinery Applications. in *52nd AIAA/ASME/ASCE/AHS/ASC Structures, Structural Dynamics and Materials Conference* (American Institute of Aeronautics and Astronautics, 2011). doi:10.2514/6.2011-1784

158. Morscher, G. N., Hurwitz, F., Yun, H. M. & Gray, H. R. High temperature Si-doped BN interphases for woven SiC/SiC composites. *Ceram. Eng. Sci. Proc.* **23,** 295–304 (2002).

159. Keller, K. A., Mah, T.-I., Parthasarathy, T. A. & Cooke, C. M. Fugitive Interfacial Carbon Coatings for Oxide/Oxide Composites. *J. Am. Ceram. Soc.* **83,** 329–336 (2004).

160. Jacobson, N. S., Morscher, G. N., Bryant, D. R. & Tressler, R. E. High-Temperature Oxidation of Boron Nitride: II, Boron Nitride Layers in Composites. *J. Am. Ceram. Soc.* **82,** 1473–1482 (2004).

161. Morscher, G. N., Bryant, D. R. & Tressler, R. E. Environmental Durability of BN-Based Interphases (for SiCf/SiCm Composites) in H2O Containing Atmospheres at Intermediate Temperatures. in *Proceedings of the 21st Annual Conference on Composites, Advanced Ceramics, Materials, and Structures—A: Ceramic Engineering and Science Proceedings, Volume 18* 525–534 (1997). doi:10.1002/9780470294437.ch58

162. Poerschke, D. L., Rossol, M. N. & Zok, F. W. Intermediate temperature oxidative strength degradation of a SiC/SiNC composite with a polymer-derived matrix. *J. Am. Ceram. Soc.* **100,** 1606–1617 (2017).

163. Jacques, S., Rapaud, O., Parolla, S. & Verdenelli, M. Which alternative to the pyrocarbon interphase in ceramic matrix composites? *Ann. Chim. Sci. des Matériaux* **30,** 609–620 (2005).

164. Lorrette, C., Weisbecker, P., Jacques, S., Pailler, R. & Goyhénèche, J. M. Deposition and characterization of hex-BN coating on carbon fibres using tris(dimethylamino)borane precursor. *J. Eur. Ceram. Soc.* **27,** 2737–2743 (2007).

165. Jacques, S., Lopez-Marure, A., Vincent, C., Vincent, H. & Bouix, J. SiC/SiC minicomposites with structure-graded BN interphases. *J. Eur. Ceram. Soc.* **20,** 1929–1938 (2000).

166. Murthy, T. S. R. C. *et al.* Role of rare earth oxide particles on the oxidation behaviour of silicon carbide coated 2.5D carbon fibre preforms. *Open Ceram.* **2,** 100018 (2020).

167. Opila, E. J. Variation of the Oxidation Rate of Silicon Carbide with Water-Vapor Pressure. *J. Am. Ceram. Soc.* **82,** 625–636 (2004).

168. Bertrand, S., Droillard, C., Pailler, R., Bourrat, X. & Naslain, R. TEM structure of (PyC/SiC)n multilayered interphases in SiC/SiC composites. *J. Eur. Ceram. Soc.* **20,** 1–13 (2000).

169. Shimoda, K., Kohyama, A. & Hinoki, T. High mechanical performance SiC/SiC composites by NITE process with tailoring of appropriate fabrication temperature to fiber volume fraction. *Compos. Sci. Technol.* **69,** 1623–1628 (2009).

170. Katoh, Y. *et al.* Current status and recent research achievements in SiC/SiC composites. *J. Nucl. Mater.* **455,** 387–397 (2014).

171. Monteverde, F., Bellosi, A. & Guicciardi, S. Processing and properties of zirconium diboride-based composites. *J. Eur. Ceram. Soc.* **22,** 279–288 (2002).

172. Yun, H. M., Gyekenyesi, J. Z., Chen, Y. L., Wheeler, D. R. & Dicarlo, J. A. Tensile Behavior of SiC\SiC Composites Reinforced by Treated Sylramic SiC Fibers. in *25th Annual Conference on Composites, Advanced Ceramics, Materials, and Structures: A: Ceramic Engineering and Science Proceedings, Volume 22, Issue 3* 521–531 (John Wiley & Sons, Inc., 2002). doi:10.1002/9780470294680.ch60

173. Li, H., Morscher, G. N., Lee, J. & Lee, W. Y. Tensile and Stress-Rupture Behavior of SiC/SiC Minicomposite Containing Chemically Vapor Deposited Zirconia Interphase. *J. Am. Ceram. Soc.* **87,** 1726–1733 (2004).

174. Naslain, R. *et al.* Boron Nitride Interphase in Ceramic-Matrix Composites. *J. Am. Ceram. Soc.* **74,** 2482–2488 (1991).

175. More, K. L. *et al.* High-Temperature Stability of SiC-Based Composites in High-Water-Vapor-Pressure Environments. *J. Am. Ceram. Soc.* **86,** 1272–1281 (2003).

176. Ogbuji, L. U. J. T. A Pervasive Mode of Oxidative Degradation in a SiC-SiC Composite. *J. Am. Ceram. Soc.* **81,** 2777–2784 (2005).

177. Plaisantin, H., Jacques, S., Danet, J., Camus, G. & Delpouve, H. TEM characterization of turbostratic and rhombohedral BN interphases synthesized by chemical vapour infiltration in SiC/SiC-Si composites. *Mater. Charact.* **172,** 110857 (2021).

178. Xu, W., Zok, F. W. & McMeeking, R. M. Model of Oxidation-Induced Fiber Fracture in SiC/SiC Composites. *J. Am. Ceram. Soc.* **97,** 3676–3683 (2014).

179. Li, D., Zhang, C.-R., Li, B., Cao, F. & Wang, S.-Q. Preparation and mechanical properties of unidirectional boron nitride fibre reinforced silica matrix composites. *Materials & Design* **34,** 401–405 (2012).

180. Fang, G., Gao, X. & Song, Y. XFEM Analysis of the Effect of Fiber Volume Fraction on

Crack Propagation in Fiber Reinforced Ceramic Matrix Composites. in *IOP Conference Series: Materials Science and Engineering* **678,** 012027 (IOP Publishing Ltd, 2019).

181. Fang, G., Gao, X. & Song, Y. XFEM analysis of crack propagation in fiber-reinforced ceramic matrix composites with different interphase thicknesses. *Compos. Interfaces* **27,** 327–340 (2020).

182. Chawla, N., Holmes, J. W. & Mansfield, J. E. Surface roughness characterization of Nicalon™ and HI-Nicalon™ ceramic fibers by atomic force microscopy. *Mater. Charact.* **35,** (1995).

183. Swaminathan, B. *et al.* Characterizing Early Damage Evolution in CMCs. in *International Conference and Exposition on Advanced Ceramics and Composites (ICACC) Presentation, Slide* 2 (2019).

184. Harris, T. K., Brookes, E. J. & Taylor, C. J. The effect of temperature on the hardness of polycrystalline cubic boron nitride cutting tool materials. *Int. J. Refract. Met. Hard Mater.* **22,** 105–110 (2004).

185. Petrescu, M. I. Boron nitride theoretical hardness compared to carbon polymorphs. *Diam. Relat. Mater.* **13,** 1848–1853 (2004).

186. Magazzeni, C. M. *et al.* Nanoindentation in multi-modal map combinations: a correlative approach to local mechanical property assessment. *J. Mater. Res. 2020 3611* **36,** 2235–2250 (2021).

187. Cherouali, H., Fantozzi, G., Reynaud, P. & Rouby, D. Analysis of interfacial sliding in brittle-matrix composites during push-out and push-back tests. *Mater. Sci. Eng. A* **250,** 169–177 (1998).

188. Parthasarathy, T. A., Jero, P. D. & Kerans, R. J. Extraction of interface properties from a fiber push-out test. *Scr. Metall. Mater.* **25,** 2457–2462 (1991).

189. Buet, E. *et al.* Influence of chemical and physical properties of the last generation of silicon carbide fibres on the mechanical behaviour of SiC/SiC composite. *J. Eur. Ceram. Soc.* **32,** 547–557 (2012).

190. Cardinale, G. F. *et al.* Analysis of residual stress in cubic boron nitride thin films using micromachined cantilever beams. *Diam. Relat. Mater.* **5,** 1295–1302 (1996).

191. Katoh, Y., Nozawa, T. & Snead, L. L. Mechanical Properties of Thin Pyrolitic Carbon Interphase SiC-Matrix Composites Reinforced with Near-Stoichiometric SiC Fibers. *J. Am. Ceram. Soc.* **88,** 3088–3095 (2005).

192. Callaway, E. B. & Zok, F. W. Weibull parameters obtained from dependence of fiber strength on fiber length and area. *J. Am. Ceram. Soc.* **101,** 4719–4731 (2018).

193. Kalton, A. F., Howard, S. J., Janczak-Rusch, J. & Clyne, T. W. Measurement of interfacial fracture energy by single fibre push-out testing and its application to the titanium–silicon carbide system. *Acta Mater.* **46,** 3175–3189 (1998).

194. Li, L. & Song, Y. An approach to estimate interface shear stress of ceramic matrix composites from hysteresis loops. *Appl. Compos. Mater.* **17,** 309–328 (2010).

195. Zawada, L. P., Pierce, J. L., Przybyla, C. P. & Katz, A. P. Evaluation of a Melt Infiltrated SiC/SiC Ceramic Matrix Composite. *Air Force Research Laboratory, Defense Technical*

Information Center, Technical Report (2017).

196. Przybyla, C. P. *et al.* Microstructure-sensitive enviro-mechanical response characterization and simulation in SiC/SiC ceramic matrix composites. in *ICCM International Conferences on Composite Materials* **2015–July,** (2015).

197. Zawada, L. P., Przybyla, C. & Pierce, J. L. Influence of Test Methodology and Environment on Stress Rupture Life of Nextel 720/AS. *Air Force Research Laboratory, Defense Technical Information Center, Technical Report* (2019).

198. Gauthier, W. & Lamon, J. Delayed Failure of Hi-Nicalon and Hi-Nicalon S Multifilament Tows and Single Filaments at Intermediate Temperatures (500°-800°C). *J. Am. Ceram. Soc.* **92,** 702–709 (2009).

199. Jacobson, N. S., Opila, E. J., Myers, D. L. & Copland, E. H. Thermodynamics of gas phase species in the Si–O–H system. *J. Chem. Thermodyn.* **37,** 1130–1137 (2005).

200. Gogotsi, Y. Oxidation and properties degradation of SiC fibres below 850 °C. *J. Mater. Sci. Lett.* **13,** 680–683 (1994).

201. Wagstaff, F. E. & Richards, K. J. Kinetics of Crystallization of Stoichiometric SiO2 Glass in H2O Atmospheres. *J. Am. Ceram. Soc.* **49,** 118–121 (1966).

202. Deal, B. E. & Grove, A. S. General Relationship for the Thermal Oxidation of Silicon. *J. Appl. Phys.* **36,** 3770–3778 (1965).

203. Parthasarathy, T. A., Przybyla, C. P., Hay, R. S. & Cinibulk, M. K. Modeling Environmental Degradation of SiC-Based Fibers. *J. Am. Ceram. Soc.* **99,** 1725–1734 (2016).

204. Shimoo, T., Okamura, K. & Morisada, Y. Active-to-passive oxidation transition for polycarbosilane-derived silicon carbide fibers heated in Ar-O2 gas mixtures. *J. Mater. Sci.* **37,** 1793–1800 (2002).

205. Jia, N., Bodet, R. & Tressler, R. E. Effects of Microstructural Instability on the Creep Behavior of Si-C-O (Nicalon) Fibers in Argon. *J. Am. Ceram. Soc.* **76,** 3051–3060 (1993).

206. Wilson, M. & Opila, E. A Review of SiC Fiber Oxidation with a New Study of Hi-Nicalon SiC Fiber Oxidation. *Adv. Eng. Mater.* **18,** 1698–1709 (2016).

207. Singhal, S. C. Oxidation kinetics of hot-pressed silicon carbide. *J. Mater. Sci.* **11,** 1246–1253 (1976).

208. Yun, H. M. & Dicarlo, J. A. Thermomechanical Behavior of Advanced SiC Fiber Multifilament Tows. in *Proceedings of the 20th Annual Conference on Composites, Advanced Ceramics, Materials, and Structures—B: Ceramic Engineering and Science Proceedings, Volume 17, Issue 4* 61–67 (John Wiley & Sons, Inc., 1996). doi:10.1002/9780470314876.ch5

209. Wing, B. L. & Halloran, J. W. Subsurface oxidation of boron nitride coatings on silicon carbide fibers in SiC/SiC ceramic matrix composites. *Ceram. Int.* **44,** 17499–17505 (2018).

210. Nasiri, N. Al, Patra, N., Ni, N., Jayaseelan, D. D. & Lee, W. E. Oxidation behaviour of SiC/SiC ceramic matrix composites in air. *J. Eur. Ceram. Soc.* **36,** 3293–3302 (2016).

211. Opila, E. J. Volatility of Common Protective Oxides in High-Temperature Water Vapor: Current Understanding and Unanswered Questions. *Mater. Sci. Forum* **461–464,** 765–774 (2004).

212. Bale, H. A. *et al.* Real-time quantitative imaging of failure events in materials under load at temperatures above 1,600°C. *Nat. Mater.* **12,** 40–46 (2013).

213. McFarland, B. & Opila, E. Boria Fluxing of SiC in Ceramic Matrix Composite Aeropropulsion Applications. *ECS Meet. Abstr.* **MA2015-01,** 1122 (2015).

214. Sheldon, B. W., Sun, E. Y., Nutt, S. R. & Brennan, J. J. Oxidation of BN-Coated SiC Fibers in Ceramic Matrix Composites. *J. Am. Ceram. Soc.* **79,** 539–543 (1996).

215. Jacobson, N., Farmer, S., Moore, A. & Sayir, H. High-Temperature Oxidation of Boron Nitride: I, Monolithic Boron Nitride. *J. Am. Ceram. Soc.* **82,** 393–398 (2004).

216. Quemard, L., Rebillat, F., Guette, A., Tawil, H. & Louchet-Pouillerie, C. Degradation mechanisms of a SiC fiber reinforced self-sealing matrix composite in simulated combustor environments. *J. Eur. Ceram. Soc.* **27,** 377–388 (2007).

217. Singh, D., Zhu, D., Zhu, Y. & Singh, M. (Mrityunjay). Design, development, and applications of engineering ceramics and composites. in *8th Pacific Rim Conference on Ceramic and Glass Technology, May 31-June 5, 2009, Vancouver, British Columbia* 336 (Wiley, 2010).

218. Arya, S. P. S. & D'Amico, A. Preparation, properties and applications of boron nitride thin films. *Thin Solid Films* **157,** 267–282 (1988).

219. Bansal, N. P. & Doremus, R. H. *Handbook of glass properties*. (Academic Press, 1986).

220. Nickel, K. G. Ceramic matrix composite corrosion models. *J. Eur. Ceram. Soc.* **25,** 1699–1704 (2005).

221. Matsuda, T. Stability to moisture for chemically vapour-deposited boron nitride. *J. Mater. Sci.* **24,** 2353–2357 (1989).

222. Diaz, O. G. *et al.* Degradation mechanisms of SiC/BN/SiC after low temperature humidity exposure. *J. Eur. Ceram. Soc.* **40,** 3863–3874 (2020).

223. Boike, M., Hilpert, K. & Muller, F. Thermodynamic Activities in B2O3-SiO2 Melts at 1475 K. *J. Am. Ceram. Soc.* **76,** 2809–2812 (1993).

224. Morscher, G. N. Tensile Stress Rupture of SiCf/SiCmMinicomposites with Carbon and Boron Nitride Interphases at Elevated Temperatures in Air. *J. Am. Ceram. Soc.* **80,** 2029–2042 (2005).

225. Parthasarathy, T. A., Mah, T., Folsom, C. A. & Katz, A. P. Microstructural Stability of Nicalon at 1000deg; C in Air after Exposure to Salt (NaCl) Water. *J. Am. Ceram. Soc.* **78,** 1992–1996 (1995).

226. Morscher, G. N., Hurst, J. & Brewer, D. Intermediate-Temperature Stress Rupture of a Woven Hi-Nicalon, BN-Interphase, SiC-Matrix Composite in Air. *J. Am. Ceram. Soc.* **83,** 1441–1449 (2000).

227. Saucedo-Mora, L. *et al.* In situ observation of mechanical damage within a SiC-SiC ceramic matrix composite. *J. Nucl. Mater.* **481,** 13–23 (2016).

228. Tang, S. & Hu, C. Design, Preparation and Properties of Carbon Fiber Reinforced Ultra-High Temperature Ceramic Composites for Aerospace Applications: A Review. *J. Mater. Sci. Technol.* **33,** 117–130 (2017).

229. Knauf, M. W., Przybyla, C. P., Ritchey, A. J., Trice, R. W. & Pipes, R. B. Residual stress

determination of silicon containing boron dopants in ceramic matrix composites. *J. Am. Ceram. Soc.* **102,** 2820–2829 (2018).

230. Anastassakis, E. Strain characterization of polycrystalline diamond and silicon systems. *J. Appl. Phys.* **86,** 249–258 (1999).

231. DiGregorio, J. F. & Furtak, T. E. Analysis of Residual Stress in 6H-SiC Particles within Al2O3/SiC Composites through Raman Spectroscopy. *J. Am. Ceram. Soc.* **75,** 1854–1857 (1992).

232. De Meyere, R. *et al.* Optimizing The Fibre Push-Out Method to Evaluate Interfacial Failure in SiC/BN/SiC Ceramic Matrix Composites. *J. Am. Ceram. Soc.* (2020).

233. Mazars, V. *et al.* Damage investigation and modeling of 3D woven ceramic matrix composites from X-ray tomography in-situ tensile tests. *Acta Mater.* **140,** 130–139 (2017).

234. Bumgardner, C. H., Baker, J. D., Ritchey, A. J. & Li, X. Probing the local creep mechanisms of SiC/SiC ceramic matrix composites with high-temperature nanoindentation. *J. Mater. Res.* 1–14 (2021). doi:10.1557/s43578-021-00128-2

235. Morales-Rodríguez, A., Reynaud, P., Fantozzi, G., Adrien, J. & Maire, E. Porosity analysis of long-fiber-reinforced ceramic matrix composites using X-ray tomography. *Scr. Mater.* **60,** 388–390 (2009).

236. Chateau, C. *et al.* In situ X-ray microtomography characterization of damage in SiC f /SiC minicomposites. *Compos. Sci. Technol.* **71,** 916–924 (2011).

237. Cloetens, P. *et al.* Observation of microstructure and damage in materials by phase sensitive radiography and tomography. *http://oasc12039.247realmedia.com/RealMedia/ads/click_lx.ads/www.aip.org/pt/adcenter/pdfcover_test/L-37/386502181/x01/AIP-PT/JAP_ArticleDL_092017/scilight717-1640x440.gif/434f71374e315a556e61414141774c75?x* (1998). doi:10.1063/1.364374

238. Croom, B. P., Xu, P., Lahoda, E. J., Deck, C. P. & Li, X. Quantifying the three-dimensional damage and stress redistribution mechanisms of braided SiC/SiC composites by in situ volumetric digital image correlation. *Scr. Mater.* **130,** 238–241 (2017).

239. Vagaggini, E., Domergue, J. -M & Evans, A. G. Relationships between Hysteresis Measurements and the Constituent Properties of Ceramic Matrix Composites: I, Theory. *J. Am. Ceram. Soc.* **78,** 2709–2720 (1995).

240. You, J. H. *et al.* Fiber push-out study of a copper matrix composite with an engineered interface: Experiments and cohesive element simulation. *Int. J. Solids Struct.* **46,** 4277–4286 (2009).

241. Thouless, M. D. Cracking and delamination of coatings. *J. Vac. Sci. Technol. A Vacuum, Surfaces, Film.* **9,** 2510–2515 (1991).

242. Buet, E. *et al.* Influence of surface fibre properties and textural organization of a pyrocarbon interphase on the interfacial shear stress of SiC/SiC minicomposites reinforced with Hi-Nicalon S and Tyranno SA3 fibres. *J. Eur. Ceram. Soc.* **34,** 179–188 (2014).

243. Vanswijgenhoven, E., Lambrinou, K., Wevers, M. & Van Der Biest, O. Comparative study of the surface roughness of Nicalon and Tyranno silicon carbide fibres. *Compos. Part A Appl. Sci. Manuf.* **29,** 1417–1423 (1998).

244. Gavalda Diaz, O., Axinte, D. A., Butler-Smith, P. & Novovic, D. On understanding the microstructure of SiC/SiC Ceramic Matrix Composites (CMCs) after a material removal process. *Mater. Sci. Eng. A* **743,** 1–11 (2019).

245. Groetsch, A. *et al.* Compressive behaviour of uniaxially aligned individual mineralised collagen fibres at the micro- and nanoscale. *Acta Biomater.* **89,** 313–329 (2019).

246. Li B.-S., Armstrong, D., Marrow, T. & Roberts, S. Measuring Fracture Resistance Behaviour of Tungsten Using Chevron-Notched Micro-Cantilevers. *Doctoral Thesis, University of Oxford* (2017).

247. Ishikawa, T. Recent developments of the SiC fiber Nicalon and its composites, including properties of the SiC fiber Hi-Nicalon for ultra-high temperature. *Compos. Sci. Technol.* **51,** 135–144 (1994).

248. Youngblood, G. E., Lewinsohn, C., Jones, R. H. & Kohyama, A. Tensile strength and fracture surface characterization of Hi-Nicalon™ SiC fibers. *J. Nucl. Mater.* **289,** 1–9 (2001).

249. Dukino, R. D. & Swain, M. V. Comparative Measurement of Indentation Fracture Toughness with Berkovich and Vickers Indenters. *J. Am. Ceram. Soc.* **75,** 3299–3304 (1992).